Molecular cloning, expression, purification, biochemical characterization and structure analysis of a novel obligate xylobiohydrolase (*Ac*GH30A) from *Acetivibrio clariflavus* ATCC 19732

PhD Thesis

by

YUMNAM ROBINSON SINGH

APRIL 2025

DEPARTMENT OF BIOSCIENCES AND BIOENGINEERING

INDIAN INSTITUTE OF TECHNOLOGY GUWAHATI

GUWAHATI 781039, ASSAM, INDIA

Molecular cloning, expression, purification, biochemical characterization and structure analysis of a novel obligate xylobiohydrolase (*Ac*GH30A) from *Acetivibrio clariflavus* ATCC 19732

A thesis submitted for the partial fulfillment of requirements for the award

of

DOCTOR OF PHILOSOPHY

by

YUMNAM ROBINSON SINGH

Under supervision of

Professor Arun Goyal

April 2025

BIOSCIENCES AND BIOENGINEERING
INDIAN INSTITUTE OF TECHNOLOGY GUWAHATI
GUWAHATI 781039, ASSAM, INDIA

Dedicated to my Parents

INDIAN INSTITUTE OF TECHNOLOGY GUWAHATI

DEPARTMENT OF BIOSCIENCES & BIOENGINEERING

STATEMENT

I do hereby declare that the content embodied in this thesis entitled as **"Molecular cloning, expression, purification, biochemical characterization and structure analysis of a novel obligate xylobiohydrolase (*Ac*GH30A) from *Acetivibrio clariflavus* ATCC 19732"** is the result of investigations carried out by me in the Department of Biosciences and Bioengineering, Indian Institute of Technology Guwahati, Guwahati, India under the guidance of Professor Arun Goyal.

In keeping with the general practice of reporting scientific observations, due acknowledgements have been made wherever the work described is based on the findings of other investigators.

April, 2025 ***Yumnam Robinson Singh***

(196106031)

INDIAN INSTITUTE OF TECHNOLOGY GUWAHATI

DEPARTMENT OF BIOSCIENCES & BIOENGINEERING

CERTIFICATE

It is certified that the work described in this thesis entitled **"Molecular cloning, expression, purification, biochemical characterization and structure analysis of a novel obligate xylobiohydrolase (*Ac*GH30A) from *Acetivibrio clariflavus* ATCC 19732" by Yumnam Robinson Singh (Roll No. 196106031)** for the award of degree of Doctor of Philosophy is an authentic record of the results obtained from the research work carried out under my supervision at the Department of Biosciences & Bioengineering, Indian Institute of Technology Guwahati, Guwahati, India and this work has not been submitted elsewhere for a degree.

Dr. Arun Goyal *(MSc, MTech, PhD)*
(FAMI, FBRS, FABAP, FNABS, FNAAS, FIFIB, FMBI, FACCTI, FSEES)
Professor (HAG) and Former Head
(Thesis Supervisor)
Department of Biosciences & Bioengineering
Indian Institute of Technology Guwahati
Guwahati, 781 039, India

ACKNOWLEDGEMENTS

The journey toward a PhD is a transformative pursuit of knowledge, growth, and self-discovery. The journey of completing this thesis has been a valuable opportunity to recognize my strengths, equipping me with the resilience and wisdom to navigate the next chapters of life. I take great pleasure in expressing my heartfelt gratitude to all whose contributions and support have significantly influenced this study, for this thesis is not merely the culmination of years of research but a testament to the unwavering support, wisdom and encouragement of many.

First and foremost, I am profoundly grateful to my thesis supervisor, Professor Arun Goyal, Department of Biosciences and Bioengineering, IIT Guwahati, for his unwavering support, invaluable guidance, and constant encouragement throughout this journey. His wisdom, patience and belief in my abilities have been instrumental in shaping this research. I deeply appreciate the opportunities he has provided, along with access to essential resources and research facilities, which have greatly enriched my academic and professional growth. His enthusiasm and joy for research and work have been inspirational and motivating. The insight, strategic planning and problem-solving skills imparted by my supervisor have not only guided my research but have also shaped my mindset and perspective on overcoming challenges.

I would also like to express my sincere gratitude to my doctoral committee members, Prof. Sachin Kumar, Dr. Anil Mukund Limaye, Dr. Sunanda Chatterjee and Prof. Arun Goyal, for their insightful suggestions and constructive criticism, which have been instrumental in refining my research and guiding me toward the successful completion of my thesis.

I am deeply thankful to the Department of Biosciences & Bioengineering and Central Instrumentation Facility (CIF), IITG, for providing infrastructural support and instruments for my research work. I am also thankful to IIT Guwahati for the Param-Ishan and Param-Kamrupa Supercomputing facility. I want to thank Dr. Ravishankar Ramachandran, Principal Scientist and his team members at CSIR-Central Drug Research Institute (CDRI), Lucknow, India, for providing the SAXS facility. I also want to thank Prof. Carlos M.G.A. Fontes, CIISA-Faculdade de Medicina Veterinária, Universidade de Lisboa, Avenida da Universidade Técnica, Lisbon, Portugal for his expert suggestions.

I also sincerely thank Guwahati Biotech Park, Guwahati, funded by the Department of Biotechnology, India, for providing essential research facilities and support.

I would also like to thank the present and former Heads of the Department of Biosciences & Bioengineering, IIT Guwahati, Prof. Utpal Bora, Prof. Rakhi Chaturvedi and Prof. Latha Rangan for providing the necessary facilities. I am highly thankful for the support received from all the other teaching and non-teaching staff members of the Department of Biosciences and Bioengineering, IIT Guwahati.

I wish to acknowledge the Ministry of Education (MoE), Govt. of India, for providing financial assistance through research scholarship.

I extend my deepest gratitude to all those with whom I shared unforgettable experiences at IIT Guwahati, particularly the members of my lab, CEBL. I am especially thankful to my seniors, Dr. Abhijeet Thakur, Dr. Sumitha Banu J., Dr. Vikky Rajulapati, Dr. Krishan Kumar and Dr. Kaustubh C. Khaire for their support, guidance and kindness, my colleagues, Dishant, Premeshwari and Jebin for their cooperation and camaraderie and my juniors, Madhulika, Vishwanath, Aishwarya, Shreya, Bipasha, Shushruta, Akshay, Ashwani and Akshita for their assistance and for fostering a vibrant and dynamic environment in the lab.

I am deeply grateful to all my batchmates and friends for their unwavering support and encouragement throughout this journey. In particular, I would like to express my heartfelt thanks to Dr. Birjit, Dr. Elizabeth, Sourav, Kishan, Suchetna and Jitendra for always being there for me.

Finally, I would like to express my heartfelt gratitude to my family, my greatest source of strength, for their unwavering trust, blessings, love and support, which have been the foundation of my journey to complete this work. I can never truly express my gratitude to my parents for their countless sacrifices, but I dedicate this thesis to parents, as their blessings have made this journey smoother and more meaningful. I would also like to thank my little sisters, Divya and Riya, for their constant support and care.

I thank God, the Almighty, whose blessings and grace have been my guiding light throughout this journey. Without his divine support, completing this thesis would not have been possible.

"Believe on yourself, Be kind to yourself."

Yumnam Robinson Singh
April, 2025

SYNOPSIS

Introduction

Lignocellulosic biomass refers to the naturally occurring biomass primarily made up of the secondary cell walls of the plant cells, which is mainly composed of cellulose, hemicellulose and lignin as primary components (Bajpai, 2016). They are abundantly generated as waste products from agriculture and forestry activities. The primary components of the lignocellulosic materials are tightly packed in a hetero-matrix configuration. In general, the lignocellulosic waste generated from agricultural activities is composed of mainly cellulose, which accounts for 40% to 50%, followed by hemicellulose 20%-30% and lignin 10%-25% (Bajpai, 2016). The lignocellulosic materials can be utilized for various industrial purposes. They can be used to make paper, fine chemicals, biofuels, and animal feed, as well as to produce industrially important enzymes (Bajpai, 1999; Garg, 2016; V. Kumar et al., 2016).

Xylan is an essential polysaccharide component of hemicellulose, primarily located in the cell walls of plants, where it contributes significantly to structural integrity and supports plant growth (Rennie & Scheller, 2014; Gigli-Bisceglia et al., 2020). Xylan is widely distributed among various plant species, forming a substantial part of the biomass in both dicots and monocots. Interestingly, xylan is also found in certain algae, where it can substitute for cellulose in the cell wall matrix (Hsieh & Harris, 2019). Xylan is characterised by a backbone of β-1,4-linked xylose residues and can include a variety of substituents, such as acetyl, feruloyl and glucuronic acid groups, which add to its structural complexity and functional diversity (Bajpai, 2014; Curry et al., 2023). The structural variations of xylan not only strengthen its role in plant defence against herbivores and pathogens but also modulate its interactions with

cellulose, influencing the overall recalcitrance of plant materials to enzymatic degradation. This complexity requires a diverse set of enzymes for its degradation, especially within microbial systems. Essential enzymes involved in xylan degradation include endo-1,4-β-xylanase, which hydrolyses to give short-chain xylooligosaccharides, β-xylosidase, hydrolyses these xylo-oligomers into xylose monomer and various other debranching enzymes, such as α-L-arabinofuranosidase and α-glucuronidase remove its side chains (Juturu & Wu, 2012). Another enzyme called xylobiohydrolase also acts on the xylans and specifically produces xylobiose by its exolytic mode of action. The synergistic action of all these enzymes is vital for the complete hydrolysis of xylans into fermentable sugars, which is essential for both natural ecosystems and industrial applications, including biofuel production and the paper industry (El Enshasy et al., 2016). Understanding the properties and ecological roles of xylanases and xylobiohydrolases is essential for harnessing their potential in various biotechnological fields. These enzymes have been harnessed for a wide range of applications, such as enhancing the quality of bread (Guo et al., 2018), clarifying must and juices (Juturu & Wu, 2012), degumming bast fibres (Wang et al., 2019), pre-bleaching kraft pulps (Kaur et al., 2016; Kumar et al., 2016), and treating hemicellulosic waste (El Enshasy et al., 2016; Jamaldheen et al., 2019).

Glycoside hydrolases (GH) constitute a large category of enzymes responsible for catalyzing the hydrolytic cleavage of glycosidic linkages in complex carbohydrates (Henrissat & Davies, 1997; Vuong & Wilson, 2010). Xylanases are a class of enzymes comprising β-(1→4)-endo xylanase, β-(1→4)- xylobiohydrolase and β-(1→4)-xylosidase which are involved in complete breakdown of xylan into xylose monomers (Collins et al., 2005). Xylanases specifically target xylan, recognizing the β-1,4-

glycosidic bonds between the xylose units in the xylan polymer. β-(1→4)-Endo xylanase hydrolyses xylan into xylooligosaccharides (XOS), which are short chains of xylose units linked by β-1,4-glycosidic bonds (El Enshasy et al., 2016). β-(1→4)-Xylobiohydrolase, reported exclusively in the GH30 family, is an exo-acting enzyme that cleaves xylan polysaccharides or XOS at the non-reducing end to release xylobiose units (Katsimpouras et al., 2019; Kadowaki et al., 2021; Puchart et al., 2021; Šuchová et al., 2021). In contrast, β-(1→4)-xylosidase hydrolyses xylan, XOS or xylobiose by sequentially removing xylose residues from the non-reducing end (Rohman et al., 2019). β-Xylanases and β-xylosidases occur in multiple glycoside hydrolase families, but family GH30 enzymes, primarily target glucuronoxylan and uniquely harbors xylobiohydrolases.

The documented enzymes exhibiting xylobiohydrolase activity to date have been only from fungal origin. Two GH30 family glucuronoxylanases, *Tc*Xyn30B from *Talaromyces cellulolyticus* (Nakamichi et al., 2020) and *Tt*Xyn30A from *Thermothelomyces thermophila* (Nikolaivits et al., 2021), have been reported to release xylobiose from the non-reducing end of xylan substrates in addition to exhibiting endoxylanase activity. However, both displayed different levels of endo- and exo-activities. In the case of *Tc*Xyn30B, the xylobiohydrolase activity was more significant than its endo-glucuronoxylanase activity, whereas *Tt*Xyn30A exhibits both modes of action at approximately equal levels. Recently, another similar glucuronoxylanase, *Sl*Xyn30A, from yeast *Sugiyamaella lignohabitans* displaying xylobiohydrolase activity was reported (Šuchová et al., 2022). The most stringent xylobiohydrolase, *Aa*Xyn30A, was reported from a cellulolytic fungus *Acremonium alcalophilum* (Šuchová et al., 2020). Numerous glycoside hydrolases from clan A of the GH30 family

following the retaining-type of reaction mechanism share a common structural feature. They contain a TIM barrel as a standard structural feature with a pair of aspartic or glutamic acid residues in the catalytic cleft primarily formed by β-α loops, participating in the catalysis (Henrissat et al., 1995; Puchart et al., 2021).

Acetivibrio clariflavus is a bacterium characterized by its thermophilic nature, anaerobic metabolism, gram-positive cell structure and ability to form spores (Artzi et al., 2014). This bacterium was initially isolated from anaerobic sludge obtained from a thermophilic methanogenic bioreactor (Shiratori et al., 2006, 2009). *Acetivibrio clariflavus* is the only thermophilic bacterium that has been reported to produce a complex cellulosomal system after the discovery of a cellulosomal system in *Clostridium thermocellum* (Artzi et al., 2014; Lamed & Bayer, 1988). It produces both cell-free and cell-bound cellulosome complexes. Several glycoside hydrolases from the *Acetivibrio clariflavus* have been characterized, but many more remain unexplored. A gene (GenBank accession number AEV68404.1) encoding a family GH30 enzyme from *Acetivibrio clariflavus* was identified and designated as *Ac*GH30A. In this study, the gene encoding *Ac*GH30A containing a GH30 family catalytic module and a dockerin 1 was cloned, expressed, and biochemically characterized. The structure and functional characteristics of xylobiohydrolase, *Ac*GH30A, were explored by *in silico* and small-angle x-ray scattering (SAXS) approaches (Fig. 1). Furthermore, the enzymatic degumming potential of *Ac*GH30A was evaluated in combination with mannanase (*Rf*GH5_7) and pectate lyase (*Ct*PL1B) for the treatment of Ramie (*Boehmeria nivea*) bast fibres and Pineapple (*Ananas comosus*) leaf fibres.

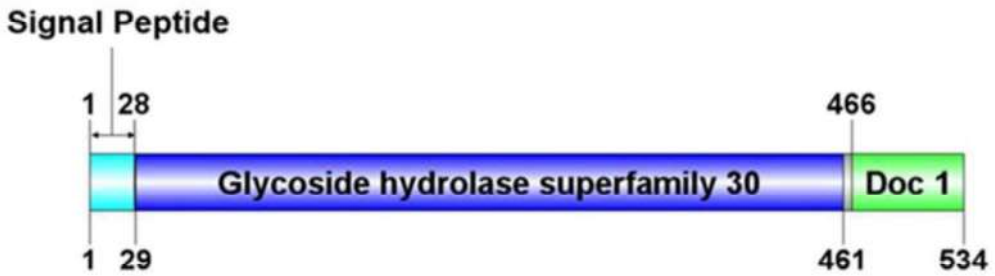

Fig. 1 Molecular organisation of the *Ac*GH30A. The amino acid sequence of *Ac*GH30A consists of 3 major domain sequences: (i) Signal peptide (1-28) at the N-terminal, (ii) GH30 catalytic module (29-461) and (iii) Dockerin 1 at C-terminal (466-534).

Present work

The present work entitled as "**Molecular cloning, expression, purification, biochemical characterization and structure analysis of a novel obligate xylobiohydrolase (*Ac*GH30A) from *Acetivibrio clariflavus* ATCC 19732**" has been divided into 5 chapters.

Chapter 1 serves as the General Introduction, providing a comprehensive overview of lignocellulosic biomass and its primary components: cellulose, hemicellulose and lignin. It discusses the structural complexity of plant cell walls, emphasizing the role of hemicellulose, particularly xylan, and its diverse structural variants, such as arabinoxylan, glucuronoxylan, and glucuronoarabinoxylan. The chapter elaborates on carbohydrate-active enzymes (CAZymes), their classification based on sequence similarities, and their enzymatic mechanisms in polysaccharide degradation. A particular focus is given to glycoside hydrolases, polysaccharide lyases, and carbohydrate esterases, detailing their catalytic functions and industrial relevance. The chapter introduces *Acetivibrio clariflavus*, a thermophilic bacterium with a

complex cellulosomal system, highlighting its potential for xylan degradation. The significance of thermostable xylanases in biomass conversion and industrial applications, including biofuel production and enzymatic degumming, is discussed. This chapter provides the necessary background for the exploration of glycoside hydrolase family 30 xylanase from *Acetivibrio clariflavus* in lignocellulosic biomass processing.

Chapter 2 describes the cloning and expression of the gene encoding xylobiohydrolase, *Ac*GH30A (GenBank accession number AEV68404.1) of glycoside hydrolase family 30 (GH30) from *Acetivibrio clariflavus* DSM 17932. The molecular architecture of *Ac*GH30A revealed an N-terminus signal peptide (28 aa) followed by a glycoside hydrolase module belonging to the GH30 family (433 aa) and a dockerin 1 module at the C-terminus (68 aa). The 1518 bp of DNA sequence encoding *Ac*GH30A was amplified by PCR from the genomic DNA of *Acetivibrio clariflavus*. The amplified PCR product carrying the desired restriction sites was ligated to the pET-28a(+) expression vector. The recombinant plasmid containing the pET-28a(+) expression vector and the gene encoding *Ac*GH30A was used for transformation of *E. coli* DH5α competent cells. The positive clone of recombinant *Ac*GH30A was confirmed by the release of its encoding gene insert after the restriction digestion using the restriction enzymes *Nhe*I and *Xho*I. The recombinant plasmid after restriction digestion showed pET-28a(+) vector DNA of ~5.3 kb size and the Insert DNA band of ~1.5 kb on agarose gel, confirming the inserted gene of interest. The *E. coli* BL21(DE3) cells were transformed by the recombinant plasmid DNA to express the recombinant enzyme,

*Ac*GH30A. The hyper-expression of *Ac*GH30A was achieved by using 1 mM as the optimum concentration of IPTG as analysed by SDS-PAGE.

Chapter 3 focuses on the purification and biochemical characterization of xylobiohydrolase, *Ac*GH30A. *Ac*GH30A was purified by immobilized metal-ion affinity chromatography followed by size exclusion chromatography. SDS-PAGE analysis of *Ac*GH30A showed a molecular mass of ~58 kDa. *Ac*GH30A demonstrated thermophilic nature with an optimum temperature of 80°C, setting it apart as the first bacterial xylobiohydrolase from the GH30 family with such an elevated optimum temperature. *Ac*GH30A displayed remarkable stability in a wide range of temperatures and pH. These findings position *Ac*GH30A as a promising candidate for applications demanding high temperatures and flexibility with pH. *Ac*GH30A exhibited an optimal pH of 7.0. *Ac*GH30A was stable (maintaining >80% of control activity) in the pH range, 4-7 and the temperature range, 30°C -70°C when incubated for 90 min. In all the enzyme assays, an enzyme reaction without the enzyme was run in parallel as a negative control. *Ac*GH30A displayed a melting temperature of 72°C and a half-life of 21 days at 4°C. Thermal stability analysis by circular dichroism (CD) spectroscopy indicated that *Ac*GH30A retained its secondary structure elements up to 70°C, with complete loss of structure at 85°C. *Ac*GH30A, with broad stability profiles, can be applied in various industries, including biofuel production, food processing, textile manufacturing, and bioremediation, offering versatility and value across different sectors. The enzyme activity of *Ac*GH30A was enhanced by 10 mM Ca^{2+} and Mg^{2+} ions by 25% and 21%, respectively, whereas 10 mM Co^{2+}, Zn^{2+}, Fe^{2+}, and Cu^{2+} ions significantly reduced it. *Ac*GH30A showed activity against various xylan polysaccharides, displaying the highest V_{max}, 139 $U.mg^{-1}$ and K_M, 0.71 $mg.ml^{-1}$ against 4-*O*-methyl glucuronoxylan

under optimum conditions, 80°C and pH 7.0. The analysis of *Ac*GH30A hydrolyzed products of beechwood xylan by TLC, HPLC and LC-MS revealed the release of only one product, xylobiose, confirming its obligate xylobiohydrolase activity. *Ac*GH30A is a novel bacterial enzyme displaying obligate xylobiohydrolase activity by orchestrating exclusive and sequential release of xylobiose from xylan polysaccharides. Therefore, *Ac*GH30A can be used for commercial production of xylobiose and other value-added products from xylan polysaccharides or lignocellulosic biomasses.

Chapter 4 describes the structure analysis and molecular dynamics of xylobiohydrolase, *Ac*GH30A. This study focuses on the solution structure and substrate binding analysis of *Ac*GH30A. A high-quality homology model of *Ac*GH30A, generated from Alphafold2, demonstrated structural accuracy, supported by Ramachandran plot analysis and secondary structure assessments. Ramachandran plot depicted that the favoured and allowed regions contained 100% amino acids and no residue in the disallowed region. The 3-dimensional model of *Ac*GH30A showed an overall quality score of 93.6% in the ERRAT server analysis. Secondary structure analysis of *Ac*GH30A in an aqueous environment using Circular Dichroism (CD) and *in silico* modeling revealed an α/β/α sandwich structure with a central β-barrel comprising eight β-strands. CD revealed 21.94% α-helices, 20.98% β-sheets and 57.08% random coils in *Ac*GH30A, aligning closely with the prediction results from Psipred, SOPMA and 2Struc servers. Superposition of the homology-modelled structure of *Ac*GH30A with its closest homolog showed that the active-site contains Glu175 and Glu268 as the catalytic residues. The molecular docking analysis revealed a significant binding affinity of *Ac*GH30A with xylobiose with a binding free energy of $-4.3\ \text{kcal.mol}^{-1}$, suggesting the xylobiohydrolase activity of *Ac*GH30A. The

molecular docking study suggested a retaining type mechanism supported by the positioning of xylobiose between the catalytic residues Glu175 and Glu268. The −1 subsite was predominantly composed of Trp123, Glu175, Asn174, and Glu268 residues forming hydrogen bonds with xylobiose. *Ac*GH30A displayed a high binding affinity with xylobiose with an association constant (K_a) of 7.83×10^5 M^{-1}, as determined by isothermal titration calorimetry. This strong affinity is characteristic of xylobiohydrolases, which are specialized to selectively bind and release xylobiose, while most other xylanases and related enzymes have lower or broader substrate affinities. Molecular dynamics (MD) simulations of *Ac*GH30A and *Ac*GH30A-xylobiose complex in solution showed reduced RMSD, R_g and SASA values, confirming the stability and compactness of the complex. MD simulations further highlighted the crucial role of Glu175 in hydrogen bonding with the ligand, which alternates between acting as an acid and as a base, depending on the stage of catalysis. MD simulations revealed consistent conformational alterations in *Ac*GH30A following the binding of the ligand, evidenced by reduced RMSD, R_g, and SASA values of the docked complex with xylobiose compared to the free *Ac*GH30A. The average RMSD, R_g and SASA values of *Ac*GH30A in the docked complex declined by 0.39, 0.32 and 22.57 nm^2, respectively. Small-angle X-ray scattering (SAXS) analysis of *Ac*GH30A showed its molecular shape as an earbud with a globular structure existing in a monodispersed state, which was corroborated by dynamic light scattering (DLS). The hydrodynamic radius (R_h) of *Ac*GH30A, determined by DLS, was 3.7 nm.

Chapter 5 presents the findings on the enzymatic degumming of ramie (*Boehmeria nivea*) bast fibres and pineapple (*Ananas comosus*) leaf (PAL) fibres using *Ac*GH30A (xylobiohydrolase) along with *Ct*PL1B (pectate lyase) and *Rf*GH5_7

(mannanase). The objective was to establish an eco-friendly alternative to conventional chemical degumming methods, which often cause fibre degradation and environmental pollution. The enzymatic degumming process was optimized by evaluating different enzyme concentrations (1-20 mg·mL^{-1}) and incubation times (15-180 min). The concentration of all three enzymes, *Ac*GH30A, *Ct*PL1B and *Rf*GH5_7, were optimized individually as well as in dual and triple combinations and the optimum degumming efficiency was observed at 15 mg·mL^{-1} enzyme concentration and 60 min incubation time. The treatments were carried out with 10 mg fibre in 1.5 mL reaction volume. The apparently high protein concentration reflects the use of crude enzyme extracts, in which the fraction of active enzyme is lower than in purified preparations. Scaling up the degumming process (100 mg fibres in 15 mL enzyme solution) confirmed the feasibility of enzymatic treatment at a larger scale. Among single-enzyme scale-up treatments, *Ct*PL1B showed the highest weight loss of 11.2 ± 0.3% for ramie and 19.1 ± 0.5% for pineapple leaf (PAL) fibres, highlighting its role in pectin degradation. Dual-enzyme mixtures exhibited a synergistic effect, with *Ac*GH30A + *Ct*PL1B achieving 11.0 ± 0.2% weight loss for ramie and *Ct*PL1B + *Rf*GH5_7 yielding 18 ± 0.4% for PAL fibres, as the best dual enzyme combination. The triple-enzyme combination resulted in 9.8 ± 0.3% weight loss for ramie and 17.3 ± 0.3% for PAL fibres. Comparatively, chemical degumming using NaOH (5 g·L^{-1}) resulted in 15.0 ± 0.6% and 21 ± 0.6% weight loss for ramie and PAL fibres, respectively. The mechanical properties of enzyme-treated fibres were significantly improved, with *Ac*GH30A + *Ct*PL1B treated ramie fibres showing the highest tensile strength (418.3 MPa) and *Ct*PL1B + *Rf*GH5_7 treated PAL fibres achieving 323.2 MPa. These values were comparable to those achieved through chemical treatment with NaOH (5 g.L^{-1}), which poses environmental

and sustainability concerns despite its higher degumming efficiency. The characterization of the enzyme-treated fibres by FESEM, ATR-FTIR, and thermogravimetric analysis confirmed the removal of pectin and hemicellulose. The FESEM images revealed smooth fibre surfaces after treatment, and ATR-FTIR analysis showed distinct changes in functional groups corresponding to the degradation of non-cellulosic components. The thermogravimetric analysis demonstrated improved thermal stability of degummed fibres, with degradation temperatures increasing to 356.3°C for ramie and 375.7°C for PAL fibres after enzymatic treatment due to increased cellulose crystallinity. Enzymatic degumming using *Ac*GH30A, *Ct*PL1B, and *Rf*GH5_7 provides a sustainable and effective method for processing natural fibres. Enzymatic degumming not only aligns with the principles of sustainable development but also addresses the limitations of conventional chemical methods, such as fibre damage and environmental pollution.

CONTENTS

Chapter 1

General Introduction

1.1 Carbohydrates

Carbohydrates are the most abundantly available biomolecule on planet Earth, constituting the largest renewable source of organic carbon (Gilbert, 2010). They serve as a primary energy source and form a substantial organic component in a variety of fruits, vegetables, legumes and cereal grains. Chemically, carbohydrates are composed of carbon, hydrogen and oxygen and can be classified as polyhydroxy aldehydes or ketones (Slavin, 2012). The presence of hydroxyl groups makes carbohydrates prone to modification by various chemical entities, resulting in a wide array of molecular structures. They can undergo modifications, such as esterification and etherification, and can also incorporate deoxy and amino groups. Furthermore, carbohydrates can form covalent bonds with proteins and lipids, resulting in glyco-conjugates, which include proteoglycans, glycoproteins and glycolipids (Slavin, 2012).

1.2 Lignocellulosic biomass

Lignocellulosic biomass refers to the naturally occurring biomass primarily made up of the secondary cell walls of the plant cells, which is mainly composed of cellulose, hemicellulose and lignin as primary components (Bajpai, 2016). They are abundantly generated as waste products from agriculture and forestry activities. The primary components of the lignocellulosic materials are tightly packed in a hetero-matrix configuration. The degree of its complexity varies according to the source and various other factors, such as the different species of plants it is composed of and the age of the plants involved. The composition of biomass in a living plant also varies according to its location, species, age, stage of growth and various other factors (Motghare et al., 2016; Singh et al., 2017). In general, the lignocellulosic waste generated from agricultural activities is composed of mainly cellulose, which accounts for 40% to 50%, followed by hemicellulose 20%-30% and lignin 10%-25% (Bajpai, 2016). The woody biomass can be divided into two classes, softwood and hardwood. Softwood, as its name implies, are low in density compared to hardwood. They are mainly sourced from coniferous and gymnosperm trees, such as pine, cypress and cedar. Whereas the hardwood belongs to the angiosperm plants, such as poplar, oak and aspen etc., most of which are deciduous. The stability and the rigidity of the hetero-matrix of the lignocellulosic materials is imparted by the hydrogen and covalent bonds present in abundance among the constituent biopolymers. The cellulose molecules bonds, with each other to form microfibers that provide the basic foundation for the matrix in which the hemicellulose and lignin is embedded. The lignocellulosic materials can be utilized for various industrial purposes. They can be used to make

paper, fine chemicals, biofuels, animal feed and for producing industrially important enzymes (Bajpai, 1999; Garg, 2016; V. Kumar et al., 2016).

1.2.1 Cellulose

Cellulose is a polysaccharide that serves as a primary structural component of plant cell walls, imparting strength and rigidity. It consists of linear glucose chains connected by β-1,4-glycosidic linkages. Extensive intermolecular hydrogen bonding between adjacent chains leads to the formation of microfibrils, resulting in a highly ordered, robust, and insoluble structure. Many enzymes hydrolyse β-glycosidic bonds, but the crystalline structure and insolubility of cellulose restrict their access, making cellulose resistant to digestion in most organisms. Its unique properties make cellulose a key contributor to the structural integrity of plant cell walls, imparting resilience and resistance to environmental stresses. Moreover, cellulose serves as a renewable source for feed stock and various industrial applications, such as the production of paper, textiles and biofuels, underscoring its significance in both biological and technological contexts.

1.2.2 Hemicellulose

Hemicellulose is a complex, heterogeneous group of polysaccharides that, together with cellulose, lignin, and pectin, forms a major structural component of plant cell walls. It comprises various polysaccharide types, including xyloglucans, xylans, mannans, glucomannans, galactans, arabinans, and β-(1→3,1→4)-glucans. The composition, structure, and abundance of hemicelluloses vary considerably across plant species and cell types. Hemicellulose plays a crucial role in cementing cellulose microfibrils, thereby influencing the overall strength and architecture of the cell wall. Hemicellulose serves as a key component in plant biomass, making it a valuable

resource for bioenergy production and various industrial applications. The structural variability and functional diversity of hemicelluloses underscore their importance in both the biological and biotechnological realms, emphasizing the need for a comprehensive understanding of these polymers in the context of plant biology and sustainable technology.

1.2.3 Xylan

Xylan is the second most abundant polymer present in the plant kingdom. It is the primary component of the hemicellulose present in plants (Fonseca-Maldonado et al., 2014; He et al., 2014). Structurally, they are heteropolysaccharides in which the backbone is composed of xylose monomers linked by β-1,4-glycosidic linkages. The main chain is embedded with a diverse group of side-chain moieties including glucuronic acid, arabinose, *p*-coumaric acid and ferulic acid (Thakur et al., 2019). Xylans are structurally very diverse and their structure differs according to the species of the plants, specific part of the plant and its age.

Since xylans are highly abundant in nature, they hold a great potential for various industrial purposes as a renewable source of energy and chemicals. In order to achieve this, they are required to be degraded into simpler forms, *viz.* monosaccharides and oligosaccharides. Their degradation can be achieved by physical process like pyrolysis or by using carbohydrate-active enzymes, such as xylanases. The enzymatic degradation is preferable due to its ecological aspects. The complexity of the xylan structure demands a consortium of enzymes that can work in combination or synergism for its degradation (Fonseca-Maldonado et al., 2014). These enzymes are widely available in nature in all types of lifeforms, including bacteria, archaea, animal gut, termite gut, fungi and plants (Biely, 1985; Bajpai, 2014). A large number of these

enzymes have been discovered and isolated in the past two decades, but majority of them are yet to be found.

Xylan is the major biopolymer present in the hemicellulosic part of the lignocellulosic biomass. They are composed of a linear backbone made up of repeating units of xylose residues, which are substituted with various side chains. Xylan and lignin play important roles in protecting the plants from the attacks of herbivores and pathogens by enhancing the recalcitrance of the cell walls. There are four main types of xylans, Arabinoxylans, Glucuronoxylans and Glucuronoarabinoxylans (Bajpai, 2014, 2016; Fernández et al., 2019).

1.2.3.1 *Arabinoxylan*

Arabinoxylans are composed of a backbone chain made up of β-(1-4)-linked xylose residues and a varying number of L-arabinofuranosyl residues, substituted with the main chain at position O-2 or O-3 (Fig. 1.1). They are found mainly in the lower plants like grasses and cereal plants such as wheat, rye, oat, barley, rice and corn. They are well suited for the baking industry because the water molecules bind to the arabinose sugar units, providing viscous property to the dough.

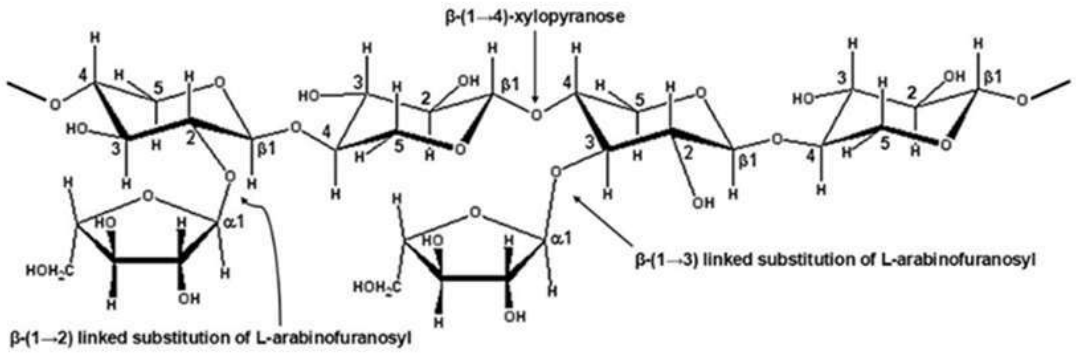

Fig. 1.1 Chemical structure of arabinoxylan showing a β(1→4)-linked D-xylopyranose backbone, substituted at the O-2 and/or O-3 positions with L-arabinofuranosyl residues.

1.2.3.2 *Glucuronoxylan*

Similar to arabinoxylan, glucuronoxylan also contains a primary chain made up of β-(1-4)-linked xylose residues. However, instead of L-arabinofuranosyl side groups, it carries α-D-glucuronic acid substituents at the C-2 or C-3 positions. These side chains are attached via α-(1→2) or α-(1→3) glycosidic linkages (Fig. 1.2).

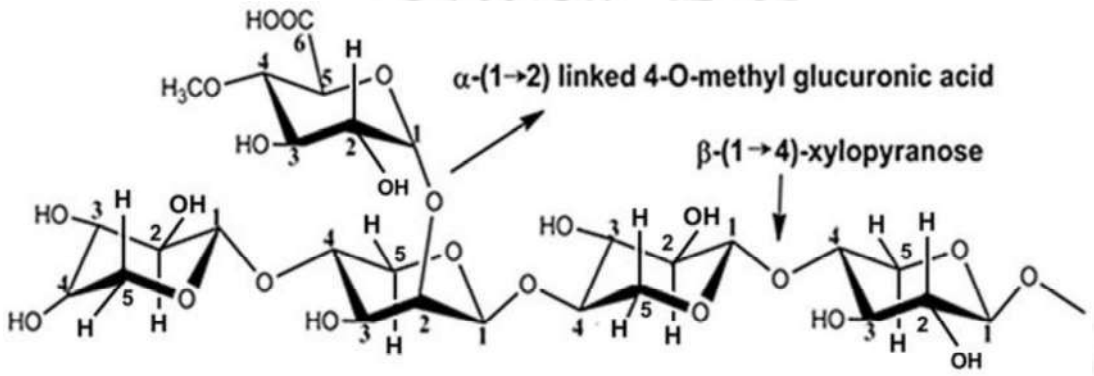

Fig. 1.2 Chemical structure of glucuronoxylan consisting of a β(1→4)-linked D-xylopyranose backbone, with α-D-glucuronic acid (GlcA) or 4-O-methyl α-D-glucuronic acid (MeGlcA) residues substituted at the O-2 positions of the xylose units (Padilha et al., 2014).

1.2.3.3 *Glucuronoarabinoxylan*

Glucuronoarabinoxylan consists of a backbone of β-(1→4)-linked xylose monomers, substituted with arabinofuranose and α-D-glucuronic acid side chains. They can also contain acetyl groups linked with xylose units and ferulic acid linked with arabinose subunits.

1.2.4 Mannan

Mannan is a complex polysaccharide primarily composed of the monomer, mannose and it plays a significant role in the structure of hemicellulose found in higher plants, particularly softwoods. Its structure can be characterized by various types, including linear mannan, galactomannan, glucomannan and galactoglucomannan. Linear mannan, also known as β(1-4)-mannan, consists of a straight chain of mannose

units linked by β(1-4) glycosidic bonds. This type is typically insoluble and serves as a storage polysaccharide. The other types of mannam are as follows,

1.2.4.1 *Galactomannan*

Galactomannan, on the other hand, features a backbone of mannose with branches of galactose linked through α(1-6) bonds, creating a more complex structure that can vary in the ratio of mannose to galactose depending on its source (Fig. 1.3).

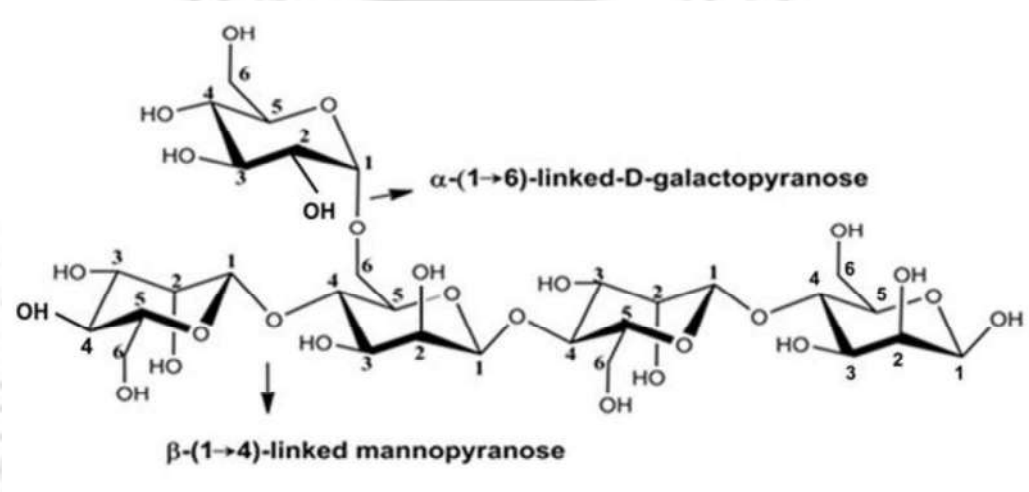

Fig. 1.3 Chemical structure of galactomannan showing a backbone composed of repeating β(1→4)-linked D-mannopyranose units, substituted with side chains of D-galactopyranose linked through α(1→6) glycosidic bonds.

1.2.4.2 *Glucomannan*

Glucomannan combines both mannose and glucose in its backbone, which are also linked by β(1-4) bonds. It includes additional branches that can be α(1-2) or α(1-3) linked (Fig. 1.4) with a length of 11 to 16 hexose residues like glucose and mannose (Hongu et al., 2005). This type is notable for its water solubility and is often utilized in dietary supplements due to its prebiotic properties. The main source of glucomannan is a corm (root, not seed) of Konjac plant (*Amorphophallus konjac*). It is also present in the cell wall of gymnosperms. It is a soluble dietary fibre used as a food additive and nutritional supplements to use as therapeutic agents in case of constipation, obesity,

high cholesterol, acne valgaris and type 2 diabetes (Passaretti et al., 1991; Vuksan et al., 1999; Walsh et al., 1984).

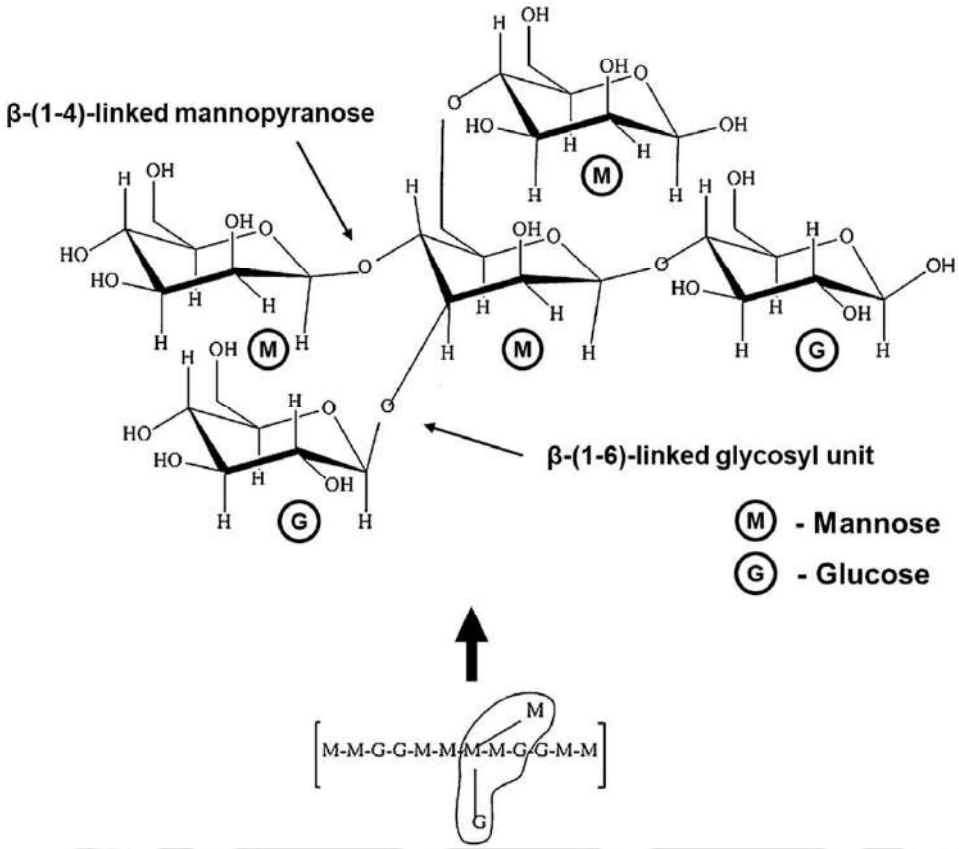

Fig. 1.4 Chemical structure of glucomannan depicting a backbone composed of β(1→4)-linked D-glucose (G) and D-mannose (M) units arranged in an M–M–G sequence. Branching occurs via β(1→6) linkages involving either mannose or glucose residues (Behera & Ray, 2016).

1.2.4.3 *Galactoglucomannan*

Galactoglucomannan is characterized by a mixed backbone composed of mannose and glucose units linked by β(1-4) bonds (Fig. 1.5). The backbone is decorated with α(1-6)-linked galactose units, contributing to its structural diversity (Chekan et al., 2014). The structural integrity of mannans is enhanced by the presence of acetyl groups and other substituents, which can influence their solubility and biological activity. Mannans are not only significant for plant structure but also have

applications in various industries, such as food, pharmaceuticals and animal nutrition due to their functional properties and health benefits (Voiniciuc, 2022).

Fig. 1.5 Chemical structure of galactoglucomannan illustrating a linear backbone of β(1→4)-linked glucose and mannose units, substituted with α(1→6)-linked galactose side chains (Yu et al., 2018).

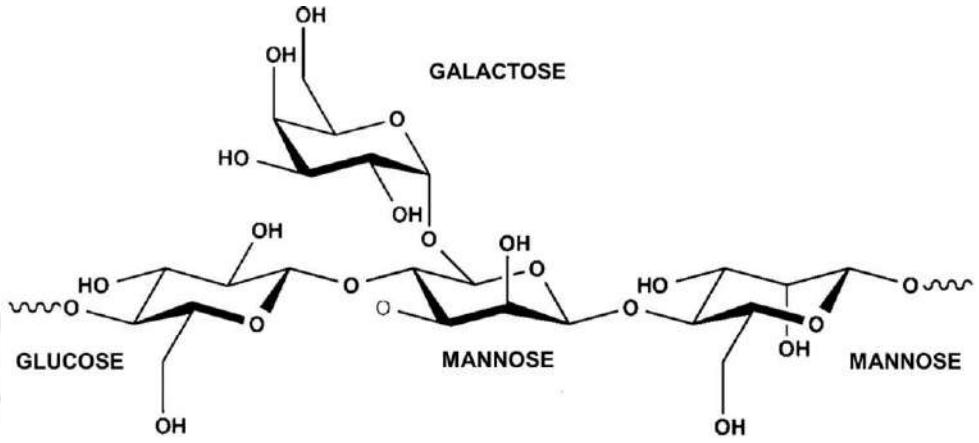

1.2.5 Pectin

Pectin is a structurally complex polysaccharide essential for maintaining the architecture and physiological functions of plant cell walls (Chandel et al., 2022). It is composed of linear chains of galacturonic acid, interspersed with neutral sugar residues, such as arabinose and galactose, pectin exhibits considerable heterogeneity in its composition (Zdunek et al., 2021). This heteropolymer contributes to the gel-like matrix in the middle lamella of plant cells, facilitating adhesion between adjacent cells and imparting stability to tissues. Pectin is involved in various physiological processes, including cell expansion, fruit ripening and response to stress. Its solubility and ability to form gels make pectin a valuable component in the food industry, where it is utilized as a thickening and gelling agent (Chandel et al., 2022). The enzymatic modification of pectin is a focus of research in biotechnology for applications in food industry, pharmaceuticals and other industrial sectors. Understanding the diverse functions and

structures of pectin is crucial for both advancing the knowledge of plant biology and harnessing its beneficial applications for various industries (Chandel et al., 2022). The main types of pectin include homogalacturonan (HG), rhamnogalacturonan I (RG-I), rhamnogalacturonan II (RG-II) and xylogalacturonan (XGA).

1.2.5.1 *Homogalacturonan*

Homogalacturonan consists of a linear chain of α-D-galacturonic acid residues, which may be methyl-esterified or O-acetylated at specific positions, contributing to its gel-forming properties (Liang et al., 2022).

1.2.5.2 *Heterogalacturonan*

1.2.5.2.1 *Rhamnogalacturonan I*

Rhamnogalacturonan I features a backbone of repeating disaccharides composed of α-L-rhamnose and α-D-galacturonic acid, with numerous neutral sugar side chains of L-arabinose and D-galactose branching off, and giving it a "hairy" appearance (Kaczmarska et al., 2022).

1.2.5.2.2 *Rhamnogalacturonan II*

Rhamnogalacturonan II is more complex and less common, contains an intricate structure with additional non-sugar components and disaccharide side chains made of apiose, rhamnose, arabinose and galactose, making it crucial for plant cell wall stability and interaction with metal ions (Pérez et al., 2003).

1.2.5.2.3 *Xylogalacturonan*

Xylogalacturonan includes xylose units attached to the galacturonic acid backbone, further diversifying the structural characteristics of pectin (Zandleven et al., 2005). The varying proportions and arrangements of these components not only influence the physical properties of pectin, such as its ability to form gels but also its

functional roles in plant biology, including cell adhesion, growth regulation and defence mechanisms against pathogens (Chandel et al., 2022). The complexity of pectin's structure allows it to serve as a vital ingredient in food processing and pharmaceuticals due to its gelling, thickening and stabilizing properties.

1.2.6 Lignin

Lignin is a complex and non-carbohydrate polymer found in the cell walls of plants, providing rigidity and strength to vascular tissues. It comprises an intricate network of phenolic compounds, including coniferyl, sinapyl and þ-coumaryl alcohol units (Ralph et al., 2019). Lignin is unique in its three-dimensional and irregular structure. This complexity renders lignin hydrophobic and resistant to microbial degradation. It acts as a binder, cementing cellulose and hemicellulose fibers in the plant cell wall, thereby enhancing structural integrity (Hatakeyama & Hatakeyama, 2010). Lignin is essential for plants to withstand mechanical stress and environmental challenges. However, its recalcitrant nature poses challenges in biomass processing for biofuel and paper production.

1.3 Carbohydrate active enzymes

Carbohydrate-active enzymes (CAZymes) are categorized into six classes based on sequence similarities and their catalytic mechanisms on substrates (Cantarel et al., 2009; Lombard et al., 2014). This classification has been maintained since 1998 in the continuously updated CAZy database (www.cazy.org). Different classes of CAZymes are as follows,

1.3.1 Glyoside hydrolases

Glycoside hydrolases (GHs) are a broad group of enzymes that hydrolyze the glycosidic bond between two or more carbohydrates or between carbohydrate and a

non-carbohydrate moiety. There are currently 171 GH families based on the sequence (Drula et al., 2022).

1.3.2 Glycosyl transferases

Glycosyl transferases (GTs) catalyze the transfer of an activated carbohydrate moiety from donor molecule to an acceptor molecule. GTs are responsible for biosynthesis of glycosidic bonds to produce polysaccharides. They are categorized into 114 families based on the sequence (Drula et al., 2022).

1.3.3 Polysaccharide lyases

Polysaccharide lyases (PLs) catalyze the cleavage of glycosidic (carbon-oxygen) bond in polysaccharides leading to the release of an unsaturated product and the elimination of an alcohol. These are categorized into 42 families based on the sequence (Drula et al., 2022).

1.3.4 Carbohydrate esterases

Carbohydrate esterases (CEs) catalyze the hydrolysis of ester bonds in plant polysaccharides and oligosaccharides, removing ester-linked side chain groups (e.g. acetyl, feruloyl or coumaroyl groups), playing a vital role in modifying and degrading plant polysaccharides. They are categorized into 19 families based on their amino acid sequence (Drula et al., 2022).

1.3.5 Carbohydrate-binding modules

Carbohydrate-binding modules (CBMs) are non-catalytic and structurally discreet protein modules, forming part of larger multi-modular enzymes. CBMs facilitate the binding of enzymes to complex carbohydrates and direct the catalytic machinery on the substrate, thus enhancing the catalytic efficiency of the multi-modular carbohydrate-active enzymes (Christiansen et al., 2009). The binding of

CBMs with the substrate are mediated through different non-covalent interactions, such as hydrogen bonds, hydrophobic interactions, and van der waals forces. They are categorized into 88 families based on sequence (Drula et al., 2022).

1.3.6 Auxiliary Activities

Auxiliary activities (AAs) are redox enzymes that help in the breakdown of the lignocellulosic biomass by acting on the lignin and providing better access for the other carbohydrate active enzymes to plant cell wall. AAs currently have 17 families (Drula et al., 2022).

1.4 Enzymatic hydrolysis of xylan

The involvement of enzymes in xylan degradation was first noted by Hopper-Seyler over a century ago (Bastawde, 1992). Xylan is a chemically complex and heterogeneous compound, necessitating various hydrolytic enzymes with distinct modes of action and specificities for its complete breakdown. The xylanolytic enzymes system comprises β-1,4-endoxylanase, β-xylosidase, xylobiohydrolases, α-glucuronidase, α-L-arabinofuranosidase, acetyl xylan esterase (Motta et al., 2013) and phenolic acid (ferulic and þ-coumaric acid) esterase (Beg et al., 2001; Dhiman et al., 2008). The synergistic action of these enzymes enables the conversion of xylan into its constituent sugars. Among xylan-degrading enzymes, endoxylanases and β-xylosidases play critical roles in breaking down xylan into monomeric pentose units. Endoxylanases cleave glycosidic bonds to produce short xylooligosaccharides, while β-xylosidases release xylose residues from the non-reducing ends of these xylooligosaccharides (Motta et al., 2013). Acetyl esterase, ferulic esterase, glucuronidase and arabinosidase are essential for removing various side chains from the xylan backbone (Dhiman et al., 2008).

1.4.1 Xylanases

Xylanases (E.C.3.2.1.8), are a large class of hydrolytic enzymes that can completely disintegrate the linear polysaccharide, xylan into simpler products (Juturu & Wu, 2012). Xylanases are divided into two key enzyme classes, endo- and exo-acting according to their mode of action. Endo-acting xylanases, mainly referred to as endo-1,4-β-xylanases, randomly cleave internal β-1,4-glycosidic bonds within the xylan backbone. In contrast, exo-acting xylanases, commonly known as β-xylosidases, target the non-reducing ends of xylooligosaccharides to release individual xylose molecules. Xylanases play a very important role in the saccharification of lignocellulosic biomass and have attracted significant attention for their ability to hydrolyze lignocellulose into simple fermentable sugars. In the carbohydrate-active enzyme database (CAZy; www.cazy.org), xylanases from various organisms have been classified into distinct GH families (5, 7, 8, 10, 11, 26, 30, 43, 51, 98 and 141) based on the similarities of their amino acid sequence and structural properties. All these enzymes present in the database present diverse ranges of substrate specificities, mode of action and physico-chemical characteristics (Poosarla & Chandra, 2014; Sharma et al., 2018a, 2018b).

1.4.1.1 *Endo-1,4-ß-xylanases*

Endo-1,4-β-xylanases (E.C.3.2.1.8) cleave the β-1,4-glycosidic linkages within the xylan polysaccharide, resulting in the production of xylooligosaccharides and xylose. Endo-1,4-β-xylanases are predominantly produced by various microorganisms, including fungi and bacteria, which utilize these enzymes to break down plant materials for nutrients (Collins et al., 2005).

1.4.1.2 *Exo-β-1,4-D-xylosidase*

Exo-β-1,4-D-xylosidase (E.C. 3.2.1.37) catalyzes the stepwise removal of D-xylose residues from the non-reducing ends of β-1,4-D-xylo-oligosaccharides through hydrolytic cleavage (Fig. 1.6). For example, β-xylosidase breaks down xylobiose leading to release of two xylose units. Exo-β-1,4-D-xylosidase have been isolated from various microorganisms, such as *Selenomonas ruminantium* (Jordan & Wagschal, 2010), *Aspergillus niger* (Scott-Craig et al., 2011), *Bacillus Subtilis* (Banka et al., 2014) *and Thermoanaerobacterium saccharolyticum* (Shao et al., 2011) .

1.4.1.3 *Xylobiohydrolases*

Xylobiohydrolases (E.C.3.2.1.-) are xylanases that release xylobiose, a disaccharide composed of two xylose units from the non-reducing end of xylooligosaccharides and xylan polysaccharides. Several xylanases from GH30 family displaying different modes of action have been reported and some showing xylobiohydrolase activity are listed in Table 1.1. Most xylobiohydrolases reported come from fungal species and they show bifunctional enzymatic activity. *Tt*Xyn30A and *Tc*Xyn30B from *Thermothelomyces thermophila* and *Talaromyces cellulolyticus*, respectively, displayed both exo- and endo-acting catalytic behaviour (Katsimpouras et al., 2019; Nakamichi et al., 2020). Both enzymes released methylglucuronic acid linked xylooligosaccharides and xylobiose from glucuronoxylan substrates. An enzyme, *Aa*Xyn30A from fungus *Acremonium alcalophilum* was reported as an almost strict xylobiohydrolase (Šuchová et al., 2020). The enzyme demonstrated maximal catalytic activity on rhodymenan, generating isomeric xylotrioses and specifically released xylobiose from the non-reducing termini of xylan chains. *Sl*Xyn30A is a GH30 xylanase from the fungus *Sugiyamaella lignohabitans* which releases acidic

xylooligosaccharides from glucuronoxylan and shows auxiliary xylobiohydrolase activity (Šuchová et al., 2022).

Table 1.1 Fungal xylobiohydrolases from GH30 family.

Organism	Enzyme	Subfamily	Optimum temperature and pH	Reference
Acremonium alcalophilum	*Aa*Xyn30A	GH30_7	50ºC, pH 7.5-10.0	(Šuchová et al., 2020)
Talaromyces cellulolyticus	*Tc*Xyn30B	GH30_7	50°C, pH 5.0	(Nakamichi et al., 2019, 2020)
Thermothelomyces thermophila	*Tt*Xyn30A	GH30_7	50°C, pH 4.0	(Nikolaivits et al., 2021)
Sugiyamaella lignohabitans	*Sl*Xyn30A	GH30_7	50°C, pH 3.5	(Šuchová et al., 2022)

1.4.2 Xylan side-chain removing enzymes

1.4.2.1 *α-L-Arabinofuranosidases*

α-L-Arabinofuranosidases (E.C.3.2.1.55) hydrolyze the terminal, non-reducing α-L-arabinofuranosyl groups of arabinans, arabinoxylans and arabinogalactans (Fig. 1.6). This enzyme is produced by fungi, actinomycetes and bacteria (Numan & Bhosle, 2006).

1.4.2.2 *α-D-Glucuronidases*

α-**D**-Glucuronidases (E.C.3.2.1.139) catalyze the hydrolysis of α-1,2-glycosidic linkage between xylose and D-glucuronic acid or its 4-O-methyl ether derivative as shown in Fig. 1.6 (Nam et al., 2016).

1.4.2.3 *Acetyl xylan esterase*

Acetyl xylan esterase (E.C.3.1.1.72) catalyzes the hydrolysis of acetyl groups from acetylated xylan and xylo-oligosaccharides, releasing acetic acid, providing better accessibility for xylanases to act on the xylan backbone (Zhang et al., 2011).

1.4.2.4 *Feruloyl esterase*

Feruloyl esterase (E.C.3.1.1.73) hydrolyzes the ester bonds between phenolic acids such as ferulic acid and *p*-coumaric acid and the arabinose residues of arabinoxylan or other polysaccharides as shown in Fig. 1.6 (Fazary & Ju, 2007).

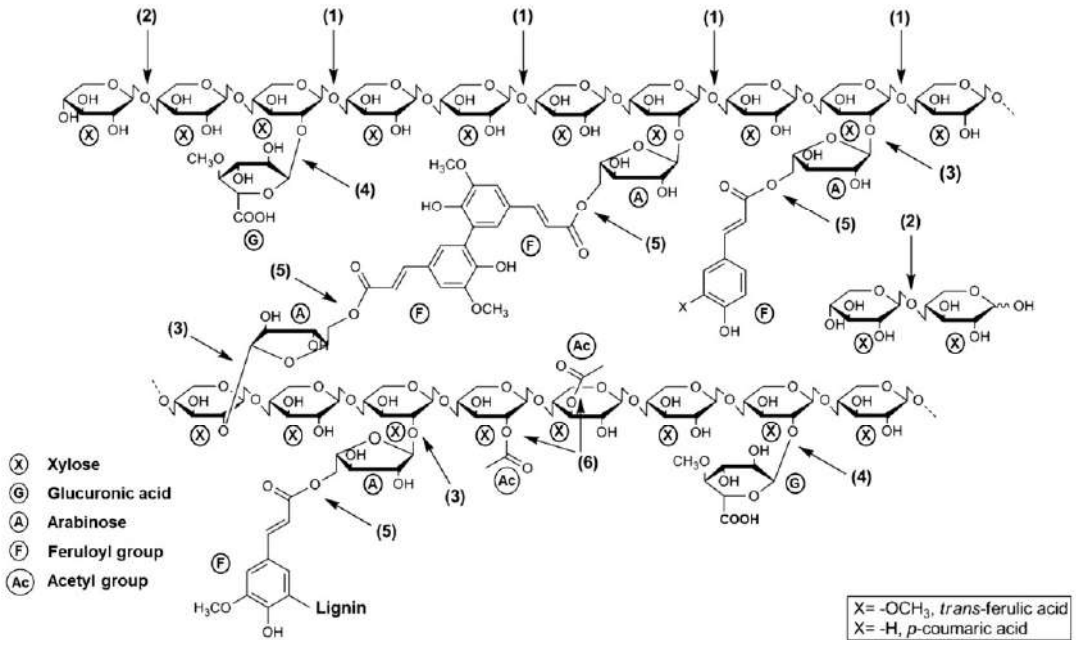

Fig. 1.6 Schematic presentation of xylan structure along with the enzymes necessary for its complete hydrolysis. 1. Endo-1,4-β-xylanase, 2. β-Xylosidase, 3. α-L-Arabinofuranosidase, 4. α-Glucuronidase, 5. Feruloyl esterase, 6. Acetylxylan esterase (Topakas et al., 2013).

1.5 Glycoside hydrolase families containing xylanase

Several glycoside hydrolase families exhibit diverse structures and enzyme activities on xylan substrates. Enzymes with endo-1,4-β-xylanase activity are present in 9 distinct glycoside hydrolase families: GH5, GH7, GH8, GH10, GH11, GH30, GH43, GH51 and GH141. However, xylobiohydrolases have been reported primarily within GH30 family. GH5 is a large family with 48,671 sequences, 628 of which are characterized, featuring broad substrate specificity and a (β/α)8-barrel fold. GH8,

containing 10,687 members, mainly includes bacterial single-domain enzymes with an (α/α)6-barrel structure, acting on xylan via an inversion mechanism (Table 1.2). The family GH10 has 12,870 sequences and primarily functions as endo-1,4-β-xylanases, using a (β/α)8-barrel fold similar to that of GH5. GH11 comprises 5,320 xylanase-only enzymes, predominantly extracellular with a β-jelly roll fold and a deep active-site cleft. Family GH43, with 14 sequences reported, is characterized by a five-bladed β-propeller architecture and includes multidomain enzymes (Table 1.2). GH51 family contains two enzymes identified by GenBank IDs AAC45377.1 and ACV57112.1, exhibiting endoxylanase activity (Eckert and Schneider, 2003; Malburg et al., 1997). The 3D structure of GH51 enzymes primarily consists of a (β/α)8-fold (Table 1.2). GH141, a recently established family, has limited characterized members, with only one xylanase, displaying broad substrate specificity and modular architecture akin to GH10 (Table 1.2). Together, these families illustrate structural diversity and specificity in xylan degradation.

1.5.1 Glycoside hydrolase family 30

The GH30 glycoside hydrolase family currently comprises 9,442 proteins, of which only 67 have been biochemically characterized. This family encompasses a diverse array of endo- and exo-xylanases, exhibiting broad and frequently multifunctional activities directed toward the β-1,4-linked backbone of xylan and xylo-oligosaccharides. These include endo-1,4-β-xylanases (EC 3.2.1.8), xylobiohydrolases (E.C.3.2.1.-), glucuronoxylanases (EC 3.2.1.136) and β-xylosidases (EC 3.2.1.37). An endo-1,4-β-xylanase, *Ct*XynGH30 from *Clostridium thermocellum*, cleaves the internal β-1,4-glycosidic linkages in the xylan backbone (Verma & Goyal, 2016). Xylobiohydrolases release xylobiose from the non-reducing-end of xylan or

xylooligosaccharides (Crooks et al., 2021; Suchova et al., 2021). Glucuronoxylanases are specific for glucuronoxylan and act on regions of the backbone substituted with glucuronic acid or methyl-glucuronic acid, releasing shorter length xylooligosaccharides (Sakka et al., 2012). GH30 family also features β-xylosidases, which release xylose from the non-reducing end of xylooligosaccharides and xylobiose (Luo et al., 2010). GH30 family also includes various other enzymes such as glucosylceramidases (EC 3.2.1.45), β-glucosidases (EC 3.2.1.21), endo-β-1,6-glucanases (EC 3.2.1.75), endo-1,6-β-galactanases (EC 3.2.1.164), β-glucuronidases (EC 3.2.1.31), α-L-Arabinofuranosidases and β-fucosidases (EC 3.2.1.38). Currently, 11 subfamilies have been proposed for GH30 (Li et al., 2022b). However, the enzymes that exhibit hydrolytic activity on xylan and xylo-oligosaccharides, are classified in 3 subfamilies GH30_7, GH30_8, and GH30_10. Both subfamilies GH30_7 and GH30_8 are associated with endo-1,4-β-xylanase activity, along with β-xylosidases and glucuronoxylanase functions, however, in GH30_10 subfamily, only one xylobiohydrolase has been reported (Crooks et al., 2021; Suchova et al., 2021). The GH30 family is primarily composed of bacterial sequences, which account for approximately, 94%, with eukaryotic sequences making up the remaining ~6%.

Due to their close evolutionary relationship, many GH30 enzymes, including several xylanases, were initially classified within the GH5 family but were later reclassified to GH30 following extensive phylogenetic and structural analyses (St John et al., 2010). Like GH5 and GH10 enzymes, GH30 members feature a $(\beta/\alpha)_8$-barrel fold structure and catalyze hydrolysis while maintaining the anomeric configuration, using two glutamic acid residues as critical catalytic amino acids (Freire et al., 2016; Nakamichi et al., 2019a, 2020b; Sainz- Polo et al., 2014; St John et al., 2011, 2014)

(Table 1.2). In contrast to GH5 and GH10 families, GH30 enzymes possess an additional structural feature: a nine-stranded aligned β-sheet, which is connected to the $(\beta/\alpha)_8$-barrel domain via conserved linker sequences at both the N- and C-termini, as well as through hydrophobic interactions with α-helices 7 and 8. Although the overall three-dimensional structures of GH30_7 and GH30_8 enzymes are highly similar, their sequence identity generally remains below 25%. Key structural differences within the $(\beta/\alpha)_8$ domain include a notably shorter β2-α2 loop and β1-α1 structures in GH30_8 enzymes, as well as the presence of an α6-helix instead of an unstructured loop. In contrast, GH30_7 enzymes contain two short β-strands (β8A and β8B) in the β8-α8 loop, two disulfide bonds, and several other minor variations in loop lengths and secondary structure positioning (Nakamichi et al., 2019a).

Table 1.2 Characteristics of xylanases from various GH families. (Mendonça et al. 2023)

Glycoside Hydrolase Family	Xylanase activities	Structure fold	3D structure	Catalytic mechanism
GH5	Endo-1,4-β-xylanase Exo-1,4-β-xylosidase	$(\beta/\alpha)_8$-fold	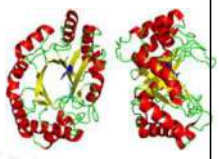	Retaining
GH8	Endo-1,4-β-xylanase Endo-1,3-β-xylosidase Exo-1,4-β-xylosidase	$(\alpha/\alpha)_6$-fold	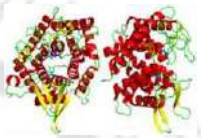	Inverting
GH10	Endo-1,4-β-xylanase Endo-1,3-β-xylosidase Exo-1,4-β-xylosidase	$(\beta/\alpha)_8$-fold	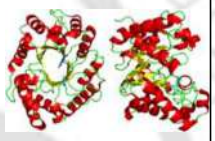	Retaining
GH11	Endo-1,4-β xylanase Exo-1,4-β-xylosidase	β-jelly roll fold	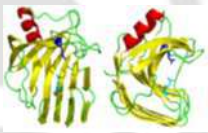	Retaining
GH30	Endo-1,4-β xylanase Glucuronoxylanase Exo-1,4-β-xylosidase	$(\beta/\alpha)_8$-fold		Retaining
GH43	Endo-1,4-β xylanase Exo-1,4-β-xylosidase Exo-1,3-β-xylosidase	5-fold β-propeller	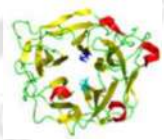	Inverting
GH51	Endo-1,4-β xylanase Exo-1,4-β-xylosidase	(β/α)8-fold		Retaining
GH141	Endo-1,4-β xylanase	β-helix	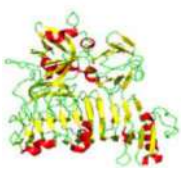	Not known

1.6 Sources of xylanase

Xylanases are ubiquitous and highly diversified in nature. Many different lifeforms from different habitats have been found to produce these enzymes, which includes terrestrial plants, seaweeds, bacteria, archaea, fungi, protozoa, crustaceans and insects (Bajpai, 2014; Smith et al., 1991; Subramaniyan & Prema, 2002). However, from the commercial point of view, the xylanase producing filamentous fungi is more interesting and has gained more attention than the rest. When grown in a medium, the fungi release the xylan-degrading enzymes in the surrounding medium, cancelling the need to destroy the cells for purifying the enzymes (Polizeli et al., 2005). Fungi also produce several additional enzymes needed to degrade substituted xylans (Bajpai, 2014). In the case of mesophilic fungi, *Aspergillus niger* and *Trichoderma reesei* have been found to be the most important xylanase producing species. In the past decade, extensive efforts have been made on isolation of enzymes from the thermophiles and extremophiles because they are found to produce enzymes with higher thermo-tolerance and stability. Several bacterial species *Bacillus licheniformis, Bacillus thermantarcticus, Dictyoglomus thermophilum, Geobacillus stearothermophilus, Thermotoga, Caldocellum saccharolyticum, Dictyoglomus thermophilum, Thermoanaerobacterium saccharolyticum, Anoxybacillus kaynarcensis, Caldanaerobius polysaccharolyticus, Thermopolyspora flexuosa* and *Clostridium thermocellum* have been reported to express xylanase enzymes (Guo et al., 2018; Khasin et al., 1993; Lüthi et al., 1990; Patel et al., 1987). In the case of fungi, multiple thermophilic species have been found to produce xylanase; some of them are *Myceliophthora thermophila, Paecilomyces themophila, Talaromyces thermophilus, melanocarpus albomyces, Humicola grisea, Thermoascus aurantiacus, Thermomyces*

lanuginosus, Scytalidium thermophilum, Myceliophthora sepedonium, Pseudocerco sporella, Rasamsonia byssochlamys, and *Thielavia australiensis* (Sunna & Antranikian, 1997). The optimal temperature for xylanases from these fungi falls between 60 and 85°C. They are found to be highly tolerant and stable in this optimal temperature range and active in the acidic pH range, 4.5-6.5.

1.7 Thermostable carbohydrate enzymes and their importance

Enzymes that are stable and show good activity at high temperatures and in both acidic and alkaline pH have always been in high demand commercially because the majority of industrial processes are conducted at high temperatures and across a broad pH range. The screening and isolation of thermophilic microorganisms that flourish in various extreme environments, such as thermal springs and salty marsh fills, has garnered great attention in the last two decades, i.e., thermophiles, mesophiles and psychrophiles (Collins et al., 2005). They are found to produce efficient thermostable enzymes appropriate for commercial purposes like bio-bleaching in the textile and, pulp and paper industry and saccharification of lignocellulosic waste (El Enshasy et al., 2016). Xylanases isolated from the thermophilic bacteria and archaea have been found to possess a remarkably long half-life at 80°C or higher temperatures, as compared with the enzymes from thermophilic fungi. Thermostable xylanases have been discovered in various GH families, such as 5, 7, 8, 10, 11, 30 and 43 (Collins et al., 2005).

1.8 Applications of xylanase

Xylanolytic enzymes produced by the microorganisms hold immense biotechnological potential for multiple industrial applications such as pulp and paper, textiles, food, beverages, animal feed, chemicals, biofuel and laundry (Juturu & Wu, 2012; V. Kumar et al., 2018; Subramaniyan & Prema, 2002) as depicted in Fig. 1.7. In textile, pulp and paper industry, the bleaching of pulp using xylanase and other carbohydrate active enzymes are commercially well accepted nowadays (Bajpai, 1999; V. Kumar et al., 2016). It has significantly decreased the usage of chlorine for bleaching, reducing the ecological harm caused by the process. In textile industries also, the use of xylanase for the refinement and processing of plant fabrics has reduced the use of harsh chemicals for bleaching (Subash & Muthiah, 2021). In the food sector, xylanase is utilized to make quality breads with varying softness and elasticity, and to extract coffee and plant oils (Maat et al., 1992). The application of xylanase on forage crops increases its digestibility when feed to the ruminant animals (Selzer et al., 2021). In the pharmaceutical sector xylanase has been used with other digestive enzymes as a dietary supplement to help people with poor digestion (Juturu & Wu, 2012).

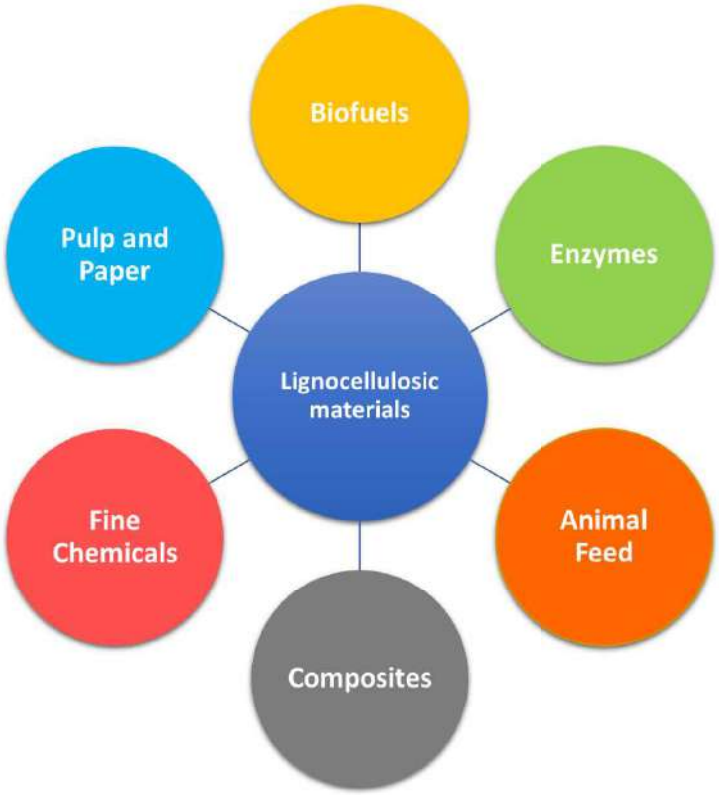

Fig. 1.7 Lignocellulosic materials conversion into value-added products.

1.8.1 Xylanase in enzymatic degumming of plant-based textile fibres

Enzymatic degumming is an eco-friendly and efficient method for eliminating non-cellulosic substances, including pectin, hemicellulose and lignin from plant fibres, particularly bast fibres like ramie, hemp and flax using pectinolytic and hemicellulolytic enzymes (Subash & Muthiah, 2021). This process utilizes specific enzymes, such as xylanases, pectinases and ligninases, to selectively breakdown the gum that binds the fibres together, facilitating their separation without compromising the structural integrity of the fibres (Abidin et al., 2023). Xylanases contribute to the degumming process by breaking down xylan from the hemicellulose portion. Pectinolytic enzymes, particularly pectate lyases, play a key role in removing pectin from the fiber surface.

Enzymatic and chemical degumming methods share the common goal of achieving cleaner fibres by removing non-cellulosic substances. Both degumming processes share some similarities, but their approaches differ significantly, with enzymatic degumming relying on biological catalysts and chemical degumming using harsh chemicals. In the beginning, plant fibres like hemp, ramie and flax are prepared by decortication, followed by cleaning and washing to remove dirt and loose particles (Fig. 1.8). The fibres are then treated with enzymes or chemicals, depending on the approach. After degumming, the fibres are washed with water to remove degraded components and residual chemicals or enzymes (Fig. 1.8). Then, the fibres are dried and sent forward for different applications. Recent advancements in enzyme technology have led to the development of customized enzyme cocktails and optimized process parameters, further enhancing the efficiency and applicability of enzymatic degumming in the textile and composite industries (Kaur et al., 2020).

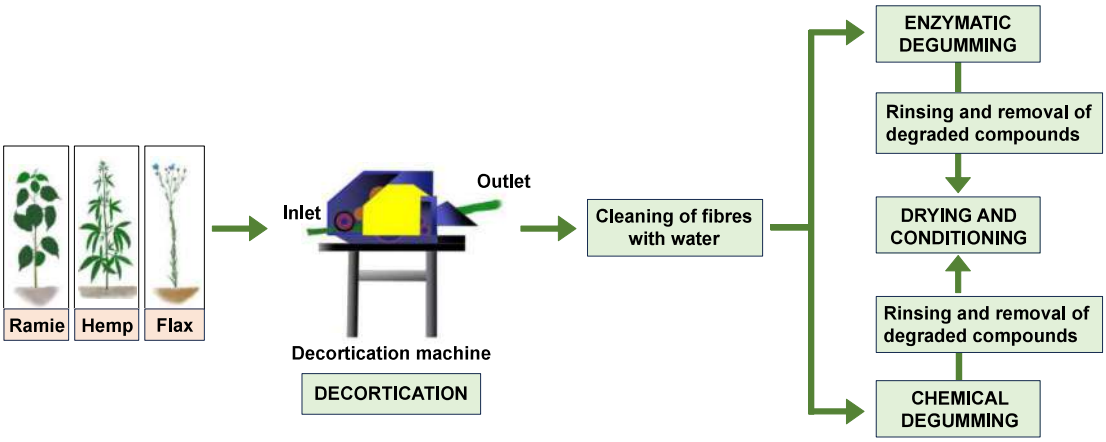

Fig. 1.8 Schematic presentation of enzymatic and chemical degumming process.

Bast fibres are an essential source of natural textile fibres, derived from the phloem of dicotyledonous plants, exhibit a complex structure and composition that contribute to their unique properties and applications. These fibres primarily consist of

cellulose, hemicellulose, lignin, pectin, and waxes, with cellulose being the most abundant component, typically comprising 60-80% of the fibre's dry weight (Kozłowski et al., 2020; Sadrmanesh and Chen, 2019). The enzymes, like xylanase, in combination with pectinase and lignase, are important for efficient and environmentally sustainable extraction of natural plant fibres from bast fibres (Abidin et al., 2023). These enzymes facilitate the retting process by specifically breaking down the non-cellulosic components, such as xylan, pectin and lignin, leading to faster fibre extraction. A degumming efficiency of 82% was achieved by using an enzymatic concoction produced by *Pectobacterium carotovorum* HG-49, containing xylanase, pectinase and mannanase for ramie fibres (Shu et al., 2020). The degumming efficiency is calculated as the percentage reduction in gum content relative to the initial gum content present in the raw material. The structural organization of bast fibres includes a primary wall of a rigid network of cellulose microfibrils embedded within a matrix of hemicellulose and pectin, which provides flexibility and strength (Fig. 1.9). The fibres are characterized by a hollow lumen that aids in nutrient transport within the plant. At the same time, the overall morphology includes elongated bundles of fibrils that exhibit a high length-to-diameter ratio, enhancing their mechanical properties (Zimniewska et al., 2011). Recent studies have highlighted the variability in the composition and properties of bast fibres, which can be affected by factors such as plant species, cultivation conditions, and extraction methods, underscoring the importance of optimizing these parameters for specific industrial applications (Santos et al., 2024).

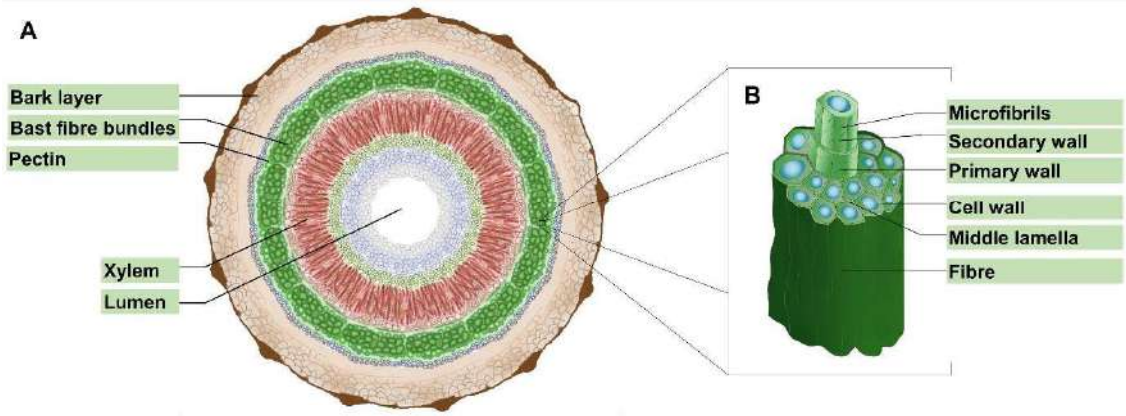

Fig. 1.9 Schematic presentation of (a) cross-section of bast stem and (b) Bast fibre bundle.

1.9 *Acetivibrio clariflavus*

Acetivibrio clariflavus is a thermophilic, anaerobic, gram-positive and cellulosome forming bacterium (Fig. 1.10). Numerous strains of *A. clariflavus* have been found to utilize both cellulose and hemicellulose as a carbon source. It was first isolated from an anaerobic sludge taken from a thermophilic methanogenic bioreactor (Shiratori et al., 2006). The whole genome of the *A. clariflavus* has been sequenced, after which many putative carbohydrate-active enzymes produced by this thermophile were found and characterized, including enzymes from glycoside hydrolase families GH5, GH9, GH10, GH11, GH30 and GH48 (Artzi et al., 2015).

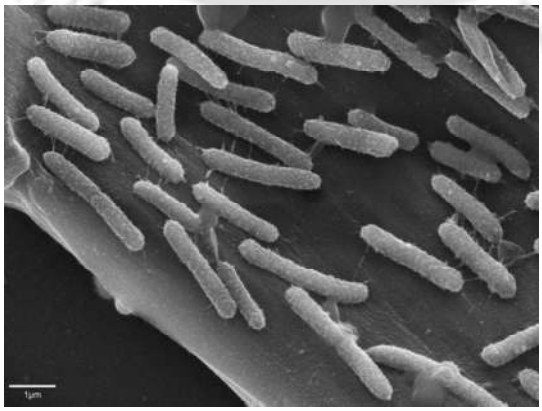

Fig. 1.10 Scanning electron micrograph of *Acetivibrio clariflavus* DSM 19732 (Izquierdo et. al., 2012).

1.9.1 Cellulosomal organisation of *Acetivibrio clariflavus*

The genome of *A. clariflavus* features 49 cohesin modules distributed across 13 distinct scaffoldins, along with 79 proteins containing dockerin domains, indicating a high potential for the formation of multiple cellulosome complexes. The modular configuration of the cohesin and dockerin modules on the 13 different scaffoldins (Sca) are displayed in Fig. 1.11 (Artzi et al., 2014). Cohesin is a protein module that serves as a primary building block of scaffoldins, which are structural proteins that organize different cellulolytic enzymes into a cohesive multi-enzyme complex called cellulosome (Handelsman et al., 2004). Cohesin modules have the ability to bind tightly to dockerin modules, forming high-affinity interactions essential for cellulosome integrity and function. Whereas, dockerin is a protein module that anchors catalytic enzyme subunits to scaffoldins via its interaction with cohesins. Dockerins exhibit a unique structural feature known as the F-hand motif, which includes a calcium-binding loop that is critical for binding to cohesins (Duarte et al., 2021). Dockerins bind with cohesins from the same species, while exhibiting less specificity towards cohesins from different species. The presence of signal peptides at the end of their N-terminus of the scaffoldins (except ScaO and ScaM (a)), indicates that they are secreted exogenously (Fig. 1.11). Among the 79 proteins reported to contain a dockerin, 4 of them have type II dockerin and 75 of them possess type I dockerin, including 57 dockerin I-containing enzymes. These enzymes are comprised of 41 glycoside hydrolases (GHs), 14 carbohydrate esterases (CEs) and 2 polysaccharide lyases (PLs), in which some of the dockerin containing enzymes are composed of more than one catalytic module and are bifunctional in nature (Artzi et al., 2014). *A. clariflavus* also contains non-catalytic dockerin containing proteins like serpin (Clocl_3968) and expansin-containing proteins

(Clocl_1298 and Clocl_1862). Serpins are serine protease inhibitors and expansins are non-catalytic proteins that loosen the cell walls during the growth of the plant. The expression of the cellulosomal proteins are regulated by the type of substrate in the growth medium (Artzi et al., 2015).

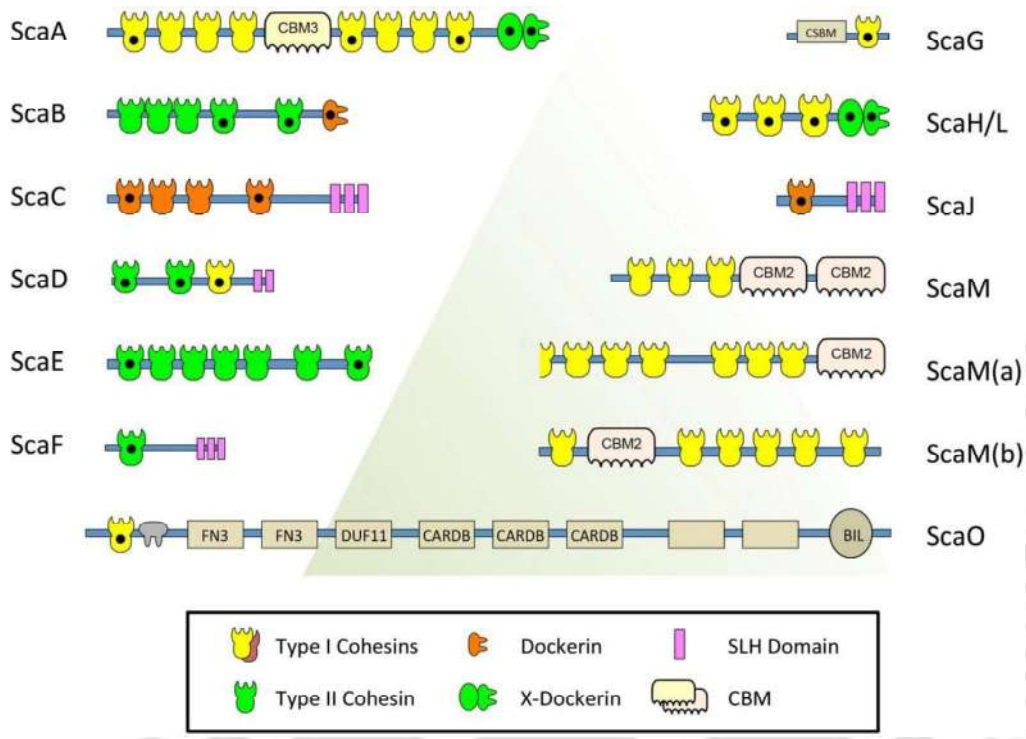

Fig. 1.11 Schematic presentation of modular arrangement of 13 putative scaffoldins (denoted as Sca) of A. clariflavus DSM 19732 genome. SLH, S-layer homology; FN3, fibronectin type III domain; CARDB, cell adhesion-related domain present in bacteria; DUF11, domain of unknown function; CSBM, cell surface-binding module; BIL, bacterial intein-like domain; CBM, carbohydrate-binding module (Artzi et al., 2014).

Discovering and revealing novel enzymes from this microorganism may help in evolving the current methodologies for the breakdown of the lignocellulosic materials. Out of various candidate organisms for thermophilic consolidated bioprocessing (CBP) (Chen et al., 2018; Gao et al., 2020), *Acetivibrio clariflavus* has obtained little attention compared to the model cellulolytic thermophile *Clostridium thermocellum*, that has been extensively studied in the last decade (Verma & Goyal,

2016). According to the carbohydrate-active enzymes database (CAZy; www.cazy.org), there are 57 putative glycoside hydrolase genes present in the genome of *Acetivibrio clariflavus,* out of which only 4 enzymes have been characterized. Considering the limited reports and attention surrounding the putative glycoside hydrolases from *Acetivibrio clariflavus*, this study focuses on the investigation on the putative glycoside hydrolase, xylobiohydrolase.

1.10 Significance of the project

Lignocellulosic biomass is an abundant, renewable and underexploited resource with immense potential to support sustainable bio-based industries. Derived mainly from agricultural and forestry residues, this biomass consists of a complex matrix of cellulose, hemicellulose and lignin. Once it is converted to simpler forms, the products can be used for various purposes. The most popular application is the production of bio-fuels and reduction in the carbon footprint caused by agricultural and forestry activities. Fuels derived from biomass do not contribute to increased atmospheric CO_2, as the CO_2 released during combustion is balanced by the amount fixed during photosynthesis (Singh et al., 2017). In India, urbanization and intense economic growth have resulted in the production of unprecedented amount of waste products, including agro-waste. Forests and agriculture activities are the two biggest sources from which biomass is generated every year. A large part of Indian population depends on agriculture for livelihood. It is estimated that around 1.79 million km^2 of land in India is utilized for agriculture (Cardoen et al., 2015; Hiloidhari et al., 2014). According to the ministry of New and Renewable Energy, Government of India, the latest estimate of the available biomass generated per year in India is 500 million metric tonnes. The availability of lignocellulosic biomass from the agriculture and forestry fields is expected to reach 281 metric tonnes per annum by 2030-31 in India (Cardoen et al., 2015; Purohit & Chaturvedi, 2018; Sadi et al., 2021). The degradation of hemicellulosic xylan requires the cooperative action of xylanases. The increasing availability of lignocellulosic biomass and the urgent need for sustainable bio-based solutions highlight the importance of enzymes capable of efficiently degrading plant polysaccharides. Xylanases also hold great potential for green chemical production,

prebiotic formulation and sustainable biobleaching in the textile, pulp and paper industries, minimizing dependence on chemical treatments.

The genome of *Acetivibrio clariflavus* contains a large repertoire of glycoside hydrolase genes, more than the genes found in *Acetivibrio thermocellus* (Izquierdo et al., 2012). *Acetivibrio clariflavus* is a thermophilic microorganism, making it a promising candidate for sourcing thermophilic enzymes. Several enzymes from the cellulosomal complex of *Acetivibrio clariflavus,* belonging to GH30 family, have been characterized but none of them was found to be thermophilic (Puchart et al., 2021). The proposed study focuses on a putative thermostable xylanase from *Acetivibrio clariflavus*, classified under glycoside hydrolase family GH30. The identified gene accession number and locus tag of the proposed enzyme, *Ac*GH30A is AEV68404.1 and Clocl_1795, respectively. The putative thermostable xylanase, *Ac*GH30A from *Acetivibrio clariflavus* can potentially contribute to the efficient degradation and processing of the lignocellulosic biomass. Expression and purification of this enzyme is designed to provide enough enzyme for biochemical and structural characterization. This will provide us with a thermophilic xylan degrading enzyme from a thermophilic microorganism. This enzyme may also be applicable in various industries, such as pulp and paper, textiles, food, beverages, animal feed, chemicals, biofuel and laundry. The *in-silico* study of the enzyme will enable us to understand its structural properties and its behaviour with different substrates or its mode of action. The 3-dimensional structure of the enzyme may be elaborately understood by the crystallization of the enzyme and X-ray diffraction methods for a better understanding of its structure.

The reasons for selecting the family 30 glycoside hydrolase from *Acetivibrio clariflavus* are summarized below:

i. The genome of *Acetivibrio clariflavus* encodes an intricate and extensive cellulosome system, housing numerous enzymes capable of degrading hemicellulose and cellulose.
ii. The functional characterization of family 30 xylanase is crucial, as all enzymes within this family share a retaining-type catalytic mechanism. Therefore, analyzing their degradation products can reveal if they follow an exo- or endo-cleavage mode.
iii. Several xylanases from GH30 have been identified as glucuronoxylanases, exhibiting specificity for xylan backbone linked to glucuronic acid moieties. Investigating GH30 glycoside hydrolases can provide insights into the molecular basis of this specificity toward glucuronoxylan.

The identification of enzymes from the thermophilic organisms, *Acetivibrio clariflavus*, offers a promising opportunity to study thermostable carbohydrate-active enzymes. By focusing on the putative glycoside hydrolase family 30 xylanase, *Ac*GH30A, this study aims to enhance the understanding of carbohydrate-active enzymes and their potential. The comprehensive characterization of *Ac*GH30A, both structurally and functionally, will pave the way for its use in different industrial applications, such as biofuel production and degumming of natural plant fibres. To achieve these goals, the following specific objectives were formulated:

1.10.1 Specific objectives

1. Cloning, expression and purification of a putative xylanase, *Ac*GH30A of family 30 Glycoside Hydrolase from *Acetivibrio clariflavus* ATCC 19732.
2. Biochemical and functional characterization of *Ac*GH30A, a putative xylanase from *Acetivibrio clariflavus* ATCC 19732.
3. Structure analysis of *Ac*GH30A by *in silico* approaches, including homology modelling and molecular dynamics simulation.
4. Structure analysis of *Ac*GH30A in an aqueous environment by circular dichroism (CD), dynamic light scattering (DLS) and small-angle X-ray scattering (SAXS).
5. Application of *Ac*GH30A in combination with other hemicellulosic enzymes in degumming of ramie (*Boehmeria nivea*) bast fibres and pineapple (*Ananas comosus*) leaf fibres.

References

1. Ahmed, S., Luis, A. S., Bras, J. L. A., Ghosh, A., Gautam, S., Gupta, M. N., Fontes, C. M. G. A., & Goyal, A. (2013). A novel α-l-arabinofuranosidase of family 43 glycoside hydrolase (Ct43Araf) from *Clostridium thermocellum*. *PLOS ONE*, *8*(9), e73575. https://doi.org/10.1371/journal.pone.0073575
2. Abidin, K. Y., Nurhayati, N., Nandyawati, D., & Sabbathini, G. C. (2023). Enzymatic degumming using xylanase and pectinase to improve brightness and fineness quality of ramie fiber (*boehmeria nivea l*.) as textile raw material. *Jurnal Bioteknologi Dan Biosains Indonesia*, 10(1), 76-85. https://ejournal.brin.go.id/JBBI/article/view/1744
3. Amel, B.-D., Nawel, B., Khelifa, B., Mohammed, G., Manon, J., Salima, K.-G., Farida, N., Hocine, H., Bernard, O., & Jean-Luc, C. (2016). Characterization of a purified thermostable xylanase from *Caldicoprobacter algeriensis* sp. Nov. Strain TH7C1T. *Carbohydrate Research*, *419*, 60–68. https://doi.org/10.1016/j.carres.2015.10.013
4. Artzi, L., Dassa, B., Borovok, I., Shamshoum, M., Lamed, R., & Bayer, E. A. (2014). Cellulosomics of the cellulolytic thermophile *Clostridium clariflavum*. *Biotechnology for Biofuels*, *7*(1), 100. https://doi.org/10.1186/1754-6834-7-100
5. Artzi, L., Morag, E., Barak, Y., Lamed, R., & Bayer, E. A. (2015). *Clostridium clariflavum*: Key cellulosome players are revealed by proteomic analysis. mBio, *6*(3). https://doi.org/10.1128/mbio.00411-15
6. Bajpai, P. (1999). Application of enzymes in the pulp and paper industry. *Biotechnology Progress*, *15*(2), 147–157. https://doi.org/10.1021/bp990013k
7. Bajpai, P. (2014). Chapter 2 - Xylan: Occurrence and structure. *In P. Bajpai (Ed.), Xylanolytic enzymes* (pp. 9–18). *Academic Press.* https://doi.org/10.1016/B978-0-12-801020-4.00002-0
8. Bajpai, P. (2016). Structure of lignocellulosic biomass. In P. Bajpai (Ed.), *Pretreatment of Lignocellulosic Biomass for Biofuel Production* (pp. 7–12). Springer. https://doi.org/10.1007/978-981-10-0687-6_2
9. Banka, A. L., Albayrak Guralp, S., & Gulari, E. (2014). Secretory expression and characterization of two hemicellulases, xylanase, and β-xylosidase, isolated from *Bacillus Subtilis* M015. *Applied Biochemistry and Biotechnology*, *174*(8), 2702–2710. https://doi.org/10.1007/s12010-014-1219-1
10. Barabote, R. D., Parales, J. V., Guo, Y.-Y., Labavitch, J. M., Parales, R. E., & Berry, A. M. (2010). Xyn10A, a thermostable endoxylanase from *Acidothermus cellulolyticus* 11B. *Applied and Environmental Microbiology*, *76*(21), 7363–7366.
11. Behera, S. S., & Ray, R. C. (2016). Konjac glucomannan, a promising polysaccharide of *Amorphophallus konjac* K. Koch in health care. *International Journal of Biological Macromolecules*, 92, 942–956. https://doi.org/10.1016/j.ijbiomac.2016.07.098
12. Biely, P. (1985). Microbial xylanolytic systems. *Trends in Biotechnology*, *3*(11), 286–290. https://doi.org/10.1016/0167-7799(85)90004-6

13. Biely, P., Puchart, V., Stringer, M. A., & Krogh, K. B. R. M. (2014). *Trichoderma reesei* XYN VI – a novel appendage-dependent eukaryotic glucuronoxylan hydrolase. *The FEBS Journal*, *281*(17), 3894–3903. https://doi.org/10.1111/febs.12925

14. Cantarel, B. L., Coutinho, P. M., Rancurel, C., Bernard, T., Lombard, V., & Henrissat, B. (2009). The carbohydrate-active enzymes database (CAZy): An expert resource for Glycogenomics. *Nucleic Acids Research*, *37*(suppl_1), D233–D238. https://doi.org/10.1093/nar/gkn663

15. Cardoen, D., Joshi, P., Diels, L., Sarma, P. M., & Pant, D. (2015). Agriculture biomass in India: Part 2. Post-harvest losses, cost and environmental impacts. *Resources, Conservation and Recycling*, *101*, 143–153. https://doi.org/10.1016/j.resconrec.2015.06.002

16. Chandel, V., Biswas, D., Roy, S., Vaidya, D., Verma, A., & Gupta, A. (2022). Current advancements in pectin: extraction, properties and multifunctional applications. *Foods,* 11(17). https://doi.org/10.3390/foods11172683

17. Chekan, J. R., Kwon, I. H., Agarwal, V., Dodd, D., Revindran, V., Mackie, R. I., Cann, I., & Nair, S. K. (2014). Structural and biochemical basis for mannan utilization by *Caldanaerobius polysaccharolyticus* Strain ATCC BAA-17. *Journal of Biological Chemistry*, *289*(50), 34965–34977. https://doi.org/10.1074/jbc.M114.579904

18. Chen, L., Du, J.-L., Zhan, Y.-J., Li, J.-A., Zuo, R.-R., & Tian, S. (2018). Consolidated bioprocessing for cellulosic ethanol conversion by cellulase–xylanase cell-surfaced yeast consortium. *Preparative Biochemistry & Biotechnology*, *48*(7), 653–661. https://doi.org/10.1080/10826068.2018.1487846

19. Christiansen, C., Abou Hachem, M., Janeček, Š., Viksø-Nielsen, A., Blennow, A., & Svensson, B. (2009). The carbohydrate-binding module family 20 – diversity, structure, and function. *The FEBS Journal*, *276*(18), 5006–5029. https://doi.org/10.1111/j.1742-4658.2009.07221.x

20. Collins, T., Gerday, C., & Feller, G. (2005). Xylanases, xylanase families and extremophilic xylanases. *FEMS Microbiology Reviews*, *29*(1), 3–23. https://doi.org/10.1016/j.femsre.2004.06.005

21. Davies, G. J., Gloster, T. M., & Henrissat, B. (2005). Recent structural insights into the expanding world of carbohydrate-active enzymes. *Current Opinion in Structural Biology*, *15*(6), 637–645. https://doi.org/10.1016/j.sbi.2005.10.008

22. Dodd, D., & Cann, I. K. (2009). Enzymatic deconstruction of xylan for biofuel production. *Gcb Bioenergy*, *1*(1), 2–17. https://doi.org/10.1111/j.1757-1707.2009.01004.x

23. Drula, E., Garron, M.-L., Dogan, S., Lombard, V., Henrissat, B., & Terrapon, N. (2022). The carbohydrate-active enzyme database: Functions and literature. *Nucleic Acids Research,* *50*(D1), D571–D577. https://doi.org/10.1093/nar/gkab1045

24. Duarte, M., Viegas, A., Alves, V. D., Prates, J. A. M., Ferreira, L. M. A., Najmudin, S., Cabrita, E. J., Carvalho, A. L., Fontes, C. M. G. A., & Bule, P. (2021). A dual cohesin–dockerin complex binding mode in *Bacteroides cellulosolvens* contributes to the size and complexity of its cellulosome. *The Journal of Biological Chemistry*, *296*, 100552. https://doi.org/10.1016/j.jbc.2021.100552

25. El Enshasy, H. A., Kandiyil, S. K., Malek, R., & Othman, N. Z. (2016). Microbial xylanases: sources, types, and their applications. In V. K. Gupta (Ed.), *Microbial Enzymes in Bioconversions of Biomass* (Vol. 3, pp. 151–213). Springer International Publishing. https://doi.org/10.1007/978-3-319-43679-1_7

26. Fazary, A. E., & Ju, Y.-H. (2007). Feruloyl esterases as biotechnological tools: current and future perspectives. *Acta Biochimica et Biophysica Sinica*, *39*(11), 811–828. https://doi.org/10.1111/j.1745-7270.2007.00348.x

27. Fan, G., Yang, S., Yan, Q., Guo, Y., Li, Y., & Jiang, Z. (2014). Characterization of a highly thermostable glycoside hydrolase family 10 xylanase from *Malbranchea cinnamomea*. *International Journal of Biological Macromolecules*, *70*, 482–489. https://doi.org/10.1016/j.ijbiomac.2014.07.025

28. Fernández, P. V., Zelaya, V. M., Cobello, L., Vega, A. S., & Ciancia, M. (2019). Glucuronoarabinoxylans and other cell wall polysaccharides from shoots of *Guadua chacoensis* obtained by extraction in different conditions. *Carbohydrate Polymers*, *226*, 115313. https://doi.org/10.1016/j.carbpol.2019.115313

29. Fonseca-Maldonado, R., Ribeiro, L. F., Furtado, G. P., Arruda, L. M., Meleiro, L. P., Alponti, J. S., Botelho-Machado, C., Vieira, D. S., Bonneil, E., & Furriel, R. dos P. M. (2014). Synergistic action of co-expressed xylanase/laccase mixtures against milled sugar cane bagasse. *Process Biochemistry*, *49*(7), 1152–1161. https://doi.org/10.1016/j.procbio.2014.03.027

30. Gao, C., Guo, L., Ding, Q., Hu, G., Ye, C., Liu, J., Chen, X., & Liu, L. (2020). Dynamic consolidated bioprocessing for direct production of xylonate and shikimate from xylan by *Escherichia coli*. *Metabolic Engineering*, *60*, 128–137. https://doi.org/10.1016/j.ymben.2020.04.001

31. Garg, S. (2016). Xylanase: Applications in biofuel production. *Current Metabolomics*, *4*(1), 23–37. https://doi.org/10.2174/2213235X03666150915211224

32. Gilbert, H. J. (2010). The biochemistry and structural biology of plant cell wall deconstruction. *Plant Physiology*, *153*(2), 444–455. https://doi.org/10.1104/pp.110.156646

33. Guo, Y., Gao, Z., Xu, J., Chang, S., Wu, B., & He, B. (2018). A family 30 glucurono-xylanase from *Bacillus subtilis* LC9: Expression, characterization and its application in chinese bread making. *International Journal of Biological Macromolecules*, *117*, 377–384. https://doi.org/10.1016/j.ijbiomac.2018.05.143

34. Handelsman, T., Barak, Y., Nakar, D., Mechaly, A., Lamed, R., Shoham, Y., & Bayer, E. A. (2004). Cohesin–dockerin interaction in cellulosome assembly: A single Asp-to-Asn mutation disrupts high-affinity cohesin–dockerin binding. *FEBS Letters, 572*(1), 195–200. https://doi.org/10.1016/j.febslet.2004.07.040

35. He, J., Su, L., Sun, X., Fu, J., Chen, J., & Wu, J. (2014). A novel xylanase from *Streptomyces* sp. FA1: Purification, characterization, identification, and heterologous expression. *Biotechnology and Bioprocess Engineering*, *19*(1), 8–17. https://doi.org/10.1007/s12257-013-0490-2

36. Hiloidhari, M., Das, D., & Baruah, D. C. (2014). Bioenergy potential from crop residue biomass in India. *Renewable and Sustainable Energy Reviews*, *32*, 504–512. https://doi.org/10.1016/j.rser.2014.01.025

37. Hinz, S. W., Pouvreau, L., Joosten, R., Bartels, J., Jonathan, M. C., Wery, J., & Schols, H. A. (2009). Hemicellulase production in *Chrysosporium lucknowense* C1. *Journal of Cereal Science*, *50*(3), 318–323. https://doi.org/10.1016/j.jcs.2009.07.005

38. Hurlbert, J. C., & Preston, J. F. (2001). Functional characterization of a novel xylanase from a corn strain of *Erwinia chrysanthemi*. *Journal of Bacteriology*, *183*(6), 2093–2100. https://doi.org/10.1128/JB.183.6.2093-2100.2001

39. Izquierdo, J. A., Goodwin, L., Davenport, K. W., Teshima, H., Bruce, D., Detter, C., Tapia, R., Han, S., Land, M., & Hauser, L. (2012). Complete genome sequence of *Clostridium clariflavum* DSM 19732. *Standards in Genomic Sciences*, *6*(1), 104–115.

40. Jordan, D. B., & Wagschal, K. (2010). Properties and applications of microbial β-D-xylosidases featuring the catalytically efficient enzyme from *Selenomonas ruminantium. Applied Microbiology and Biotechnology*, *86*(6), 1647–1658. https://doi.org/10.1007/s00253-010-2538-y

41. Juturu, V., & Wu, J. C. (2012). Microbial xylanases: Engineering, production and industrial applications. *Biotechnology Advances*, *30*(6), 1219–1227. https://doi.org/10.1016/j.biotechadv.2011.11.006

42. Kaczmarska, A., Pieczywek, P. M., Cybulska, J., & Zdunek, A. (2022). Structure and functionality of Rhamnogalacturonan I in the cell wall and in solution: A review. *Carbohydrate Polymers*, *278*, 118909. https://doi.org/10.1016/j.carbpol.2021.118909

43. Katsimpouras, C., Dedes, G., Thomaidis, N. S., & Topakas, E. (2019). A novel fungal GH30 xylanase with xylobiohydrolase auxiliary activity. *Biotechnology for Biofuels*, *12*(1), 1–14. https://doi.org/10.1186/s13068-019-1455-2

44. Kaur, A., Varghese, L. M., Battan, B., Patra, A. K., Mandhan, R. P., & Mahajan, R. (2020). Bio-degumming of banana fibers using eco-friendly crude xylano-pectinolytic enzymes. *Preparative Biochemistry & Biotechnology, 50*(5), 521–528. https://doi.org/10.1080/10826068.2019.1710713

45. Khasin, A., Alchanati, I., & Shoham, Y. (1993). Purification and characterization of a thermostable xylanase from *Bacillus stearothermophilus* T-6. *Applied and Environmental Microbiology*, *59*(6), 1725–1730. https://doi.org/10.1128/aem.59.6.1725-1730.1993

46. Kumar, K. S., Manimaran, A., Permaul, K., & Singh, S. (2009). Production of β-xylanase by a *Thermomyces lanuginosus* MC 134 mutant on corn cobs and its

application in biobleaching of bagasse pulp. *Journal of Bioscience and Bioengineering*, *107*(5), 494–498. https://doi.org/10.1016/j.jbiosc.2008.12.020

47. Kumar, P. R., Eswaramoorthy, S., Vithayathil, P. J., & Viswamitra, M. A. (2000). The tertiary structure at 1.59 Å resolution and the proposed amino acid sequence of a family-11 xylanase from the thermophilic fungus *Paecilomyces varioti*. *Journal of Molecular Biology*, *295*(3), 581–593. https://doi.org/10.1006/jmbi.1999.3348
48. Kumar, V., Chhabra, D., & Shukla, P. (2017). Xylanase production from *Thermomyces lanuginosus* VAPS-24 using low cost agro-industrial residues via hybrid optimization tools and its potential use for saccharification. *Bioresource Technology*, *243*, 1009–1019. https://doi.org/10.1016/j.biortech.2017.07.094
49. Kumar, V., Dangi, A. K., & Shukla, P. (2018). Engineering thermostable microbial xylanases toward its industrial applications. *Molecular Biotechnology*, *60*(3), 226–235. https://doi.org/10.1007/s12033-018-0059-6
50. Kumar, V., Marín-Navarro, J., & Shukla, P. (2016). Thermostable microbial xylanases for pulp and paper industries: Trends, applications and further perspectives. *World Journal of Microbiology and Biotechnology*, *32*(2), 34. https://doi.org/10.1007/s11274-015-2005-0
51. Liang, Z., Song, M., Yin, Z., Wang, G., Wang, J., Liu, L., & Kang, W. (2022). Structural characterization and anticoagulant activity of homogalacturonan from durian peel. *Journal of Molecular Structure*, *1248*, 131467. https://doi.org/10.1016/j.molstruc.2021.131467
52. Lombard, V., Golaconda Ramulu, H., Drula, E., Coutinho, P. M., & Henrissat, B. (2014). The carbohydrate-active enzymes database (CAZy) in 2013. *Nucleic Acids Research*, *42*(D1), D490–D495. https://doi.org/10.1093/nar/gkt1178
53. Luo, H., Yang, J., Li, J., Shi, P., Huang, H., Bai, Y., Fan, Y., & Yao, B. (2010). Molecular cloning and characterization of the novel acidic xylanase XYLD from *Bispora sp*. MEY-1 that is homologous to family 30 glycosyl hydrolases. *Applied Microbiology and Biotechnology*, *86*(6), 1829–1839. https://doi.org/10.1007/s00253-009-2410-0
54. Lüthi, E., Jasmat, N. B., & Bergquist, P. L. (1990). Xylanase from the extremely thermophilic bacterium *Caldocellum saccharolyticum*: Overexpression of the gene in Escherichia coli and characterization of the gene product. *Applied and Environmental Microbiology*, *56*(9), 2677–2683. https://doi.org/10.1128/aem.56.9.2677-2683.1990
55. Maat, J., Roza, M., Verbakel, J., Stam, H., daSilra, M. J. S., Egmond, M. R., Hagemans, M. L. D., van Garcom, R. F. M., Hessing, J. G. M., & van Derhondel, C. (1992). Xylanases and their application in baking *In: Xylan and Xylanases* (pp 349–360). Elsevier.
56. Maheshwari, R., Bharadwaj, G., & Bhat, M. K. (2000). Thermophilic fungi: Their physiology and enzymes. *Microbiology and Molecular Biology Reviews*, *64*(3), 461–488. https://doi.org/10.1128/mmbr.64.3.461-488.2000

57. Mendonça, M., Barroca, M., & Collins, T. (2023). Endo-1,4-β-xylanase-containing glycoside hydrolase families: Characteristics, singularities and similarities. *Biotechnology Advances*, *65*, 108148. https://doi.org/10.1016/j.biotechadv.2023.108148

58. Motghare, K. A., Rathod, A. P., Wasewar, K. L., & Labhsetwar, N. K. (2016). Comparative study of different waste biomass for energy application. *Waste Management*, *47*, 40–45. https://doi.org/10.1016/j.wasman.2015.07.032

59. Nakamichi, Y., Fouquet, T., Ito, S., Watanabe, M., Matsushika, A., & Inoue, H. (2019). Structural and functional characterization of a bifunctional GH30-7 xylanase B from the filamentous fungus *Talaromyces cellulolyticus*. *Journal of Biological Chemistry*, *294*(11), 4065–4078. https://doi.org/10.1074/jbc.RA118.007207

60. Nakamichi, Y., Watanabe, M., Matsushika, A., & Inoue, H. (2020). Substrate recognition by a bifunctional GH30-7 xylanase B from *Talaromyces cellulolyticus*. *FEBS Open Bio*, *10*(6), 1180–1189. https://doi.org/10.1002/2211-5463.12873

61. Nam, G.-H., Jang, M.-U., Kim, M.-J., Lee, J.-M., Lee, M.-J., & Kim, T.-J. (2016). Enzymatic characterization of *Paenibacillus amylolyticus* xylanases GH10 and GH30 for xylan hydrolysis. *Korean Journal of Microbiology*, *52*(4), 463–470. https://doi.org/10.7845/kjm.2016.6068

62. Nikolaivits, E., Pentari, C., Kosinas, C., Feiler, C. G., Spiliopoulou, M., Weiss, M. S., Dimarogona, M., & Topakas, E. (2021). Unique features of the bifunctional GH30 from *Thermothelomyces thermophila* revealed by structural and mutational studies. *Carbohydrate Polymers*, *273*, 118553. https://doi.org/10.1016/j.carbpol.2021.118553

63. Nishitani, K., & Nevins, D. J. (1991). Glucuronoxylan xylanohydrolase. A unique xylanase with the requirement for appendant glucuronosyl units. *Journal of Biological Chemistry*, *266*(10), 6539–6543. https://doi.org/10.1016/S0021-9258(18)38151-1

64. Padilha, I. Q., Valenzuela Mayorga, S. V., Grisi, T., Díaz Lucea, P., de Araújo, D., & Pastor Blasco, F. I. J. (2014). A glucuronoxylan-specific xylanase from a new *Paenibacillus favisporus* strain isolated from tropical soil of Brazil. *International Microbiology, 2014, Vol. 17, Num. 3, p. 175-184*. http://dx.doi.org/10.2436/20.1501.01.220.

65. Patel, B. K., Morgan, H. W., Wiegel, J., & Daniel, R. M. (1987). Isolation of an extremely thermophilic chemoorganotrophic anaerobe similar to *Dictyoglomus thermophilum* from New Zealand hot springs. *Archives of Microbiology*, *147*(1), 21–24. https://doi.org/10.1007/BF00492899

66. Pérez, S., Rodríguez-Carvajal, M. A., & Doco, T. (2003). A complex plant cell wall polysaccharide: Rhamnogalacturonan II. A structure in quest of a function. *Biochimie*, *85*(1), 109–121. https://doi.org/10.1016/S0300-9084(03)00053-1

67. Ping, L., Wang, M., Yuan, X., Cui, F., Huang, D., Sun, W., Zou, B., Huo, S., & Wang, H. (2018). Production and characterization of a novel acidophilic and thermostable xylanase from *Thermoascus aurantiacu*. *International Journal of*

Biological Macromolecules, *109*, 1270–1279. https://doi.org/10.1016/j.ijbiomac.2017.11.130

68. Polizeli, M., Rizzatti, A. C. S., Monti, R., Terenzi, H. F., Jorge, J. A., & Amorim, D. S. (2005). Xylanases from fungi: Properties and industrial applications. *Applied Microbiology and Biotechnology*, *67*(5), 577–591. https://doi.org/10.1007/s00253-005-1904-7

69. Poosarla, V. G., & Chandra, T. S. (2014). Purification and characterization of novel halo-acid-alkali-thermo-stable xylanase from *Gracilibacillus* sp. TSCPVG. *Applied Biochemistry and Biotechnology*, *173*(6), 1375–1390. https://doi.org/10.1007/s12010-014-0939-6

70. Puchart, V., Katapodis, P., Biely, P., Kremnickỳ, L., Christakopoulos, P., Vršanská, M., Kekos, D., Macris, B. J., & Bhat, M. K. (1999). Production of xylanases, mannanases, and pectinases by the thermophilic fungus *Thermomyces lanuginosus*. *Enzyme and Microbial Technology*, *24*(5–6), 355–361. https://doi.org/10.1016/S0141-0229(98)00132-X

71. Puchart, V., Šuchová, K., & Biely, P. (2021). Xylanases of glycoside hydrolase family 30–An overview. *Biotechnology Advances*, 107704. https://doi.org/10.1016/j.biotechadv.2021.107704

72. Purohit, P., & Chaturvedi, V. (2018). Biomass pellets for power generation in India: A techno-economic evaluation. *Environmental Science and Pollution Research*, *25*(29), 29614–29632. https://doi.org/10.1007/s11356-018-2960-8

73. Sakka, M., Tachino, S., Katsuzaki, H., van Dyk, J. S., Pletschke, B. I., Kimura, T., & Sakka, K. (2012). Characterization of Xyn30A and Axh43A of *Bacillus licheniformis* SVD1 identified by its genomic analysis. *Enzyme and Microbial Technology*, *51*(4), 193–199. https://doi.org/10.1016/j.enzmictec.2012.06.003

74. Scott-Craig, J. S., Borrusch, M. S., Banerjee, G., Harvey, C. M., & Walton, J. D. (2011). Biochemical and molecular characterization of secreted α-xylosidase from *Aspergillus niger*. *Journal of Biological Chemistry*, *286*(50), 42848–42854. https://doi.org/10.1074/jbc.M111.307397

75. Sadi, M., Chakravarty, K. H., Behzadi, A., & Arabkoohsar, A. (2021). Techno-economic-environmental investigation of various biomass types and innovative biomass-firing technologies for cost-effective cooling in India. *Energy*, *219*, 119561. https://doi.org/10.1016/j.energy.2020.119561

76. Selzer, K., Hassen, A., Akanmu, A. M., & Salem, A. Z. M. (2021). Digestibility and rumen fermentation of a high forage diet pre-treated with a mixture of cellulase and xylanase enzymes. *South African Journal of Animal Science*, *51*(3). https://doi.org/10.4314/sajas.v51i3.14

77. Shang, S., Qian, L., Zhang, X., Li, K., & Chagan, I. (2013). *Themoanaerobacterium calidifontis* sp. Nov., a novel anaerobic, thermophilic, ethanol-producing bacterium from hot springs in China. *Archives of Microbiology*, *195*(6), 439–445. https://doi.org/10.1007/s00203-013-0895-5

78. Sharma, K., Antunes, I. L., Rajulapati, V., & Goyal, A. (2018a). Low-resolution SAXS and comparative modeling based structure analysis of endo-β-1,4-xylanase a family 10 glycoside hydrolase from *Pseudopedobacter saltans comb. nov. International Journal of Biological Macromolecules*, *112*, 1104–1114. https://doi.org/10.1016/j.ijbiomac.2018.02.037

79. Sharma, K., Antunes, I. L., Rajulapati, V., & Goyal, A. (2018b). Molecular characterization of a first endo-acting β-1,4-xylanase of family 10 glycoside hydrolase (*Ps*GH10A) from *Pseudopedobacter saltans comb. nov. Process Biochemistry*, *70*, 79–89. https://doi.org/10.1016/j.procbio.2018.03.025

80. Shao, W., Xue, Y., Wu, A., Kataeva, I., Pei, J., Wu, H., & Wiegel, J. (2011). Characterization of a novel β-xylosidase, XylC, from *Thermoanaerobacterium saccharolyticum* JW/SL-YS485. *Applied and Environmental Microbiology*, *77*(3), 719–726. https://doi.org/10.1128/AEM.01511-10

81. Shiratori, H., Ikeno, H., Ayame, S., Kataoka, N., Miya, A., Hosono, K., Beppu, T., & Ueda, K. (2006). Isolation and characterization of a new *Clostridium* sp. that performs effective cellulosic waste digestion in a thermophilic methanogenic bioreactor. *Applied and Environmental Microbiology*, *72*(5), 3702–3709. https://doi.org/10.1128/AEM.72.5.3702-3709.2006

82. Shiratori, H., Sasaya, K., Ohiwa, H., Ikeno, H., Ayame, S., Kataoka, N., Miya, A., Beppu, T., & Ueda, K. (2009). *Clostridium clariflavum* sp. nov. and *Clostridium caenicola* sp. nov., moderately thermophilic, cellulose-/cellobiose-digesting bacteria isolated from methanogenic sludge. *International Journal of Systematic and Evolutionary Microbiology*, *59*(7), 1764–1770. https://doi.org/10.1099/ijs.0.003483-0

83. Shu, T., Bai, Y., Wang, Y., Wang, H., Li, P., Xiang, M., Yu, T., Xu, H., & Yu, L. (2020). A high-efficiency and eco-friendly degumming process for ramie fibers. *Journal of Cleaner Production,* *276*, 124217. https://doi.org/10.1016/j.jclepro.2020.124217

84. Singh, Y. D., Mahanta, P., & Bora, U. (2017). Comprehensive characterization of lignocellulosic biomass through proximate, ultimate and compositional analysis for bioenergy production. *Renewable Energy*, *103*, 490–500. https://doi.org/10.1016/j.renene.2016.11.039

85. Slavin, J. L. (2012). Structure, nomenclature, and properties of carbohydrates. In M. Stipanuk & M. Caudill (Eds.), *Biochemical, Physiological & Molecular Aspects of Human Nutrition* (pp. 60–65). Elsevier.

86. Smith, D. C., Bhat, K. M., & Wood, T. M. (1991). Xylan-hydrolyzing enzymes from thermophilic and mesophilic fungi. *World Journal of Microbiology and Biotechnology*, *7*(4), 475–484. https://doi.org/10.1007/BF00303373

87. Subash, M. chares, & Muthiah, P. (2021). Eco-friendly degumming of natural fibers for textile applications: A comprehensive review. *Cleaner Engineering and Technology*, *5*, 100304. https://doi.org/10.1016/j.clet.2021.100304

88. Subramaniyan, S., & Prema, P. (2002). Biotechnology of microbial xylanases: Enzymology, molecular biology, and application. *Critical Reviews in Biotechnology*, *22*(1), 33–64. https://doi.org/10.1080/07388550290789450

89. Šuchová, K., Chyba, A., Hegyi, Z., Rebroš, M., & Puchart, V. (2022). Yeast GH30 xylanase from *Sugiyamaella lignohabitans* is a glucuronoxylanase with auxiliary xylobiohydrolase activity. *Molecules*, *27*(3), Article 3. https://doi.org/10.3390/molecules27030751

90. Šuchová, K., Puchart, V., Spodsberg, N., Mørkeberg Krogh, K. B. R., & Biely, P. (2020). A novel GH30 xylobiohydrolase from *Acremonium alcalophilum* releasing xylobiose from the non-reducing end. *Enzyme and Microbial Technology*, *134*, 109484. https://doi.org/10.1016/j.enzmictec.2019.109484

91. Sunna, A., & Antranikian, G. (1997). Xylanolytic enzymes from fungi and bacteria. *Critical Reviews in Biotechnology*, *17*(1), 39–67. https://doi.org/10.3109/07388559709146606

92. Topakas, E., Panagiotou, G., & Christakopoulos, P. (2013). Xylanases: characteristics, sources, production, and applications. In *Bioprocessing Technologies in Biorefinery for Sustainable Production of Fuels, Chemicals, and Polymers* (pp. 147–166). John Wiley & Sons, Ltd. https://doi.org/10.1002/9781118642047.ch9

93. Thakur, A., Sharma, K., & Goyal, A. (2019). α-L-arabinofuranosidase: A potential enzyme for the food industry. In *Green bio-processes* (pp. 229–244). Springer.

94. Thebti, W., Riahi, Y., Gharsalli, R., & Belhadj, O. (2016). Screening and characterization of thermo-active enzymes of biotechnological interest produced by thermophilic *Bacillus* isolated from hot springs in Tunisia. *Acta Biochimica Polonica*, *63*(3), 581–587. http://dx.doi.org/10.18388/abp.2016_1271

95. Valenzuela, S. V., Diaz, P., & Pastor, F. J. (2012). Modular glucuronoxylan-specific xylanase with a family CBM35 carbohydrate-binding module. *Applied and Environmental Microbiology*, *78*(11), 3923–3931. https://doi.org/10.1128/AEM.07932-11

96. Van Dyk, J. S., & Pletschke, B. I. (2012). A review of lignocellulose bioconversion using enzymatic hydrolysis and synergistic cooperation between enzymes—Factors affecting enzymes, conversion and synergy. *Biotechnology Advances*, *30*(6), 1458–1480. https://doi.org/10.1016/j.biotechadv.2012.03.002

97. Verma, A. K., & Goyal, A. (2014). In silico structural characterization and molecular docking studies of first glucuronoxylan-xylanohydrolase (Xyn30A) from family 30 glycosyl hydrolase (GH30) from *Clostridium thermocellum*. *Molecular Biology*, *48*(2), 278–286. https://doi.org/10.1134/S0026893314020022

98. Verma, A. K., & Goyal, A. (2016). A novel member of family 30 glycoside hydrolase subfamily 8 glucuronoxylan endo-β-1, 4-xylanase (*Ct*XynGH30) from *Clostridium thermocellum* orchestrates catalysis on arabinose decorated xylans. *Journal of Molecular Catalysis B: Enzymatic*, *129*, 6–14. https://doi.org/10.1016/j.molcatb.2016.04.001

99. Vocadlo, D. J., Davies, G. J., Laine, R., & Withers, S. G. (2001). Catalysis by hen egg-white lysozyme proceeds via a covalent intermediate. *Nature*, *412*(6849), 835–838. https://doi.org/10.1038/35090602

100. Voiniciuc, C. (2022). Modern mannan: A hemicellulose's journey. *New Phytologist*, *234*(4), 1175–1184. https://doi.org/10.1111/nph.18091

101. Wang, R., Liu, Z., Cheng, L., Duan, S., Feng, X., Zheng, K., Cheng, Y., & Zeng, J. (2019). A novel endo-β-1, 4-xylanase GH30 from *Dickeya dadantii* DCE-01: Clone, expression, characterization, and ramie biological degumming function. *Textile Research Journal*, *89*(4), 463–472. https://doi.org/10.1177/0040517517748511

102. Weng, V., Cardeira, M., Bento-Silva, A., Serra, A. T., Brazinha, C., & Bronze, M. R. (2023). Arabinoxylan from corn fiber obtained through alkaline extraction and membrane purification: relating bioactivities with the phenolic compounds. *Molecules*, *28*(15), Article 15. https://doi.org/10.3390/molecules28155621

103. Winger, A. M., Heazlewood, J. L., Chan, L. J. G., Petzold, C. J., Permaul, K., & Singh, S. (2014). Secretome analysis of the thermophilic xylanase hyper-producer *Thermomyces lanuginosus* SSBP cultivated on corn cobs. *Journal of Industrial Microbiology and Biotechnology*, *41*(11), 1687–1696. https://doi.org/10.1007/s10295-014-1509-1

Chapter 2

Cloning and expression of glycoside hydrolase family 30 xylobiohydrolase, *Ac*GH30A from *Acetivibrio clariflavus* ATCC 19732

2.1 Introduction

Xylan is an essential polysaccharide component of hemicellulose, primarily located in the cell walls of plants, where it contributes significantly to structural integrity and supports plant growth (Rennie & Scheller, 2014; Gigli-Bisceglia et al., 2020). Xylan is widely distributed among various plant species, forming a substantial part of the biomass in both dicots and monocots. Xylan content varies from 10% to 35% in hardwoods and from 10% to 15% in softwoods (Faik, 2010; Peña et al., 2016). Interestingly, xylan is also found in certain algae, where it can substitute for cellulose in the cell wall matrix (Hsieh & Harris, 2019). Xylan is characterised by a backbone of β-1,4-linked xylose residues and can include a variety of substituents, such as acetyl, feruloyl and glucuronic acid groups, as discussed in Chapter 1, which add to its structural complexity and functional diversity (Bajpai, 2014; Curry et al., 2023). The structural variations of xylan not only strengthen its role in plant defence against

herbivores and pathogens, but also modulate its interactions with cellulose, influencing the overall recalcitrance of plant materials to enzymatic degradation. This complexity requires a diverse set of enzymes for its degradation, especially within microbial systems. Essential enzymes involved in xylan degradation include endo-1,4-β-xylanase, which hydrolyses to give short chain xylooligosaccharides, β-xylosidase, hydrolyses these xylo-oligomers into xylose monomer and various other debranching enzymes, such as α-L-arabinofuranosidase and α-glucuronidase remove its side chains (Juturu & Wu, 2012). Another enzyme called xylobiohydrolase also acts on the xylans and substituted xylans and specifically produce xylobiose by its exolytic mode of action (Ref.). The synergistic action of all these enzymes is vital for the complete hydrolysis of xylans into fermentable sugars, which is essential for both natural ecosystems and industrial applications, including biofuel production and the paper industry (El Enshasy et al., 2016). These enzymes are produced by a diverse array of organisms, including bacteria, fungi, yeast and even some marine algae, with microbial sources being particularly significant for industrial applications due to their efficiency and adaptability (Topakas et al., n.d.). The biochemical properties of xylanases, such as molecular weight, optimal pH and temperature, widely vary and depend on the type of microorganism and its habitat (El Enshasy et al., 2016). The ability of xylanases to facilitate the breakdown of lignocellulosic biomass is crucial not only for industrial applications but also for ecological processes, as they contribute to the recycling of organic matter in natural ecosystems (Abdulhadi et al., 2023). Moreover, advancements in biotechnology, including recombinant DNA technology, are enhancing the production and efficiency of these enzymes, allowing for tailored applications that meet specific industrial needs. Understanding the properties and ecological roles of xylanases

and xylobiohydrolases is essential for harnessing their potential in various biotechnological fields.

These enzymes have been harnessed for a wide range of applications, such as enhancing the quality of bread (Guo et al., 2018), clarifying must and juices (Juturu & Wu, 2012), degumming bast fibres (Wang et al., 2019), pre-bleaching kraft pulps (Kaur et al., 2016; Kumar et al., 2016), and treating hemicellulosic waste (El Enshasy et al., 2016; Jamaldheen et al., 2019). The versatility of xylanolytic enzymes makes them valuable tools for improving processes and products in different industries. They are also extensively used for the production of ethanol, furfural and xylitol (Dodd & Cann, 2009; Garg, 2016). Proper utilisation of pentose sugars present in hemicellulose is an essential step in the cost reduction of bioethanol production processes (Garg, 2016).

In the present study, the sequence data of gene encoding a glycoside hydrolase family 30, *Ac*GH30A from *Acetivibrio clariflavus* with GenBank accession No. AEV68404.1 was retrieved from the NCBI (http://www.ncbi.nlm.nih) database. The conserved domains present in the gene were found by using the NCBI conserved domain database (CDD) (http://www.ncbi.nlm.nih.gov/cdd/). The signal peptide sequence contained by the gene was determined by the SignalP 5.0 server (https://services.healthtech.dtu.dk/services/SignalP-5.0/).

The full-length gene (GenBank accession AEV68404.1) encoding the enzyme, *Ac*GH30A is a 534 amino acid protein whose molecular framework revealed the presence of a signal peptide of 28 amino acids (1-28 aa) at the N-terminal followed by a GH30 family catalytic module of 433 amino acid residues (29-461 aa) and a dockerin type I of 68 amino acids (466-534 aa) at the C-terminus, connected by a linker sequence of 5 amino acids (432-465 aa) to a GH30 catalytic domain (Fig. 2.1). The presence of

a dockerin I indicates the potential participation of *Ac*GH30A in cellulosome assembly and protein-protein interactions.

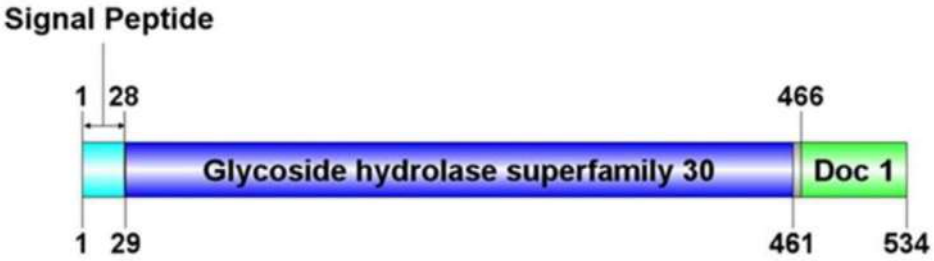

Fig. 2.1 Molecular organisation of the *Ac*GH30A. The amino acid sequence of *Ac*GH30A consists of 3 major domain sequences: (i) Signal peptide (1-28) at the N-terminal, (ii) GH30 catalytic module (29-461) and (iii) Dockerin 1 at the C-terminal (466-534).

In the present study, the gene encoding full-length *Ac*GH30A, which consists of catalytic and dockerin type I domains, was cloned and expressed in *E. coli* bacterial cells for purification and further biochemical, functional and structural characterisation.

2.2 Materials and Methods

2.2.1 Bacterial strains, vectors and chemicals

The genomic DNA of *Acetivibrio clariflavus* was procured from the collection of microorganisms and cell culture, DSMZ (Deutsche Sammlung von Mikroorganismen und Zellkulturen), Germany. *Escherichia coli* strains DH5α and BL21 (DE3) were used for cloning and recombinant enzyme expression, respectively. Reagents including dNTPs, $MgCl_2$, RNase solution (20 $mg \cdot mL^{-1}$), glacial acetic acid (99.9% purity), Trizma base, ethidium bromide, nuclease-free water (pH 8.0), and polyacrylamide gel electrophoresis components, along with the GenElute Miniprep Plasmid Isolation Kit and Gel-Extraction Kit, were sourced from Sigma-Aldrich, India. DNA was electrophoresed on agarose gels prepared using Agarose, with low EEO purchased from Sigma-Aldrich, India. The DNA ladder was purchased from New England Biolabs (NEB), USA. The PCR-amplified products were cloned and expressed using the pET28a(+) expression vector. pET28a(+) plasmid, *E. coli*. DH5α and BL21 (DE3) cells were acquired from Novagen (Madison, WI). SDS-PAGE was performed using a Mini-PROTEAN Tetra Cell system from Bio-Rad Laboratories, USA. The protein marker was procured from HiMedia Laboratories Private Limited, India.

2.2.2 Microorganisms

The *E. coli* DH5α and *E. coli* BL-21 (DE3) cells utilised in this study were procured from Novagen, Germany.

2.2.3 PCR amplification of genes encoding *Ac*GH30A

The amplification of gene (GenBank accession AEV68404.1) encoding *Ac*GH30A, spanning a length of 1518 base pairs, was performed via polymerase chain reaction (PCR) using Taq DNA polymerase and specific oligonucleotide primers. The

genomic DNA of *Acetivibrio clariflavus* was used as the template for the amplification. For directional cloning, *Nhe*I/*Xho*I restriction sites were utilised to incorporate the PCR product into the expression vector pET28a(+). The oligonucleotide primers utilised in this process were:

Forward primer 5′-GGTGGTGCTAGCGCATCAACTGTTACCGTTGATTGGGAC-3′

Reverse primer 5′-ACCACCCTCGAGTTATTGTTCTACCGGGAATTTTTGAATC-3′

The total volume of the PCR mix containing the template, polymerase enzyme, primers, dNTPs and buffer was 60 µL (Table 2.2.1). After the initial denaturation of the template DNA at 95°C for 5 min, the PCR was conducted for 30 cycles under the parameters mentioned in Table 2.2.2, using the PCR system, Bio-Rad T100, USA. The PCR products were analysed by 0.8% (w/v) agarose gel electrophoresis to check their size and purity.

Table 2.2.1 PCR mixture for amplification of *Ac*GH30A from *Acetivibro clariflavus.*

PCR components	Volume (µl)	Final concentration
10x reaction buffer	6.0	1x
100 mM dNTP mix	0.2	0.33 mM
Forward primer (15 µM)	1.5	0.37 µM
Reverse primer (15 µM)	1.5	0.37 µM
Sigma water, pH 8.0	49.8	--
Genomic DNA (20.0 $\mu g.mL^{-1}$)	0.5	10.0 ng
Taq DNA polymerase (1 $U.\mu l^{-1}$)	0.5	0.008 U
Total	60.0	--

Table 2.2.2 PCR conditions for *Ac*GH30A

Cycle step	Temperature	Time	Cycle
Initial denaturation	95°C	5 min	1
Denaturation	95°C	30 sec	
Annealing	50-70°C	45 sec	30
Extension	72°C	90 Sec	
Final Extension	72°C	10 min	1

2.2.4 Agarose gel electrophoresis of PCR amplified products

The PCR-amplified products were electrophoresed on a 0.8% (w/v) agarose gel prepared with 1x TAE buffer. In accordance with Sambrook and Russell (2001), a TAE buffer stock solution was formulated with component concentrations at 10x (400 mM Tris-acetate, 10 mM EDTA, pH 8.0). The agarose gel was prepared for 0.8% (w/v) and 1% (w/v) concentration by mixing 400 mg and 500 mg agarose powder in 50 mL of 1x TAE buffer, respectively. The mixtures were heated in a microwave to obtain a transparent solution. The agarose solution was cooled to 50°C, then mixed with 5.0 µL of ethidium bromide (5.0 mg·mL^{-1}). The solution was poured into the casting apparatus, and combs were inserted to form wells. After allowing the gel to solidify for 30 min, 1x TAE (Tris-acetate-EDTA) buffer was used as the electrophoresis buffer (Sambrook & Russell, 2001). The DNA sample was combined with DNA loading dye in a 4:1 ratio, and electrophoresis was carried out at 60 V until the dye had migrated over 70% of the gel length. DNA bands were visualized under UV light using a gel documentation system (BioRad XR).

2.2.4.1 *DNA loading buffer*

The DNA or sample loading buffer was prepared by mixing the components mentioned below in Table 2.2.3. A stock solution (5x) of DNA loading buffer was formulated. Prior to loading, 4 volumes of DNA were mixed with 1 volume of the stock solution to obtain 1x. The pH of the DNA loading dye was adjusted to 8.0.

Table 2.2.3 Composition of 5x DNA loading buffer.

Components	Final concentration (5x)
Tris-HCl (pH 8.0)	50 mM
Glycerol	25% (w/v)
EDTA	5.0 mM
Bromophenol blue	0.2% (w/v)
Xylene cyanol	0.2% (w/v)

2.2.5 Extraction of DNA from agarose gel

The DNA or other plasmids, amplified through PCR, were extracted and purified from agarose gel utilising a kit (Sigma GenElute), following the manufacturer's protocol outlined in Section 2.2.5.1. The resultant DNA was eluted using 30 µL of elution buffer provided with the kit (Sigma-Aldrich, USA).

2.2.5.1 *Protocol for extraction of DNA from agarose gel*

1. A sterile 1.5 mL microcentrifuge tube was weighed and the result was recorded.
2. The PCR-amplified DNA or plasmid was carefully excised from the agarose gel using a sterile scalpel and transferred into a pre-weighed microcentrifuge tube. After re-recording the weight of the tube, the weight of the excised gel was determined by subtracting the initial weight of the tube.
3. Subsequently, 3 volumes of Gel Solubilisation Solution were added for every 1 volume of gel (approximately 100 mg ~ 100 µL).
4. The microcentrifuge tube containing the excised gel was incubated at 50°C for 10 min or until complete dissolution of the gel slice occurred.
5. To this solution, an equivalent, 1 volume of isopropanol was introduced.
6. The GenElute binding column G was inserted within a 2 mL collection tube supplied with the kit. 500 µL of column preparation solution was dispensed over the column membrane and centrifuged at 16,000*g* for 1 min. The flow-through was discarded.
7. The PCR-amplified DNA or plasmid solution (~700 µL) was introduced to DNA binding columns, followed by centrifugation at 16,000*g* for 1 minute at room temperature, with the subsequent removal of the flow-through. In instances where the volume exceeded 700 µL, the remaining solution was centrifuged and the flow-through was discarded as before.
8. Each DNA-bound spin column was added with 700 µL of Wash Solution, followed by centrifugation at 16,000*g* for 1 minute at room temperature, with subsequent removal of the flow-through. An additional spin of 1 minute at 16,000*g* was performed to ensure complete elimination of residual ethanol.
9. The column containing the bound DNA was transferred to a fresh, sterile 1.5 mL microcentrifuge tube. To the centre of the column, 30 µL of DNase-free water (Sigma-Aldrich, USA) or elution buffer (10 mM Tris-Cl, pH 8.5) was added. The column was incubated at room temperature for 2 min, followed by centrifugation at 16,000***g*** for 1 min. For optimal DNA recovery, the elution solution was preheated to 65°C before introducing to the membrane, improving DNA recovery by 2 to 3-fold.

10. The DNA or plasmid amplified through PCR was eluted from the GenElute spin columns and collected in a sterile 1.5 mL microcentrifuge tube, and stored at -20°C for future use.

2.2.6 Preparation of Luria-Bertani medium

The Luria-Bertani (LB) medium for cultivating *E. coli* cells containing recombinant plasmids was prepared by dissolving the specified ingredients (Table 2.2.4) in 800 mL of deionised water. The pH of the medium was adjusted to 7.2, and the final volume was made up to 1 litre. An aliquot of 100 mL of this LB medium was dispensed into a 250 mL conical flask and sterilized by autoclaving at 121°C and 15 psi for 20 min. The filter-sterilised antibiotic (Kanamycin; 50 $\mu g.mL^{-1}$) was mixed with the autoclaved and cooled LB medium before inoculation.

Table 2.2.4 Composition of Luria-Bertani medium (Sambrook *et al*., 1989)

Component	Final concentration (%, w/v)
Tryptone	1.0
Yeast extract powder	0.5
Sodium chloride	1.0

2.2.7 Preparation of SOC medium

The SOC (super optimal medium with catabolic repression) was prepared by using the ingredients mentioned in Table 2.2.5 (Sambrook *et al*., 1989). It is a modified SOB (super optimal broth) with the addition of glucose (Hanahan, 1983). Bactotryptone, yeast extract powder and NaCl were autoclaved. The stock solutions 1M each of KCl, $MgCl_2$, $MgSO_4$ and glucose were filter-sterilised, and the required quantities were added to the above solution in the laminar hood to make the SOC medium.

Table 2.2.5 Composition of SOC medium.

Component	Final concentration
Bactotryptone	2.0 (%, w/v)
Yeast extract powder	0.5 (%, w/v)
NaCl	10 mM
KCl	2.5 mM
$MgCl_2$	10 mM
$MgSO_4$	10 mM
Glucose	20 mM

2.2.8 Preparation of Luria-Bertani (LB)-Agar medium

The LB-Agar medium was prepared by dissolving 2% (w/v) Agar Agar type 1 in the LB-broth medium, as described in Section 2.2.6. The solution was autoclaved at 121°C at 15 psi for 20 min for sterilisation. The medium was cooled to approximately 50 °C, and filter-sterilised kanamycin (50 µg.mL^{-1}) was aseptically added under a laminar airflow hood. The LB-Agar medium was poured over the sterile petri plates and left to solidify for 15-20 min. The petri plates were stored in an inverted position at 4°C to prevent contamination.

2.2.9 Preparation of *E. coli* DH5α competent cells calcium chloride method

Day 1

1. 50 µL glycerol stock of *E. coli* DH5α cells was inoculated into 5.0 mL LB medium (Sambrook et al., 1989) in a test tube and grown overnight at 37ºC and 180 rpm.
2. A solution of 0.1 M $CaCl_2$ was filter-sterilised by passing it through a 0.22 µm filter in a laminar airflow environment and afterwards stored in the refrigerator.

Day 2

3. 1.0 mL from the day 1 culture was introduced into a 100 mL LB medium placed in a 250 mL conical flask. The mixture was then incubated at 37ºC with 180 rpm until the optical density of the cells reached a range of 0.4-0.6 at 550 nm.
4. Microcentrifuge tubes, 50 mL centrifuge tubes with round bottoms and micro tips, were autoclaved, cooled on ice and kept inside a laminar airflow hood.
5. 40 mL culture was transferred to round bottom centrifuge tubes in a sterile environment.
6. The tubes were centrifuged at 4ºC with at 4000x***g*** for 10 min. This step was repeated until the entire 100 mL culture volume had been processed.

7. The cell pellet was re-suspended in 3-4 mL sterile, ice-chilled 0.1 M $CaCl_2$ solution, and the final volume was adjusted to 20 mL. The cell suspension was incubated on ice for 10 min, followed by centrifugation at 4000***g*** and 4°C for 10 min.
8. The supernatant was carefully decanted, and the pellet was re-suspended in 3.0 mL of sterile, ice-cold 0.1 M $CaCl_2$ solution.
9. An aliquot of 200 µL of competent cells was transferred into sterile 1.5 mL microcentrifuge tubes containing 10% (v/v) glycerol to achieve the final concentration, and the tubes were stored at −80°C for subsequent use.

2.2.10 Cloning of gene encoding *Ac*GH30A into pET28a(+) vector

2.2.10.1 *The restriction map of the pET-28a(+) expression vector*

The expression vector, pET-28a(+) is designed for the expression of recombinant proteins in *Escherichia coli*. It features a robust T7 promoter system that allows for high levels of protein expression driven by the T7 RNA polymerase. The T7 promoter system was initially developed by Studier and colleagues (Studier and Moffatt, 1986; Studier et al., 1990). The expression of genes introduced into pET plasmids is governed by the T7 bacteriophage promoter, transcribed by the host cell's T7 RNA polymerase. In the uninduced state, the cloned genes within pET vectors remain transcriptionally inactive. The proteins encoded by these cloned genes possess a His6-Tag, facilitating single-step purification through affinity chromatography. The pET-28a(+) vector enables the integration of an expressed protein with an N-terminal His6-Tag/thrombin/T7-Tag, along with the option of including a C-terminal His6-Tag sequence (refer to Fig. 2.2). The figure displays the locations of the sequence encoding the His-Tag, T7 promoter, T7 terminator, kanamycin resistance and f1 origin.

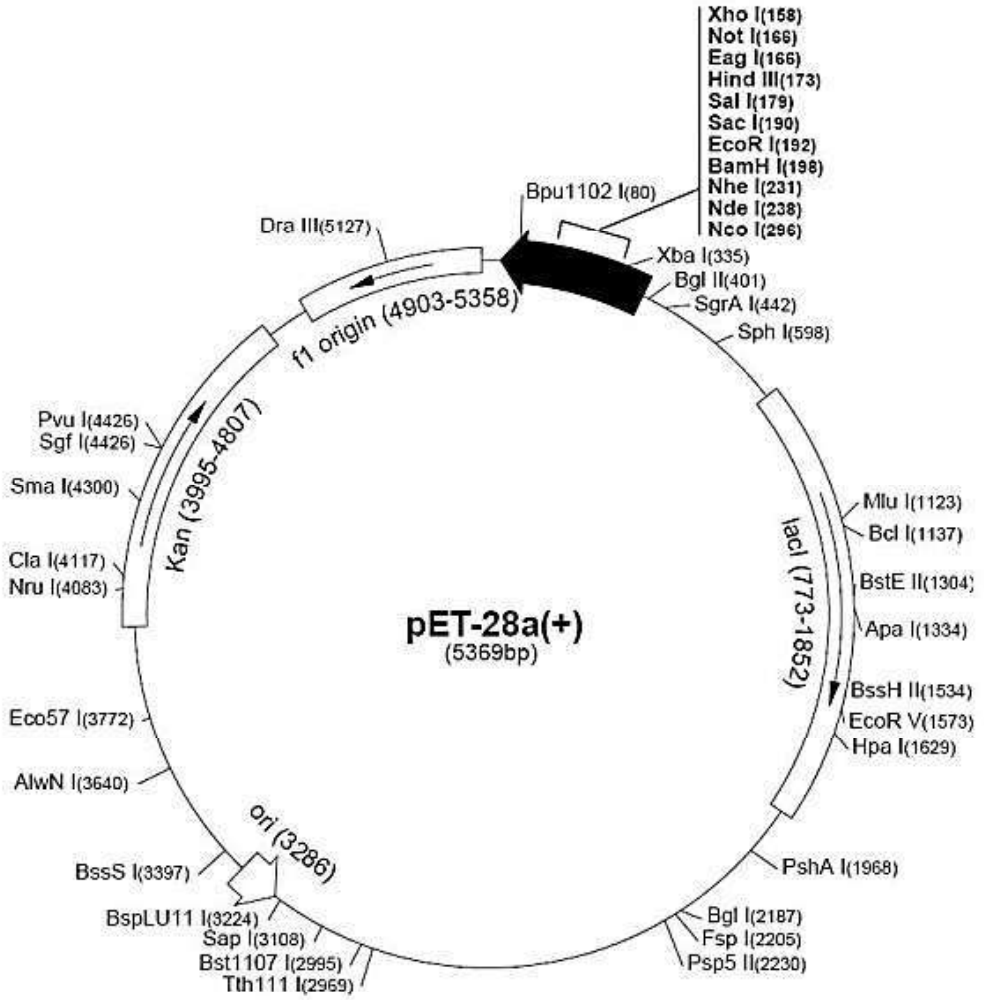

Fig. 2.2 Restriction map of the pET-28a(+) expression vector showing multiple cloning sites and restriction enzyme sites.

2.2.10.2 *Restriction digestion of PCR amplified gene encoding AcGH30A and pET-28a(+) plasmid DNA*

The pET-28a(+) vector was digested using *NheI-XhoI* restriction enzymes (refer to Table 2.2.6). PCR-amplified genes encoding *Ac*GH30A were also subjected to *NheI-XhoI* digestion, preparing them for subsequent ligation with the restriction-digested pET-28a(+) vector (see Table 2.2.7). These digestion reactions were incubated in a water bath at 37°C for 90 min. Following digestion, the *NheI-XhoI*-

digested pET vector and PCR-amplified gene were purified from the agarose gel using the method outlined in Section 2.2.5.1.

Table 2.2.6 Restriction enzyme digestion of pET-28a (+) plasmid DNA.

Reaction components	**Volume (µL)**
10x buffer	3.0
Nuclease free water	4.5
Bovine serum albumin (10 $mg.mL^{-1}$)	0.5
Plasmid DNA (approx. 13 $ng.\mu l^{-1}$)	20.0
*Nhe*I (10 $U.\mu l^{-1}$)	1.0
*Xho*I (10 $U.\mu l^{-1}$)	1.0
Total	30.0

Table 2.2.7 Restriction enzyme digestion of PCR amplified gene encoding *Ac*GH30A.

Reaction component	**Gene encoding *Ac*GH30A (µL)**
10x buffer	3.0
Nuclease-free water	4.5
Bovine serum albumin (10 $mg.mL^{-1}$)	0.5
PCR amplified product	20 (~125 ng)
*Nhe*I (10 $U.\mu l^{-1}$)	1
*Xho*I (10 $U.\mu l^{-1}$)	1
Total	30

2.2.10.3 *Ligation of gene encoding AcGH30A into pET-28a(+) vector*

The gene encoding *Ac*GH30A, which has been digested with *Nhe*I-*Xho*I, was ligated into the pET-28a(+) vector. The vector itself was also subjected to digestion using the same *Nhe*I-*Xho*I restriction enzymes, as detailed in Section 2.2.10.2. Ligation reaction was established utilising the components specified in Table 2.2.8. This reaction was then incubated at 16°C overnight to maximise the number of transformants. The insert:vector molar ratio for the setup was 3:1, with the amount of the insert calculated according to the method outlined below:

$$\frac{\text{amount of vector (ng)} \times \text{size of insert (kb)}}{\text{Size of vector (kb)}} \times \text{insert vector molar ratio} = \text{amount of insert (ng)}$$

$$\frac{72\ (\text{ng}) \times 1.5\ (\text{kb})}{5.369\ (\text{kb})} \times \frac{3}{1} = 60\ \text{ng}\ (\textit{Ac}\text{GH30A})$$

Table 2.2.8 Components of reaction for ligating gene encoding *Ac*GH30A into pET-28a (+) expression vector

Reaction component	Gene encoding *Ac*GH30A (µL)
10x Rapid Ligation Buffer	1.5
pET-28a(+) Vector	4 (100 ng)
Restriction digested product	6 (60 ng)
T4 DNA Ligase (3 Units/µl)	1
Nuclease-free water	2.5
Total	15

2.2.11 Screening of recombinant plasmid DNA for positive clones

2.2.11.1 *Transformation of ligated recombinant DNA into E. coli DH5a cells*

The competent cells, *E. coli* DH5α were transformed with ligation reactions following the overnight ligation. The method of preparation of *E. coli* competent cells has been described in Section 2.2.9.

The step-wise transformation protocol is described below:

1. The micro-centrifuge tube containing competent cells (200 µL) was taken out from -80°C and kept on ice for 5 min.
2. 10 µL of ligation mixture was added to cells, and the tube was gently tapped 4-5 times and kept on ice for 30 min. The cells were occasionally tapped gently during 30 min incubation.
3. The cells were given a heat shock at 42°C for 40s.
4. The cells were immediately transferred back to the ice and kept for 5 min.
5. 800 µL of super optimal medium with catabolite repression (SOC) (Hanahan, 1983; Sambrook *et al*., 1989; given in Section 2.2.7) (previously incubated at 37°C) was added to the transformed cells.
6. The transformed cells were incubated at 37°C in a shaking incubator at 220 rpm for 1h.
7. The cells were centrifuged at 2000*g*, 25°C for 5 min.
8. 800 µL supernatant was discarded, and the cell pellet was re-suspended in the remaining 200 µL supernatant.

9. The 200 µL cells were spread-plated on LB agar plates as described in Section 2.2.8, supplemented with antibiotics. The LB agar plates were incubated overnight at 37°C.
10. The transformation efficiency was calculated using the following formula,

$$\text{Transformation efficiency} = \frac{\text{No. of colonies on LB plate}}{\text{Amount of insert (µg)}} = \text{cfu/µg}$$

The 15-20 µL of ligation mixture was added to 200 µL *E. coli* DH5α competent cells, following the above transformation protocol. The transformed DH5α cells were plated on LB plates supplemented with kanamycin (50 µg.mL^{-1}) and grown overnight at 37°C, 180 rpm.

2.2.11.2 *Isolation of plasmid DNA from transformed colonies by miniprep kit*

Plates incubated overnight were examined for the presence of colonies. Colonies, preferably selected from the central region of the plate, were randomly chosen in a laminar airflow hood and cultured overnight in 10 mL LB medium supplemented with kanamycin (50 µg.mL^{-1}). The plasmid DNA from this 5 mL culture was isolated using a miniprep kit from Sigma-Aldrich (USA), following the protocol mentioned below in Section 2.2.11.2.1

2.2.11.2.1 Plasmid isolation protocol by miniprep kit

1. 9 mL from each of the grown cultures containing recombinant plasmid were pelleted in a 1.5 mL microcentrifuge tube aseptically.
2. The cells were then centrifuged at 14000*g* for 1 min and the process was repeated six times with 1.5 mL culture (Total 9 mL culture).
3. The resulting cell pellet of each recombinant derivative was re-suspended in 200 µL resuspension solution and vortexed. RNAse at a final concentration of 0.3 mg.mL^{-1} was added to the resuspension solution prior to use.
4. 200 µL of lysis solution was added to each tube, and the tubes were inverted gently 5-6 times to ensure mixing and allowed to stand for 2-5 min.
5. 350 µL of neutralisation solution was added to the mixture, and the tubes were inverted again for 4–6 times to mix properly.

6. The mixture was centrifuged at 16,000*g* for 10 min.
7. The DNA binding columns were equilibrated by applying 500 µL of column preparation solution, followed by centrifugation at 14,000***g*** for 1 min. The resulting flow-through in the collection tube was discarded.
8. The clear lysate was then transferred to the activated DNA binding column, centrifuged at 14,000*g* for 1 min and the flow through in the collection tube was discarded again.
9. The plasmid DNA bound to the column was washed with wash solution and spun at 14,000*g* for 1 min. The flow-through was discarded and the column was given another 1 min spin at 14,000***g*** for removing the wash solution completely.
10. The DNA binding column was transferred to a fresh sterile microcentrifuge tube and 30 µL of TE buffer solution or DNAse free water was added at the centre of the binding column. The microcentrifuge tube was allowed to stand for 10 min at room temperature and then plasmid DNA was eluted by centrifugation at 14,000*g* for 1 min.
11. The eluted plasmid DNA in a sterile microcentrifuge tube was stored at -20°C.

2.2.11.3 *Confirmation of positive clones by restriction digestion of plasmid DNA*

15 µL of recombinant plasmids from pET-28a(+) clones of *Ac*GH30A that were isolated in the last step were taken in separate fresh sterile micro-centrifuge tubes for restriction enzyme digestion analysis. The recombinant plasmid DNA of each of the above-mentioned derivatives was digested with restriction enzymes, *Nhe*I and *Xho*I, to verify the presence of positive clones, using a 30 µL reaction mixture as outlined in Table 2.2.6.

2.2.12 Hyper-expression of recombinant plasmid with gene encoding *Ac*GH30A

2.2.12.1 *Preparation of competent E. coli BL-21 cells*

The competent *E. coli* BL-21 (DE3) cells were prepared using the calcium chloride method following the protocol discussed in Section 2.2.9. Finally, 10% (v/v) glycerol (final concentration) was added to competent cells and 200 µL aliquots were made in sterile microcentrifuge tubes and stored at -80°C for further use.

2.2.12.2 *Transformation of recombinant plasmid containing genes encoding AcGH30A into E. coli BL-21 cells*

Two microliters of the recombinant plasmid of positive pET-28a(+) clone isolated in Section 2.2.11.2, were used to transform 200 µL of *E. coli* BL21(DE3) cells for protein expression, following the transformation protocol described in Section 2.2.11.1. The recombinant plasmid, encoding the *Ac*GH30A gene, was introduced into *E. coli* BL21(DE3) cells, which were then plated on LB agar containing kanamycin (50 µg·mL^{-1}) and incubated overnight at 37°C.

2.2.12.3 *Expression of recombinant AcGH30A*

E. coli BL21(DE3) cells used as a host for expression of *Ac*GH30A were cultured in 100 mL of LB medium supplemented with kanamycin (50 µg.mL^{-1}) at 37°C, 180 rpm. After the cell growth reached mid-exponential phase (A_{600} = 0.6), the cells expressing *Ac*GH30A were cooled and Isopropyl-β-D-thiogalactopyranoside (IPTG) induction was carried out at 24°C. IPTG was added at a final concentration of 1 mM and the culture was further incubated at 180 rpm for 20 h.

2.2.12.3.1 *Determination of the optimum IPTG concentration required for hyper-expression of AcGH30A*

E. coli BL21(DE3) cells containing the recombinant plasmid with the *Ac*GH30A gene were cultured in 5 mL of LB medium supplemented with kanamycin (50 µg·mL^{-1}) at 37°C and 180 rpm. Once the culture reached mid-exponential phase (A_{600} = 0.6), the temperature was lowered to 24°C, and protein expression was induced by adding IPTG to a final concentration between 0.25 and 1.0 mM. Following IPTG induction, cells were incubated at 24°C for 20 h at 180 rpm. From each culture, 200 µL broth was collected, centrifuged at 13,000x***g*** for 5 min and the supernatant was removed. The cell pellet was resuspended in 200 µL of distilled water, centrifuged

again at 13,000x***g*** for 5 min and then resuspended in 40 µL of distilled water and to this 10 µL of 5X SDS-PAGE sample loading buffer was added. Recombinant *Ac*GH30A expression was confirmed by loading equal volumes (10 µL) of uninduced and all IPTG induced cell samples onto an SDS-PAGE gel and analyzing by comparison.

2.2.13 Analysis of recombinant *Ac*GH30A expression by SDS-PAGE

The recombinant protein, *Ac*GH30A expression was analysed by Sodium dodecyl sulphate-Polyacrylamide gel electrophoresis (SDS-PAGE) using a 12% (w/v) gel.

2.2.13.1 *Preparation of SDS-PAGE gel*

The constituents of SDS-PAGE gel include 30% (w/v) acrylamide, a resolving gel (Tris-HCl, pH 8.8), a stacking gel (Tris-HCl, pH 6.8), 10% (w/v) Sodium Dodecyl Sulfate (SDS), 10% (w/v) Ammonium persulfate (APS), N,N,N′,N′ - Tetramethylethylenediamine (TEMED), a sample loading buffer (pH 6.8), and an electrophoretic running or tank buffer (pH 8.3-8.5). The detailed description of SDS-PAGE gel and buffer components are given in the Sections 2.2.13.2 to 2.2.13.5.

2.2.13.2 *Preparation of acrylamide solution*

The acrylamide solution (30% w/v) was prepared by first dissolving 0.8 g of bis-acrylamide in 50 mL of ultra-pure deionised water (MilliQ) in an amber-color bottle on a magnetic stirrer (IKA, C-MAG HS7, Germany). After its dissolution, 29.2 g of acrylamide was added and the solution was stirred with a magnetic stirrer until it became a clear solution. The volume was adjusted to 100 mL with deionized water. The acrylamide solution was subsequently filtered through Whatman No. 1 filter paper and stored in an amber-colored bottle at 4°C.

2.2.13.3 *Polymerisation of SDS-PAGE gel*

The resolving gel and stacking gels were prepared according to the protocols outlined by Sambrook et al. (1989), using the composition of reagents specified in Tables 2.2.9 and 2.2.9. The resolving gel was prepared by sequentially adding all components, as listed in Table 2.2.9, into a 50 mL conical flask, maintaining the final acrylamide concentration at 12.0% (w/v). The stacking gel (4%, w/v) was prepared by dissolving the specified components, as outlined in Table 2.2.10.

Table 2.2.9 Composition of SDS-PAGE components for preparation of resolving gel.

Component	**Gel (12%, w/v) Volume (mL)**
Acrylamide solution (30%,w/v)	4.0
Deionised water	0.7
SDS (10%,w/v)	1.0
Glycerol (50%,v/v)	1.0
1.5 M Tris-HCl (pH 8.8)	3.3
TEMED	0.01
APS (10%,w/v)	0.1
Total	10 mL

Table 2.2.10 Composition of SDS-PAGE components for preparation of stacking gel.

Components	**Gel (4%, w/v) volume (mL)**
Acrylamide solution (30%, w/v)	0.7
Deionised water	2.8
SDS (10%, w/v)	0.5
0.5 M Tris-HCl (pH 6.8)	1.0
TEMED	0.005
APS (10%, w/v)	0.05
Total	5.055

2.2.13.4 *Preparation of SDS-PAGE running buffer*

SDS-PAGE was performed using 1× Tris-Glycine running buffer (pH 8.3) at a constant current of 2 mA per lane. The running buffer, 1x Tris-Glycine was prepared from the 5x stock solution, as described in Table 2.2.11. One litre of 5× Tris-Glycine buffer was prepared by dissolving 15.14 g of Tris-HCl and 94 g of glycine in 800 mL

of deionized water in a 1 L beaker. Then, 50 mL of 10% (w/v) SDS was added, and the pH was adjusted to 8.3. The final volume was adjusted to 1 L. The buffer was then filtered through Whatman No. 1 filter paper and stored at 4°C.

Table 2.2.11 Composition of 5x Tris-Glycine, running buffer.

Components	Final concentration (5x buffer)	Final concentration (1x buffer)
Tris-HCl	0.125 M	0.025 M
Glycine	1.25 M	0.25 M
SDS	0.5 % (w/v)	0.125% (w/v)

2.2.13.5 ***Preparation of sample loading buffer***

The sample loading buffer (5x) was prepared by dissolving the components in sequence at the concentrations specified in Table 2.2.12 and the pH of the buffer was adjusted to 6.8. The final concentration of the sample buffer when loading onto an SDS-PAGE gel was always maintained at 1x.

Table 2.2.12 Composition of 5x sample loading buffer (Laemmli, 1970).

Components	Final concentration (5x buffer)
Tris-HCl (pH 6.8)	62.5 mM
Glycerol	20.0 (%, v/v)
SDS	2.0 (%, w/v)
Bromophenol Blue	0.025 (%, w/v)
β-Mercaptoethanol	5.0 (%, w/v)

2.2.13.6 ***Preparation of staining and destaining solutions***

The staining solution (100 mL) for SDS-PAGE gel was prepared by dissolving 250 mg (0.25% w/v) of Coomassie Brilliant Blue (CBB R-250) dye in 50 mL of deionised water. The solution was mixed overnight in an amber-color bottle using a magnetic stirrer. Then, 40 mL of methanol and 10 mL of glacial acetic acid were added, resulting in a final ratio of 5:4:1 (deionised water:methanol:acetic acid). The solution was stirred overnight, filtered, and stored at 4°C. The destaining solution (100 mL) was prepared by mixing deionised water, methanol, and glacial acetic acid in the 5:4:1 ratio.

The gels were destained by immersing them in the destaining solution with gentle shaking, and the solution was replaced every 30 min until the protein bands became visible.

2.3 Results and Discussion

2.3.1 PCR amplification of genes encoding *Ac*GH30A

The gene encoding *Ac*GH30A was amplified from genomic DNA of *Acetivibrio clariflavus* ATCC 19732 using the conditions outlined in Section 2.2.3 and detected on 0.8% (w/v) agarose gel and are displayed in Fig. 2.3 below. The PCR products were purified from gel using gel extraction kit described in Section 2.2.5 and stored at -20°C.

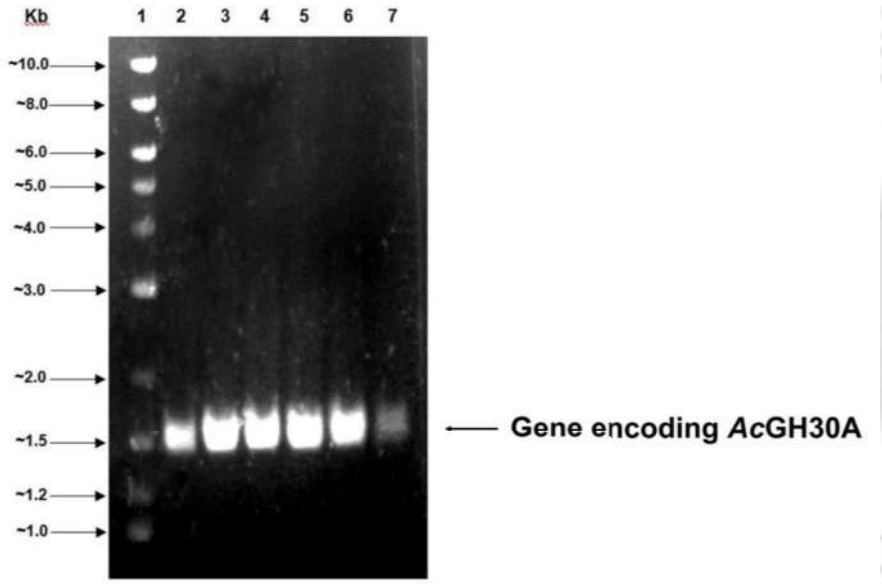

Fig. 2.3 Agarose gel (0.8%, w/v) analysis of amplified *Ac*GH30A. Lane 1- DNA Ladder (NEB, USA), Lane 2- 50 °C, Lane 3- 54°C, Lane 4- 58°C, Lane 5- 62°C, Lane 6- 66°C, Lane 7- 70°C.

2.3.2 Digestion of PCR insert DNA and vector DNA by restriction enzymes

The PCR insert DNA and vector DNA were enzymatically digested following the procedure outlined in Section 2.2.10.2. The double-digested insert DNA and vector DNA were analysed on a 0.8% (w/v) agarose gel, followed by purification using the gel extraction kit, as described in Section 2.2.5.1. Agarose gels illustrating the digested

pET-28a(+) vector (~5.3 kb) and the gene encoding *Ac*GH30A (~1.5 kb) are presented in Fig. 2.4.

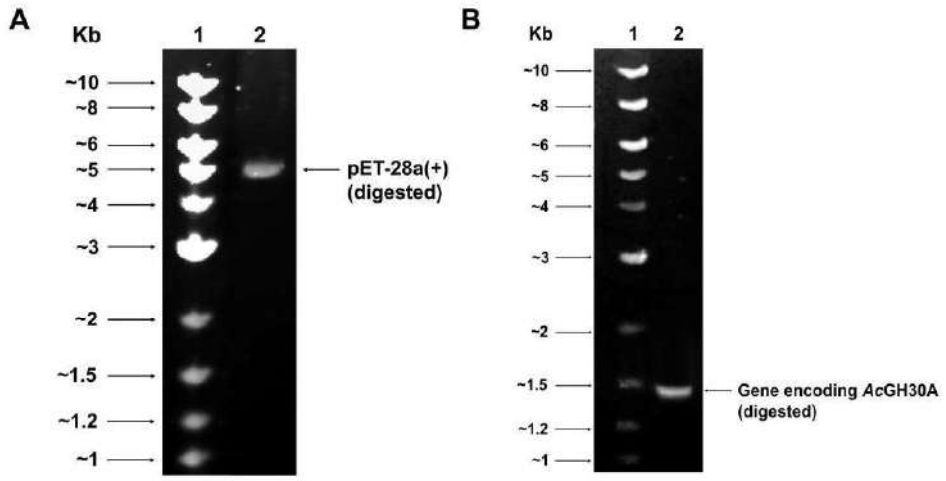

Fig. 2.4 Agarose gels (0.8%, w/v) showing (A) Lane 1- DNA ladder (1 kb DNA ladder, NEB, USA) and Lane 2- pET-28a(+) vector digestion by *Nhe*I and *Xho*I enzymes (B) Lane 1- DNA Ladder (1 kb DNA ladder, NEB, USA) and Lane 2- PCR-DNA insert digested by *Nhe*I and *Xho*I enzymes.

2.3.3 Cloning of genes encoding *Ac*GH30A into pET-28a (+) vector

The restriction enzyme-digested gene encoding *Ac*GH30A was ligated with the linearized fragments of the pET-28a(+) vector, following the protocol outlined in Section 2.2.10.3. The ligation product was then transformed into *E. coli* DH5α competent cells, which were grown overnight on LB agar plates at 37°C under stationary conditions. The transformation efficiency of *E. coli* DH5α competent cells was 1.5 x10^6.

2.3.3.1 *Isolation of recombinant plasmid DNA*

Plasmid DNA from the colonies resulting from cloning into pET-28a(+) was isolated using a plasmid miniprep kit, following the protocol outlined in Section 2.2.11.2. The isolated plasmids were visualised after electrophoresis on 0.8% (w/v)

agarose gel. Positive clones were confirmed by restriction digestion of the isolated plasmid DNA.

2.3.3.2 *Restriction digestion of isolated plasmid DNA for confirmation of positive clones*

The isolated plasmid was digested with *Nhe*I and *Xho*I restriction enzymes to confirm the positive clones. The plasmid after restriction digestion was electrophoresed on 0.8% (w/v) agarose gels alongside the undigested recombinant plasmid (Fig. 2.5). *Nhe*I and *Xho*I digested fragments of gene encoding *Ac*GH30A (Fig. 2.5; Lane 2), were visualised on agarose gels around ~1.5 kb. After restriction digestion, the linearised pET-28a(+) vector was observed at around ~5.3 kb.

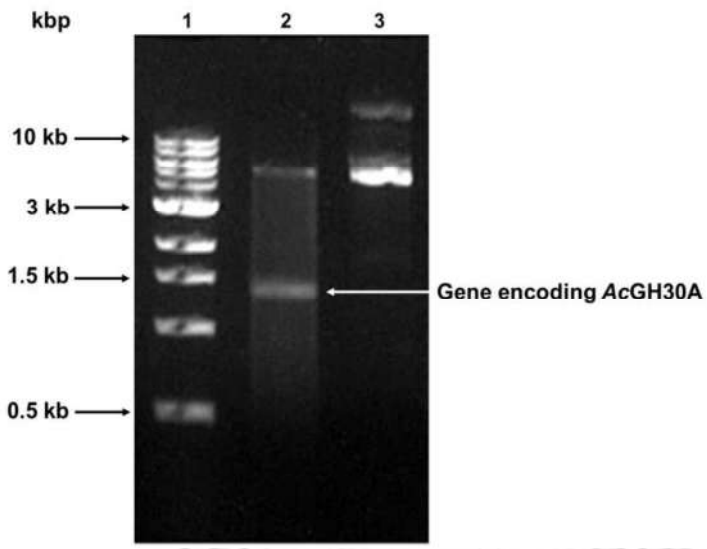

Fig. 2.5 Agarose gel (0.8%, w/v) showing, Lanes 1: DNA Ladder, 2: *Nhe*I-*Xho*I digested recombinant plasmid containing gene encoding *Ac*GH30A and 3: Undigested plasmid.

2.3.4 Expression of recombinant protein, AcGH30A

The cloned and expressed *Ac*GH30A protein comprised 514 amino acids, including an N-terminal His_6-tag preceded by 2 amino acids derived from the vector sequence. The GH30 catalytic module spans residues 9 to 441, while the C-terminal Dockerin 1 domain extends from residues 446 to 504 (Fig. 2.6). The 1518 bp DNA sequence corresponds to 506 amino acids of the native *Ac*GH30A, excluding the 8 additional N-terminal residues introduced from the expression vector.

Fig. 2.6 Molecular architecture of cloned *Ac*GH30A showing amino acid sequence of catalytic module (purple), flanked by vector sequence (cyan) at the N-terminal and Dockerin 1 (green) at C-terminal.

2.3.4.1 *Protein expression analysis*

The protein *Ac*GH30A by the transformed *E. coli* BL-21 (DE3) cells was expressed after induction with 1 mM IPTG at the mid-exponential stage, as described in Section 2.2.12.3. The protein *Ac*GH30A expression was analysed by SDS-PAGE using a 12% (w/v) gel with uninduced and induced cells loaded into adjacent wells, as illustrated in Fig. 2.7. Overexpression of the *Ac*GH30A gene yielded a protein with a molecular mass of approximately, 58 kDa.

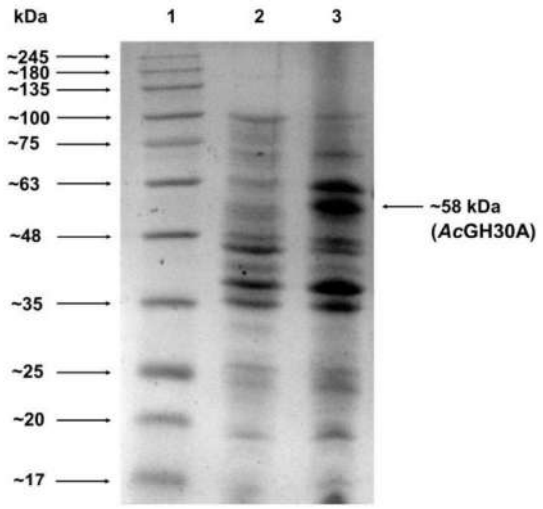

Fig. 2.7 SDS-PAGE (12%, w/v gel) showing expression of *Ac*GH30A. Lanes 1: Protein molecular-mass marker, 2: Un-induced *E. coli* BL-21 DE3 cells pellet, 3: Induced *E. coli* BL-21 DE3 cell pellet.

The minimum concentration of IPTG required for adequate expression of the recombinant enzyme, *Ac*GH30A was determined by inducing the *E. coli* BL-21 (DE3) cells with different concentrations from 0.25 to 1.0 mM IPTG. The optimum concentration of IPTG for *Ac*GH30A protein expression was 1.0 mM (Fig. 2.8).

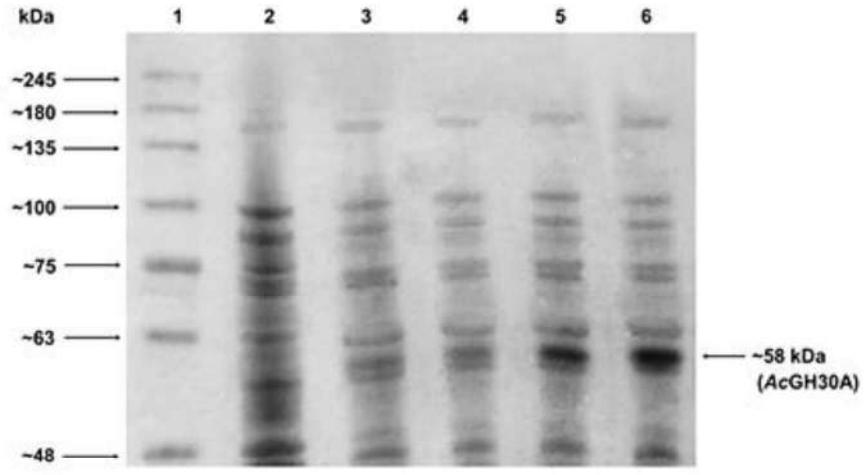

Fig. 2.8 SDS-PAGE (12%, w/v gel) analysis showing hyper-expression of *Ac*GH30A by *E. coli* BL-21 cells at different IPTG concentrations. Lanes 1: Protein molecular-mass marker (HiMedia Labs Pvt. Ltd., India), 2: Un-induced cells pellet, 3: Induced cells pellet (0.25 mM), 4: Induced cells pellet (0.5 mM), 5: Induced cells pellet (0.75 mM) and 6: Induced cells pellet (1.0 mM IPTG).

2.4 Conclusion

The gene encoding *Ac*GH30A (AEV68404.1) of glycoside hydrolase family 30 (GH30) from *Acetivibrio clariflavus* DSM 17932 was cloned and expressed. The molecular architecture of *Ac*GH30A revealed an N-terminus signal peptide (28 aa) followed by a glycoside hydrolase module belonging to the GH30 family (433 aa) and a dockerin 1 module at the C-terminus (68 aa). The 1518 bp of DNA sequence encoding *Ac*GH30A was amplified by PCR from the genomic DNA of *Acetivibrio clariflavus*. The amplified PCR product carrying the desired restriction sites was ligated to the pET-28a(+) expression vector. The recombinant plasmid containing the pET-28a(+) expression vector and the gene encoding *Ac*GH30A was used for transformation of *E.coli* DH5α competent cells. The positive clone of recombinant *Ac*GH30A was confirmed by the release of its encoding gene insert after the restriction digestion using the restriction enzymes *Nhe*I and *Xho*I. The recombinant plasmid after restriction digestion showed pET-28a(+) vector DNA of ~5.3 kb size and the Insert DNA band of ~1.5 kb on agarose gel confirming the inserted gene of interest. The *E. coli* BL21(DE3) cells were transformed by the recombinant plasmid DNA to express the recombinant enzyme, *Ac*GH30A. The hyper-expression of *Ac*GH30A was achieved by using 1 mM as the optimum concentration of IPTG as analysed by SDS-PAGE.

References

1. Abdulhadi, Y., Kaur, K., & Vyas, A. (2023). Chapter 3—Role of microbial xylanases in biorefinery platform and its impact on ecosystem services. In J. Samuel, A. Kumar, & J. Singh (Eds.), Relationship between microbes and the environment for sustainable ecosystem services (pp. 43–59). Elsevier. https://doi.org/10.1016/B978-0-323-89936-9.00013-8

2. Ajeje, S. B., Hu, Y., Song, G., Peter, S. B., Afful, R. G., Sun, F., Asadollahi, M. A., Amiri, H., Abdulkhani, A., & Sun, H. (2021). Thermostable Cellulases / Xylanases from thermophilic and hyperthermophilic microorganisms: Current Perspective. *Frontiers in Bioengineering and Biotechnology*, 9, 794304. https://doi.org/10.3389/fbioe.2021.794304

3. Bajpai, P. (2014). Chapter 2 - Xylan: Occurrence and structure. In P. Bajpai (Ed.), Xylanolytic enzymes (pp. 9–18). Academic Press. https://doi.org/10.1016/B978-0-12-801020-4.00002-0

4. Collins, T., Gerday, C., & Feller, G. (2005). Xylanases, xylanase families and extremophilic xylanases. *FEMS Microbiology Reviews*, 29(1), 3–23.

5. Curry, T. M., Peña, M. J., & Urbanowicz, B. R. (2023). An update on xylan structure, biosynthesis, and potential commercial applications. *The Cell Surface*, 9, 100101. https://doi.org/10.1016/j.tcsw.2023.100101

6. El Enshasy, H. A., Kandiyil, S. K., Malek, R., & Othman, N. Z. (2016) Microbial xylanases: Sources, types, and their applications. In V. K. Gupta (Ed.), Microbial Enzymes in Bioconversions of Biomass (Vol. 3, pp. 151–213). Springer International Publishing. https://doi.org/10.1007/978-3-319-43679-1_7.

7. Faik, A. (2010). Xylan Biosynthesis: News from the Grass. *Plant Physiology*, 153(2), 396–402. https://doi.org/10.1104/pp.110.154237

8. Fonseca-Maldonado, R., Ribeiro, L. F., Furtado, G. P., Arruda, L. M., Meleiro, L. P., Alponti, J. S., Botelho-Machado, C., Vieira, D. S., Bonneil, E., & Furriel, R. dos P. M. (2014) Synergistic action of co-expressed xylanase/laccase mixtures against milled sugar cane bagasse. *Process Biochemistry*, 49(7), 1152–1161. https://doi.org/10.1016/j.procbio.2014.03.027.

9. Gigli-Bisceglia, N., Engelsdorf, T., & Hamann, T. (2020). Plant cell wall integrity maintenance in model plants and crop species-relevant cell wall components and underlying guiding principles. *Cellular and Molecular Life Sciences*, 77(11), 2049–2077. https://doi.org/10.1007/s00018-019-03388-8

10. He, J., Su, L., Sun, X., Fu, J., Chen, J., & Wu, J. (2014). A novel xylanase from *Streptomyces* sp. FA1: Purification, characterisation, identification and heterologous expression. *Biotechnology and Bioprocess Engineering*, 19(1), 8–17. https://doi.org/10.1007/s12257-013-0490-2.

11. Henrissat, B. (1991) A classification of glycosyl hydrolases based on amino acid sequence similarities. *Biochemical Journal*, 280, 309-316. https://doi.org/10.1042/bj2800309.

12. Hsieh, Y. S. Y., & Harris, P. J. (2019). Xylans of red and green algae: What is known about their structures and how they are synthesised? *Polymers*, 11(2), Article 2. https://doi.org/10.3390/polym11020354

13. Juturu, V., & Wu, J. C. (2012) Microbial xylanases: Engineering, production and industrial applications. *Biotechnology Advances*, 30(6), 1219–1227. https://doi.org/10.1016/j.biotechadv.2011.11.006.

14. Katsimpouras, C., Dedes, G., Thomaidis, N. S., & Topakas, E. (2019). A novel fungal GH30 xylanase with xylobiohydrolase auxiliary activity. *Biotechnology for Biofuels*, 12(1), 120. https://doi.org/10.1186/s13068-019-1455-2

15. Laemmli, U.K. (1970) Cleavage of structural proteins during the assembly of the head of bacteriophage T4. *Nature*, 227, 680-685. https://doi.org/10.1038/227680a0.

16. Moreira, L. R. S., & Filho, E. X. F. (2016) Insights into the mechanism of enzymatic hydrolysis of xylan. *Applied Microbiology and Biotechnology*, 100(12), 5205–5214. https://doi.org/10.1007/s00253-016-7555-z.

17. Meyer, T.S., and Lambert, B, L. (1965) Use of coomassie brilliant blue R250 for the electrophoresis of microgram quantities of parotid saliva proteins on acrylamide-gel strips. *Biochimica et Biophysica Acta (BBA)-General Subjects*, 107, 144-145. https://doi.org/10.1016/0304-4165(65)90403-4.

18. Peña, M. J., Kulkarni, A. R., Backe, J., Boyd, M., O'Neill, M. A., & York, W. S. (2016). Structural diversity of xylans in the cell walls of monocots. *Planta*, 244(3), 589–606. https://doi.org/10.1007/s00425-016-2527-1

19. Rennie, E. A., & Scheller, H. V. (2014). Xylan biosynthesis. *Current Opinion in Biotechnology*, 26, 100–107. https://doi.org/10.1016/j.copbio.2013.11.013

20. Sepulchro, A. G. V., Pellegrini, V. O. A., Briganti, L., de Araujo, E. A., de Araujo, S. S., & Polikarpov, I. (2020) Transformation of xylan into value-added biocommodities using *Thermobacillus composti* GH10 xylanase. *Carbohydrate Polymers*, 247, 116714. https://doi.org/10.1016/j.carbpol.2020.116714.

21. Sambrook, J., Fritsch, E.F. and Maniatis, T. (1989) In (2nd ed.) Molecular Cloning: A Laboratory Manual, Vol. 1. Plainview, Cold Spring Harbor Laboratory Press, Woodbury, New York.

22. Sambrook, J. and Russel, D.W (2001) In (3rd ed.) Molecular Cloning: A Laboratory Manual, Vol. 1. Cold Spring Harbor Laboratory Press, Woodbury, New York.

23. Studier, F.W. and Moffatt, B.A. (1986) Use of bacteriophage T7 RNA polymerase to direct selective high-level expression of cloned genes. *Journal of molecular biology*, 189, 113-130. https://doi.org/10.1016/0022-2836(86)90385-2.

24. Topakas, E., Panagiotou, G., & Christakopoulos, P. (n.d.). Xylanases: Characteristics, sources, production, and applications. In bioprocessing technologies in biorefinery for sustainable production of fuels, chemicals, and polymers (pp. 147–166). John Wiley & Sons, Ltd. https://doi.org/10.1002/9781118642047.ch

Chapter 3

Purification, biochemical and functional characterization of the recombinant *Ac*GH30A from *Acetivibrio clariflavus* ATCC 19732

3.1 Introduction

Xylans, the primary component of hemicellulose present in lignocellulosic biomass, are the second most prevalent polysaccharides present in plants, succeeded by cellulose (Fonseca-Maldonado et al., 2014; He et al., 2014). They are heteropolysaccharides that principally consist of xylose and arabinose. The backbone of xylan is a linear polymer composed of xylopyranosyl residues linked by β-1,4-glycosidic bonds, having an equatorial configuration. The polysaccharide structure contains a variety of substituted groups, including arabinose, ferulic acid, glucuronic acid, acetyl and *p*-coumaric acid, that are integrated within the backbone (Moreira & Filho, 2016). The complete depolymerization of xylan is a complex process that requires the enzymes capable of breaking the backbone glycosidic linkages as well as enzymes that can remove substituted groups (Juturu & Wu, 2012).

Xylanases (EC 3.2.1.8) are a class of glycoside hydrolases that can hydrolyze the linear polysaccharide β-1,4-xylan into simpler products, such as xylooligosaccharides, xylobiose and xylose (Juturu & Wu, 2012; Sepulchro et al., 2020). Xylanases have been harnessed for a wide range of applications, such as enhancing the quality of bread (Guo et al., 2018), clarifying must and juices (Juturu & Wu, 2012), degumming bast fibres (Wang et al., 2019), pre-bleaching kraft pulps (Kaur et al., 2016; Kumar et al., 2016), and treating hemicellulosic waste (El Enshasy et al., 2016; Jamaldheen et al., 2019).

Endo-β-1,4-xylanases belonging to glycoside hydrolase family 30 exhibits significant catalytic diversity. The family GH30 contains endo-β-1,4-xylanases which hydrolyse xylans containing 4-O-methyl-D-glucuronic acid or D-glucuronic acid side chain residues and are called glucuronoxylanase (Puchart et al., 2021). A specific glucuronoxylanase, *St*Xyn30A from *Streptomyces turgidiscabies* C56, has a conserved arginine residue at the subsite -2, which is essential for recognizing glucuronic acid side chains (Maehara et al., 2018). These enzymes are primarily found in the bacterial GH30_8 subfamily. The family GH30 also contains non-D-glucuronic acid specific xylanases, such as *Tl*Xyn30A from *Talaromyces leycettanus (*Šuchová et al., 2021), which are not specific to glucuronoxylan and can also hydrolyze arabinoxylan and rhodymenan. Numerous xylanases from the GH30 family displaying different modes of action have been studied, among which only a limited number showing xylobiohydrolase activity have been reported. Xylobiohydrolases from the GH30 family reported till now majorly come from fungal sources, and they show two different modes of action. *Tt*Xyn30A (Katsimpouras et al., 2019) and *Tc*Xyn30B (Nakamichi et al., 2019) from *Thermothelomyces thermophila* and *Talaromyces cellulolyticus*,

respectively, displayed both exo- and endo-acting catalytic behaviour. Both enzymes released 4-O-methyl-D-glucuronic acid embedded xylooligosaccharides and xylobiose from glucuronoxylan substrates. *Aa*Xyn30A from the fungus *Acremonium alcalophilum* was reported as an almost strict xylobiohydrolase (Šuchová et al., 2020). *Aa*Xyn30A cleaves xylobiose from the non-reducing end of the xylan. *Sl*Xyn30A from the yeast *Sugiyamaella lignohabitans* is a GH30 xylanase that releases acidic xylooligosaccharides from glucuronoxylan and shows auxiliary xylobiohydrolase activity (Šuchová et al., 2022). The first enzymes identified to selectively release xylobiose from birchwood and oat spelt xylan were xylanase V from *Aeromonas caviae* ME-1 (Kubata et al., 1994) and xylobiohydrolase from *Aspergillus sydowii* MG49 (Ghosh & Nanda, 1994). To date, their catalytic mechanisms have not been thoroughly elucidated, and their glycoside hydrolase (GH) family affiliations remain unclassified. Subsequent investigations led to the isolation and characterization of xylobiohydrolases from the GH11 and GH30 families. Two enzymes from the GH11 family, compost 21_GH11 (Evangelista et al., 2019) and MetXyn11 (Mello et al., 2017), were found to hydrolyze xylan with complete selectivity towards xylobiose as the sole reaction product, despite the GH11 family predominantly comprising endo-acting xylanases.

Acetivibrio clariflavus is a bacterium characterized by its thermophilic nature, anaerobic metabolism, gram-positive cell structure and ability to form spores (Artzi et al., 2014). This bacterium was initially isolated from anaerobic sludge obtained from a thermophilic methanogenic bioreactor (Shiratori et al., 2006, 2009). The analysis of the *Acetivibrio clariflavus* genome revealed that the bacterium utilizes an elaborate system of cellulosomal complexes containing multiple enzymes to break down lignocellulosic biomass into simpler products (Dassa et al., 2012). *Acetivibrio clariflavus* is the only

thermophilic bacterium that has been reported to produce a complex cellulosomal system after the discovery of a cellulosomal system in *Clostridium thermocellum* (Artzi et al., 2014; Lamed & Bayer, 1988). It produces both cell-free and cell-bound cellulosome complexes. Bioinformatics studies revealed the presence of 79 dockerin containing proteins in *Acetivibrio clariflavus*, indicating the possibility of multiple cellulosome structures (Artzi et al., 2014). Several glycoside hydrolases from the *Acetivibrio clariflavus* have been characterized, but many more remain unexplored. The gene (GenBank accession number AEV68404.1) encoding a putative xylanolytic enzyme, *Ac*GH30A from the cellulosomal complex of *Acetivibrio clariflavus,* belongs to the GH30 family.

In this study, the gene encoding the xylobiohydrolase (*Ac*GH30A) was purified and characterized. During the study of the enzyme, *Ac*GH30A, Šuchová et al., (2021) and Crooks et al., (2021) also reported their work on the same enzyme. Despite some overlaps in the findings, our report presents more detailed and valuable data on the characteristics of *Ac*GH30A. It is hypothesized that the in-depth biochemical characterization of *Ac*GH30A will enhance the understanding regarding its capabilities as a thermophilic xylobiohydrolase of bacterial origin. The new results from the current study, shed light on the greater potential of the enzyme with regard to its commercial usage, such as its thermophilic enzyme properties, stability and capability to produce xylobiose from wide variety of xylan polymers. The biochemical characteristics of *Ac*GH30A discovered in this study may be beneficial for the enzymatic digestion of xylan based biomasses to produce xylobiose, renowned for its superior prebiotic properties (Manisseri & Gudipati, 2012).

3.2 Materials and Methods

3.2.1 Substrates and reagents

Sodium hydroxide, copper sulphate pentahydrate, sodium carbonate, sodium potassium tartarate, sodium bicarbonate, sodium sulphate, sodium phosphate (monobasic), sodium phosphate (dibasic) and salts of metal ions viz. $CaCl_2$, $MgCl_2$, $CuCl_2$, $CoCl_2$, $FeCl_3$, $MgSO_4$, $MnSO_4$, $ZnSO_4$, $NiSO_4$, $CuSO_4$, NaCl and KCl were procured from HiMedia Laboratories Pvt. Ltd., India. Multiple xylan polysaccharides, each composed of a primary chain formed by a linear sequence of xylose units linked through β-1,4-glycosidic bonds, were obtained from different sources. Natural xylan polysaccharides *viz.* Beechwood xylan, larchwood xylan, rye arabinoxylan and wheat arabinoxylan (low viscosity), birchwood acetylated xylan and standards *viz*. D-xylose, xylobiose, xylotriose, xylotetraose and xylopentaose were procured from Megazyme Ltd., Ireland. Xylan, M.W. 20000-30000 and xylan corn cob were purchased from Carbosynth Ltd., UK. The polysaccharides, 4-O-Methyl glucuronoxylan, oat spelt xylan and carboxy methyl cellulose sodium salt were purchased from Sigma-Aldrich Co. LLC., USA. Various in-house xylan substrates namely, banana stem xylan, water hyacinth xylan, sugarcane tops xylan (Khaire et al., 2021), alkali pretreated sugarcane tops xylan (Khaire et al., 2022), neem saw dust xylan (Sharma et al., 2020) and acacia sawdust xylan (Sharma et al., 2020) were also used for the study. Sodium arsenate, ammonium molybdate, sulphuric acid, hydrochloric acid, acetone, acetonitrile, acetic acid and Folin's reagent were purchased from Merck Limited, India. The silica-coated plates for thin-layer chromatography (TLC Silica gel 60 F_{254}, 20 cm × 20 cm) were acquired from Merck, India.

3.2.2 Purification of recombinant protein, *Ac*GH30A

The recombinant protein *Ac*GH30A, engineered with an N-terminal His_6-tag, was purified using immobilized metal-ion affinity chromatography (IMAC), as detailed in Section 3.2.2.1. Purification was performed utilizing a 1.0 mL Sepharose-based column (HiTrap Chelating HP, GE Healthcare). The compositions of the binding and elution buffers employed during affinity purification are listed in Table 3.1. The recombinant protein, *Ac*GH30A, was further purified by size-exclusion chromatography (SEC), as mentioned in Section 3.2.2.2.

Table 3.1 Composition of buffers required for purification of recombinant proteins by affinity purification.

Buffers	Composition
Equilibration buffer	50 mM sodium phosphate, pH 7.5 300 mM NaCl, 50 mM Imidazole
Elution buffer	50 mM sodium phosphate, pH 7.5 300 mM NaCl, 300 mM Imidazole
Column cleaning buffer	50 mM sodium phosphate, pH 7.5 300 mM NaCl, 50 mM EDTA

3.2.2.1 *Purification protocol of recombinant AcGH30A by IMAC*

1. Bacterial cells obtained from a 100 mL culture were harvested by centrifugation at 10,000***g*** for 10 min at 4°C. The resulting cell pellet was resuspended in 5 mL of 50 mM Tris-HCl buffer, adjusted to pH 8.5.
2. The cells were sonicated on ice for 15 min using a pulse cycle of 10s on and 15s off at 33% amplitude. The sonicated suspension was centrifuged at 12,000***g*** for 30 min at 4°C to obtain the crude cell-free extract.
3. The cell-free extract was passed through a 0.45 µm filter membrane before loading onto 1mL HiTrap chelating HP column. The column was pre-washed with 5 volumes of filtered and degassed water to remove the alcohol.
4. Column was charged using 2.0 mL of 0.1 M $NiSO_4$ solution, and the unbound Ni^{2+} ions were washed away with 2-5 volumes of water.
5. The column was equilibrated with 10 column volumes of equilibration buffer prior to sample loading (Table 3.1).
6. The filtered cell-free extract of recombinant protein was applied onto the column at a flow rate of 0.5 $mL.min^{-1}$.

7. The column was subsequently washed with 50 column volumes of equilibration buffer to eliminate unbound proteins.
8. The bound recombinant protein was eluted using the elution buffer by applying a linear gradient of 0-100% imidazole concentration. Eluate was collected in 1 mL fractions (Carvalho *et al.,* 2004).
9. The column was cleaned using the cleaning buffer outlined in Table 3.1, followed by washing with 5 column volumes of water. The column was then incubated with 1N NaOH at 4°C for 2h. After incubation, it was washed with 20 column volumes of water to remove any residual NaOH, and finally stored in 20% (v/v) ethanol at 4°C.

The purified recombinant protein *Ac*GH30A was dialyzed against 50 mM sodium phosphate buffer, pH 7.0. The purity and molecular mass of the recombinant protein was assessed by SDS-PAGE, as detailed in Section 2.2.13.

3.2.2.2 *Purification of AcGH30A by Size-exclusion chromatography*

The purified protein, *Ac*GH30A, obtained after IMAC was further purified by Size-exclusion chromatography (SEC) at 25ºC, using 120 mL, HiLoad Superdex 75 pg column (GE Healthcare, Chicago, IL, USA) installed on a fast protein liquid chromatography (FPLC) system (AKTA Prime, GE Healthcare, Chicago, IL, USA). The sodium phosphate buffer (50 mM, pH 7.0) was utilized as the mobile phase at a flow rate of 1 $mL.min^{-1}$. The column was initially equilibrated using the mobile phase before loading the protein sample. The fractions (2.0 mL) were collected under peak area and analysed for protein by Folin-Lowry (Lowry et al., 1951) method as described in Section 3.2.3.1 and purity by SDS-PAGE as described in Section 2.2.13. After the elution, the column was washed with 1 column volume of 0.5 M NaOH solution followed by 5 column volume of degassed and deionized water. The column was stored with 20% v/v ethanol inside the resin to prevent contamination.

3.2.3 Protein concentration determination of purified recombinant proteins by using Folin-Lowry and UV method

The concentration of the purified *Ac*GH30A was determined by Folin-Lowry method (Lowry et al., 1951) using bovine serum albumin (BSA) as standard. The BSA standard at different concentrations (10-1000 µg.mL^{-1}) and the unknown *Ac*GH30A fraction samples were treated with an alkaline reagent composed of sodium carbonate and copper sulfate, which binds to peptide bonds and forms a blue complex. Subsequently, the Folin-Ciocalteu reagent, which contains phosphomolybdic and phosphotungstic acids, was added, resulting in a color change due to the reduction of these acids by the tyrosine and tryptophan residues in proteins. The intensity of the resulting blue color, which develops over a 30-minute incubation period, was measured spectrophotometrically at 660 nm. By comparing the absorbance values of the samples to those of a standard curve generated from known BSA concentrations, the protein concentration in the *Ac*GH30A was quantified.

3.2.3.1 *Composition of reagents used in the Folin-Lowry method*

Reagent A: Sodium carbonate (2.0 g) and sodium hydroxide (0.4 g) dissolved 100 mL of distilled water.

Reagent B1: Potassium sodium tartrate tetrahydrate (2.0 g) dissolved in 10 mL distilled water.

Reagent B2: Copper sulphate pentahydrate (1.0 g) dissolved in 100 mL distilled water.

Reagent C: Freshly prepared prior the experiment by dissolving reagent B1, A and B2 in a ratio of B1:A:B2 = 1:100:1.

Folin-Ciocalteu reagent : 1 N Folin-Ciocalteu reagent.

3.2.3.2 *Protocol of Folin-Lowry method for protein estimation*

1. ***Standard curve preparation***

   A series of dilutions of the BSA standard was prepared to generate a range of protein concentrations (10-1000 $\mu g.mL^{-1}$) for making the standard curve.

2. ***Sample preparation***

   0.2 mL of the protein sample or standard solution was placed into labeled test tubes.

3. ***Addition of Reagent C (Alkaline Copper Solution)***

   1.0 mL of freshly prepared Reagent C was added to each tube (containing either protein standards or unknown samples). The mixtures were incubated at room temperature for 10 min to allow color development.

4. ***Addition of Folin-Ciocalteu reagent***

   0.1 mL of 1 N Folin-Ciocalteu reagent was added to the sample solutions. The solution was mixed and incubated at room temperature for 30 min.

5. ***Measurement***

   The absorbance was measured at 660 nm using a spectrophotometer.

6. ***Protein concentration determination:***

   The absorbance readings of the standards were utilized to generate a standard curve. The protein concentrations of the unknown samples were determined by reference to this standard curve.

The amount of recombinant protein was estimated using the following equation,

$$\text{Protein concentration} = \frac{\Delta A_{660} \times C \times V}{v}$$

Where,

ΔA_{660} = change in absorbance of the sample
V = volume of the protein-buffer mixture (mL)
C = 1 OD equivalent of BSA from the standard plot ($mg.mL^{-1}$)
v = volume of the protein used for assay (mL)

3.2.3.3 *Ultra-Violet method for protein estimation*

The concentration of purified protein was also determined from their corresponding absorbance at 280 nm using the equation below (Layne, 1957;

Stoscheck, 1990). Absorbance was measured after proper dilution of the protein using a spectrophotometer (Gene Quant, GE) having a path length of 1 cm. The molar extinction co-efficient 122730 $M^{-1}cm^{-1}$ for *Ac*GH30A was used for the calculation.

$$\text{Concentration of protein (mg.mL}^{-1}\text{)} = \frac{\text{Absorbance at 280 nm x Mol. weight (Da)}}{\text{Extinction coefficient (M}^{-1}\text{cm}^{-1}\text{) x Path length (1 cm)}}$$

3.2.4 Assay of enzyme activity

The assays for biochemical characterization of *Ac*GH30A were performed using a working solution of *Ac*GH30A (50 µg.mL^{-1}) prepared by diluting the *Ac*GH30A stock (500 µg.mL^{-1}) obtained after SEC. The assays were conducted with a reaction mixture of 100 µL containing 10 µL of *Ac*GH30A (50 µg.mL^{-1}) and 2.0% (w/v) final concentration of beechwood xylan in sodium phosphate buffer (50 mM, pH 7.0) by incubating at 80°C for 2 min. A negative control, containing only 2.0%, (w/v) beechwood xylan in 100 µL of sodium phosphate buffer (50 mM, pH 7.0) without the enzyme, was run in parallel for each reaction. The activity of *Ac*GH30A against various xylan substrates were examined. The enzyme activity of crude *Ac*GH30A enzyme and after IMAC and SEC purification steps was determined by using 2.0% (w/v) beechwood xylan following the same conditions as mentioned above. The activity of the enzyme was calculated by quantifying the amount of reducing sugars produced from the enzyme-substrate reactions using the method developed by Nelson (Nelson, 1944) and Somogyi (Somogyi, 1945) with plotting a standard curve for D-xylose. 25 parts of the copper reagent A (NS-A) were added with 1 part of copper reagent B (NS-B) to make Nelson-Somogyi-D (NS-D) solution (Nelson, 1944). After the completion of the enzyme-substrate reaction, 100 µL of the enzyme-substrate mixture was mixed with 100 µL of NS-D reagent, followed by incubation in a boiling water bath for 20 min for

deactivating the enzyme and the reaction between the NS-D and reducing sugars. The mixture was cooled and 100 µL of arsenomolybdate colour reagent (NS-C) reagent was added. The volume of the mixture was adjusted to 1 mL by further adding 700 µL sodium phosphate (50 mM, pH 7.0) buffer. The absorbance of the final mixture was recorded at 500 nm using a spectrophotometer (Multiskan SkyHigh, Thermo Fisher Scientific, Waltham, MA, USA).

3.2.4.1 *Preparation of reagents for reducing sugar estimation*

Reagent A

Sodium carbonate anhydrous	6.25 g
Sodium potassium tatarate	6.25 g
Sodium bicarbonate	5.0 g
Sodium sulphate anhydrous	50.0 g

The above specified components were dissolved in 100 mL of deionized water and the total volume was adjusted to 250 mL. The resulting solution was filtered using Whatman No. 1 filter paper and stored at temperature of 30°C.

Reagent B

Reagent B was formulated by dissolving 15 g of copper sulfate ($CuSO_4$) in 50 mL of deionized water, with the addition of one or two drops of concentrated sulfuric acid. The final volume of the resulting solution was adjusted to 100 mL and filtered using Whatman No. 1 filter paper. The solution was stored at temperature of 30°C.

Reagent C

Reagent C was prepared in a dimly lit environment through a two-step process. Initially, 2.5 g of ammonium molybdate were dissolved in 45 mL of deionized water using a 100 mL beaker, followed by the addition of 2.1 mL of concentrated sulfuric acid. Simultaneously, in another beaker, 0.3 g of sodium arsenate was dissolved in 2.5

mL of deionized water. Subsequently, the sodium arsenate solution was mixed with ammonium molybdate solution resulting in a total volume of approximately 50 milliliters. The resulting solution was then filtered using Whatman No. 1 filter paper in low-light conditions and stored at 37°C. The solution was utilized after a 24 h incubation period.

Reagent D

Reagent D was prepared by combining reagent A and reagent B in a ratio of 25:1. The composite reagent D was freshly prepared for the assay.

3.2.4.2 ***Generation of a standard plot of D-xylose***

The standard plot for D-xylose was created by altering its concentration within the range of 10-100 µg.mL^{-1}. 100 µl reaction mixture containing 50 mM sodium phosphate buffer pH 7.0 with D- xylose in a 1.5 mL microcentrifuge was added with 100 µl of solution D (Section 3.2.4.1). The reaction mixture was then heated in a boiling water bath for 20 min, followed by cooling to room temperature. 100 µL of solution C (Section 3.2.4.1) was added and the components were mixed. Then 700 µL sodium phosphate (50 mM, pH 7.0) buffer was added to adjust the final volume to 1 mL. The absorbance at 500 nm (A_{500}) was measured using a UV-Visible spectrophotometer (Thermo, Multiskan) against a buffer blank. A standard plot of A_{500} versus D- xylose concentration (µg.mL^{-1}) was developed and 1 A_{500} equivalent of D- xylose (µg.mL^{-1}) was calculated. 1 A_{500} equivalent of D- xylose (µg.mL^{-1}) was converted into mg.mL^{-1} for the determination of enzyme activity.

3.2.4.3 ***Calculation of enzyme activity of AcGH30A***

The enzyme activity was quantified in units per milliliter (U.mL^{-1}), while its specific activity was measured in units per milligram of protein (U.mg^{-1}). One unit (U)

of enzyme (1 µmol.min^{-1}) was defined as the enzyme quantity needed to generate 1 µmole of xylose per minute. The enzyme activity (U.mL^{-1} or µmol.min^{-1}.mL^{-1}) is defined as the amount of enzyme per mL needed to generate 1 µmole of xylose per min. Whereas, the specific enzyme activity (U.mg^{-1} or µmol.min^{-1}.mg^{-1}) is defined as the enzyme quantity per milligram required to produce 1 µmole of xylose, per minute under the optimum conditions of reaction. The enzyme activity of *Ac*GH30A was calculated as described below,

$$\text{Enzyme activity (U.mL}^{-1}) = \frac{\Delta A_{500} \times C \times V}{150 \times t \times v} = (\mu\text{mole.min}^{-1}.\text{mL}^{-1})$$

where,

ΔA_{500} = change in absorbance of the sample at 500 nm
C = 1 OD equivalent D-xylose concentration from the standard plot
V = volume of the reaction mixture (mL)
t = time of reaction (min)
150 = molecular weight of D-xylose
v = volume of the enzyme taken in assay (mL) for reducing sugar estimation.

3.2.5 Determination of optimum pH and pH stability

The optimum pH of *Ac*GH30A was investigated by conducting enzyme-substrate reactions with beechwood xylan at different pH. Different buffer systems for various pH range used were sodium acetate buffer (pH 3.5–5.5), sodium phosphate buffer (pH 6.0–8.0) and glycine-NaOH buffer (pH 8.5–10.5) at 50 mM concentration. To examine the stability of *Ac*GH30A at different pH environment, the recombinant enzyme, *Ac*GH30A was incubated for 90 min at 25°C using different buffers with a pH range of 4.0 to 8.0. From this, an aliquot of 10 µL enzyme was taken for 100 µL reaction mixture and assayed under optimum conditions of 80°C for 2 min. The level of activity shown by the enzyme after the incubation period was determined by quantifying the

reducing sugars released after the reaction, as previously described. In all the assays, an enzyme reaction without the enzyme was run in parallel as a negative control.

3.2.6 Determination of optimum temperature and thermal stability

The optimum temperature required for the activity of *Ac*GH30A was evaluated by conducting the identical enzyme-substrate reactions at different temperatures, spanning from 20 to 95°C. The reaction mixture, 100 µL containing 10 µL of *Ac*GH30A (50 $\mu g.mL^{-1}$) and 2.0% (w/v) beechwood xylan in sodium phosphate buffer (50 mM, pH 7.0) were incubated at varying temperatures for 2 min. The reactions were terminated after 2 min of incubation and the reducing sugar analysis was performed by using the methods of Nelson (Nelson, 1944) and Somogyi (Somogyi, 1945). In all assays, substrate and buffer without enzyme were included in parallel as negative controls. The thermostability of *Ac*GH30A was investigated by incubating the stock solution of the enzyme at different temperatures for 90 min, prior to the enzyme-substrate reactions conducted at optimum temperature and pH. 10 µL of *Ac*GH30A (50 $\mu g.mL^{-1}$) from the incubated stocks was added with 90 µL of 2.0% (w/v) beechwood xylan at 80°C for 2 min in a sodium phosphate buffer system (50 mM, pH 7.0). The thermal properties of *Ac*GH30A were also assessed by Circular Dichroism (CD) spectroscopy, using the purified enzyme at 1 $mg.mL^{-1}$ concentration, dissolved in sodium phosphate buffer (50 mM, pH 7.0). Variations in the spectrum as a function of temperature was measured using a spectropolarimeter (JASCO J-815, Jasco Corp., Heckmondwike, UK). The enzyme sample and the corresponding buffer without enzyme were analyzed at the rate of 50 $nm.min^{-1}$ and bandwidth of 1 nm. Far-UV (190-240 nm) CD spectrum was recorded at the intervals of 5°C, with increase in the temperature from 25°C to 110°C. CD ellipticity was plotted against wavelength and

temperature to analyze the thermal properties of *Ac*GH30A. The melting temperature (T_m) of *Ac*GH30A was calculated by plotting the change in CD spectra captured at 222 nm (FAR-UV) and examining the pattern of thermal denaturation. The transition curve at 222 nm was normalized using the formula: %denaturation = $(\theta_{25} - \theta_{Temp}) / (\theta_{25} - \theta_{110})$. The T_m value was calculated through non-linear fitting using the Boltzmann method (Ruíz et al., 2022). The half-life ($t_{1/2}$) of *Ac*GH30A at different temperatures was determined by incubating the enzyme at 4°C, 30°C, 60°C and 70°C and an aliquot of enzyme was taken at different time intervals *viz.*, 0 to 24 h. All the assays were performed at an optimum temperature of 80°C and optimum pH of 7.0 using 2% beechwood xylan as substrate. The half-life was calculated by plotting relative residual activity against the incubation period. The half-life of *Ac*GH30A was calculated based on the assumption that enzyme degradation followed first-order kinetics, where the half-life ($t_{1/2}$) = ln2/k, with 'k' representing the rate constant (Han & Lim, 2004; Sárossy et al., 2013).

3.2.7 Substrate specificity analysis of *Ac*GH30A

The enzyme activity of *Ac*GH30A against various commercial, natural and pretreated substrates was investigated under optimized assay conditions. Each assay mixture of 100 µL containing 10 µL of *Ac*GH30A (50 µg.mL^{-1}) and 2.0%, (w/v) of respective substrates in sodium phosphate buffer (50 mM, pH 7.0) was incubated at 80°C for 2 min. The reducing sugar analysis and the enzyme activity calculation was performed as mentioned in Section 3.2.4.

3.2.8 Determination of kinetic parameters

The kinetic properties of *Ac*GH30A were examined by conducting enzyme assays, with varying concentrations (from 0.005%, w/v to upto 3.0 %, w/v) of

substrates, at optimum temperature and pH conditions. The substrates employed for the enzyme kinetics investigation included 4-O-methyl glucuronoxylan (Sigma-Aldrich, USA), xylan M.W. 20000-30000 (Carbosyth Ltd., USA), beechwood xylan (Megazyme Ltd., Ireland) and larchwood xylan (Megazyme Ltd., Ireland). In each assay, 90 µL of the respective substrate was mixed and added with 10 µL of *Ac*GH30A (50 µg.mL^{-1}). Identical reaction mixtures without the enzymes were used as negative controls. The estimation of reducing sugars and the subsequent calculation of enzyme activity after the enzyme reaction were conducted as outlined in Section 3.2.4. The values for K_m, V_{max}, and the turnover number (k_{cat}) were determined using the Michaelis-Menten equation, assuming steady-state conditions. All enzyme reactions were executed in triplicate. The calculated data are presented as mean values with their corresponding standard deviations (mean ± SD). The GraphPad Prism software was used to calculate the kinetic parameters (Swift, 1997).

3.2.9 Influence of metal ions and chemical agents on enzyme activity

The capability of the different metal ions to change the catalytic activity of *Ac*GH30A was investigated. For this study, enzyme-substrate reactions were supplemented separately with different metal salts, including $CaCl_2$, $MgCl_2$, $CuCl_2$, $CoCl_2$, $FeCl_3$, $MgSO_4$, $MnSO_4$, $ZnSO_4$, $NiSO_4$, $CuSO_4$, NaCl and KCl. The effect of the chelating agents like EDTA and EGTA on the activity of *Ac*GH30A were also examined. The enzyme was pretreated with each additive at two different concentrations, i.e., 1 mM and 10 mM, by diluting it with the respective additive solution. Twenty microliters of enzyme, *Ac*GH30A (500 µg.mL^{-1}) with respective additive in 200 µL total volume was incubated at 25°C for 20 min. Afterwards, the pretreated enzyme samples were subjected to standard enzyme assays against 2% (w/v)

beechwood xylan, as previously described in Section 3.2.4. The activity was expressed as a percentage of the activity level in the absence of each additive (control sample).

3.2.10 Study of the hydrolytic mechanism by *Ac*GH30A by TLC

The hydrolysis products generated by *Ac*GH30A from various xylan substrates were examined using thin-layer chromatography (TLC). To prepare the samples for TLC analysis, 20 µL of *Ac*GH30A solution (50 µg.mL^{-1}) was incubated with 180 µL of xylan substrates (1%, w/v). The xylan substrates used were beechwood xylan, larchwood xylan, 4-O-methyl glucuronoxylan, rye arabinoxylan, wheat arabinoxylan and oat spelt xylan. These substrates were dissolved with sodium phosphate buffer (50 mM, pH 7.0) and incubated at 70°C for 60 min. The time-dependent TLC analysis of *Ac*GH30A hydrolysed beechwood xylan was performed to investigate the pattern of product formation over time. For this analysis, 10 µL of *Ac*GH30A solution (50 µg.mL^{-1}) and 90 µL of 1% (w/v) beechwood xylan in sodium phosphate buffer (50 mM, pH 7.0), was incubated at 40°C for different time durations *viz.* 1, 2, 5, 10, 15, 30, and 60 min and 2, 4, 6, 12, and 24 h. A negative control consisting of an equal volume of the reaction mixture without the enzyme was included in the study. To inactivate the enzyme, present in reaction mixtures, an equal volume of absolute ethanol was added. The reaction mixture was centrifuged at 14,000g for 10 min at 25°C to separate the undigested substrate. The resulting clear supernatant (~200 µL), containing enzyme reaction product, was carefully moved to a fresh 1.5 mL microcentrifuge tube. The hydrolysed products present in the supernatant were concentrated to 10-20 µL in a hot air oven at 70°C for 12 h. D-xylose, xylobiose, xylotriose, xylotetraose and xylopentaose (each 1.0 mg.mL^{-1}) were utilized as the standards. The concentrated hydrolyzed samples (0.6 µL each) and 1.0 µL (1 mg.mL^{-1}) of each standard were loaded

over the TLC plate (Silica gel-coated aluminium plate, Merck, Germany). The TLC plate was inserted into a developing chamber containing a solvent system composed of chloroform, glacial acetic acid and water mixed with a ratio of 6:7:1 (Valls et al., 2010). After drying the TLC plate in a hot air oven, the spots developed on the plate were visualized by using a staining solution consisting of 0.5% (w/v) α-naphthol and sulfuric acid/methanol in a 5:95 ratio (v/v).

3.2.11 HPLC analysis of *Ac*GH30A hydrolyzed products

The hydrolytic mechanism of *Ac*GH30A against beechwood xylan was investigated by analyzing the hydrolyzed products using high-performance liquid chromatography (HPLC). The enzyme, *Ac*GH30A, 120 µL (100 µg.mL^{-1}) with 1.0% (w/v) beechwood xylan dissolved in sodium phosphate buffer (50 mM, pH 7.0) in total volume of 1.2 mL reaction mixture was incubated at 70°C for 60 min. The reaction was stopped by inactivating the enzyme by adding an equal volume of absolute ethanol and the rest of the further procedure was followed as outlined in Section 3.2.10 for preparing the hydrolyzed product sample. The supernatant was dried in a hot air oven at 75°C for 24 h, after which it was re-dissolved in 500 µL of distilled water. The sample was then filtered through a 0.45 µm membrane using a syringe filter to remove any impurities. Xylobiose at a concentration of 1 mg mL^{-1} was used as the standard. The column for oligosaccharide separation (Rezex RSO-Oligosaccharide column, 200 × 10 mm, Phenomenex, Inc., Torrance, CA, USA) with a guard column (Rezex RSO-Oligosaccharide guard, 60 × 10 mm, Phenomenex, Inc., Torrance, CA, USA) attached with HPLC (Shimadzu Corporation, Kyoto, Japan) was used. Milli-Q water was utilized as the mobile phase with a flow rate of 0.3 mL.min^{-1}. The samples were run in

the isocratic mode with injection volume of 20 µL. The column temperature was set at 80°C. The eluted samples were analyzed by using a refractive index detector.

3.2.12 Liquid chromatography-mass spectrometry of *Ac*GH30A hydrolyzed product

The enzyme, *Ac*GH30A reaction product released from beechwood xylan was prepared according to the protocol described in Section 3.2.11. 500 µL of the reaction mixture was used to prepare the analyte samples, consisting of 50 µL of *Ac*GH30A (100 $\mu g.mL^{-1}$) and 1.0% (w/v) beechwood xylan dissolved in sodium phosphate buffer (50 mM, pH 7.0). The mixture was incubated at 70°C for 60 min. The reaction was terminated by inactivating the enzyme by adding an equal volume of absolute ethanol to the reaction mixture. Subsequently, the product was dried at 75°C for 12 h. The dried sample was reconstituted in 500 µL of acetonitrile/Milli-Q water (1:1) and analyzed. This sample containing *Ac*GH30A hydrolysed products were analysed by Liquid chromatography-mass spectrometry, (LC-MS) instrument (Agilent 6410 Triple Quad MS-MS, Agilent Technologies, Inc., Santa Clara, CA, USA). A carbohydrate column (4.6 x 150 mm, ZORBAX, Agilent Technologies, Inc., Santa Clara, CA, USA) encased with 5 µm size particles for chromatography was used. The mobile phase comprised acetonitrile/Milli-Q water (70:30). The flow rate of the mobile phase through the column was 600 $\mu L.min^{-1}$. Electrospray ionization was operated in positive ion mode. The scan range was set at 25-1200 m/z.

3.3 Results and Discussion

3.3.1 Purification of the recombinant protein by immobilized metal-ion affinity chromatography

The recombinant proteins were purified by immobilized metal-ion affinity chromatography (IMAC) as described in Section 3.2.2.1 and then dialyzed for removal of imidazole and sodium chloride. The recombinant *Ac*GH30A was expressed as soluble protein and following purification, an additional band was observed above the expected molecular mass on SDS-PAGE gels (Fig. 3.1, Lane 7). The calculated molecular mass of the recombinant *Ac*GH30A, including the N-terminal histidine tag, was 57.78 kDa, which closely matched the observed value on the SDS-PAGE gels.

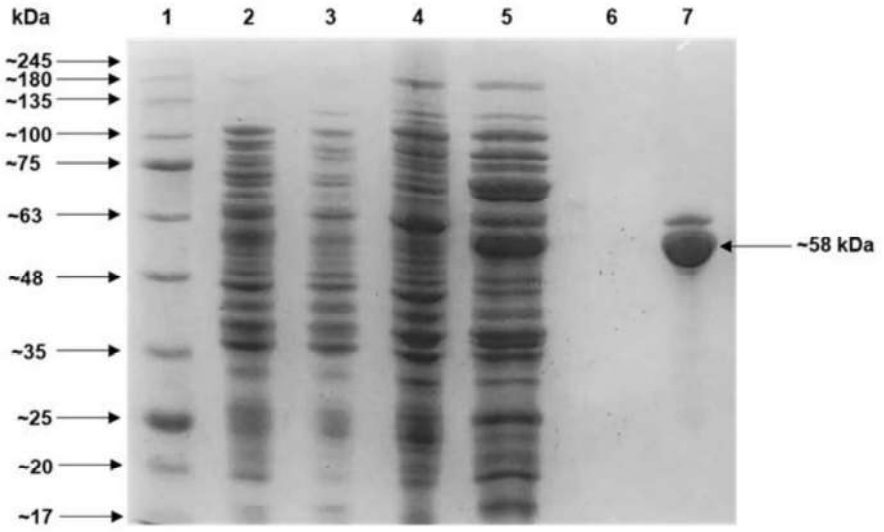

Fig. 3.1 SDS-PAGE (12%, w/v gel) showing expression and purification of *Ac*GH30A. Lanes, 1: Protein molecular-mass marker, 2: Un-induced *E. coli* BL-21 cells pellet, 3: Induced *E. coli* BL-21 cells pellet of, 4: Induced cells pellet of *E. coli* BL-21 cells after sonication, 5: Cell extract, 6: Last wash from column, 7: Purified protein *Ac*GH30A (~58 kDa).

3.3.2 *Ac*GH30A protein purification by Size-Exclusion Chromatography

The recombinant enzyme *Ac*GH30A, initially purified by immobilized metal-ion affinity chromatography (IMAC) was further purified by Size-Exclusion Chromatography (SEC) using HiLoad Superdex 75 pg column connected to FPLC

system. The elution chromatogram showed two peaks, peak 1 and peak 2, corresponding to the two bands of protein observed on SDS-PAGE after the purification by IMAC (Fig. 3.2). Enzyme activity assays indicated that Peak 2 exhibited xylobiohydrolase activity, while Peak 1 showed only negligible activity under standard assay conditions. Therefore, Peak 2, collected between 62-80 mL, was selected for further biochemical characterization. The peak 1 at 45 mL represents the undesired protein band, while the peak 2 at 64 mL corresponds to the pure *Ac*GH30A. The purified *Ac*GH30A collected from 62-80 mL elution (peak 2) after SEC exhibited a single homogeneous protein band on SDS-PAGE analysis (Fig. 3.3, lane 8), indicating a molecular mass of approximately, 58 kDa. This molecular mass closely matched the theoretically calculated value of 57.78 kDa.

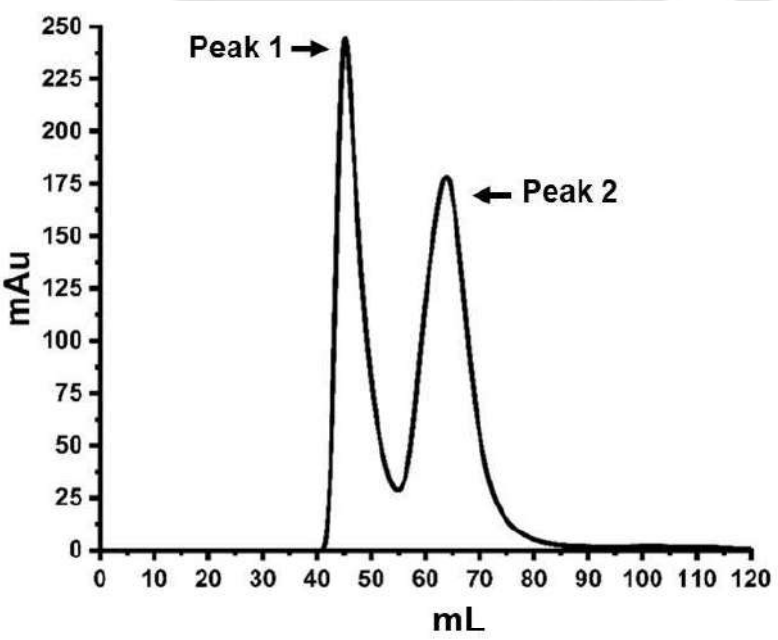

Fig. 3.2 FPLC chromatogram of *Ac*GH30A purification. IMAC purified *Ac*GH30A was further purified by size exclusion chromatography (SEC) at 25°C, using HiLoad Superdex 75 pg column (GE Healthcare, GE Healthcare, Chicago, IL, USA) installed with fast protein liquid chromatography (FPLC) system (AKTA Prime, GE Healthcare, Chicago, IL, USA). The sodium phosphate buffer (50 mM, pH 7.0) was utilized as the mobile phase.

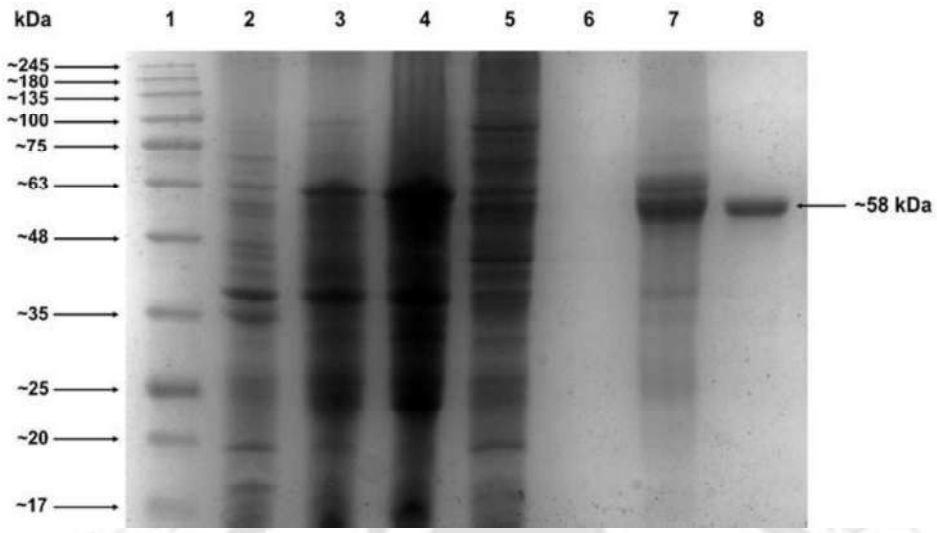

Fig. 3.3 SDS-PAGE (12%, w/v gel) showing expression and purification of *Ac*GH30A after metal ion affinity chromatography and Size-Exclusion Chromatography. Lanes, 1: Protein molecular-mass marker (Himedia, India), 2: Un-induced *E. coli* BL-21 DE3 cells pellet, 3: Induced cells pellet of *E. coli* BL-21 DE3, 4: Induced cells pellet of *E. coli* BL-21 DE3 cells after sonication, 5: Cell extract (Supernatant obtained after centrifugation of the sonicated induced cells pellet of *E. coli* BL-21 DE3), 6: Last wash from column, 7: Purified protein *Ac*GH30A after metal ion affinity chromatography and 8: Purified protein *Ac*GH30A (~58 kDa) after Size-Exclusion Chromatography.

3.3.3 Purification and yield analysis of *Ac*GH30A enzyme activity

Specific activity and percent yield of enzyme activity of *Ac*GH30A were calculated and compared as the purification process proceeded. The cell lysate obtained after sonification of the induced *E. coli* BL21(DE3) cells gave a specific activity of 6.2 $U.mg^{-1}$. The enzyme, *Ac*GH30A purified from the cell lysate, using IMAC showed specific activity of 87.5 $U.mg^{-1}$, displaying 14-fold purification as compared with cell lysate (Table 3.2). On further purification of IMAC purified *Ac*GH30A by SEC, the specific activity increased to 109.6 $U.mg^{-1}$, giving over 16-fold purification as compared with the cell lysate (Table 3.2). The specific activity of the enzyme, *Ac*GH30A was found to increase with enhancement in purity after each step of purification step. The total yield of enzyme activity of *Ac*GH30A after IMAC and SEC

was determined to be 91% and 72%, respectively. The amount of purified *Ac*GH30A protein after SEC obtained from 500 mL culture grown in Luria-Bertani medium was 7 mg. The yield of *Ac*GH30A enzyme was 4.4 mg per gram dry weight of *E. coli* cells.

Table 3.2 Purification of *Ac*GH30A enzyme.

Fractionation step	Volume (mL)	*Ac*GH30A			Protein concentration ($mg.mL^{-1}$)	SA** ($U.mg^{-1}$)	Fold purification
		EA* ($U.mL^{-1}$)	Total Units	Overall % yield			
Cell lysate	10	106	1060	100	17	6.2	1
IMAC	10	96.3	962.5	90.8	1.1	87.5	14
SEC	14	54.8	723.5	72.4	0.5	109.6	17

Enzyme activity was determined against 2.0%, (w/v) beechwood xylan in sodium phosphate buffer (50 mM, pH 7.0), at 80°C for 2 min.
**Enzyme activity, **Specific enzyme activity*

3.3.4 Determination of optimum pH and pH stability

The enzyme, *Ac*GH30A exhibited above 85% activity over a wide range of pH, between 5 to 8 with a maximum enzymatic activity at pH 7.0 (Fig. 3.4A). The pH stability analysis of *Ac*GH30A after 90 min incubation at 25°C showed that, the activity remained above 80% between pH 4.0 and 7.0 (Fig. 3.4B). At pH 8, the enzyme maintained 67% of activity, suggesting excellent flexibility with pH, which can be beneficial for various commercial applications. *Aa*Xyn30A, a fungal xylobiohydrolase purified from *Acremonium alcalophilum* showed similar optimum pH in the alkaline range, 7.5-10 (Šuchová et al., 2020). Other fungal xylanases, *Tt*Xyn30A (Nakamichi et al., 2020), *Sl*Xyn30A (Šuchová et al., 2022) and *Tc*Xyn30B (Katsimpouras et al., 2019) with auxiliary xylobiohydrolase activity showed optimum pH in the acidic range with pH 4.0, 3.5 and 5.0, respectively.

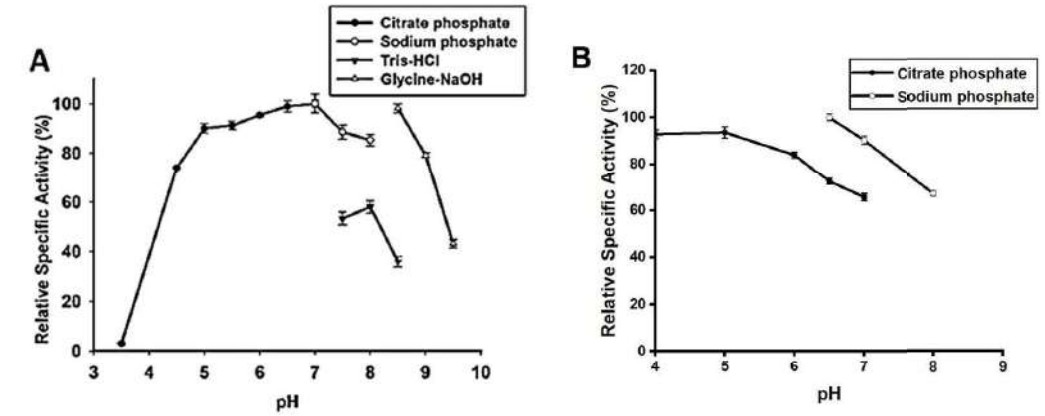

Fig. 3.4 Effect of pH on enzyme activity of *Ac*GH30A. (A) The optimum pH profile in different buffer systems (B) pH stability profile at different pH.

3.3.5 Determination of optimum temperature and thermal stability of *Ac*GH30A

Assays of *Ac*GH30A at different temperatures revealed its maximum activity at 80°C. *Ac*GH30A retained over 94% of its residual activity up to 85°C, thereafter it drastically decreased and showed ~30% activity at 100°C (Fig. 3.5A). This makes it an exceptionally superior bacterial thermophilic xylobiohydrolase characterized so far within the GH30 family. To the best of our knowledge, this is the first bacterial xylobiohydrolase from GH30 family showing optimum temperature as high as 80°C. The investigation of thermostability of *Ac*GH30A showed that it retained 77% of its residual activity at 70°C for 90 min (Fig. 3.5B). Crooks et al., (2021) reported the thermal properties of the catalytic module, *Ac*Xbh30A-CD of the full-length *Ac*Xbh30A xylobiohydrolase (named *Ac*GH30A in present study) displaying a similar pattern with optimum temperature of 73°C at pH 6.0 (four-component HPLC-compatible buffer). The optimum temperature and thermostability of *Ac*GH30A were much higher when compared with other GH30 family enzymes with xylobiohydrolase activity. A xylobiohydrolase, *Aa*Xyn30A from *Acremonium alcalophilum* exhibited optimum temperature within a range of 40 to 50 °C, giving maximum activity (Šuchová et al.,

2020). *Aa*Xyn30A displayed limited stability at 50 °C, retaining only 6% of its activity after 1 h incubation, whereas it maintained 68% of its activity at 40°C. *Tt*Xyn30A, a xylanase with auxiliary xylobiohydrolase activity isolated from *Thermothelomyces thermophila* showed highest enzyme activity at 50°C, but it experienced a rapid decline in activity at temperature above 55°C (Katsimpouras et al., 2019). Similarly, *Tc*Xyn30B (Nakamichi et al., 2019) from *Talaromyces cellulolyticus* and *Sl*Xyn30A (Šuchová et al., 2022) from *Sugiyamaella lignohabitans,* showed a decline in their activity after 50°C. The distinctive thermostability of *Ac*GH30A can be advantageous and favourable as compared with the other commercial xylobiohydrolases for a variety of biotechnological applications. The combination of *Ac*GH30A with thermophilic xylanases is advantageous, since *Ac*GH30A remains stable and active at elevated temperatures, thereby lowering the risk of microbial contamination, consistent with properties reported for other thermophilic enzymes (Collins et al., 2005). Furthermore, combining *Ac*GH30A with complementary enzymes, such as the thermostable β-glucanase reported by Zhang et al., which retains substantial activity after 30 min at temperatures above 70 °C, can improve the enzymatic hydrolysis of complex plant cell wall polysaccharides, thereby facilitating the production of biofuels and other value-added bioproducts (Zhang et al., 2023; Ajeje et al., 2021). A thermostable β-1,3-1,4-glucanase has been developed with high stability and activity at elevated temperatures, retaining significant activity after 30 minutes at temperatures above 70°C.

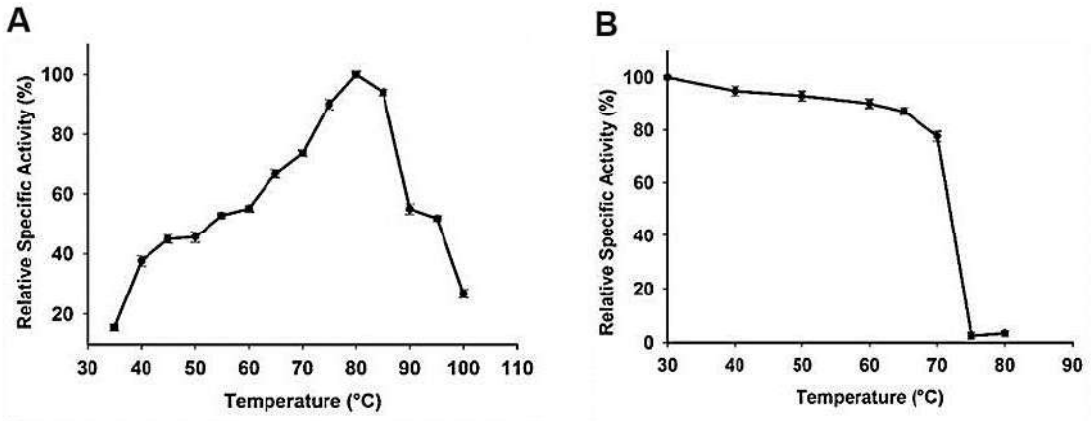

Fig. 3.5 Effect of temperature on enzyme activity of *Ac*GH30A. (A) The optimum temperature profile and (B) Thermo-stability profile of *Ac*GH30A. Enzyme assays were conducted with 100 µL reaction mixtures containing 10 µL of *Ac*GH30A (50 µg·mL^{-1}) and 2% (w/v) beechwood xylan in 50 mM sodium phosphate buffer (pH 7.0), and all reactions were performed in triplicate.

Thermal stability analysis of *Ac*GH30A, by measuring the changes observed in the CD spectrum with increasing temperature revealed that the secondary structure elements remained intact up to 70°C (Fig. 3.6A). However, secondary structure was partially unfolded at 75°C and completely denatured at 85°C. The melting temperature, T_m of *Ac*GH30A where the folded and unfolded state of protein is in 50:50 ratio, calculated by the CD data obtained at 222 nm was found to be ~72°C (Fig. 3.6B).

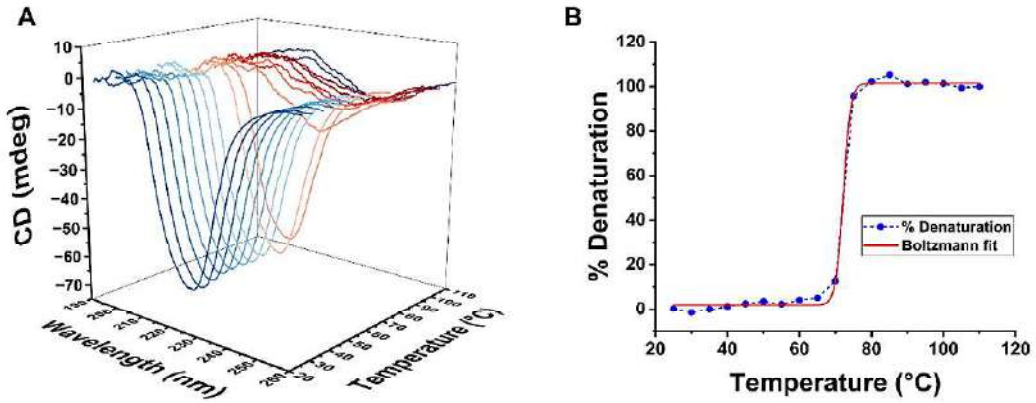

Fig. 3.6 Circular dichroism spectra of *Ac*GH30A (1.0 mg.mL^{-1}) in 50 mM sodium phosphate pH 7.0 (A) Circular dichroism spectra as a function of wavelength and temperature against temperature (B) Plot of percent (%) denaturation vs temperature for calculating melting temperature, T_m. CD data were obtained at wavelength 222 nm.

The half-life, $t_{1/2}$ of *Ac*GH30A were 1.75 h and 21 days at temperatures 70°C and 4°C, respectively. The $t_{1/2}$ of enzyme at 30°C and 60°C were 6.5 and 2 days, respectively (Fig. 3.7).

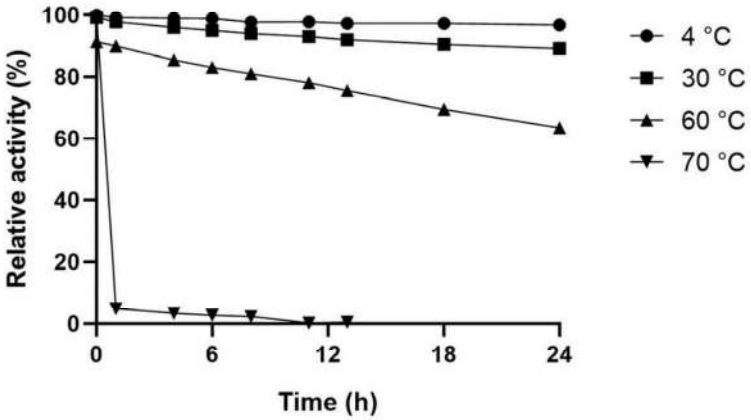

Fig. 3.7 Time course of inactivation of *Ac*GH30A at different temperatures 4, 30, 60 and 70°C. Plot of residual enzyme activity vs time. All the assays were performed at an optimum temperature of 80°C and optimum pH of 7.0 using 2% beechwood xylan as substrate.

3.3.6 Substrate specificity analysis of *Ac*GH30A

The enzyme activity of *Ac*GH30A against various natural substrates was investigated under optimum assay conditions. *Ac*GH30A displayed efficient hydrolysis of the xylan main-chain-based polysaccharides and showed a preference for glucuronoxylans as compared with arabinoxylans (Table 3.3). *Ac*GH30A demonstrated maximum specific activity of 136.2 $U.mg^{-1}$ against 4-O-Methyl glucuronoxylan followed by xylan M. W. 20000-30000 (130.4 $U.mg^{-1}$), beechwood xylan (126.2 $U.mg^{-1}$), Larchwood xylan (122.1 $U.mg^{-1}$) and other xylan substrates. It also showed a moderate activity of 52.3 $U.mg^{-1}$ towards oat spelt xylan. *Ac*GH30A showed limited specific activity against low viscosity (9.3 $U.mg^{-1}$) and insoluble (9.1 $U.mg^{-1}$) wheat arabinoxylan, followed by rye arabinoxylan (3.2 $U.mg^{-1}$) (Table 3.3). *Ac*GH30A gave much higher xylobiohydrolase activity against beechwood xylan containing 13%

glucuronic acid side chains as compared with the arabinoxylans where the percentage of arabinose side chains is much higher (37-39%) (Liab et al., 2000; Weng et al., 2023). *Ac*GH30A was not able to fully convert them to xylobiose due to the presence of side chain moieties. This suggest that the activity of *Ac*GH30A may potentially be improved by pre-treating xylan substrates with enzymes like β-glucuronidase and arabinofuranosidase, which can cleave the side chain components, glucuronic acid and arabinose residues, respectively. Consequently, this process would enhance the accessibility of the xylan backbone for *Ac*GH30A action.

In the case of the *in-house* xylan substrates, *Ac*GH30A showed higher activity of 77.3 $U.mg^{-1}$ with neem saw dust xylan (Sharma et al. 2020a) and 88.2 $U.mg^{-1}$ with acacia sawdust xylan (Sharma et al 2020b) and lower activity, 63.3 $U.mg^{-1}$ with xylan isolated from sugarcane tops and 26 $U.mg^{-1}$ with alkali pretreated sugarcane top (Khaire et al., 2021). Neem saw dust xylan and acacia sawdust xylan were reported to contain ~10.5% (w/w) and 15% (w/w) of glucuronic acid units, respectively. Neem saw dust xylan had lower glucuronic acid than acacia xylan, but showed lower activity which could be due to the differences in their solubility and the exact branching structure. Sugarcane tops xylan showed the presence of 16% (w/w) D-glucuronic acid and 10% (w/w) of L-arabinose residues (Khaire et al., 2021). Alkali pretreated sugarcane tops xylan contained 15% (w/w) D-glucuronic acid and 11% (w/w) L-arabinose residues (Khaire et al., 2022). 4-O-Methyl glucuronoxylan has a primary chain made up of β-(1→4)-linked D-xylopyranosyl units that contains varying number of 4-O-methyl α-D-glucuronic acid at the 2 position as side-chain substitutions, which are linked by α-(1→2) glycosidic bonds to the main chain (Barbat et al., 2008). The chemical composition and structure of natural xylan substrates, such as beechwood,

birchwood and larchwood xylan can vary slightly depending on the source and extraction method (Teleman et al., 2002). The general structure of these xylans is a linear polymer of xylose residues linked by (1→4) glycosidic bonds, with several xylose units substituted with groups like acetyl, glucuronic acid and 4-O-methyl glucuronic acid. Beechwood xylan is reported to have a ratio of monosaccharide composition of Xylose: Glucuronic Acid: Other sugars = 80.8: 11.4: 7.8 (Nieto-Domínguez et al., 2019). Overall, the structure of xylan substrates is characterized by a backbone of β-(1,4)-linked xylose residues, which are substituted with various side chains, making them important components of hemicellulosic plant cell wall polysaccharides. Arabinoxylans are also composed of a backbone chain made up of β-(1→4)-linked xylose residues with L-arabinofuranosyl residues as side chain substitutions linked with the main chain at positions 2 or 3 (He et al., 2021).

Xylanases of GH30 family are usually glucuronoxylanases, which require the presence of glucuronic acid substitutions for substrate recognition and their activity, but the capability of *Ac*GH30A to cleave arabinoxylans, a polysaccharide devoid of glucuronic acid, to produce xylobiose suggest that it does not require the presence of glucuronic acid moieties for its action. Similar broad substrate specificity of enzyme activity was also observed with other xylobiohydrolases from the GH30 family, such as *Aa*Xyn30A, which generated xylobiose as the main product from beechwood glucuronoxylan, rhodymenan and wheat arabinoxylan (Šuchová et al., 2020). Other GH30 family xylanases with auxiliary xylobiohydrolase activity from fungal origin, *Tt*Xyn30A (Katsimpouras et al., 2019) and *Sl*Xyn30A (Šuchová et al., 2022) also showed activity, preferably against glucuronoxylan followed by arabinoxylan. This result suggests that the activity of *Ac*GH30A resembles more to the fungal GH30

xylanases, which show broad substrate specificity, rather than with bacterial GH30 xylanases, which show activity only with glucuronoxylans. *Ac*GH30A also showed enzyme activity on various in-house xylan substrates, listed in Table 3.3.

Table 3.3 Substrate specificity of *Ac*GH30A from *Acetivibrio clariflavus.*

Substrate (2%, w/v)	**Specific activity (U.mg^{-1})**
4-O-Methyl glucuronoxylan (Sigma)	136.2 ± 0.6
Xylan, M.W. 20000-30000 (Carbosynth)	130.4 ± 1.1
Beechwood xylan (Megazyme)	126.2 ± 2.5
Larchwood xylan (Megazyme)	122.1 ± 3.2
Acacia sawdust xylan[a]	88.2 ± 1.4
Neem saw dust xylan[a]	77.3 ± 0.7
Sugarcane tops xylan[a]	63.3 ± 1.0
Banana stem xylan[a]	51.5 ± 2.2
Oat spelt xylan (Sigma)	52.3 ± 0.5
Alkali pretreated Sugarcane tops xylan[a]	26.0 ± 1.0
Wheat arabinoxylan, Low viscosity (Megazyme)	9.3 ± 0.3
Wheat arabinoxylan, insoluble (Megazyme)	9.1 ± 0.9
Water hyacinth xylan[a]	4.8 ± 0.9
Rye arabinoxylan (Megazyme)	3.2 ± 0.4
Birchwood Acetylated (Megazyme)	–
Xylan Corn Cob (Carbosynth)	–
Carboxy methyl cellulose (Sigma)	–

– No activity detected; [a] *in-house xylan substrates*
All the assays were performed at an optimum temperature of 80°C and optimum pH of 7.0 using 2% xylan substrate.

*Ac*GH30A showed no activity against the cellulosic substrates, a beneficial property needed for the extraction of cellulose fibres in the textile and paper processing industries by selectively degrading the xylan components of the plant biomass. These findings suggested that xylobiohydrolase, *Ac*GH30A can also contribute to the degumming of plant fibers used in textiles in combination with other enzymes, such as endoxylanases and pectinolytic enzymes (Bhalla et al., 2015; Chiliveri et al., 2016).

3.3.7 Kinetic parameters of *Ac*GH30A

The kinetic parameters of *Ac*GH30A were determined by using 4-O-methyl glucuronoxylan (Fig. 3.8A), xylan M.W. 20000-30000 (Fig. 3.8B) beechwood xylan (Fig. 3.8C) and larchwood xylan (Fig. 3.8D) as substrate at 80°C in 50 mM sodium phosphate buffer, pH 7.0. All the kinetic parameters obtained for the 4 substrates are mentioned in Table 3.4. Out of 4 substrates, 4-O-methyl glucuronoxylan gave maximum V_{max}, 139 (U.mg^{-1}) followed by xylan M.W. 20000-30000 (132 U.mg^{-1}), beechwood xylan (129 U.mg^{-1}), larchwood xylan (128 U.mg^{-1}) shown in Fig. 3.8 and Table 3.4. The reaction of *Ac*GH30A with 4-O-Methyl glucuronoxylan gave the turn over number (k_{cat}) 134.2 s^{-1} and catalytic efficiency (k_{cat}/K_M) 189.1 mL.mg^{-1}.s^{-1} (Table 3.4). However, Šuchová and colleagues (2021), reported a significantly lower k_{cat} value of 17.7 s^{-1} for *Hc*Xyn30A (named in present study as *Ac*GH30A) for beechwood 4-O-methylglucuronoxylan (GX) at 37°C in 50 mM sodium phosphate buffer pH 6.0. The k_{cat} value of *Ac*GH30A against GX found was much higher in our studies, which could be due to the analysis of kinetic parameters at optimum temperature, 80°C and optimum pH 7.0. A fungal xylobiohydrolase, *Aa*Xyn30A showed a V_{max}, 9.03 U.mg^{-1} and k_{cat} of 7.85 s^{-1} for 4-O-methylglucuronoxylan at 50ºC (Šuchová et al., 2020), which were also much lower than the reported values in the present study.

Table 3.4 Kinetic properties of *Ac*GH30A.

Substrate	**V_{max} (U.mg^{-1})**	**K_m (mg.ml^{-1})**	**k_{cat} (s^{-1})**	**k_{cat}/K_m (ml.mg^{-1}s^{-1})**
4-O-Methyl glucuronoxylan (Sigma, USA)	139 ± 6	0.71 ± 0.04	134.2 ± 3	189.1 ± 3.8
Xylan, M. W. 20000-30000 (Carbosynth, UK)	132 ± 3	0.49 ± 0.03	126.9 ± 2.2	259.1 ± 4.1
Beechwood xylan (Megazyme, Ireland)	129 ± 5	0.45 ± 0.05	124 ± 3	275.5 ± 3.7
Larchwood xylan (Megazyme, Ireland)	128 ± 6	0.41 ± 0.04	123.3 ± 4.2	301.1 ± 2.2

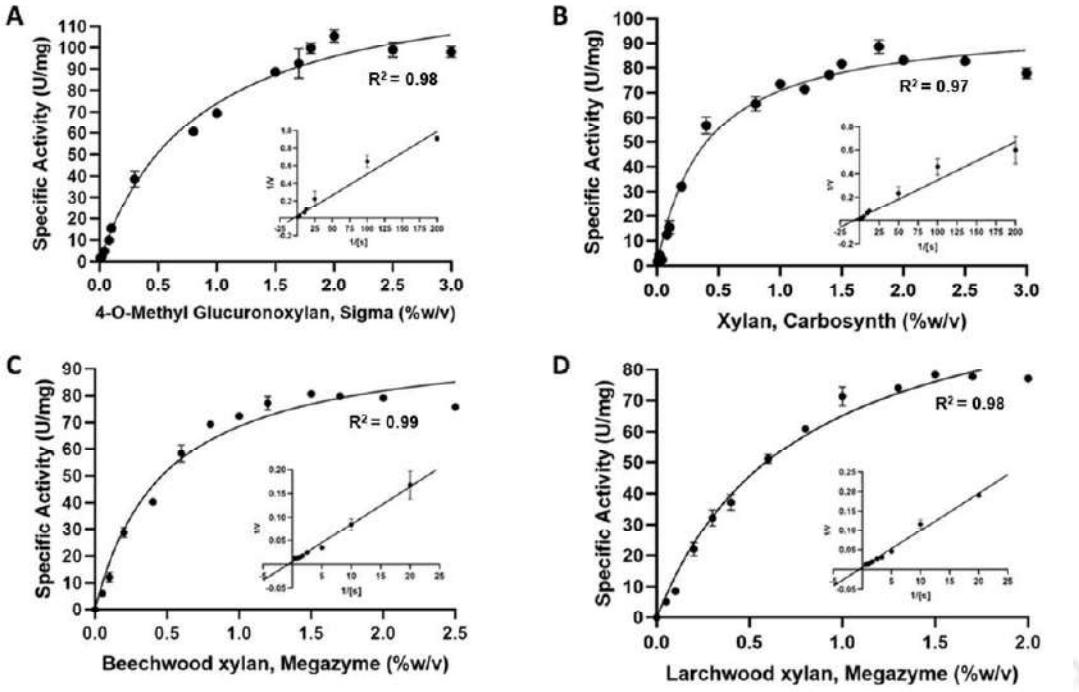

Fig. 3.8 Michaelis-Menten kinetics of AcGH30A against (A) 4-O-Methyl glucuronoxylan (Sigma-Aldrich, USA) (B) Xylan, M.W. 20000-30000 (Carbosynth Ltd., UK) (C) Beechwood xylan (Megazyme Ltd., Ireland) (D) Larchwood xylan (Megazyme Ltd., Ireland). The enzyme assays were conducted at pH of 7.0 and 80°C. The reaction mixtures contained of 10 µL of *Ac*GH30A (50 µg.mL^{-1}) and different concentrations of substrates dissolved in 90 µL of sodium-phosphate buffer (pH 7.0). The enzyme assays were conducted in triplicate. The inset graphs are Lineweaver-Burk plots of *Ac*GH30A with respective substrate.

Most xylobiohydrolases, such as *Sl*Xyn30A (Šuchová et al., 2022), *Tt*Xyn30A (Katsimpouras et al., 2019) and *Tc*Xyn30B (Nakamichi et al., 2019), reported to date are strongly bifunctional in nature having core endoxylanase activity. A GH30 glucuronoxylanase, *Sl*Xyn30A from *S. lignohabitans* with auxiliary xylobiohydrolase activity, showed V_{max}, 24.2 U.mg^{-1}, k_{cat} of 20.2 s^{-1} and k_{cat}/K_M of 1.2 mL.mg^{-1}.s^{-1} with glucuronoxylan (GX). Another bifunctional, glucuronoxylanase, *Tt*Xyn30A from *T. thermophila* displayed V_{max}, 24.3 U.mg^{-1}, k_{cat} of 7.21 s^{-1} and a catalytic efficiency k_{cat}/K_M of 4.24 mL.mg^{-1}.s^{-1} against beechwood glucuronoxylan, whereas, *Tc*Xyn30B

from *Talaromyces cellulolyticus* gave V_{max}, 7.1 U.mg^{-1}, k_{cat} of 20.9 s^{-1} and k_{cat}/K_M of 1.1 mL.mg^{-1}.s^{-1}, at their optimum assay conditions. Evidently, *Ac*GH30A showed the higher V_{max}, turnover number and catalytic efficiency against the natural xylan substrates as compared with the other xylobiohydrolases reported to date, with the observed differences also reflecting the influence of varying assay conditions on enzyme performance. A higher V_{max} of *Ac*GH30A will allow a faster conversion of substrate into product, which is crucial in various biotechnological processes. Enhanced turnover number and catalytic efficiency suggest that a smaller amount of enzyme is required to achieve the same level of substrate conversion compared to other reported enzymes.

3.3.8 Effects of metal ions and chemical agents on *Ac*GH30A activity

The enzyme activity of *Ac*GH30A was investigated in the presence of different metal ions and chemical agents at concentrations of 1 and 10 mM and outcomes were presented in Table 3.5. Ca^{2+} and Mg^{2+} ions enhanced the enzyme activity of *Ac*GH30A at both the concentrations of 1 and 10 mM. The enzyme activity of *Ac*GH30A at 10 mM concentration of Ca^{2+} and Mg^{2+} increased by 25% and 23%, respectively, whereas, Co^{2+}, Zn^{2+}, Fe^{2+} and Cu^{2+} ions, drastically reduced the enzyme activity. The decrease in enzymatic activity in the presence of heavy metal ions might be due to their interference with the amino acid residues at the active site. The chelating agents, EDTA, which can chelate a broad range of metal ions and EGTA, which has high affinity for calcium ions, effectively reduce the activity of xylanases that contain metal ions at their catalytic sites (Prakash et al., 2012). However, in the case of *Ac*GH30A, they showed no significant effect on the activity of the enzyme. It indicated that *Ac*GH30A does not necessarily require metal ions for its enzymatic activity.

Table 3.5 Effect of metal-ions and chelating agents on the activity of *Ac*GH30A.

Metal-ion/Reagent additive	Relative enzyme activity (%) of *Ac*GH30A	
	1 mM	10 mM
Control	100	100
Ca^{2+}	108.9 ± 1.5	125.1 ± 1.3
Mg^{2+}	116.7 ± 1.4	123.0 ± 1.7
Mn^{2+}	99.7 ± 1.4	103.0 ± 1.5
K^{+}	99.7 ± 2.3	92.3 ± 1.9
Ni^{2+}	104.8 ± 2.8	99.5 ± 2.4
Na^{+}	97.6 ± 3.2	96.0 ± 2.9
Co^{2+}	84.7 ± 1.6	79.0 ± 1.2
Fe^{2+}	91.5 ± 2.7	80.2 ± 2.2
Cu^{2+}	69.7 ± 1.6	66.9 ± 1.6
Zn^{2+}	73.1 ± 1.1	58.9 ± 1.3
EDTA	100.9 ± 2.5	99.2 ± 2.1
EGTA	99.5 ± 3.4	98.1 ± 3.3

3.3.9 Analysis of hydrolytic mechanism of *Ac*GH30A by TLC

The TLC chromatogram of enzyme hydrolyzed products released from different xylan substrates *viz.*, beechwood xylan, larchwood xylan, 4-O-methyl glucuronoxylan, rye arabinoxylan, wheat arabinoxylan and oat spelt xylan, by *Ac*GH30A displayed the presence of the same and only one product, xylobiose (Fig. 3.9). The low intensity spots of xylobiose produced from arabinoxylans and oat spelt xylan showed the low activity of *Ac*GH30A against these substrates.

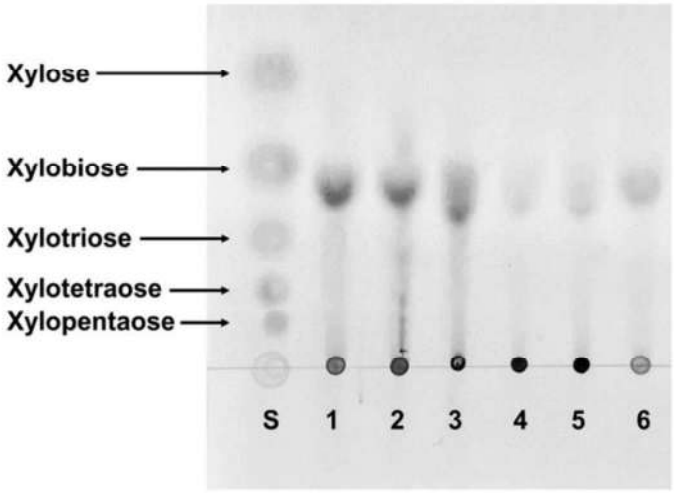

Fig. 3.9 Thin-layer chromatography (TLC) analysis with various xylan substrates. The reaction mixture (100 µL) contained 10 µL *Ac*GH30A (50 µg.mL^{-1}) and 0.5% (w/v) substrate dissolved in 50 mM sodium phosphate buffer (pH 7.0), incubated at 80°C for 2 min. Lane 1. Beechwood xylan, Lane 2. Larchwood xylan, Lane 3. 4-O-Methyl glucuronoxylan, Lane 4. Rye arabinoxylan, Lane 5. Wheat arabinoxylan and Lane 6. Oat spelt xylan with standards (Lane S) xylose, xylobiose, xylotriose, xylotetraose and xylopentaose.

The TLC chromatogram of time-dependent hydrolysis of beechwood xylan by *Ac*GH30A at 40°C also showed the release of the sole product, xylobiose (Fig. 3.10A). The time-dependent TLC analysis did not show the presence of any other hydrolyzed products as the incubation time progressed except the quantitative increase of the xylobiose amount (Fig. 3.10B). *Ac*GH30A produced 26 µg.mL^{-1} of reducing sugar from beechwood xylan at 1 min reaching up to 319 µg.mL^{-1} at 24 h incubation (Fig. 3.10B).

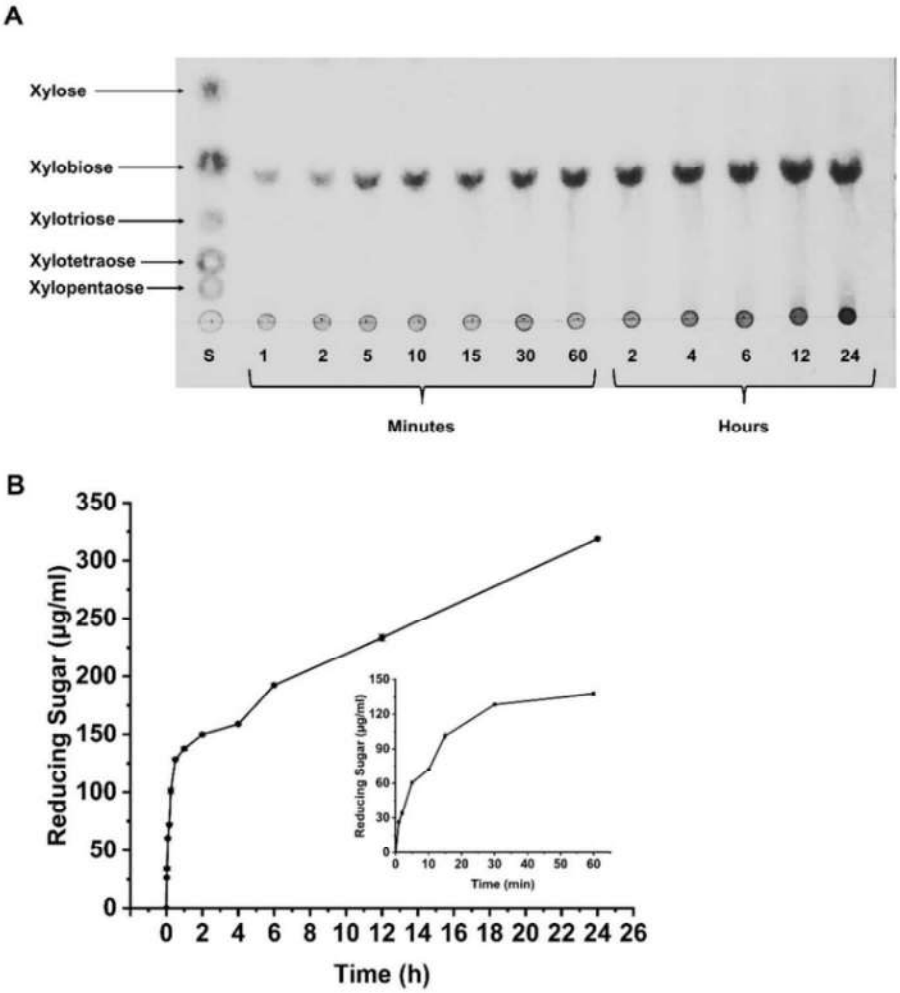

Fig. 3.10 Thin-layer chromatography (TLC) analysis of time-dependent hydrolysis of beechwood xylan (1%, w/v) at 40°C, pH 7.0 incubating with *Ac*GH30A for 1 min to 24 h. (A) TLC chromatogram. Standards (S) used were xylose, xylobiose, xylotriose, xylotetraose and xylopentaose and (B) Quantitative graph of reducing sugar produced with time by *Ac*GH30A at different time periods.

3.3.10 Explication of the hydrolytic mechanism of *Ac*GH30A by HPLC analysis

The hydrolyzed products of beechwood xylan by *Ac*GH30A analysed by HPLC showed a distinct peak at retention time, 35.8 min corresponding to xylobiose (Fig. 3.11). The HPLC profile of enzyme-hydrolyzed product was compared with those of control containing only substrate and the standard xylobiose (Fig. 3.11). The common peaks with retention times ~16.5 and ~13 min was observed in both the enzyme

hydrolysate and the control corresponding to undigested polysaccharide which were not detectable by TLC (Fig. 3.11). The HPLC results revealed the release of the only product, xylobiose from beechwood xylan by *Ac*GH30A. These results confirmed that *Ac*GH30A is an obligate xylobiohydrolase enzyme.

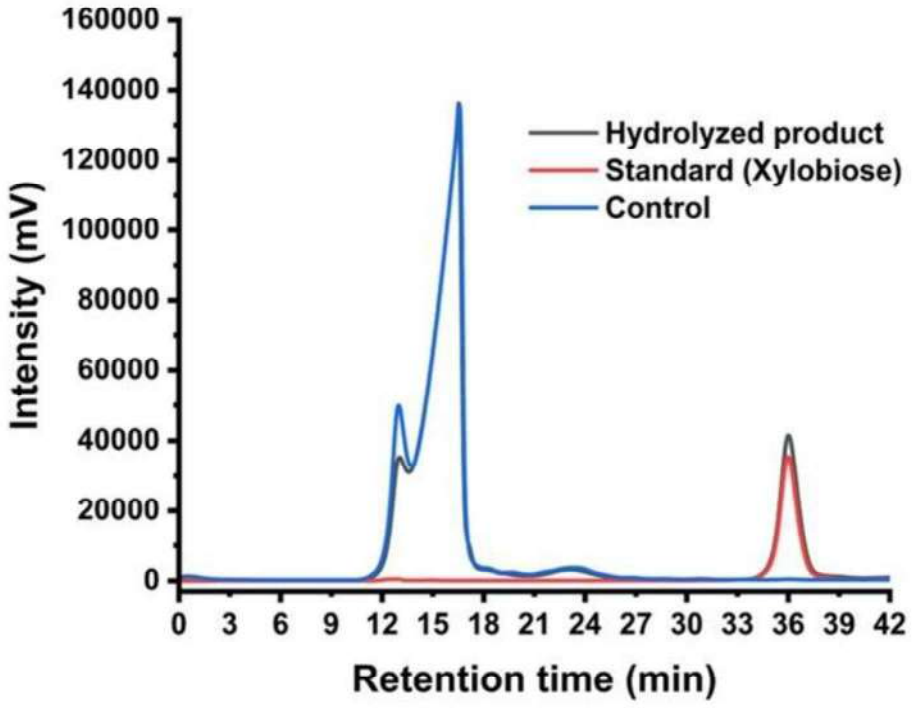

Fig. 3.11 HPLC analysis of *Ac*GH30A hydrolyzed products from beechwood xylan showing chromatogram of enzyme hydrolyzed product (in Black), control containing beechwood xylan without enzyme (in Blue) and standard xylobiose (in Red). The enzyme-substrate reaction was carried out using 100 µg.mL^{-1} of enzyme, *Ac*GH30A with 1% (w/v) beechwood xylan in 50 mM sodium phosphate buffer, pH 7.0 at 70°C for 60 min.

3.3.11 Analysis of hydrolysed products of *Ac*GH30A by LC-MS

The analysis of *Ac*GH30A hydrolyzed products of beechwood xylan by LCMS showed a single charge species at m/z 325.2 9 $[M+ACN+H]^+$ depicting the xylobiose (Fig. 3.12A), which corresponded to mass spectrum of standard xylobiose showing a single peak at m/z 305.0 $[M+Na]^+$ (Fig. 3.12B). LC-MS analysis confirmed that *Ac*GH30A releases xylobiose as the sole product from beechwood xylan. In contrast,

fungal xylobiohydrolases, such as *Aa*Xyn30A (Šuchová et al., 2020), *Tt*Xyn30A (Nakamichi et al., 2020), and *Tc*Xyn30B (Nakamichi et al., 2019), on hydrolyzing beechwood 4-O-methyl glucuronoxylan, produced xylobiose along with other xylo-oligosaccharides.

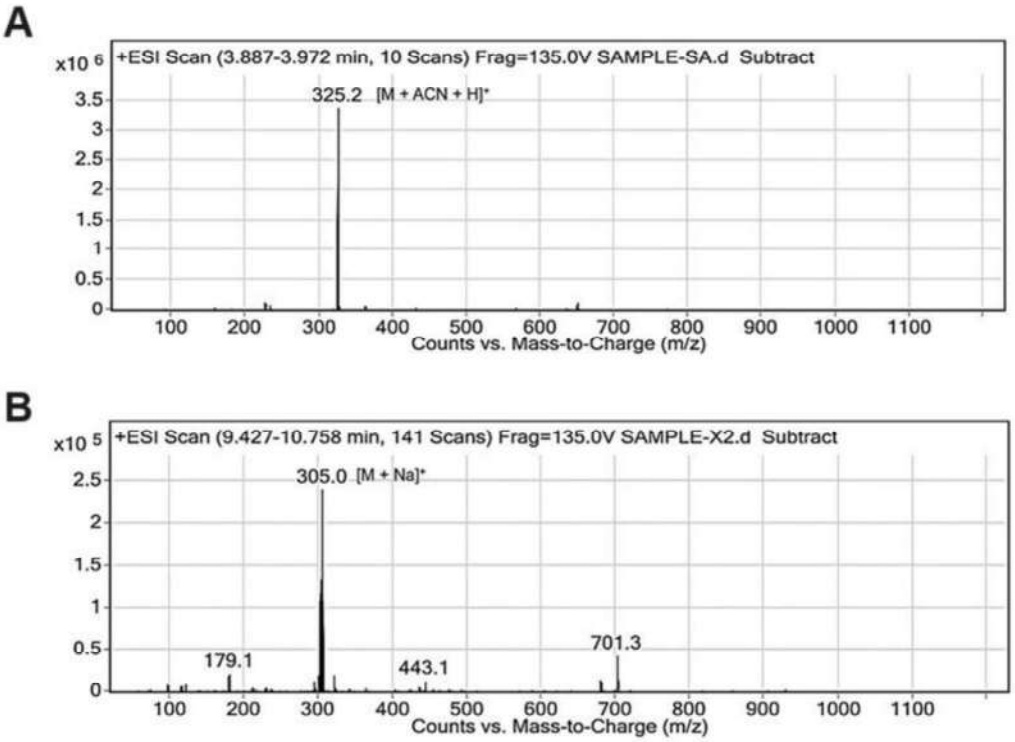

Fig. 3.12 (A) Positive ESI ion MS analysis of *Ac*GH30A hydrolyzed product from beechwood xylan and (B) Positive ESI ion MS analysis of xylobiose (Standard). The reaction was carried out using 100 µg.mL^{-1} of enzyme, *Ac*GH30A with 1% (w/v) beechwood xylan in 50 mM sodium phosphate buffer, pH 7.0 at 70°C for 60 min.

3.4 Conclusion

The recombinant enzyme, *Ac*GH30A expressed a soluble protein and after purification by IMAC followed by SEC showed a homogeneous single protein of molecular size, ~58 kDa on SDS-PAGE analysis. The total yield of enzyme activity of *Ac*GH30A after SEC purification was 72%. The enzyme, *Ac*GH30A displayed maximum activity against 4-O-methyl glucuronoxylan followed by xylan, beechwood xylan, larchwood xylan and other xylan substrates. *Ac*GH30A demonstrated thermophilic nature with an optimum temperature of 80°C, setting it apart as the first bacterial xylobiohydrolase from GH30 family with such an elevated optimum temperature. *Ac*GH30A displayed remarkable stability in a wide range of temperature and pH. The thermostability analysis of *Ac*GH30A showed 77% of residual activity at 70°C when incubated for 90 min. *Ac*GH30A showed an optimum of pH 7.0 and residual enzyme activity was above 85% in a wide pH range 5-8. The pH stability analysis of *Ac*GH30A showed above 80% of residual activity between pH 4.0 and 7.0 when incubated at 25°C for 90 min. These findings position *Ac*GH30A as a promising candidate for applications demanding high temperatures and flexibility with pH. Thermal stability analysis of *Ac*GH30A by circular dichroism (CD) spectroscopy, indicated that it retains secondary structure elements up to 70°C and displays complete loss of structure at 85°C. The T_m of *Ac*GH30A obtained from CD was found to be ~72°C. The half-life, $t_{1/2}$ of *Ac*GH30A at 70°C, 30°C and 4°C were 1.75 h, 6.5 days and 21 days, respectively. *Ac*GH30A with broad stability profiles can be applied in various industries, including biofuel production, food processing, textile manufacturing, and bioremediation, offering versatility and value across different sectors. *Ac*GH30A showed activity against various xylan polysaccharides displaying the highest V_{max}, 139

U.mg^{-1}, k_{cat}, 134.2 s^{-1} and K_M, 0.7 mg.ml^{-1} against 4-*O*-methyl glucuronoxylan under optimum conditions. The enzyme activity of *Ac*GH30A was enhanced by 10 mM Ca^{2+} and Mg^{2+} ions by 25% and 21%, respectively, whereas 10 mM Co^{2+}, Zn^{2+}, Fe^{2+}, and Cu^{2+} ions significantly reduced it. The analysis of *Ac*GH30A hydrolyzed products of beechwood xylan by TLC, HPLC and LC-MS revealed the release of only one product, xylobiose, confirming its obligate xylobiohydrolase activity. *Ac*GH30A is a novel bacterial enzyme displaying obligate xylobiohydrolase activity by orchestrating exclusive and sequential release of xylobiose from xylan polysaccharides. This study highlights the potential of *Ac*GH30A as an industrially valuable enzyme owing to its thermal and pH stability. Therefore, *Ac*GH30A can be used for commercial production of xylobiose and other value-added products from xylan polysaccharides or lignocellulosic biomasses.

References

1. Ajeje, S. B., Hu, Y., Song, G., Peter, S. B., Afful, R. G., Sun, F., Asadollahi, M. A., Amiri, H., Abdulkhani, A., & Sun, H. (2021). Thermostable cellulases / xylanases from thermophilic and hyperthermophilic microorganisms: Current perspective. *Frontiers in Bioengineering and Biotechnology*, *9*, 794304. https://doi.org/10.3389/fbioe.2021.794304
2. Artzi, L., Dassa, B., Borovok, I., Shamshoum, M., Lamed, R., & Bayer, E. A. (2014). Cellulosomics of the cellulolytic thermophile *Clostridium clariflavum*. *Biotechnology for Biofuels*, *7*(1), 100. https://doi.org/10.1186/1754-6834-7-100
3. Barbat, A., Gloaguen, V., Moine, C., Sainte-Catherine, O., Kraemer, M., Rogniaux, H., Ropartz, D., & Krausz, P. (2008). Structural characterization and cytotoxic properties of a 4-O-methylglucuronoxylan from *Castanea sativa*. 2. evidence of a structure-activity relationship. *Journal of Natural Products*, *71*(8), 1404–1409. https://doi.org/10.1021/np800207g
4. Bhalla, A., Bischoff, K. M., & Sani, R. K. (2015). Highly thermostable xylanase production from a thermophilic Geobacillus sp. Strain WSUCF1 utilizing lignocellulosic biomass. *Frontiers in Bioengineering and Biotechnology*, *3*. https://www.frontiersin.org/articles/10.3389/fbioe.2015.00084
5. Chadha, B. S., Kaur, B., Basotra, N., Tsang, A., & Pandey, A. (2019). Thermostable xylanases from thermophilic fungi and bacteria: Current perspective. *Bioresource Technology*, *277*, 195–203. https://doi.org/10.1016/j.biortech.2019.01.044
6. Chiliveri, S. R., Koti, S., & Linga, V. R. (2016). Retting and degumming of natural fibers by pectinolytic enzymes produced from *Bacillus tequilensis* SV11-UV37 using solid state fermentation. *SpringerPlus*, *5*, 559. https://doi.org/10.1186/s40064-016-2173-x
7. Collins, T., Gerday, C., & Feller, G. (2005). Xylanases, xylanase families and extremophilic xylanases. *FEMS Microbiology Reviews*, *29*(1), 3–23. https://doi.org/10.1016/j.femsre.2004.06.005
8. Crooks, C., Bechle, N. J., & St John, F. J. (2021). A new subfamily of glycoside hydrolase family 30 with strict xylobiohydrolase function. *Frontiers in Molecular Biosciences*, *8*. https://doi.org/10.3389/fmolb.2021.714238
9. Dassa, B., Borovok, I., Lamed, R., Henrissat, B., Coutinho, P., Hemme, C. L., Huang, Y., Zhou, J., & Bayer, E. A. (2012). Genome-wide analysis of *Acetivibrio cellulolyticus* provides a blueprint of an elaborate cellulosome system. *BMC Genomics*, *13*(1), 210. https://doi.org/10.1186/1471-2164-13-210
10. Dodd, D., & Cann, I. K. (2009). Enzymatic deconstruction of xylan for biofuel production. *Gcb Bioenergy*, *1*(1), 2–17. https://doi.org/10.1111/j.1757-1707.2009.01004.x
11. El Enshasy, H. A., Kandiyil, S. K., Malek, R., & Othman, N. Z. (2016). Microbial Xylanases: Sources, Types, and Their Applications. In V. K. Gupta (Ed.), *Microbial Enzymes in Bioconversions of Biomass* (Vol. 3, pp. 151–213). Springer International Publishing. https://doi.org/10.1007/978-3-319-43679-1_7

12. Espinoza, K., & Eyzaguirre, J. (2018). Identification, heterologous expression and characterization of a novel glycoside hydrolase family 30 xylanase from the fungus *Penicillium purpurogenum*. *Carbohydrate Research*, *468*, 45–50. https://doi.org/10.1016/j.carres.2018.08.006

13. Evangelista, D. E., de Oliveira Arnoldi Pellegrini, V., Santo, M. E., McQueen-Mason, S., Bruce, N. C., & Polikarpov, I. (2019). Biochemical characterization and low-resolution SAXS shape of a novel GH11 exo-1,4-β-xylanase identified in a microbial consortium. *Applied Microbiology and Biotechnology*, *103*(19), 8035–8049. https://doi.org/10.1007/s00253-019-10033-8

14. Fonseca-Maldonado, R., Ribeiro, L. F., Furtado, G. P., Arruda, L. M., Meleiro, L. P., Alponti, J. S., Botelho-Machado, C., Vieira, D. S., Bonneil, E., & Furriel, R. dos P. M. (2014). Synergistic action of co-expressed xylanase/laccase mixtures against milled sugar cane bagasse. *Process Biochemistry*, *49*(7), 1152–1161. https://doi.org/10.1016/j.procbio.2014.03.027

15. Froger, A., & Hall, J. E. (2007). Transformation of plasmid DNA into *E. coli* using the heat shock method. *Journal of Visualized Experiments: JoVE, 6*, 253. https://doi.org/10.3791/253

16. Garg, S. (2016). Xylanase: applications in biofuel production. *Current Metabolomics*, *4*(1), 23–37. https://doi.org/10.2174/2213235X03666150915211224

17. Ghosh, M., & Nanda, G. (1994). Purification and some properties of a xylanase from *Aspergillus sydowii* MG49. *Applied and Environmental Microbiology*, *60*(12), 4620–4623. https://doi.org/10.1128/aem.60.12.4620-4623.1994

18. Guo, Y., Gao, Z., Xu, J., Chang, S., Wu, B., & He, B. (2018). A family 30 glucurono-xylanase from *Bacillus subtilis* LC9: Expression, characterization and its application in Chinese bread making. *International Journal of Biological Macromolecules*, 117, 377–384. https://doi.org/10.1016/j.ijbiomac.2018.05.143

19. Han, J.-A., & Lim, S.-T. (2004). Structural changes of corn starches by heating and stirring in DMSO measured by SEC-MALLS-RI system. *Carbohydrate Polymers*, *55*(3), 265–272. https://doi.org/10.1016/j.carbpol.2003.09.007

20. He, J., Su, L., Sun, X., Fu, J., Chen, J., & Wu, J. (2014). A novel xylanase from Streptomyces sp. FA1: Purification, characterization, identification and heterologous expression. *Biotechnology and Bioprocess Engineering*, *19*(1), 8–17. https://doi.org/10.1007/s12257-013-0490-2

21. He, H.-J., Qiao, J., Liu, Y., Guo, Q., Ou, X., & Wang, X. (2021). Isolation, structural, functional, and bioactive properties of cereal arabinoxylan -A critical review. *Journal of Agricultural and Food Chemistry*, *69*(51), 15437–15457. https://doi.org/10.1021/acs.jafc.1c04506

22. Izquierdo, J. A., Pattathil, S., Guseva, A., Hahn, M. G., & Lynd, L. R. (2014). Comparative analysis of the ability of *Clostridium clariflavum* strains and *Clostridium thermocellum* to utilize hemicellulose and unpretreated plant material. *Biotechnology for Biofuels*, *7*(1), 136. https://doi.org/10.1186/s13068-014-0136-4

23. Jamaldheen, S. B., Thakur, A., Moholkar, V. S., & Goyal, A. (2019). Enzymatic hydrolysis of hemicellulose from pretreated Finger millet (*Eleusine coracana*) straw by recombinant endo-1,4-β-xylanase and exo-1,4-β-xylosidase. *International Journal of Biological Macromolecules*, 135, 1098–1106. https://doi.org/10.1016/j.ijbiomac.2019.06.010

24. Juturu, V., & Wu, J. C. (2012). Microbial xylanases: Engineering, production and industrial applications. *Biotechnology Advances*, *30*(6), 1219–1227. https://doi.org/10.1016/j.biotechadv.2011.11.006

25. Katsimpouras, C., Dedes, G., Thomaidis, N. S., & Topakas, E. (2019). A novel fungal GH30 xylanase with xylobiohydrolase auxiliary activity. *Biotechnology for Biofuels*, *12*(1), 1-14. https://doi.org/10.1186/s13068-019-1455-2

26. Kaur, P., Bhardwaj, N. K., & Sharma, J. (2016). Pretreatment with xylanase and its significance in hemicellulose removal from mixed hardwood kraft pulp as a process step for viscose. *Carbohydrate Polymers*, 145, 95–102. https://doi.org/10.1016/j.carbpol.2016.03.023

27. Khaire, K. C., Moholkar, V. S., & Goyal, A. (2022). A biorefinery approach for sequential extraction of commercial grade xylan and alkali lignin from alkali pretreated sugarcane tops hydrolysate. *Industrial Crops and Products*, *187*, 115545. https://doi.org/10.1016/j.indcrop.2022.115545

28. Khaire, K. C., Sharma, K., Thakur, A., Moholkar, V. S., & Goyal, A. (2021). Extraction and characterization of xylan from sugarcane tops as a potential commercial substrate. *Journal of Bioscience and Bioengineering*, *131*(6), 647–654. https://doi.org/10.1016/j.jbiosc.2021.01.009

29. Kubata, B. K., Suzuki, T., Horitsu, H., Kawai, K., & Takamizawa, K. (1994). Purification and characterization of Aeromonas caviae ME-1 Xylanase V, which produces exclusively xylobiose from xylan. *Applied and Environmental Microbiology*, *60*(2), 531–535. https://doi.org/10.1128/aem.60.2.531-535.1994

30. Kumar, V., Marín-Navarro, J., & Shukla, P. (2016). Thermostable microbial xylanases for pulp and paper industries: Trends, applications and further perspectives. *World Journal of Microbiology and Biotechnology*, *32*(2), 34. https://doi.org/10.1007/s11274-015-2005-0

31. Laemmli, U. K. (1970). Cleavage of structural proteins during the assembly of the head of bacteriophage T4. *Nature*, *227*(5259), 680–685. https://doi.org/10.1038/227680a0

32. Lamed, R., & Bayer, E. A. (1988). The Cellulosome of *Clostridium thermocellum*. In A. I. Laskin (Ed.), *Advances in Applied Microbiology* (Vol. 33, pp. 1–46). Academic Press. https://doi.org/10.1016/S0065-2164(08)70203-X

33. Liab, K., Azadi, P., Collins, R., Tolan, J., Kim, J. S., & Eriksson, K. L. (2000). Relationships between activities of xylanases and xylan structures. *Enzyme and Microbial Technology*, *27*(1), 89–94. https://doi.org/10.1016/S0141-0229(00)00190-3

34. Lowry, O. H., Rosebrough, N. J., Farr, A. L., & Randall, R. J. (1951). Protein measurement with the Folin phenol reagent. *Journal of Biological Chemistry*, *193*(1), 265-275.

35. Luo, H., Yang, J., Li, J., Shi, P., Huang, H., Bai, Y., Fan, Y., & Yao, B. (2010). Molecular cloning and characterization of the novel acidic xylanase XYLD from Bispora sp. MEY-1 that is homologous to family 30 glycosyl hydrolases. *Applied Microbiology and Biotechnology*, *86*(6), 1829–1839. https://doi.org/10.1007/s00253-009-2410-0

36. Maehara, T., Yagi, H., Sato, T., Ohnishi-Kameyama, M., Fujimoto, Z., Kamino, K., Kitamura, Y., St John, F., Yaoi, K., & Kaneko, S. (2018). GH30 glucuronoxylan-specific xylanase from *Streptomyces turgidiscabies* C56. *Applied and Environmental Microbiology*, *84*(4), e01850-17. https://doi.org/10.1128/AEM.01850-17

37. Manisseri, C., & Gudipati, M. (2012). Prebiotic activity of purified xylobiose obtained from ragi (*Eleusine coracana*, Indaf-15) bran. *Indian Journal of Microbiology*, *52*(2), 251–257. https://doi.org/10.1007/s12088-011-0176-4

38. Mello, B. L., Alessi, A. M., Riaño-Pachón, D. M., deAzevedo, E. R., Guimarães, F. E. G., Espirito Santo, M. C., McQueen-Mason, S., Bruce, N. C., & Polikarpov, I. (2017). Targeted metatranscriptomics of compost-derived consortia reveals a GH11 exerting an unusual exo-1,4-β-xylanase activity. *Biotechnology for Biofuels*, *10*(1), 254. https://doi.org/10.1186/s13068-017-0944-4

39. Moreira, L. R. S., & Filho, E. X. F. (2016). Insights into the mechanism of enzymatic hydrolysis of xylan. *Applied Microbiology and Biotechnology*, *100*(12), 5205–5214. https://doi.org/10.1007/s00253-016-7555-z

40. Nakamichi, Y., Fouquet, T., Ito, S., Watanabe, M., Matsushika, A., & Inoue, H. (2019). Structural and functional characterization of a bifunctional GH30-7 xylanase B from the filamentous fungus *Talaromyces cellulolyticus*. *Journal of Biological Chemistry*, *294*(11), 4065–4078. https://doi.org/10.1074/jbc.RA118.007207

41. Nakamichi, Y., Watanabe, M., Matsushika, A., & Inoue, H. (2020). Substrate recognition by a bifunctional GH30-7 xylanase B from *Talaromyces cellulolyticus*. *FEBS Open Bio*, *10*(6), 1180–1189. https://doi.org/10.1002/2211-5463.12873

42. Nelson, N. (1944). A photometric adaptation of the Somogyi method for the determination of glucose. *Journal of Biological Chemistry*, *153*(2), 375–380. https://doi.org/10.1016/S0021-9258(18)71980-7

43. Nieto-Domínguez, M., Martínez-Fernández, J. A., de Toro, B. F., Méndez-Líter, J. A., Cañada, F. J., Prieto, A., de Eugenio, L. I., & Martínez, M. J. (2019). Exploiting xylan as sugar donor for the synthesis of an antiproliferative xyloside using an enzyme cascade. *Microbial Cell Factories*, *18*(1), 174. https://doi.org/10.1186/s12934-019-1223-9

44. Prakash, B., Vidyasagar, M., Jayalakshmi, S. K., & Sreeramulu, K. (2012). Purification and some properties of low-molecular-weight extreme halophilic

xylanase from *Chromohalobacter sp*. TPSV 101. *Journal of Molecular Catalysis B: Enzymatic*, *74*(3), 192–198. https://doi.org/10.1016/j.molcatb.2011.10.004

45. Puchart, V., Šuchová, K., & Biely, P. (2021). Xylanases of glycoside hydrolase family 30–An overview. *Biotechnology Advances*, 107704. https://doi.org/10.1016/j.biotechadv.2021.107704

46. Ruíz, I., Gómez, J. A., & García, L. (2022). Use of Circular Dichroism in the characterization of the fusion protein SARS-CoV-2 S protein (RBD)-hFc. *Pure and Applied Chemistry*, *94*(7), 829–838. https://doi.org/10.1515/pac-2021-1014

47. Sárossy, Z., Tenkanen, M., Pitkänen, L., Bjerre, A.-B., & Plackett, D. (2013). Extraction and chemical characterization of rye arabinoxylan and the effect of β-glucan on the mechanical and barrier properties of cast arabinoxylan films. *Food Hydrocolloids*, *30*(1), 206–216. https://doi.org/10.1016/j.foodhyd.2012.05.022

48. Sepulchro, A. G. V., Pellegrini, V. O. A., Briganti, L., de Araujo, E. A., de Araujo, S. S., & Polikarpov, I. (2020). Transformation of xylan into value-added biocommodities using *Thermobacillus composti* GH10 xylanase. *Carbohydrate Polymers*, 247, 116714. https://doi.org/10.1016/j.carbpol.2020.116714

49. Sharma, K., Morla, S., Khaire, K. C., Thakur, A., Moholkar, V. S., Kumar, S., & Goyal, A. (2020a). Extraction, characterization of xylan from *Azadirachta indica* (neem) sawdust and production of antiproliferative xylooligosaccharides. *International Journal of Biological Macromolecules*, *163*, 1897–1907. https://doi.org/10.1016/j.ijbiomac.2020.09.086

50. Sharma, K., Khaire, K. C., Thakur, A., Moholkar, V. S., & Goyal, A. (2020b). Acacia xylan as a substitute for commercially available xylan and its application in the production of xylooligosaccharides. *ACS Omega*, *5*(23), 13729–13738. https://doi.org/10.1021/acsomega.0c00896

51. Shiratori, H., Ikeno, H., Ayame, S., Kataoka, N., Miya, A., Hosono, K., Beppu, T., & Ueda, K. (2006). Isolation and characterization of a new *Clostridium sp.* That performs effective cellulosic waste digestion in a thermophilic methanogenic bioreactor. *Applied and Environmental Microbiology, 72*(5), 3702–3709. https://doi.org/10.1128/AEM.72.5.3702-3709.2006

52. Shiratori, H., Sasaya, K., Ohiwa, H., Ikeno, H., Ayame, S., Kataoka, N., Miya, A., Beppu, T., & Ueda, K. (2009). *Clostridium clariflavum sp. Nov. and Clostridium caenicola sp. Nov.*, moderately thermophilic, cellulose-/cellobiose-digesting bacteria isolated from methanogenic sludge. *International Journal of Systematic and Evolutionary Microbiology, 59*(7), 1764–1770. https://doi.org/10.1099/ijs.0.003483-0

53. Simmons, T. J., Mortimer, J. C., Bernardinelli, O. D., Pöppler, A.-C., Brown, S. P., deAzevedo, E. R., Dupree, R., & Dupree, P. (2016). Folding of xylan onto cellulose fibrils in plant cell walls revealed by solid-state NMR. *Nature Communications*, *7*(1), Article 1. https://doi.org/10.1038/ncomms13902

54. Somogyi, M. (1945). A new reagent for the determination of sugars. *Journal of Biological Chemistry, 160(*1), 61–68. https://doi.org/10.1016/s0021-9258(18)43097-9

55. Šuchová, K., Chyba, A., Hegyi, Z., Rebroš, M., & Puchart, V. (2022). Yeast GH30 xylanase from *Sugiyamaella lignohabitans* is a glucuronoxylanase with auxiliary xylobiohydrolase activity. *Molecules, 27*(3), Article 3. https://doi.org/10.3390/molecules27030751

56. Šuchová, K., Puchart, V., & Biely, P. (2021). A novel bacterial GH30 xylobiohydrolase from *Hungateiclostridium clariflavum*. *Applied Microbiology and Biotechnology, 105*(1), 185–195. https://doi.org/10.1007/s00253-020-11023-x

57. Šuchová, K., Puchart, V., Spodsberg, N., Mørkeberg Krogh, K. B. R., & Biely, P. (2020). A novel GH30 xylobiohydrolase from Acremonium alcalophilum releasing xylobiose from the non-reducing end. *Enzyme and Microbial Technology,* 134, 109484. https://doi.org/10.1016/j.enzmictec.2019.109484

58. Šuchová, K., Puchart, V., Spodsberg, N., Mørkeberg Krogh, K. B. R., & Biely, P. (2021). Catalytic diversity of GH30 Xylanases. *Molecules*, *26*(15), Article 15. https://doi.org/10.3390/molecules26154528

59. Swift, M. L. (1997). GraphPad Prism, Data Analysis, and Scientific Graphing. *Journal of Chemical Information and Computer Sciences, 37*(2), 411–412. https://doi.org/10.1021/ci960402j

60. Teleman, A., Tenkanen, M., Jacobs, A., & Dahlman, O. (2002). Characterization of O-acetyl-(4-O-methylglucurono) xylan isolated from birch and beech. *Carbohydrate Research*, *337*(4), 373–377. https://doi.org/10.1016/S0008-6215(01)00327-5

61. Valls, C., Vidal, T., Gallardo, O., Diaz, P., Javier Pastor, F. I., & Blanca Roncero, M. (2010). Obtaining low-HexA-content cellulose from eucalypt fibres: Which glycosyl hydrolase family is more efficient? *Carbohydrate Polymers, 80*(1), 154–160. https://doi.org/10.1016/j.carbpol.2009.11.006

62. Verma, A. K., & Goyal, A. (2016). A novel member of family 30 glycoside hydrolase subfamily 8 glucuronoxylan endo-β-1, 4-xylanase (*Ct*XynGH30) from *Clostridium thermocellum* orchestrates catalysis on arabinose decorated xylans. *Journal of Molecular Catalysis B: Enzymatic*, *129*, 6–14.

63. Wang, R., Liu, Z., Cheng, L., Duan, S., Feng, X., Zheng, K., Cheng, Y., & Zeng, J. (2019). A novel endo-β-1,4-xylanase GH30 from *Dickeya dadantii* DCE-01: Clone, expression, characterization, and ramie biological degumming function. *Textile Research Journal, 89*(4), 463–472. https://doi.org/10.1177/0040517517748511

64. Weng, V., Cardeira, M., Bento-Silva, A., Serra, A. T., Brazinha, C., & Bronze, M. R. (2023). Arabinoxylan from corn fiber obtained through alkaline extraction and membrane purification: Relating bioactivities with the phenolic compounds. *Molecules*, *28*(15), Article 15. https://doi.org/10.3390/molecules2815562

Chapter 4

Small angle X-ray scattering and *in silico* based structure and function analysis of xylobiohydrolase (*Ac*GH30A) from *Acetivibrio clariflavus*

4.1 Introduction

Xylans are the second most abundant polymer present in the plant kingdom. They are the primary component of the hemicellulose present in plants (Fonseca-Maldonado et al., 2014; He et al., 2014). Structurally, they are heteropolysaccharides in which the backbone is composed of xylose monomers linked by β-1,4-glycosidic linkages (Curry et al., 2023). The main chain is decorated with a diverse group of side-chain moieties *viz*., glucuronic acid, arabinose, *p*-coumaric acid and ferulic acid (Thakur et al., 2019). Xylans are structurally very diverse and their structures differ based on the species, the specific part and the age of the plant. Xylans hold great potential to be used for various industrial purposes as a renewable source of energy and chemicals. To harness the energy and chemicals from xylan, they are required to be broken down into simpler forms *viz.* oligosaccharides and monosaccharides. The degradation process of xylans is complex and its degradation can be achieved by

physical process like pyrolysis or enzymatic hydrolysis by using xylanases. The enzymatic breakdown of xylan requires a combined and systematic action of several xylanolytic and auxiliary enzymes. These auxiliary enzymes are acetyl xylan esterase, α-arabinofuranosidase, feruloyl esterase, xylan methylesterase and β-glucuronidase (Moreira, 2016). The enzymatic degradation process is preferable owing to its environment friendly nature (Juturu & Wu, 2012).

Glycoside hydrolases (GH) constitute a large category of enzymes responsible for catalyzing the hydrolytic cleavage of glycosidic linkages present in complex carbohydrates (Henrissat & Davies, 1997; Vuong & Wilson, 2010). Xylanases are a class of enzymes comprising β-(1→4)-endo xylanase, β-(1→4)- xylobiohydrolase and β-(1→4)-xylosidase which are involved in complete breakdown of xylan into xylose monomers (Collins et al., 2005). Xylanases specifically target xylan, recognizing the β-1,4-glycosidic bonds between the xylose units in the xylan polymer. β-(1→4)-Endo xylanase hydrolyses xylan into xylooligosaccharides (XOS) which are short chains of xylose units linked by β-1,4-glycosidic bonds (El Enshasy et al., 2016). β-(1→4)-Xylobiohydrolase acts on xylan polysaccharides or XOS and releases xylobiose units (Kadowaki et al., 2021; Katsimpouras et al., 2019). β-(1→4)-Xylosidase utilizes, xylan, XOS or xylobiose as substrates cleaving the xylose units from the non-reducing end (Rohman et al., 2019). β-Xylanase and β-xylosidase from various glycoside hydrolase families have been reported, while xylobiohydrolase has been reported from only the GH30 family (Puchart et al., 2021; Šuchová et al., 2021). The catalytic mechanism of xylobiohydrolase involves the nucleophilic attack of a catalytic residue (usually a glutamate or aspartate) on the glycosidic bond, leading to its cleavage (Puchart et al., 2021; Šuchová et al., 2020, 2021, 2022). The GH30 family contains xylanases primarily

targeting glucuronoxylan. The family GH30 exclusively included xylobiohydrolases which are exo-acting enzymes, releasing xylobiose units from the non-reducing ends of xylan chains or XOS (Puchart et al., 2021).

The documented enzymes exhibiting xylobiohydrolase activity till date have been only from fungal origin. Two glucuronoxylanases from GH30 family, *Tc*Xyn30B (Nakamichi et al., 2020) and *Tt*Xyn30A (Nikolaivits et al., 2021) from *Talaromyces cellulolyticus* and *Thermothelomyces thermophila*, respectively have been found to release xylobiose from the non-reducing end of xylan substrates, along with their endoxylanase activity. However, both displayed different levels of endo- and exo-activities. In the case of *Tc*Xyn30B, the xylobiohydrolase activity was more significant than its endo-glucuronoxylanase activity, whereas *Tt*Xyn30A exhibits both modes of action at approximately equal levels. Recently, another similar glucuronoxylanase, *Sl*Xyn30A from yeast *Sugiyamaella lignohabitans* displaying xylobiohydrolase activity was reported (Šuchová et al., 2022). The most stringent xylobiohydrolase, *Aa*Xyn30A was reported from a cellulolytic fungus *Acremonium alcalophilum* (Šuchová et al., 2020). Numerous glycoside hydrolases from clan A of the GH30 family following the retaining-type of reaction mechanism share a common structural feature. They contain TIM barrel as a standard structural feature with a pair of aspartic or glutamic acid residues in the catalytic cleft primarily formed by β-α loops, participating in the catalysis (Henrissat et al., 1995; Puchart et al., 2021).

Acetivibrio clariflavus is a thermophilic, anaerobic, gram-positive, spore-forming bacterium. The whole genome of *C. clariflavum* has been sequenced and several enzymes produced by it have been characterized. Exploring new and novel enzymes from this microorganism may help current methodologies by improving the

efficacy of lignocellulosic materials breakdown. Out of various candidate organisms for thermophilic consolidated bioprocessing (Chen et al., 2018; Gao et al., 2020), *Acetivibrio clariflavus* has attained little attention as compared with the model cellulolytic thermophile *Clostridium thermocellum*, which has been extensively studied in the last decade (Verma & Goyal, 2016). A gene encoding a family GH30 enzyme from *Acetivibrio clariflavus* was identified and designated as *Ac*GH30A. *Ac*GH30A is a xylobiohydrolase of family 30 of glycoside hydrolases belonging to the cellulosomal complex from *Acetivibrio clariflavus*. The gene encoding *Ac*GH30A containing a GH30 family catalytic module and a dockerin 1 was cloned, expressed, and biochemically characterized in previous chapters.

In the current study, the structure and functional characteristics of xylobiohydrolase, *Ac*GH30A were explored by *in silico* and small-angle x-ray scattering (SAXS) approaches. The molecular structure of *Ac*GH30A using its amino acid sequence by homology modeling was generated and validated. Molecular dynamics (MD) simulation of *Ac*GH30A model was conducted to evaluate the stability and structural characteristics. Molecular docking studies with ligands were performed to assess the catalytic mechanism and the amino acid residues involved in ligand binding. The docked complex of *Ac*GH30A with the ligand was analysed by MD simulation to detect the structural changes after the ligand binding. The solution structure characteristics of *Ac*GH30A was investigated by small angle X-ray scattering (SAXS) and dynamic light scattering (DLS). During the present study of the enzyme, *Ac*GH30A, St John et al., (2022) reported the crystal structure of the catalytic module (named as *Ac*Xbh30A) of the full length xylobiohydrolase, *Ac*GH30A. While there are certain similarities in the results, our report provides more valuable information

regarding the solution structure characteristics of the full-length xylobiohydrolase, *Ac*GH30A, containing the additional Dockerin 1 domain at C-terminal. The structure analyses of *Ac*GH30A by computational methods also provided the detailed understanding of ligand binding and perfect matching of the modeled structure with its solution structure by SAXS.

4.2 Materials and Methods

4.2.1 Analysis of amino acid sequence and expression of *Ac*GH30A

The amino acid sequence of a xylobiohydrolase belonging to family 30 glycoside hydrolase here named *Ac*GH30A (514 aa) from bacterium *Acetivibrio clariflavus* ATCC 19732 (Uniprot id: G8LU16), was obtained from NCBI database (https://www.ncbi.nlm.nih.gov/protein/AEV68404.1). The locus tag and GenBank accession number are Clocl_1795 and AEV68404.1. The physicochemical parameters of *Ac*GH30A, such as theoretical molecular weight and isoelectric point, were calculated by the protparam server (https://web.expasy.org/protparam/) (Gasteiger et al., 2005). The identification of the sequences responsible for the constituent domains of *Ac*GH30A was accomplished by entering the sequence in the conserved domain database (http://www.ncbi.nlm.nih.gov/cdd/) provided by National Center for Biotechnology Information and using the Interproscan (http://www.ebi.ac.uk/interpro/) server (Jones et al., 2014). The *Ac*GH30A amino acid sequence was checked for the signal peptide sequences by using the PSignal (http://www.cbs.dtu.dk/services/SignalP-3.0) server. The domains present in *Ac*GH30A sequence were outlined and illustrated using DOG 2.0 software (Ren et al., 2009). To compare and obtain the similarity index with the homologous proteins, the PSI-BLAST program was performed using the amino acid sequence of *Ac*GH30A against the PDB database. Multiple sequence alignment (MSA) of *Ac*GH30A was performed with homologous protein sequences with reported structures, obtained after PSI-BLAST, to examine its conserved sequences, semi-conserved and catalytic amino acid residues. The amino acid sequences of *Ac*GH30A homologs were obtained from the Uniprot database (http://www.uniprot.org) and incorporated into MSA analysis.

Sequence alignment was carried out using the Clustal Omega tool (http://www.ebi.ac.uk/Tools/msa/clustalo/), provided by EMBL-EBI services (Madeira et al., 2022). The alignment results were visualized using ESPript 3.0 (http://espript.ibcp.fr/ESPript/ESPript/) (Robert & Gouet, 2014).

The homologs of *Ac*GH30A, identified through PSI-BLAST were *Ca*Xyn30A (Uniprot ID: Q97TI2; PDB ID: 5CXP) from *Clostridium acetobutylicum* ATCC 824 and *Cp*Xyn30A (Uniprot id: F1TBY8; PDB ID: 4FMV) from *Clostridium papyrosolvens* C71. *Ca*Xyn30A and *Cp*Xyn30A were the top two homologous proteins, both belonging to the genus *Clostridium*. The other similar homologues of *Ac*GH30A were two mutants, E188A and EE of *Tt*Xyn30A (PDB ID: 7O0E) from *Thermothelomyces thermophilus*, XynA (Uniport id: Q46961; PDB ID: 1NOF) from *Dickeya chrysanthemi* and Xyn30B (Uniprot id: A0A4V8H018; PDB ID: 6IUJ) from *Talaromyces cellulolyticus* CF-2612 and XynC (Uniprot id: A0A6M4JGU4; PDB ID: 3GTN). The amino acid sequences of *Ac*GH30A homologs were obtained from the Uniprot database (http://www.uniprot.org). Complete amino acid sequences of *Ac*GH30A, *Tt*Xyn30A, Xyn30B, XynA, *Ca*Xyn30A, *Cp*Xyn30A and XynC were incorporated in MSA analysis.

4.2.2 Artificial intelligence-based homology modelling of *Ac*GH30A

The *in silico* 3-dimensional model of *Ac*GH30A was constructed by using the amino acid sequence (with His-tag at N-terminal) in the Alphafold2 Google Colab platform (https://colab.research.google.com/github/sokrypton/ColabFold/blob/main/AlphaFold2.ipyn), also known as ColabFold (Mirdita et al., 2022). AlphaFold2 is an artificial intelligence-based deep learning algorithm developed by DeepMind technologies (Jumper et al., 2021). ColabFold utilizes MMseqs2 (Many-against-Many

sequence searching) homology search along with AlphaFold2 for fast structure prediction. ColabFold is composed of three major parts. First is the MMseqs2-based homology search server to prepare MSAs and to acquire the suitable template sequences. The second part is a Python library linked with the MMseqs2 server to prepare data for structural inference and visualization. The third part is the Jupyter Notebooks for accessing and using the Python library. The topology of secondary structural elements of the *Ac*GH30A model was obtained by using the PDBSum server (http://www.ebi.ac.uk/thornton-srv/databases/pdbsum/Generate. html) (Laskowski et al., 2018). The CASTp 3.0 server (http://sts. bioe.uic.edu/castp/calculation.html) was utilized to determine the potential ligand-binding sites of *Ac*GH30A and the accessibility of these sites to solvent molecules, including the area with a default probe radius of 1.4Å (Tian et al., 2018).

4.2.3 Evaluation and validation of the computational quality of the modeled *Ac*GH30A structure

The 3D structure model generated from Alphafold2 was relaxed and energy minimized by submitting it to the Yasara energy minimization server (http://www.yasara.org/minimizationserver.htm) (Land & Humble, 2018). The quality of the energy-minimized 3D model generated from Alphafold2 was analysed and verified by submitting the structure to SAVES v6.0 (https://saves.mbi.ucla.edu/) validation server for calculating multiple structural parameters such as ERRAT and Verify3D score (Lüthy et al., 1992). The structural accuracy of the 3D structure model of *Ac*GH30A was evaluated by generating a Ramachandran plot using the Procheck server (MacArthur et al., 1994). The statistical Z-score of the 3D modeled structure, a statistical metric that evaluates the correspondence between the energy of a provided

structure and that of experimental structures (PDB and NMR) was computed and graphically represented through ProSA server (https://prosa.services.came.sbg.ac.at/prosa.php) to detect the erroneous structural elements (Wiederstein & Sippl, 2007).

4.2.4 Determination of secondary structure elements of *Ac*GH30A

The quantitative prediction of the secondary structural components of *Ac*GH30A was conducted by using various web-based services, namely Psipred (http://bioinf.cs.ucl.ac.uk/psipred/) (McGuffin et al., 2000), SOPMA (https://npsa-prabi.ibcp.fr/NPSA/npsa_sopma.html) (Geourjon & Deléage, 1995) and 2Struc (http://2struc.cryst.bbk.ac.uk/twostruc) (Klose et al., 2010). The relative amount of distinct secondary structure elements in *Ac*GH30A was examined using circular dichroism (CD). Purified *Ac*GH30A at a concentration of 0.5 $mg.ml^{-1}$ in a 50 mM sodium phosphate buffer at pH 7.0 was utilized for the CD analysis. The concentrated protein sample was adjusted to align with the ideal range suitable for the CD instrument (Greenfield, 2006). The CD spectrum of *Ac*GH30A within the far-UV region (190-240 nm) was recorded using a spectropolarimeter (JASCO J-815, Jasco Corporation). CD data was obtained with the sample temperature set at 25 °C, with a scanning rate of 50 $nm.min^{-1}$ and a spectral range of 1 nm. Molar residual weight ($g.mol^{-1}$), millidegrees, and protein concentration ($g.L^{-1}$) were used to calculate the molar residual ellipticity (MRE, $10^3.deg.cm^2dmol^{-1}$). To depict as a function of wavelength, the molar residual ellipticity (MRE, $10^3.deg.cm^2dmol^{-1}$) was transformed into the molar extinction coefficient (Δε, decilitre $mol^{-1}cm^{-1}$). The range of Δε values spanning from 190 nm to 240 nm was submitted to K2D3 server (http://cbdm-01.zdv.uni-mainz.de/~andrade/k2d3/) for the quantification of α-helix and β-sheets proportions

(Louis-Jeune et al., 2012). The resulting mean residue ellipticity, was plotted as a function of wavelength. The resulting data pertaining to secondary structure elements from both the circular dichroism (CD) analysis and web-based servers were compared.

4.2.5 Molecular dynamics simulation of *Ac*GH30A modelled structure

The molecular dynamics (MD) simulation of the *Ac*GH30A structure was carried out using GROMACS v5.1.4 software (Berendsen et al., 1995) and the Gromos53a6 force field. The simulation was run on the Param-Ishan High-Performance Computing facility at the Indian Institute of Technology Guwahati, India. The GROMACS topology file was generated through the pdb2gmx command. A simulation box was created using the single point charge (SPC) model, which contained 46,968 water molecules and 15 Cl^- counter ions. The Cl^- ions were added to neutralize the charge present over the 3D model of *Ac*GH30A generated by Alphafold. The energy of the protein simulation system was minimized using gmx_mpi grompp to remove steric clashes. The system was equilibrated by executing position-restrained (NVT) and pressure-restrained (NPT) runs to relax the system gradually. Each equilibration step was performed for 500 ps with a time step of 2 fs (Hess et al., 2008). The final protein-solvent system was used for the subsequent molecular dynamics (MD) simulation, which lasted 100 ns with a 2 fs time step. The Root Mean Square Deviation (RMSD) and Root Mean Square Fluctuation (RMSF) of the amino acid residues were evaluated over time to examine variations in the protein backbone during the simulation. The radius of gyration (R_g) and solvent accessible surface area (SASA) was computed to obtain insights of the overall shape and surface characteristics of *Ac*GH30A.

4.2.6 Protein-ligand interaction study of *Ac*GH30A by molecular docking and isothermal titration calorimetry

Molecular docking simulation of *Ac*GH30A was performed with appropriate ligands to determine the catalytically participating amino acid residues by evaluating the interactions with the ligands. Autodock 4.2.1 (Morris et al., 2009), a software package provided with MGLTools 1.5.6 (http://mgltools. scripps.edu/) was utilized for the study. The ligands used were glucuronic acid, xylobiose, xylotriose, xylotetraose and 2^2-(4-O-Methyl-α-D-Glucuronyl)-xylobiose. The ligands were downloaded in 3D SDF format from the PubChem database (http://pubchem.ncbi.nlm.nih.gov) and subsequently converted to PDB format using OpenBabel 2.3.2a software (O'Boyle et al., 2011). The docking procedure followed the methodology outlined in a previous study (Ahmed et al., 2021). The grid box dimensions around the active site were set to 34, 36, and 48 Å for the x, y, and z axes, respectively. The spacing between the sites was 0.375 Å. The coordinates for the center grid box were established at 7.028 (x), 14.306 (y), and -8.472 Å (z). Fifty iterations of the Lamarckian Genetic Algorithm were performed to acquire 50 distinct conformations for each ligand. The Gibbs free energy (ΔG), also referred to as binding free energy, corresponding to different ligands-*Ac*GH30A molecular docking, was obtained and analyzed. ΔG denotes the change in Gibbs free energy related to the binding of a ligand molecule to a receptor or protein target (Morris et al., 2009). A more negative ΔG value indicates a stronger binding affinity between the ligand and the receptor, suggesting a more stable complex formation. The ligand-protein conformation with the lowest ΔG (binding free energy) was selected to generate the protein and ligand complex for subsequent investigations. The 2D schematic diagram of the docked complexes between the protein and ligand

was visualized using Ligplot+ software (Laskowski & Swindells, 2011) to analyze the polar and non-polar interactions.

The binding affinity of *Ac*GH30A with the best ligand, xylobiose, was experimentally assessed using isothermal titration calorimetry (MicroCal ITC, Malvern Panalytical Pvt. Ltd., UK). The concentration of protein and ligand was 1 $mg.mL^{-1}$ (0.0173 mM) and 0.025 $mg.mL^{-1}$ (0.09 mM), respectively. The titrations were executed at 30ºC. The enzyme *Ac*GH30A and the ligand were dissolved in sodium phosphate buffer (50 mM, pH 7.0). During titration, *Ac*GH30A solution in the reaction cell was continuously stirred at 300 $rev.min^{-1}$. The titration was carried out with 25 successive injections of 1.5 µl ligand at 150 s intervals. The results were analyzed by non-linear regression using a single-site binding model using the system-integrated software Microcal ORIGIN, version 5.0. The association (K_a) and dissociation (K_d) constants were calculated from the fitted data.

4.2.7 MD simulation of *Ac*GH30A-ligand complex

Molecular dynamics (MD) simulation was conducted to investigate the interactions between *Ac*GH30A and the ligand using GROMACS v5.14 software with the GROMOS96 43A1 force field to compute the protein forces. The docked complex of *Ac*GH30A with the xylobiose was chosen for the simulation due to their least binding energy of -4.3 $kcal.mol^{-1}$. The ligand topology for xylobiose was generated using the PRODRG server (Schüttelkopf & van Aalten, 2004). An SPC cubic simulation box was constructed containing 31,044 solvent (water) molecules along with the protein-ligand complex. The charge neutralization of the docked complex of *Ac*GH30A-xylobiose was achieved by further adding 15 Cl^- counter ions. The energy of the protein-ligand simulation system was minimized using gmx_mpi grompp to remove steric clashes.

The system was equilibrated by executing position-restrained (NVT) and pressure-restrained (NPT), followed by the execution of final molecular dynamics (MD) simulation for 100 ns, as mentioned in Section 4.2.5. Following the simulation, the interactions between the ligand and the catalytic residues at the active site of the docked complexes were examined using PyMOL V2.3.3 software (Yuan et al., 2017). Time-dependent analysis of the Root Mean Square Deviation (RMSD) and Root Mean Square Fluctuation (RMSF) of amino acid residues was performed to evaluate the structural variations in the protein backbone during the simulation. The RMSD and RMSF values were computed using the commands gmx_mpi rmsd and gmx_mpi rmsf, respectively. The radius of gyration (R_g) and solvent-accessible surface area (SASA) were calculated using the gmx_mpi sasa and gmx_mpi gyrate commands, respectively. The simulation results of the complex were compared with the results of ligand-free *Ac*GH30A. A 2D representation of the protein-ligand interactions was generated using Ligplot+ software (Laskowski & Swindells, 2011).

4.2.8 Small angle X-ray scattering analysis of *Ac*GH30A

The low-resolution scattering data for *Ac*GH30A at a concentration of 3 mg.ml^{-1} were obtained utilizing a small-angle X-ray scattering system (SAXSpace, Anton Paar) to investigate the molecular shape and conformational behaviour of *Ac*GH30A in solution. Before the collection of SAXS data, the *Ac*GH30A samples and the corresponding buffer were centrifuged at 22,000***g*** for 45 min at 4°C. The incident X-rays were generated using a line collimation system and were directed through the sample, contained within a thermostated 1 mm diameter quartz capillary. The source of X-rays in the SAXSpace machine was a Primux 3000 sealed tube (Anton Paar, Austria) with copper (Cu) as the anode, emitting the incident radiation of fixed wavelength of

1.5 Å. The scattering of x-rays at small angles (0.1° to 10°) from protein at a temperature of 10°C was recorded from two separate exposures, each lasting 30 min. The scattering pattern of the matched buffer (50 mM sodium phosphate, pH 7.0) was also recorded and subtracted from the *Ac*GH30A sample and the absolute scattering pattern of only the protein was obtained.

SAXS Quant software was used to generate the SAXS profile from the protein molecules in solution by subtracting the buffer contribution, yielding the scattering intensity (I) as a function of the momentum-transfer vector (q) (where $q = 4\pi\sin\theta/\lambda$, with q=scattering vector, λ = wavelength, and 2θ = scattering angle) (Roblin et al., 2013). The processing of data, normalization to an absolute scale, and averaging procedures were carried out using the ATSAS package. Initial data processing was performed using PRIMUS software. The radius of gyration (R_g) was determined using the Guinier equation and the indirect Fourier transform method using the GNOM package. The maximum diameter, D_{max} was derived from the distance distribution function, p(r), which was computed using GNOM. The persistence length (L) of *Ac*GH30A was determined through the formula $[\sqrt{12}\{(R_g^2) - (R_c^2)\}]$ (Balasubramaniam et al., 2019). The molecular weight of *Ac*GH30A was determined from the scattering pattern using the Qp package. The *ab initio* method was utilized to produce the low-resolution shapes of *Ac*GH30A from the scattering curve generated by DAMMIF. The reconstruction of dummy structural models for *Ac*GH30A was executed through the implementation of 20 independent iterations of DAMMIF. The verification of these 20 models was subsequently conducted using DAMAVER to establish the resultant *ab initio* configuration. The reconstruction of the scattering shape of *Ac*GH30A was achieved through the application of GASBOR, an ab initio modeling-based, chain-like

ensemble modeling program. The modelled structures of the *Ac*GH30A were visualized by using UCSF Chimera (Pettersen et al., 2004).

4.2.9 Size distribution analysis of *Ac*GH30A by dynamic light scattering (DLS)

The DLS analysis of *Ac*GH30A was conducted using the Litesizer 500 Particle Analyzer (Anton Paar in Graz, Austria) to determine the hydrodynamic diameter (D_h) of *Ac*GH30A at concentrations of 1 and 3 mg.mL^{-1}. The DLS of *Ac*GH30A was also performed in the presence of xylobiose (X2) procured from Tokyo Chemical Industry Co., Ltd., Japan, to observe its effect on the D_h of *Ac*GH30A. Two separate mixtures were prepared by dissolving *Ac*GH30A with different final concentrations of X2, 0.0173 mM and 0.0346 mM. *Ac*GH30A without xylobiose was used as a control. The final concentration of *Ac*GH30A mixed with xylobiose was kept at 0.0173 mM (1 mg.mL^{-1}). Protein solutions (1.5 mL) were centrifuged at 13,000×***g*** for 15 min. The supernatant obtained was then filtered through a 0.45 µm PVDF filter membrane using a syringe filter prior to analysis. Measurements were acquired through a 40 mW diode laser with a wavelength of 658 nm, positioned at a backscatter angle of 175°. Experiments were performed at a constant temperature of 25°C, controlled by a Peltier-based temperature regulator. Particle size analysis was carried out using the Kalliope software. Dynamic light scattering (DLS) measurements were performed in triplicate at each concentration.

4.3 Results and Discussion

4.3.1 Sequence analysis of *Ac*GH30A

The amino acid sequence of xylobiohydrolase, *Ac*GH30A consists of different modules. Sequence analysis of *Ac*GH30A the SignalP 3.0 server revealed that it contains a signal peptide of 28 amino acid residues at the N-terminus, suggesting that *Ac*GH30A is an extracellular enzyme and a part of the secretory pathway. The catalytic module of *Ac*GH30A, belonging to the glycoside hydrolase superfamily 30, comprises 454 amino acids, followed by dockerin 1 spanning 58 amino acids at the C-terminal of the sequence, as mentioned in chapter 2 (Fig. 2.1). These two modules are linked by a linker sequence of 5 amino acids. The presence of dockerin 1 module indicates the participation of *Ac*GH30A in the cellulosomal complex of *Acetivibrio clariflavus*.

The pBLAST similarity search revealed identical homologues of *Ca*Xyn30A (PDB ID: 5CXP) from *Clostridium acetobutylicum,* followed by *Cp*Xyn30A (PDB ID: 4FMV) from *Ruminiclostridium papyrosolvens*, *Tt*Xyn30A mutant E188A (PDB ID: 7O0E_A), and *Tt*Xyn30A double mutant EE (PDB ID: 7O0E_AAA) from *Thermothelomyces thermophilus*, XynA (PDB ID: 1NOF) from *Dickeya chrysanthemi*, and Xyn30B (PDB ID: 6IUJ) from *Talaromyces cellulolyticus* (Table 4.1). *Ca*Xyn30A and *Cp*Xyn30A are two exceptional enzymes among all the reported GH30 enzymes that have been reported to show non-specific endoxylanase activity. Their non-specific mode of action is the result of differences in the configuration of their catalytic clefts. In *Ca*Xyn30A, a typical glucuronoxylan-specific xylanases arginine was replaced by Gly271 residue, whereas in *Cp*Xyn30A, it was replaced by Trp269, making it capable of cleaving both arabinoxylan and glucuronoxylan (St John et al., 2014, 2018). The high homology of *Ac*GH30A with non-specific xylanases, which does not require the

presence of glucuronic acid substitutions for their action, suggests a lack of requirement for the availability of the glucuronic acid moiety for its catalytic activity. The presence of the conserved arginine residue was found to be important for another GH30 glucuronoxylan-specific xylanase A (*St*Xyn30A) isolated from *Streptomyces turgidiscabies* (Maehara et al., 2018). Molecular modelling of *St*Xyn30A suggested Arg296 as a conserved residue. To better understand the mechanism involved in the recognition of glucuronic acid moieties, Arg296 mutants of *St*Xyn30A were prepared and analyzed. The enzymatic activity of the Arg296 mutant against glucuronoxylan was significantly reduced compared to that of the wild-type enzyme (Maehara et al., 2018). The amino acid sequence of *Ac*GH30A also showed high similarity with fungal xylanases. The closest fungal homologues were *Tt*Xyn30A (PDB ID: 7O0E) from *Thermothelomyces thermophila* (Nikolaivits et al., 2021) and Xyn30B (PDB ID: 6IUJ) (Nakamichi et al., 2020) from *Talaromyces cellulolyticus* (Table 4.1). Both fungal xylanases show bifunctional endo- and exo-xylanase activities.

Table 4.1. Homologous protein sequences of *Ac*GH30A obtained from pBLAST.

Protein name	Organism	Max Score	Query Cover (%)	E value	% Identity	Accession Length	Accession ID
*Ca*Xyn30A	*Clostridium aceto-butylicum* ATCC 824	198	83	4.00E-58	32.71	390	5CXP_A
*Cp*Xyn30A	*Ruminiclostridium papyrosolvens* DSM 2782	194	83	3.00E-56	32.88	396	4FMV_A
*Tt*Xyn30A *mutant E188A*	*Thermothelomyces thermophilus* ATCC 42464	191	78	2.00E-54	32.27	452	7O0E_A
*Tt*Xyn30A *double mutant EE*	*Thermothelomyces thermophilus* ATCC 42464	189	78	1.00E-53	32.04	482	7NCX_AAA
XynA	*Dickeya chrysanthemi*	168	82	7.00E-47	31.55	383	1NOF_A
Xyn30B	*Talaromyces cellulolyticus* CF-2612	168	83	8.00E-46	29.87	474	6IUJ_A

The alignment of the amino acid sequence of *Ac*GH30A with multiple GH30 xylanases identified Glu175 and Glu268 as the conserved catalytic residues. Glu175 functions as an acid/base, whereas Glu268 serves as a nucleophile (Fig. 4.1). The relative surface accessibility of the amino acid residues was analyzed using ESPript 3.0. The accessibility of the residues is displayed by a bar below the MSA, where blue is accessible, cyan is intermediate and white is buried inside the core (Fig. 4.1). The MSA analysis also revealed the presence of a conserved bacterial arginine residue, Arg349, located on the β13 strand in *Ac*GH30A. A study of the crystal structure of *Ec*Xyn30A (PDB ID: 1NOF), a GH30 glucuronoxylanase from *Erwinia chrysanthemi*, showed that the methyl glucuronic acid interacts with the positively charged guanidium group of Arg293 (Urbániková et al., 2011). The residue, Arg349 of *Ac*GH30A aligned with Arg293 of *Ec*Xyn30A in the MSA analysis. This arginine residue has been found to be highly conserved in bacterial GH30 glucuronoxylanases.

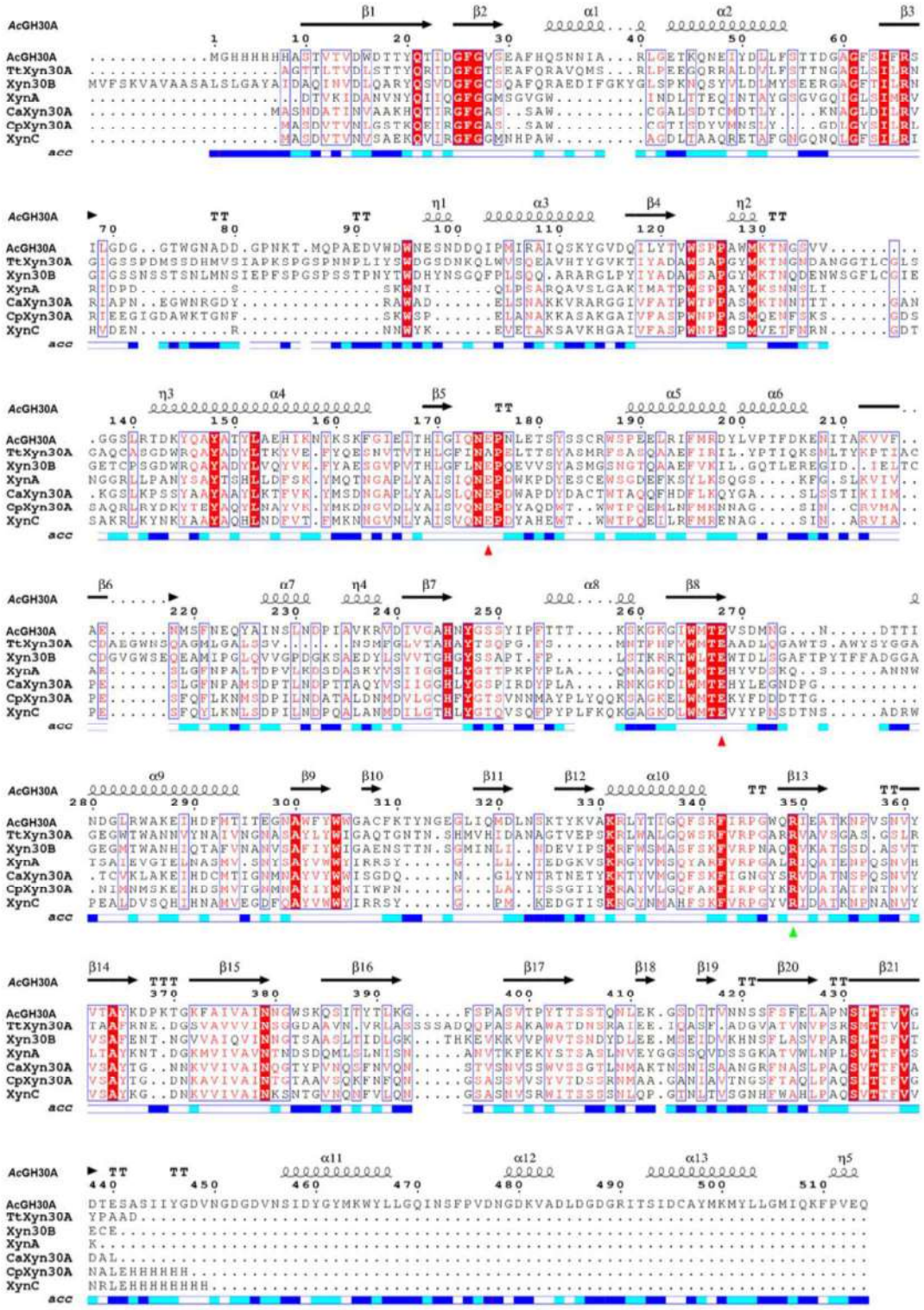

Fig. 4.1 Multiple sequence alignment analysis. Catalytic residues are marked with red triangles and the conserved bacterial arginine residue is marked with green triangle. Accessibility of *Ac*GH30A is rendered by a bar below: blue is accessible, cyan is intermediate, white is buried.

4.3.2 Homology modeling of *Ac*GH30A

Five homology models of *Ac*GH30A were acquired from ColabFold and were ranked between 1-5. The rank 1 model was used in subsequent studies. The selected model was visualized in a 3D cartoon and surface view using the USCF Chimera (Fig. 4.2A & B). The per-residue estimate of the confidence of the model was examined using a predicted local distance difference test (pLDDT) plot (Fig. 4.2C). The pLDDT score for the majority of amino acids was above 90, indicating the high confidence and quality of the predicted model. The number of templates utilized for generating the models was assessed by the sequence coverage plot (Fig. 4.2D), which revealed that the prediction of the homology modelled structures was executed using more than 4000 templates for the majority of the amino acid sequence.

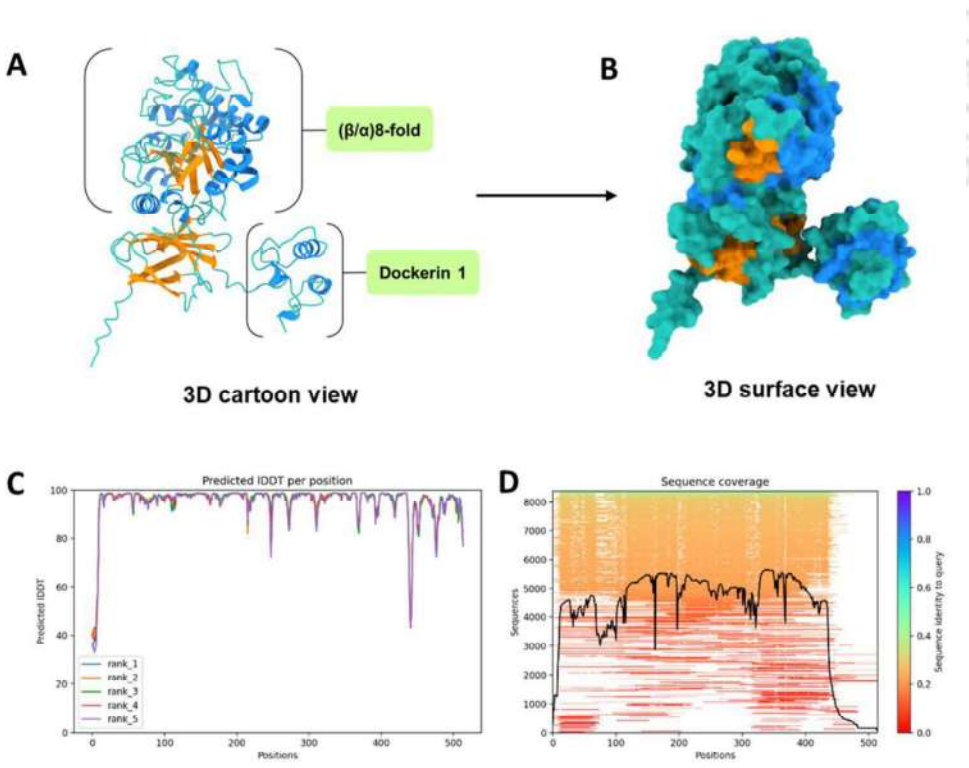

Fig. 4.2 (A) 3D cartoon and surface view of homology modelled structure of *Ac*GH30A (Blue- Helices, Prusian green- Coils and Orange- β strands), (B) 3D surface view of the homology model, (C) pLDDT plot, and (D) Sequence coverage plot.

The topology diagram of the *Ac*GH30A modelled structure illustrated the number of secondary structural elements (Fig. 4.3A). As per the plot, there were 21 β-strands in total. The central β-barrel within the (β/α)8-fold contained eight parallel β-strands. The catalytic residues Glu175 and Glu298 of *Ac*GH30A, identified through MSA with other homologues, are situated in the catalytic cleft at the entrance of the β-barrel, allowing accessibility to the substrate (Fig. 4.3B). Similar crystal structures were observed for *Tt*Xyn30A (PDB ID: 7O0E) and *Ca*Xyn30A (PDB ID: 5CXP) within the GH30 family (Kadowaki et al., 2021; St John et al., 2018). The formation of the catalytic duo is facilitated by loops L6 (red) and β8 (blue), as shown in Fig. 4.3C. L6 contains the nucleophile Glu175, whereas Glu268 is located at β8. Both Glu175 and Glu268 were found in conserved regions. In the modeled structure of *Ac*GH30A, it was observed that L6 and β8 played a role in bringing these two amino acids near to the active-site, thereby promoting the creation of the catalytic duo. Fig. 4.3B displays the superposition of the modeled structure of *Ac*GH30A with the crystal structures of *Ca*Xyn30A (PDB ID: 5CXP) and *Cp*Xyn30A (PDB ID: 4FMV). The RMSD values for the superposition of *Ac*GH30A with *Ca*Xyn30A and *Cp*Xyn30A were 1.179 and 1.149 Å, respectively, indicating excellent alignment. This superposition highlights a consistent alignment of the catalytic residues in the homologues, specifically corresponding to Glu175 and Glu268. The configuration of the catalytic duo in the active-site of *Ac*GH30A and the two other homologues, *Ca*Xyn30A and *Cp*Xyn30A, are shown in Fig. 4.3B. In the modeled structure of *Ac*GH30A, the distances between the catalytic duo were assessed using PyMOL v2.3.3. The minimum distance between Glu175 and Glu268 was 4 Å. Active-site analysis, conducted using the CASTp server, elucidated the features of the ligand-binding site of *Ac*GH30A (Fig. 4.3D). The CASTp-

calculated solvent-accessible surface area and volume of the catalytic site and ligand-binding pocket were 112.582 Å² and 53.260 Å³, respectively.

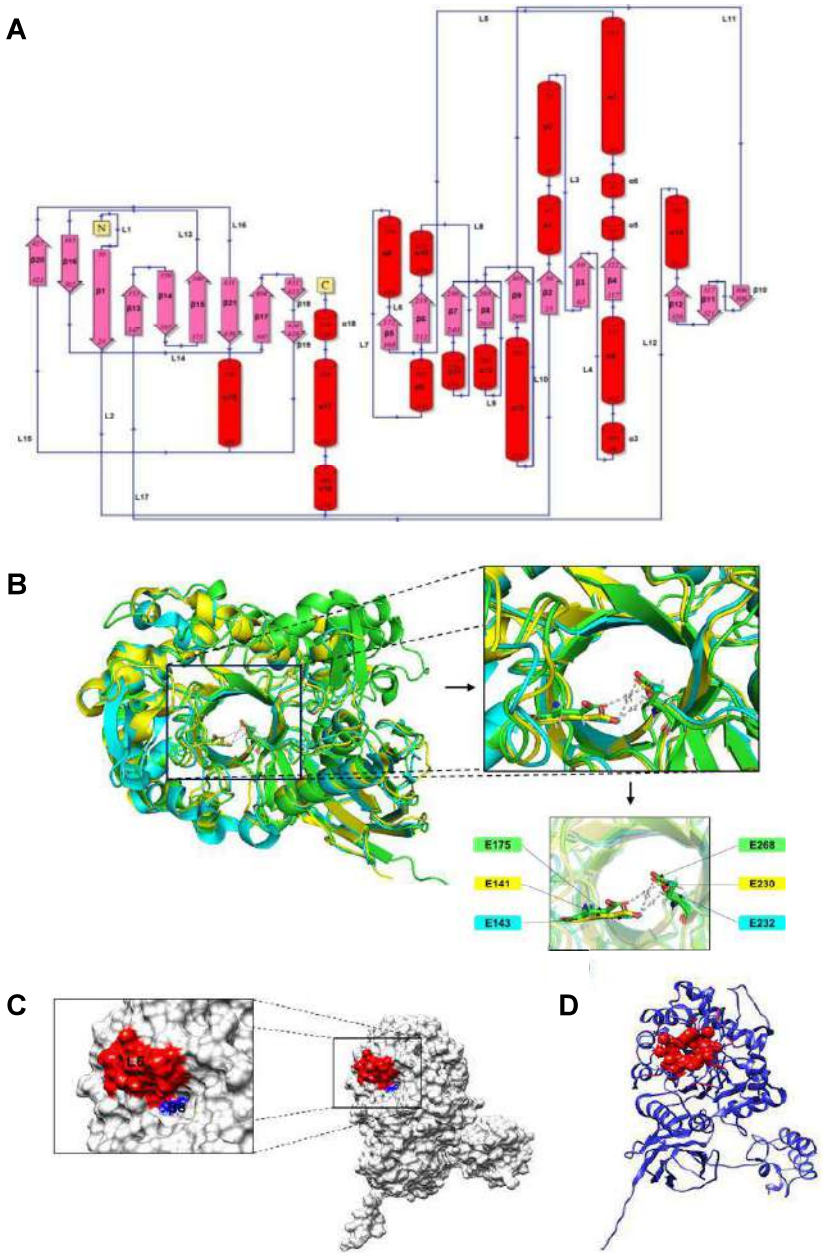

Fig. 4. 3 Structural features and catalytic architecture of *Ac*GH30A. (A) Topology diagram of *Ac*GH30A with N- and C- terminal and secondary structure elements (α-helices, β-sheets and turns), (B) Superposition of *Ac*GH30A modeled structure (Green) with closest homologues *Ca*Xyn30A (Yellow) and *Cp*Xyn30A (Cyan) and catalytic residues in the magnified black square, (C) Surface view of *Ac*GH30A shows loop 6 (L6) in red and β-strand 8 (β8) in blue forming the catalytic duo (in red) (D) Catalytic cleft (red) predicted by CastP server.

4.3.3 Quality assessment and validation of the modeled structure of *Ac*GH30A

Ramachandran plot from the Procheck server was used to examine the dihedral angles (Ψ and Φ) of the amino acid residues constituting the backbone of the *Ac*GH30A modeled structure (Fig. 4.4A). The plot revealed that the favoured region has 87.6% residues, the allowed region has 12.4% residues, and there is no amino acid residue present in the disallowed zone. Overall model quality *Ac*GH30A, assessed via the ProSA server, showed an error-free model within the X-ray zone, obtaining a Z-score of -9.5 (Fig. 4.4B). The local model quality, examined using ProSA, indicated the accuracy of every component in the modeled structure, with no amino acid residue exhibiting a positive value in the local energy plot (Fig. 4.4C). The quality assessment of *Ac*GH30A via the UCLA Saves server showed a successful VERIFY 3D test, achieving an average 3D-1D score of ≥ 0.2 (Fig. 4.4D). The overall quality score of the *Ac*GH30A modelled structure was determined to be 93.6% by the ERRAT server, confirming the high quality of the *Ac*GH30A modelled structure. The model's refinement, as well as the findings of its quality assessment, were satisfactory for further research.

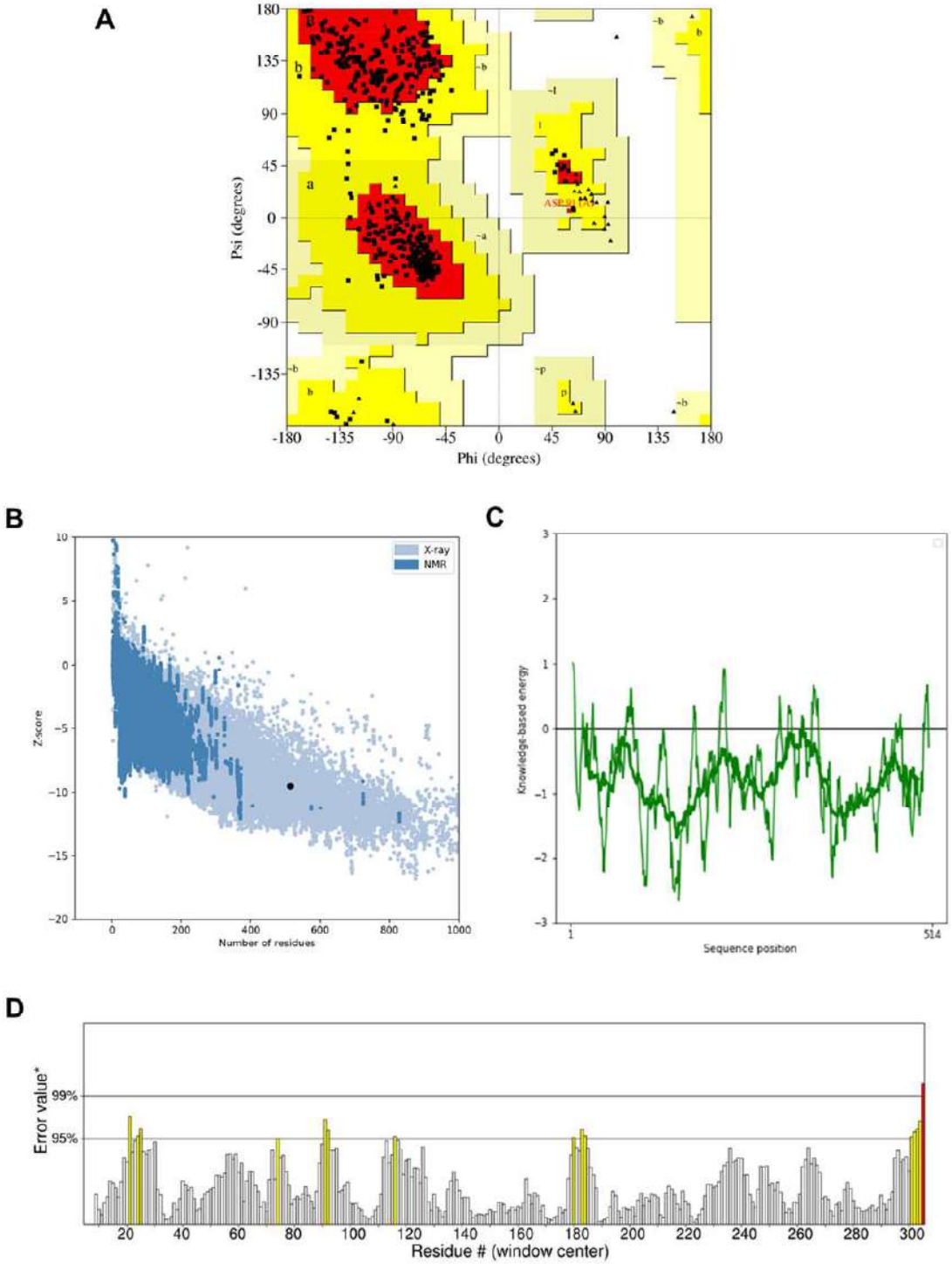

Fig. 4.4 Validation and quality assessment of *Ac*GH30A modeled structure. (A) Ramachandran plot generated by Procheck showing favoured, allowed and model quality, (B) Prosa plot indicating the overall model quality factor (Z-score) (C) ProSA plot of residue scores, and (D) VERIFY 3D showing the 3D-1D averaged score of the amino acid residues.

4.3.4 Secondary structure analysis of *Ac*GH30A

PsiPred 4.0, a web-based system was used to determine the secondary structure elements of *Ac*GH30A from its amino acid sequence. According to the Psipred data *Ac*GH30A has 23.7% α-helices, 22.9% β-strands and 46.7% random coils. SOPMA and 2Struc servers were also used for determining the composition of secondary structures present in the *Ac*GH30A. SOPMA predicted the relative proportions of α-helices, β-sheets, and random coils to be 23.93%, 23.93% and 45.91%, respectively, and with 2Struc server it was 28.2%, 22.8% and 49.0%, respectively (Table 4.2). The results from the web servers suggested that the majority of *Ac*GH30A residues fold into random coils with a similar composition of α-helices and β-strands. The *in-silico* 3D model of *Ac*GH30A generated by Alphafold2 also showed similar proportions of secondary structures with 23.46% α-helices, 22.17% β-sheets and 54.4% of random coils. The CD analysis results for secondary structure prediction, obtained through the K2D3 server, indicated the presence of 21.94% α-helices, 20.98% β-sheets, and 57.08% random coils (Fig. 4.5 and Table 4.2). These CD findings aligned with the predictions made by web servers for analyzing secondary structure.

Table 4.2. Secondary structure analysis of *Ac*GH30A.

SERVER/TOOL	α-Helix (%)	β-Strands (%)	Random Coils (%)
Psipred	23.7	22.9	53.4
2struct	28.2	22.8	49.0
SOPMA	23.93	23.93	52.14
Alphafold2	23.46	22.17	54.4
CD	20.98	21.94	57.08

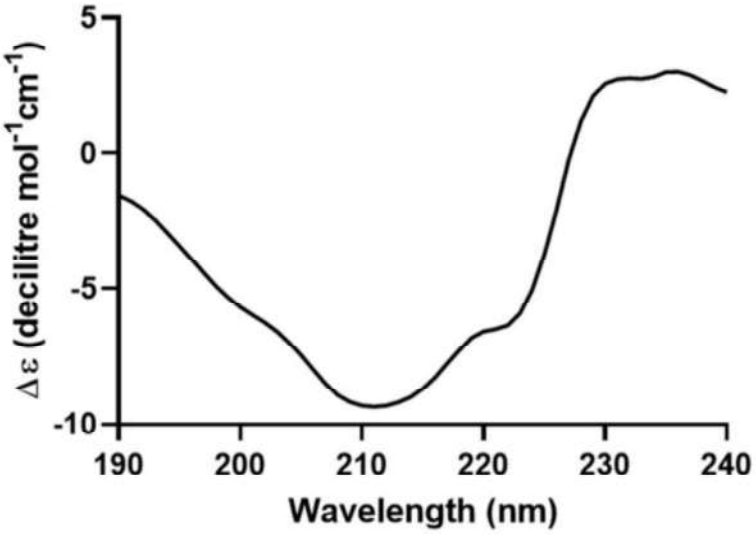

Fig. 4.5 Far UV-CD spectrum of *Ac*GH30A analysed by K2D3 server for determination of secondary structure elements. The CD spectrum of purified *Ac*GH30A (0.5 mg.ml^{-1} in 50 mM sodium phosphate buffer at pH 7.0) in the far-UV region (190-240 nm) was obtained at 25 °C with scanning rate of 50 nm.min^{-1} and spectral range of 1 nm.

4.3.5 MD simulation of *Ac*GH30A modelled structure

The dynamic behaviour and interactions of atoms and molecules over time, globularity and stability of the *Ac*GH30A modelled structure were investigated by molecular dynamics (MD) simulation for 100 ns. By using values of the root mean square deviation (RMSD), the structural deviation from the original structure was calculated. The RMSD vs. time graph (Fig. 4.6A) showed significant fluctuation, ranging from 0.01 nm to 1.31 nm up to 53 ns, after which the structure stabilized between 1.18 nm and 1.45 nm from 54 ns to 100 ns. The average RMSD of the whole simulation period was found to be 1.04 nm. The radius of gyration (R_g) fluctuated between 2.5 nm and 2.8 nm, between 1 ns to 49 ns (Fig. 4.6B). From 50 ns onwards, R_g values varied between 2.76 nm to 2.78 nm showing minimal fluctuations. The R_g became stable after 49 ns till the end of 100 ns, demonstrating the structure's global

compactness (Fig. 4.6B). The average R_g was found to be 2.7 nm. The solvent accessible surface area (SASA) of *Ac*GH30A gradually declined from an initial 221.01 nm^2 to 218.21 nm^2 at 100 ns, indicating very little change, giving an average SASA value, 221.98 nm^2 (Fig. 4.6C). The variation in SASA values was minimal, suggesting that there is no hindrance to the catalytic residues due to deformities, and therefore, they remain accessible to the substrate.

Following molecular dynamics (MD) simulation, the Root Mean Square Fluctuations (RMSF) of Cα atoms within amino acid residues were computed to evaluate the displacement of atoms across various regions in the simulated structure. The N- and C-terminal of *Ac*GH30A were identified as highly flexible regions, while residues involved in secondary structures demonstrated reduced flexibility, in contrast to those within the loop regions. The catalytic residues, Glu175 in loop L6 and Glu268 in β8 (highlighted by the red arrow), exhibited lower flexibility and greater stability compared to other residues in L6 and β8 (Fig. 4.6D). The MD simulation study demonstrated that the modeled structure of *Ac*GH30A is both compact and stable, making it suitable for additional structural investigations.

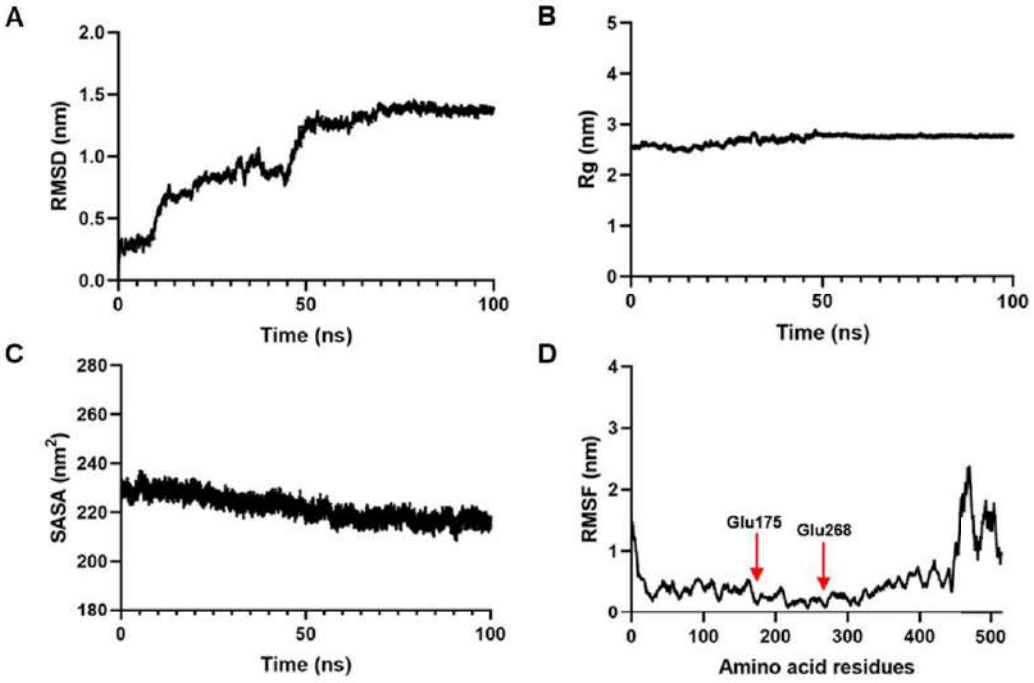

Fig. 4.6 MD simulation analysis of *Ac*GH30A modelled structure after 100 ns simulation. (A) RMSD plot, (B) Radius of gyration (R_g) plot, (C) SASA plot and (D) RMSF plot.

4.3.6 Protein-ligand interaction study of *Ac*GH30A by molecular docking and isothermal titration calorimetry

The molecular docking analysis of *Ac*GH30A with different ligands revealed its maximum binding affinity with xylobiose (binding free energy, -4.3 kcal.mol^{-1}) followed by glucuronic acid (-3.06 kcal.mol^{-1}), xylotriose (-2.36 kcal.mol^{-1}) and 2^2-(4-O-Methyl-α-D-Glucuronyl)-xylobiose (-0.98 kcal.mol^{-1}) as shown in Table 4.3. The highest binding affinity of *Ac*GH30A for xylobiose supports the presence of xylobiohydrolase activity.

The Ligplot software was utilized to analyse the 2-dimensional interactions between ligands and amino acid residues within the catalytic cleft. In the docked complex, xylobiose was positioned in the catalytic cleft with two subsites, -1 and -2. Fig. 4.7A & B displays the docked complex of *Ac*GH30A with xylobiose, with the

amino acid residues involved in the subsites -1 and -2. *Ac*GH30A formed four hydrogen bonds with xylobiose, involving Trp123, Glu175, Asn174, and Glu268 (Table 4.3). Similar amino acids were found to be forming hydrogen bonds with xylobiose in the crystal structure of catalytic module of *Ac*GH30A (dubbed as *Ac*Xbh30A) (St John et al., 2022). The corresponding amino acid residues in the crystal structure were Trp116, Glu168, Asn167 and Glu261. The catalytic nucleophile Glu268 and the acid/base catalyst Glu175 of *Ac*GH30A were positioned at 2.9 Å and 2.6 Å, respectively, from -1 xylose (Fig. 4.7B). Moreover, Trp123 and Asn174 were located 2.8 Å and 3 Å away from -1 xylose. The residues, Leu178, Tyr182, Phe32, Met219, Met272, Tyr247 and Trp304 of *Ac*GH30A participated in establishing hydrophobic interactions with xylobiose (Table 4.3). The -2 subsite was primarily composed of Leu178, Tyr182 and Met219. The conserved bacterial amino acid residue, Arg349 present in β13 sheet of *Ac*GH30A was distantly located from the catalytic cleft and was not involved in any interaction during molecular docking, suggesting its non-participation in catalysis. This indicated that *Ac*GH30A may not recognise or require the presence of glucuronic acid moiety as happens in glucuronoxylanse, *Ec*Xyn30A for binding and catalysis of the xylan substrate (Urbániková et al., 2011).

Table 4.3. Amino acid residues of *Ac*GH30A involved in ligand binding.

Ligand	Binding energy (kcal.mol^{-1})	Polar interaction	Hydrophobic interaction
Xylobiose	- 4.3	Asn174, Glu175, Glu268	Phe32, Leu178, Tyr182, Met219, Tyr247, Met272, Trp304
Glucuronic acid	- 3.06	Thr255, Lys258, Thr296, Glu297	Phe254, Pro253
Xylotriose	- 2.36	Glu223, Thr255	Asn222, Ile252, Pro253, Ile295,
Xylotetraose	- 1.66	Thr19, Lys258,	Tyr20, Pro253, Thr255, Ser259, Glu297, Thr296,
2^2-(4-O-Methyl-α-D-Glucuronyl)-xylobiose	- 0.98	Asn174, Glu175, Tyr182, Glu315	Phe32, Trp123, Leu178, Glu268, Ser270, Trp305, Lys310, Tyr312, Asn313

Molecular docking of AcGH30A was performed using AutoDock 4.2.1. The grid box around the active site was set to dimensions of 34 × 36 × 48 Å (x, y, z) with a spacing of 0.375 Å, and centered at coordinates 7.028, 14.306, and -8.472 Å for x, y, and z, respectively.

The cleavage of a glycosidic bond by glycoside hydrolases follows two different types of mechanisms, *viz.* retaining- and inverting-type (Brüx et al., 2006; Davies & Henrissat, 1995; Okuyama et al., 2009). In the case of retaining-type enzymes, the nucleophilic catalytic residue is in closer proximity to the anomeric carbon of the sugar when compared with the inverting-type enzymes. The average distance between the catalytic duo in retaining-type enzymes is 5.5 Å, while in inverting-type it is 10 Å (Davies & Henrissat, 1995; Okuyama et al., 2009). The molecular docking study of the docked complex, *Ac*GH30A-xylobiose revealed that xylobiose is placed between the catalytic duo, Glu175 and Glu268. The analysis further showed that the distance between these two catalytic residues in *Ac*GH30A was 4 Å, suggesting that it follows the retaining-type mechanism (Fig. 4.7A & B).

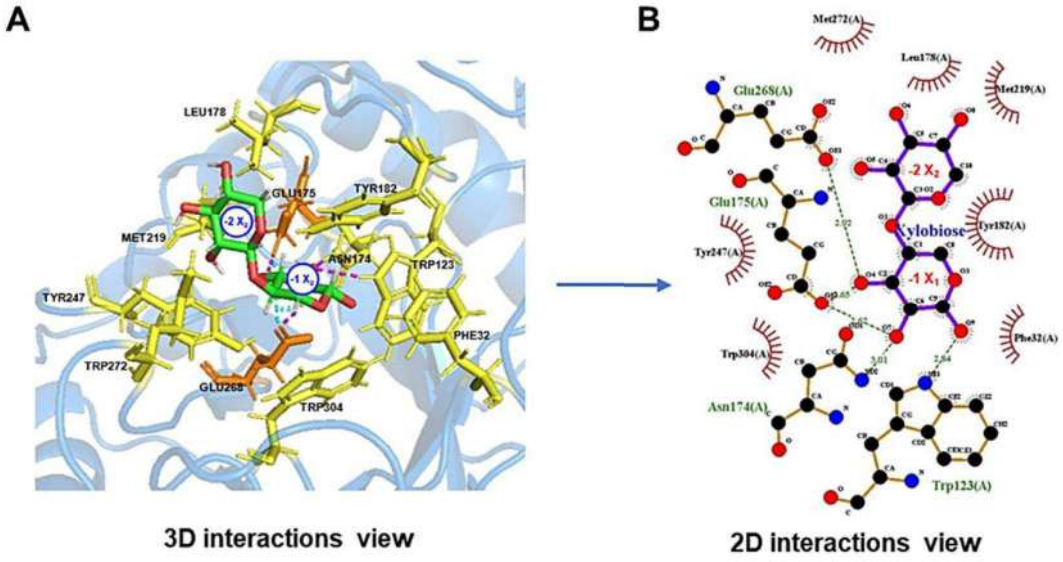

Fig. 4.7 Docking analysis of *Ac*GH30A with the xylobiose showing (A) 3D schematic presentation and (B) 2D schematic presentation of the orientation of active-site residues with xylobiose.

Isothermal titration calorimetry of *Ac*GH30A was carried out using xylobiose as a ligand, since *Ac*GH30A displayed the highest binding affinity with xylobiose during molecular docking. A strong binding between *Ac*GH30A and xylobiose was observed with an association constant (K_a) of 7.83×10^5 M^{-1} which also gave the value of a dissociation constant (K_d) of 1.28×10^{-6} M (Fig. 4.8).

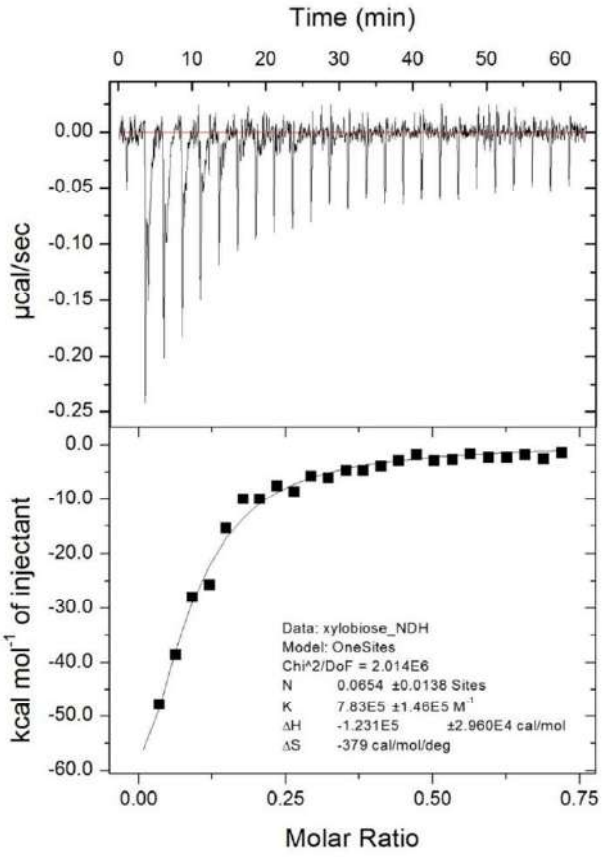

Fig. 4.8 Isothermal titration calorimetry of *Ac*GH30A binding to xylobiose. The concentrations of *Ac*GH30A, 1 mg.mL^{-1} (0.0173 mM) and xylobiose, 0.025 mg.mL^{-1} (0.09 mM) was used. The titrations were performed at 30°C, involving 25 consecutive injections of 1.5 µl ligand at 150 s intervals.

4.3.7 MD simulation of *Ac*GH30A-ligand complex

The RMSD, R_g, SASA and RMSF of the complex *Ac*GH30A-xylobiose were calculated and analysed. Comparative molecular dynamics analysis between the *Ac*GH30A-xylobiose complex and *Ac*GH30A was performed to assess various parameters, evaluating the stability and compactness of the docked complex after molecular dynamics simulation. The docked complex displayed an average RMSD value of 0.65 nm after 40 ns, with oscillation within ±0.03 nm until 100 ns. Remarkably, this was 0.39 nm lower than the RMSD observed for *Ac*GH30A without the ligand (Fig. 4.9A). The RMSD value of the simulated docked complex decreased significantly,

reflecting conformational changes induced by the binding of xylobiose within the active site of *Ac*GH30A, as compared to the unbound *Ac*GH30A structure. The consistent RMSD values confirmed the structural equilibrium and stability of the docked complex. Over the 100 ns simulation, the radius of gyration (R_g) for the docked complex maintained a range of 2.31 nm to 2.61 nm, with an average R_g of 2.38 nm (Fig. 4.9B). The R_g of the docked complex was 0.32 nm lower than that of *Ac*GH30A alone, indicating that ligand binding increased the overall compactness and rigidity of the complex. The SASA progressively decreased during the simulation, following a trend similar to that of the unbound *Ac*GH30A throughout the 100 ns trajectory (Fig. 4.9C). The average SASA during the whole simulation was found to be 199.41 nm^2, which was lower from the calculated SASA of only *Ac*GH30A by ~22.57 nm^2. This suggested that the binding of the ligand to the catalytic cleft of *Ac*GH30A in the docked complex led to a reduction in solvent accessibility. The RMSF plot from the MD simulation of the complex exhibited a similar trend to that of *Ac*GH30A, with the N- and C-terminal residues displaying high flexibility (Fig. 4.9D).

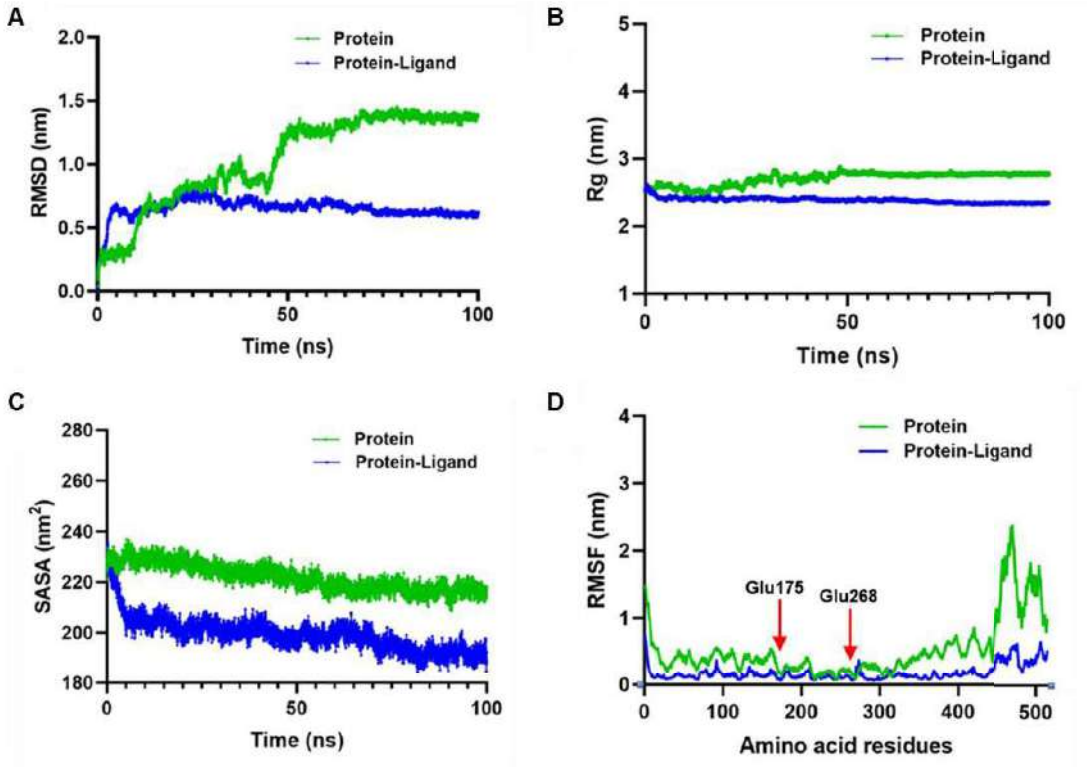

Fig. 4.9 Comparative molecular dynamic simulation analysis of xylobiose bound *Ac*GH30A and unbound *Ac*GH30A, presenting (A) RMSD plot, (B) Radius of gyration (R_g) plot, (C) SASA plot, (D) RMSF plot.

In the MD simulation, the *Ac*GH30A-xylobiose docked complex showed lower-level of flexibility as compared to the *Ac*GH30A model. The decreased flexibility at the N- and C-termini of the complex suggests enhanced stability and compactness in the *Ac*GH30A-xylobiose complex compared to the unbound *Ac*GH30A. The RMSF values of the catalytic residues, Glu175 and Glu268 were found to be stable (Fig. 4.9D). These residues exhibited negligible mobility, suggesting their geometric accuracy and capability to adopt productive catalytical conformations. In the final 3D model of the enzyme-ligand complex generated after the completion of simulation, xylobiose was bound to the catalytic cleft present at the opening of the TIM-motif (Fig. 4.10A & B), similar to the configuration observed after molecular docking. After 100 ns, the amino acid residues, Glu175, Ser220 and Asn222 established hydrogen bonds with the ligand,

whereas Gln224, Tyr225, and Asn218 developed hydrophobic contacts with xylobiose in the catalytic cleft (Fig. 4.10C & D). The MD simulation study further showed that Arg349 present in β13 sheet of *Ac*GH30A is far from the catalytic cleft and therefore not involved in any interaction with xylobiose, corroborating its non-participation in catalysis. In the final 3D model of the enzyme-ligand complex generated after the completion of simulation, the ligand was found to be bound with Glu175 and in the close proximity of Glu268. It is evident from the ligand bound model generated after molecular dynamics simulation for 100 ns that the ligand is stable and bound to the catalytic cleft with high binding affinity.

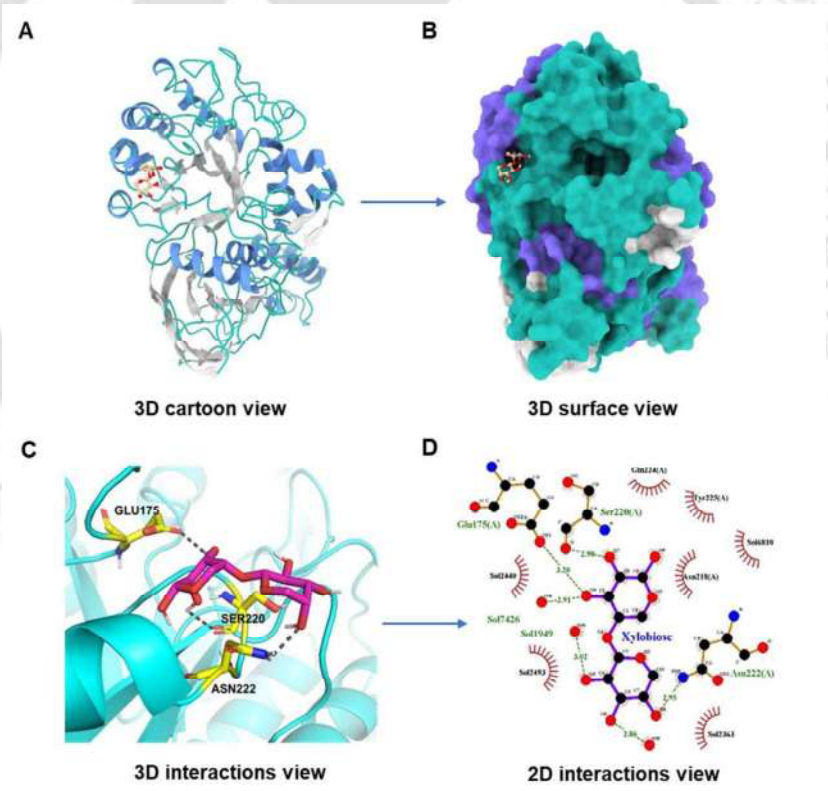

Fig. 4.10 Molecular dynamics simulation analysis of *Ac*GH30A in complex with xylobiose. (A) 3D cartoon view of simulated complex structure of *Ac*GH30A with xylobiose, (B) 3D surface view of simulated complex structure of *Ac*GH30A with xylobiose (Blue- Helices, Prusian green- Coils and Light grey- β strands), (C) 2D schematic representation of orientation of active-site residues of *Ac*GH30A with Xylobiose after 100 ns of simulation, and (D) 2D schematic representation of interactions between xylobiose and the protein residues.

Distance-versus-time analysis of the *Ac*GH30A-xylobiose complex revealed that the catalytic residues Glu175 and Glu268 consistently maintained distances below ~3.5 Å with the ligand hydroxyl groups O7 and O4 throughout the simulation, indicating persistent hydrogen bonding and confirming their central role in catalysis (Fig. 4.11). In contrast, Glu174 displayed more fluctuating distances, often approaching or exceeding 3.5 Å, suggesting a transient stabilizing interaction rather than direct catalytic involvement. These dynamic observations validate the polar interactions predicted by docking (Section 4.3.6) and complement the hydrogen-bond occupancies and interaction mapping shown in Figure 4.10.

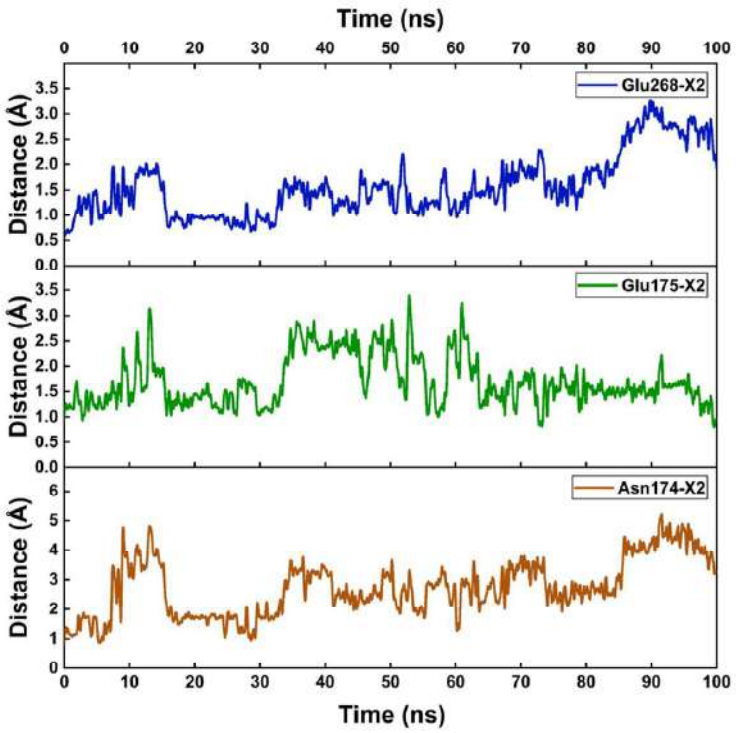

Fig. 4.11 Distance-versus-time plots of polar interactions between key active-site residues of *Ac*GH30A and xylobiose during the 100 ns MD simulation. Distances were measured between OE1 of Glu175, ND2 of Glu268 and OE1 of Glu174 with the O7 and O4 atoms of xylobiose. OE1 and ND2 of the catalytic residues are oxygen and nitrogen atoms, respectively. O7 and O4, part of the hydroxyl groups of xylobiose are the oxygen atoms. Distances below 3.5 Å for Glu175 and Glu268 confirm their stable interactions with the ligand, whereas Glu174 shows more variable contacts, suggesting a transient role in substrate stabilization.

4.3.8 Small angle X-ray scattering analyses of *Ac*GH30A

The recombinant *Ac*GH30A consisting of a GH30A family catalytic module (433 aa) and the dockerin 1 (68 aa) including the linker sequence of 5 amino acids between the modules was cloned, expressed and purified (Chapter 3). The SDS-PAGE analysis showed the estimated molecular mass of 58 kDa (Section 3.3.3). The experimentally estimated molecular mass of *Ac*GH30A was similar to the theoretical molecular mass of 57.78 kDa calculated by the ExPASy ProtParam server along with the theoretical isoelectric pH of 5.22.

The structural conformation of *Ac*GH30A in solution was assessed through SAXS studies. The SAXS data for *Ac*GH30A at a concentration of 3.0 $mg.ml^{-1}$ were processed, analysed, and the findings are presented in Table 4.4. The monodisperse nature of the *Ac*GH30A was confirmed through the visual inspection and initial processing of the *Ac*GH30A scattering profiles (Fig. 4.12A). Analysis of the P(R) function, derived from the Fourier transformation of *Ac*GH30A scattering profiles, displayed a symmetric distribution, characteristic of globular macromolecules (Fig. 4.12B), indicating the presence of *Ac*GH30A in its monomeric state. The maximum diameter (D_{max}) and R_g of *Ac*GH30A, calculated from the P(R) plot were 10.88 nm and 3.6 nm, respectively. The D_{max} is 3.02 times greater than the R_g, indicating that *Ac*GH30A adopts an extended, non-globular conformation. The overall compactness and conformational flexibility of *Ac*GH30A in solution were further evaluated using Kratky plot analysis (Fig. 4.12C). The Kratky plot analysis of *Ac*GH30A revealed bell-shaped peaks in the low q-region, corroborating a compact and folded structure, consistent with previous reports (Ernst et al., 2020). Guinier analysis showed that the R_g of *Ac*GH30A for globular and rod shape was 3.59 ± 0.44 nm and 1.07 ± 0.01 nm,

respectively. The persistence length (L) of the *Ac*GH30A molecule was found to be 11.87 nm. The linear behaviour of the fit line in the low q-region of the Guinier plot indicated the absence of aggregation and the monodispersity of *Ac*GH30A (Fig. 4.12D).

Table 4.4. SAXS data collection and derived parameters of *Ac*GH30A at 3.0 mg.ml^{-1}.

Data-collection parameters	***Ac*GH30A**
Instrument	SAXSpace Anton-Paar
Wavelength (Å)	1.54
Q range (nm^{-1})	0.135-5.95
Exposure time (min)	30 x 2
Temperature (°C)	10
Protein Concentration (mg.ml^{-1})	3
Structural parameters	
Q range (nm^{-1}) used for R_g analysis	1.6-3.5
$I(0)$ au from Guinier	72349.9 ± 6667.96
R_g nm from Guinier	3.59 ± 0.44
$I(0)$ from P(r)	66530
R_g nm from P(r)	3.6
D_{max} (nm)	10.88
Porod volume estimate (nm^3)	91.9
Persistent length (nm)	11.87
Resolution (nm)	5.0
Molecular mass determination	
Theoretical molecular mass (kDa)	57.79
Molecular mass from Qp (kDa)	58.27
Modelling parameters	
χ^2	0.3123
NSD	0.866 ± 0.087
Software employed	
Data processing	primus
P(r) function calculation	GNOM
Ab initio modeling	DAMMIF
Validation and averaging	DAMAVER
Structure superposition	SUPCOMB
3D graphical representation	UCSF Chimera

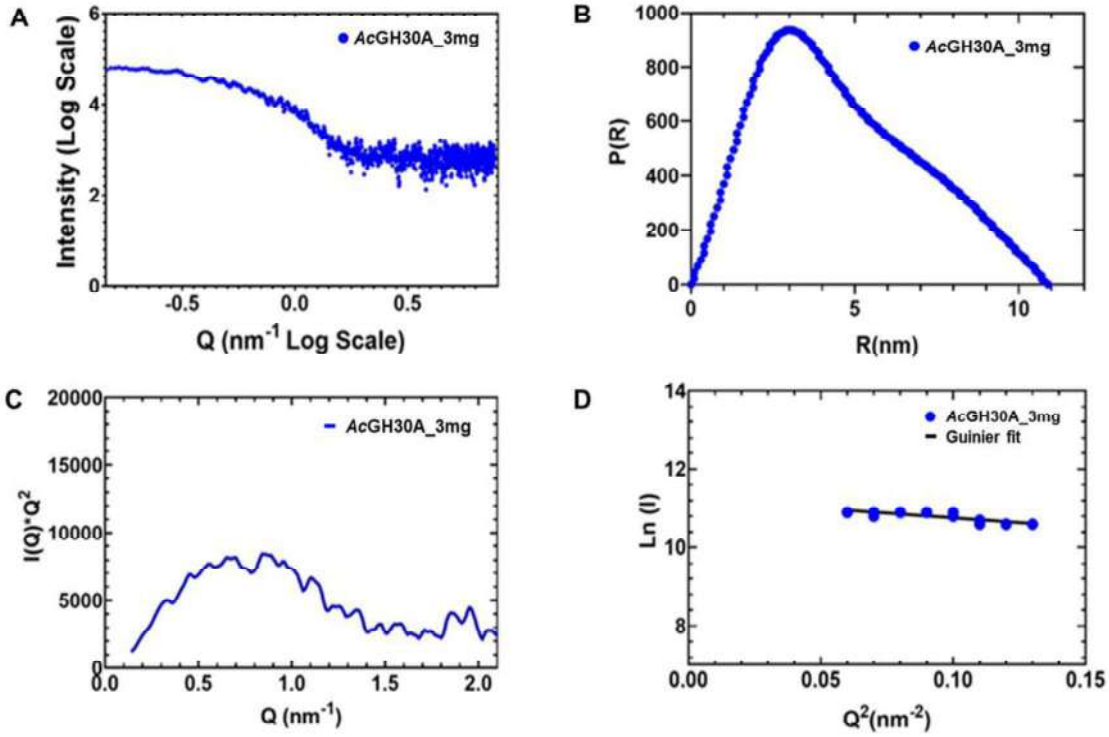

Fig. 4.12 SAXS analysis of *Ac*GH30A at 3.0 mg.ml^{-1}. (A) Intensity profile obtained through SAXS, (B) P(R) curve of *Ac*GH30A as a function of R, (C) Kratky plot of SAXS data, and (D) Guinier plot of the SAXS intensities.

The molecular mass of *Ac*GH30A, determined from the SAXS scattering profile using the Qp package, was found to be 58.27 kDa. This value aligns closely with both the theoretically and experimentally determined molecular mass of 57.79 kDa, further indicating the presence monomeric state of *Ac*GH30A in the solution. A total of 20 reconstructed models were averaged to develop the most representative *ab initio* model using DAMAVER (Ficko-Blean et al., 2009). The *ab initio* model generated by the DAMAVER program revealed a structure consists of two globular structures, one significantly larger than the other. The molecular shape of the *ab initio* model showed an earbud-shaped envelope. When the *ab initio* model was overlayed with the 3D model of *Ac*GH30A, it evidently showed that the large globular structure belongs to the catalytic module of the enzyme and the smaller one corresponds to the dockerin 1

module (Fig. 4.13). Both the *ab initio* and 3D model of *Ac*GH30A showed high similarity in terms of globularity and the shape. The χ^2 value of 0.3123 indicates excellent agreement between the experimental SAXS data and the theoretical scattering from the model (Table 4.4). The NSD value of 0.866 ± 0.087 reflects high consistency among independent *ab initio* models. Together, these parameters confirm the accuracy and reliability of the SAXS model of *Ac*GH30A.

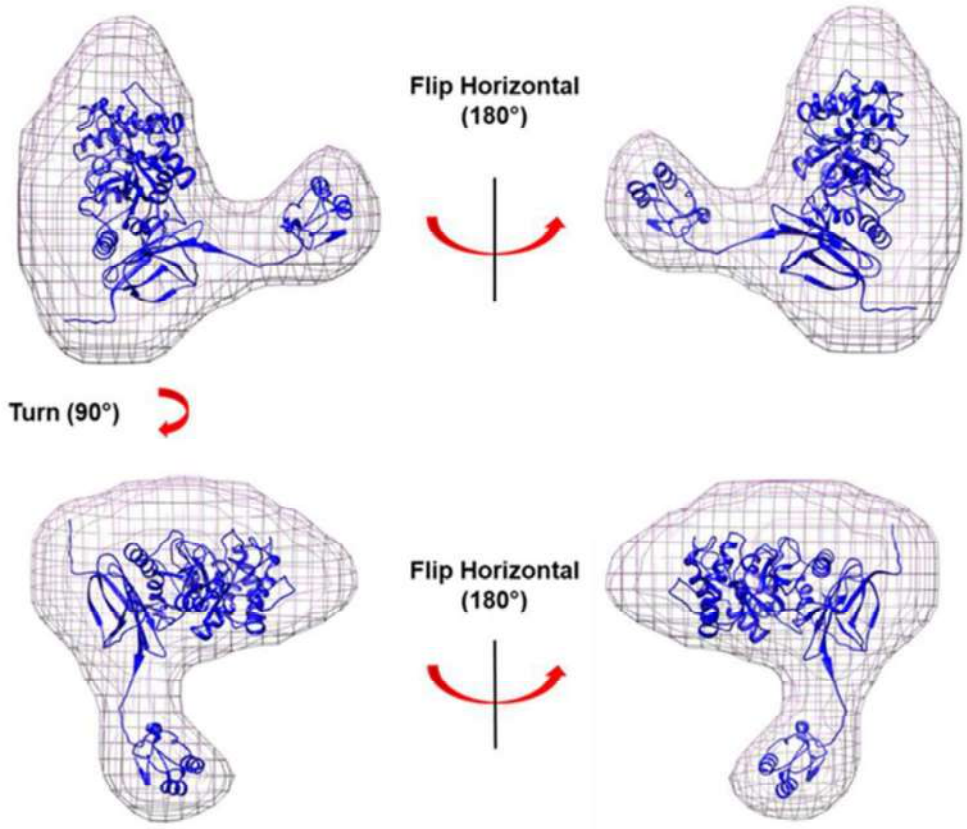

Fig. 4.13 SAXS envelope of *Ac*GH30A at a protein concentration of 3 mg.mL^{-1}, visualized from multiple orientations. The *ab initio* molecular envelope of *Ac*GH30A was fitted with its structural model using UCSF Chimera.

4.3.9 Dynamic light scattering (DLS) analysis of *Ac*GH30A

DLS examination of particle diameter in relation to scattering intensity (%) for *Ac*GH30A at protein concentrations of 1 and 3 mg.mL^{-1} and in the presence of xylobiose exhibited singular peaks, indicating the exceptional monodispersity of *Ac*GH30A (Fig. 4.14). The hydrodynamic diameter (D_h) at both 1 and 3 mg.mL^{-1} concentrations was 7.4 nm, with a hydrodynamic radius (R_h) of 3.7 nm, consistent with the SAXS data. The hydrodynamic radius of the protein is close to the value of R_g, which was determined to be 3.6 nm by SAXS analysis. The addition of xylobiose did not show any change in the D_h of *Ac*GH30A, resulting in a constant R_h of 3.7 nm. However, a slight increase in the scattering intensity of *Ac*GH30A was observed in the presence of xylobiose as compared with *Ac*GH30A only. Moreover, the scattering intensity further increased as the concentration of xylobiose was increased in the mixture.

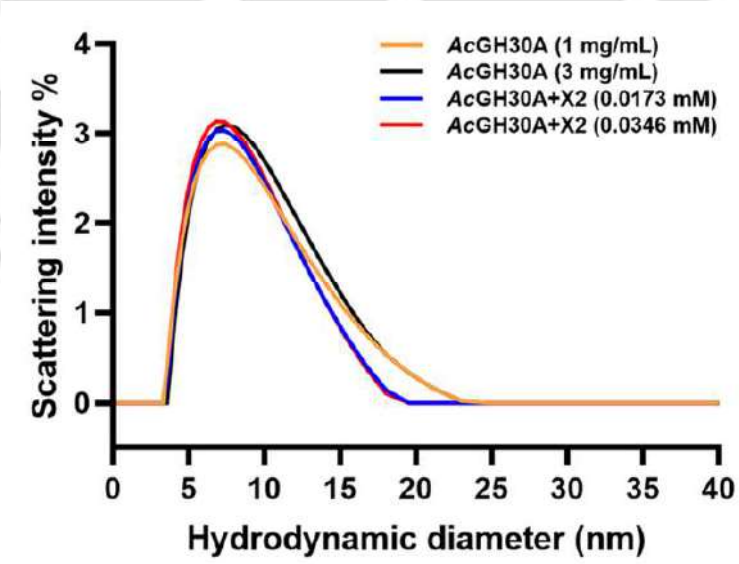

Fig. 4.14 Particle diameter analysis of *Ac*GH30A at different concentrations of 1.0 mg.mL^{-1} (orange) and 3.0 mg.mL^{-1} (black) and in the presence of two different concentrations of xylobiose (X2), 0.0173 mM (blue) and 0.0346 mM (red) by DLS. The final concentration of *Ac*GH30A mixed with X2 was 1 mg.mL^{-1}.

4.4 Conclusion

A high-quality homology model of *Ac*GH30A, generated from Alphafold2, demonstrated structural accuracy, supported by Ramachandran plot analysis and secondary structure assessments. The Ramachandran plot depicted that the favoured and allowed regions contained 100% of the amino acids and no residue in the disallowed region. The 3-dimensional model of *Ac*GH30A showed an overall quality score of 93.6% in the ERRAT server analysis. The secondary structure analysis of *Ac*GH30A in an aqueous environment using circular dichroism and *in silico* modeling revealed an α/β/α sandwich structure with a central β-barrel comprising eight β-strands. CD analysis revealed that *Ac*GH30A contained 21.94% α-helices, 20.98% β-sheets and 57.08% random coils aligning closely with the prediction results from Psipred, SOPMA and 2Struc servers. The molecular docking analysis revealed a significant binding affinity of *Ac*GH30A with xylobiose with a binding free energy of -4.3 kcal.mol^{-1}, showcasing polar interactions with the catalytic amino acids, validating the xylobiohydrolase activity of *Ac*GH30A. The molecular docking study suggested a retaining type mechanism supported by the positioning of xylobiose between the catalytic residues Glu175 and Glu268. The -1 subsite was predominantly composed of Trp123, Glu175, Asn174, and Glu268 residues forming hydrogen bonds with xylobiose. Isothermal titration calorimetry determined the high binding affinity of *Ac*GH30A with xylobiose with an association constant (K_a) of 7.83×10^5 M^{-1}. Molecular dynamics simulations revealed consistent conformational alterations in *Ac*GH30A following the binding of the ligand, evidenced by reduced RMSD, R_g, and SASA values of the docked complex with xylobiose compared to the free *Ac*GH30A. The average RMSD, R_g and SASA values of *Ac*GH30A in the docked complex declined by 0.39 nm,

0.32 nm and 22.57 nm^2, respectively. These reduced values confirmed the compactness and stability of *Ac*GH30A-ligand complex. MD simulations further highlighted the crucial role of Glu175 in hydrogen bonding with the ligand, which acts as an acid or base. Small-angle X-ray scattering (SAXS) studies confirmed the monodispersity and compact globular structure of *Ac*GH30A in aqueous environment, showcasing its molecular shape resembling an earbud. The DLS analysis of *Ac*GH30A also showed the monodisperse state with a hydrodynamic radius (R_h) of 3.7 nm. This comprehensive study highlights the mode of action of *Ac*GH30A as a xylobiohydrolase, shedding light on its unique structural and functional features. This study will enrich our understanding of industrial xylanases, particularly in terms of their structure and functions, which will facilitate rational enzyme engineering to improve their properties.

References

1. Ahmed, J., Kumar, K., Sharma, K., Fontes, C. M. G. A., & Goyal, A. (2021) Computational and SAXS-based structure insights of pectin acetyl esterase (*Ct*Pae12B) of family 12 carbohydrate esterase from *Clostridium thermocellum* ATCC 27405. *Journal of Biomolecular Structure and Dynamics*, *40*, 18. https://doi.org/10.1080/07391102.2021.1911858.
2. Balasubramaniam, K., Sharma, K., & Goyal, A. (2019) Structure and dynamics analysis of a new member heparinase II/III of family 12 polysaccharide lyase from *Pseudopedobacter saltans* by computational modeling and small-angle X-ray scattering. *Journal of Biomolecular Structure and Dynamics*. https://doi.org/10.1080/07391102.2019.1622453.
3. Berendsen, H. J. C., van der Spoel, D., & van Drunen, R. (1995) GROMACS: A message-passing parallel molecular dynamics implementation. *Computer Physics communications*, *91*, 43–56. https://doi.org/10.1016/0010-4655(95)00042-E.
4. Brüx, C., Ben-David, A., Shallom-Shezifi, D., Leon, M., Niefind, K., Shoham, G., Shoham, Y., & Schomburg, D. (2006) The structure of an inverting GH43 β-Xylosidase from *Geobacillus stearothermophilus* with its substrate reveals the role of the three catalytic residues. *Journal of Molecular Biology, 359*, 97–109. https://doi.org/10.1016/j.jmb.2006.03.005.
5. Chen, L., Du, J.-L., Zhan, Y.-J., Li, J.-A., Zuo, R.-R., & Tian, S. (2018) Consolidated bioprocessing for cellulosic ethanol conversion by cellulase–xylanase cell-surfaced yeast consortium. *Preparative Biochemistry and Biotechnology, 48*, 653–661. https://doi.org/10.1080/10826068.2018.1487846.
6. Collins, T., Gerday, C., & Feller, G. (2005) Xylanases, xylanase families and extremophilic xylanases, *FEMS Microbiology Reviews, 29*, 3–23. https://doi.org/10.1016/j.femsre.2004.06.005.
7. Curry, T. M., Peña, M. J., & Urbanowicz, B. R. (2023) An update on xylan structure, biosynthesis, and potential commercial applications, *The Cell Surface, 9*, 100101. https://doi.org/10.1016/j.tcsw.2023.100101.
8. Davies, G., & Henrissat, B. (1995) Structures and mechanisms of glycosyl hydrolases. *Structure, 3,* 853–859. https://doi.org/10.1016/S0969-2126(01)00220-9.
9. El Enshasy, H. A., Kandiyil, S. K., Malek, R., & Othman, N. Z. (2016) Microbial Xylanases: Sources, Types, and Their Applications, in: V.K. Gupta (Ed.), *Microbial Enzymes in Bioconversions of Biomass* (Vol. 3, pp. 151–213). *Springer International Publishing*. https://doi.org/10.1007/978-3-319-43679-1_7.
10. Ernst, H. A., Mosbech, C., Langkilde, A. E., Westh, P., Meyer, A. S., Agger, J. W., & Larsen, S. (2020) The structural basis of fungal glucuronoyl esterase activity on natural substrates. *Nature Communications*, *11*, 1–12. https://doi.org/10.1038/s41467-020-14833-9.

11. Ficko-Blean, E., Gregg, K. J., Adams, J. J., Hehemann, J.-H., Czjzek, M., Smith, S. P., & Boraston, A. B. (2009) Portrait of an enzyme, a complete structural analysis of a multimodular β-N-Acetylglucosaminidase from *Clostridium perfringens*. *Journal of Biological Chemistry, 284*, 9876–9884. https://doi.org/10.1074/jbc.M808954200.

12. Fonseca-Maldonado, R., Ribeiro, L. F., Furtado, G. P., Arruda, L. M., Meleiro, L. P., Alponti, J. S., Botelho-Machado, C., Vieira, D. S., Bonneil, E., & Furriel, R. dos P. M. (2014) Synergistic action of co-expressed xylanase/laccase mixtures against milled sugar cane bagasse. *Process Biochemistry, 49,* 1152–1161. https://doi.org/10.1016/j.procbio.2014.03.027.

13. Gao, C., Guo, L., Ding, Q., Hu, G., Ye, C., Liu, J., Chen, X., & Liu, L. (2020) Dynamic consolidated bioprocessing for direct production of xylonate and shikimate from xylan by *Escherichia coli*. *Metabolic Engineering, 60*, 128–137. https://doi.org/10.1016/j.ymben.2020.04.001.

14. Gasteiger, E., Hoogland, C., Gattiker, A., Duvaud, S., Wilkins, M. R., Appel, R. D., & Bairoch, A. (2005) Protein identification and analysis tools on the ExPASy Server, in: J.M. Walker (Ed.), *The Proteomics Protocols Handbook* (pp. 571–607). *Humana Press,* Totowa. https://doi.org/10.1385/1-59259-890-0:571.

15. Geourjon, C., & Deléage, G. (1995) SOPMA: significant improvements in protein secondary structure prediction by consensus prediction from multiple alignments. *Bioinformatics, 11*, 681–684. https://doi.org/10.1093/bioinformatics/11.6.681.

16. Greenfield, N. J. (2006) Using circular dichroism spectra to estimate protein secondary structure. *Nature Protocols, 1,* 2876–2890. https://doi.org/10.1038/nprot.2006.202.

17. He, J., Su, L., Sun, X., Fu, J., Chen, J., & Wu, J. (2014) A novel xylanase from *Streptomyces sp*. FA1: purification, characterization, identification, and heterologous expression. *Biotechnology and Bioprocess Engineering, 19*, 8–17. https://doi.org/10.1007/s12257-013-0490-2.

18. Henrissat, B., Callebaut, I., Fabrega, S., Lehn, P., Mornon, J. P., & Davies, G. (1995) Conserved catalytic machinery and the prediction of a common fold for several families of glycosyl hydrolases. *Proceedings of the National Academy of Sciences, 92*, 7090–7094. https://doi.org/10.1073/pnas.92.15.7090.

19. Henrissat, B., & Davies, G. (1997) Structural and sequence-based classification of glycoside hydrolases. *Current Opinion in Structural Biology, 7*, 637–644. https://doi.org/10.1016/S0959-440X(97)80072-3.

20. Hess, B., Kutzner, C., van der Spoel, D., & Lindahl, E. (2008) GROMACS 4: Algorithms for highly efficient, load-balanced, and scalable molecular simulation. *Journal of Chemical Theory and Computation, 4*, 435–447. https://doi.org/10.1021/ct700301q.

21. Jones, P., Binns, D., Chang, H.-Y., Fraser, M., Li, W., McAnulla, C., McWilliam, H., Maslen, J., Mitchell, A., Nuka, G., Pesseat, S., Quinn, A. F., Sangrador-Vegas, A., Scheremetjew, M., Yong, S.-Y., Lopez, R., & Hunter, S. (2014) InterProScan 5: genome-scale protein function classification. *Bioinformatics, 30*, 1236–1240. https://doi.org/10.1093/bioinformatics/btu031.

22. Jumper, J., Evans, R., Pritzel, A., Green, T., Figurnov, M., Ronneberger, O., Tunyasuvunakool, K., Bates, R., Žídek, A., Potapenko, A., Bridgland, A., Meyer, C., Kohl, S. A. A., Ballard, A. J., Cowie, A., Romera-Paredes, B., Nikolov, S., Jain, R., Adler, J. Hassabis, D. (2021) Highly accurate protein structure prediction with AlphaFold. *Nature, 596*, 583–589. https://doi.org/10.1038/s41586-021-03819-2.

23. Juturu, V., & Wu, J. C. (2012) Microbial xylanases: Engineering, production and industrial applications. *Biotechnology Advances, 30*, 1219–1227. https://doi.org/10.1016/j.biotechadv.2011.11.006.

24. Kadowaki, M. A. S., Briganti, L., Evangelista, D. E., Echevarría-Poza, A., Tryfona, T., Pellegrini, V. O. A., Nakayama, D. G., Dupree, P., & Polikarpov, I. (2021) Unlocking the structural features for the xylobiohydrolase activity of an unusual GH11 member identified in a compost-derived consortium. *Biotechnology and Bioengineering, 118*, 4052–4064. https://doi.org/10.1002/bit.27880.

25. Katsimpouras, C., Dedes, G., Thomaidis, N. S., & Topakas, E. (2019) A novel fungal GH30 xylanase with xylobiohydrolase auxiliary activity. *Biotechnology for Biofuels, 12,* 1–14. https://doi.org/10.1186/s13068-019-1455-2.

26. Klose, D. P., Wallace, B. A., & Janes, R. W. (2010) 2Struc: the secondary structure server. *Bioinformatics, 26*, 2624–2625. https://doi.org/10.1093/bioinformatics/btq480.

27. Land, H., & Humble, M. S. (2018) YASARA: A tool to obtain structural guidance in biocatalytic investigations. *Protein engineering: Methods and protocols,* 1685, 43–67. https://doi.org/10.1007/978-1-4939-7366-8_4.

28. Laskowski, R. A., Jabłońska, J., Pravda, L., Vařeková, R. S., & Thornton, J. M. (2018) PDBsum: Structural summaries of PDB entries. *Protein Science, 27*, 129–134. https://doi.org/10.1002/pro.3289.

29. Laskowski, R. A., & Swindells, M. B. (2011) LigPlot+: Multiple ligand–protein interaction diagrams for drug discovery. *Journal of Chemical Information and Modeling, 51*, 2778–2786. https://doi.org/10.1021/ci200227u.

30. Louis-Jeune, C., Andrade-Navarro, M. A., & Perez-Iratxeta, C. (2012) Prediction of protein secondary structure from circular dichroism using theoretically derived spectra. *Proteins: Structure, Function, and Bioinformatics, 80*, 374–381. https://doi.org/10.1002/prot.23188.

31. Lüthy, R., Bowie, J. U., & Eisenberg, D. (1992) Assessment of protein models with three-dimensional profiles. *Nature, 356*, 83–85. https://doi.org/10.1038/356083a0.

32. MacArthur, M. W., Laskowski, R. A., & Thornton, J. M. (1994) Knowledge-based validation of protein structure coordinates derived by X-ray crystallography and NMR spectroscopy. *Current Opinion in Structural Biology, 4*, 731–737. https://doi.org/10.1016/S0959-440X(94)90172-4.

33. Madeira, F., Pearce, M., Tivey, A. R. N., Basutkar, P., Lee, J., Edbali, O., Madhusoodanan, N., Kolesnikov, A., & Lopez, R. (2022) Search and sequence analysis tools services from EMBL-EBI in 2022. *Nucleic Acids Research*, W276-W279. https://doi.org/10.1093/nar/gkac240.

34. Maehara, T., Yagi, H., Sato, T., Ohnishi-Kameyama, M., Fujimoto, Z., Kamino, K., Kitamura, Y., St John, F., Yaoi, K., & Kaneko, S. (2018) GH30 glucuronoxylan-specific xylanase from *Streptomyces turgidiscabies* C56. *Applied and Environmental Microbiology, 84.* https://doi.org/10.1128/AEM.01850-17.

35. McGuffin, L. J., Bryson, K., & Jones, D. T. (2000) The PSIPRED protein structure prediction server. *Bioinformatics, 16*, 404–405. https://doi.org/10.1093/bioinformatics/16.4.404.

36. Mirdita, M., Schütze, K., Moriwaki, Y., Heo, L., Ovchinnikov, S., & Steinegger, M. (2022) ColabFold: making protein folding accessible to all. *Nature Methods, 19*, 679–682. https://doi.org/10.1038/s41592-022-01488-1.

37. Moreira, L. R. S. (2016) Insights into the mechanism of enzymatic hydrolysis of xylan. *Applied Microbiology and Biotechnology, 100*, 5205–5214. https://doi.org/10.1007/s00253-016-7555-z.

38. Morris, G. M., Huey, R., Lindstrom, W., Sanner, M. F., Belew, R. K., Goodsell, D. S., & Olson, A. J. (2009) AutoDock4 and AutoDockTools4: Automated docking with selective receptor flexibility. *Journal of Computational Chemistry, 30*. https://doi.org/10.1002/jcc.21256.

39. Nakamichi, Y., Watanabe, M., Matsushika, A., & Inoue, H. (2020) Substrate recognition by a bifunctional GH30-7 xylanase B from *Talaromyces cellulolyticus. FEBS Open Bio, 10*, 1180–1189. https://doi.org/10.1002/2211-5463.12873.

40. Nikolaivits, E., Pentari, C., Kosinas, C., Feiler, C. G., Spiliopoulou, M., Weiss, M. S., Dimarogona, M., & Topakas, E. (2021) Unique features of the bifunctional GH30 from *Thermothelomyces thermophila* revealed by structural and mutational studies. *Carbohydrate Polymers, 273,* 118553. https://doi.org/10.1016/j.carbpol.2021.118553.

41. O'Boyle, N. M., Banck, M., James, C. A., Morley, C., Vandermeersch, T., & Hutchison, G. R. (2011) Open Babel: An open chemical toolbox. *Journal of Cheminformatics, 3*, 33. https://doi.org/10.1186/1758-2946-3-33.

42. Okuyama, M., Kitamura, M., Hondoh, H., Kang, M.-S., Mori, H., Kimura, A., Tanaka, I., & Yao, M. (2009) Catalytic mechanism of retaining α-galactosidase belonging to glycoside hydrolase family 97. *Journal of Molecular Biology, 392*, 1232–1241. https://doi.org/10.1016/j.jmb.2009.07.068.

43. Pettersen, E. F., Goddard, T. D., Huang, C. C., Couch, G. S., Greenblatt, D. M., Meng, E. C., & Ferrin, T. E. (2004) UCSF Chimera—a visualization system for exploratory research and analysis. *Journal of Computational Chemistry, 25(13),* 1605-1612. https://doi.org/10.1002/jcc.20084.

44. Puchart, V., Šuchová, K., & Biely, P. (2021) Xylanases of glycoside hydrolase family 30–An overview, *Biotechnology Advances*, 107704. https://doi.org/10.1016/j.biotechadv.2021.107704.

45. Ren, J., Wen, L., Gao, X., Jin, C., Xue, Y., & Yao, X. (2009) DOG 1.0: illustrator of protein domain structures. *Cell Research, 19*, 271–273. https://doi.org/10.1038/cr.2009.6.

46. Robert, X., & Gouet, P. (2014) Deciphering key features in protein structures with the new ENDscript server. *Nucleic Acids Research, 42,* W320–W324. https://doi.org/10.1093/nar/gku316.

47. Roblin, P., Potocki-Véronèse, G., Guieysse, D., Guérin, F., Axelos, M. A. V., Perez, J., & Buleon, A. (2013) SAXS conformational tracking of amylose synthesized by amylosucrases. *Biomacromolecules, 14*, 232–239. https://doi.org/10.1021/bm301651y.

48. Rohman, A., Dijkstra, B. W., & Puspaningsih, N. N. T. (2019) β-Xylosidases: Structural diversity, catalytic mechanism, and inhibition by monosaccharides. *International Journal of Molecular Sciences, 20*, 5524. https://doi.org/10.3390/ijms20225524.

49. Schüttelkopf, A. W., & van Aalten, D. M. F. (2004) PRODRG: a tool for high-throughput crystallography of protein–ligand complexes. *Acta Crystallographica Section D: Biological Crystallography, 60,* 1355–1363. https://doi.org/10.1107/S0907444904011679.

50. St John, F. J., Crooks, C., Kim, Y., Tan, K., & Joachimiak, A. (2022) The first crystal structure of a xylobiose-bound xylobiohydrolase with high functional specificity from the bacterial glycoside hydrolase family 30, subfamily 10. *FEBS letters, 596*, 2449–2464. https://doi.org/10.1002/1873-3468.14454.

51. St John, F. J., Dietrich, D., Crooks, C., Balogun, P., de Serrano, V., Pozharski, E., Smith, J. K., Bales, E., & Hurlbert, J. (2018) A plasmid borne, functionally novel glycoside hydrolase family 30 subfamily 8 endoxylanase from solventogenic *Clostridium*. *Biochemical Journal, 475*, 1533–1551. https://doi.org/10.1042/BCJ20180050.

52. St John, F. J., Dietrich, D., Crooks, C., Pozharski, E., González, J. M., Bales, E., Smith, K., & Hurlbert, J. C. (2014) A novel member of glycoside hydrolase family 30 subfamily 8 with altered substrate specificity. *Acta Crystallographica Section D: Biological Crystallography, 70*, 2950–2958. https://doi.org/10.1107/S1399004714019531.

53. Šuchová, K., Chyba, A., Hegyi, Z., Rebroš, M., & Puchart, V. (2022) Yeast GH30 xylanase from *Sugiyamaella lignohabitans* is a glucuronoxylanase with auxiliary xylobiohydrolase activity. *Molecules. 27*, 751. https://doi.org/10.3390/molecules27030751.

54. Šuchová, K., Puchart, V., Spodsberg, N., Mørkeberg Krogh, K. B. R., & Biely, P. (2020) A novel GH30 xylobiohydrolase from *Acremonium alcalophilum* releasing xylobiose from the non-reducing end. *Enzyme and Microbial Technology, 134*, 109484. https://doi.org/10.1016/j.enzmictec.2019.109484.

55. Šuchová, K., Puchart, V., Spodsberg, N., Mørkeberg Krogh, K. B. R., & Biely, P. (2021) Catalytic diversity of GH30 xylanases. *Molecules. 26*, 4528. https://doi.org/10.3390/molecules26154528.

56. Thakur, A., Sharma, K., & Goyal, A. (2019) α-L-arabinofuranosidase: a potential enzyme for the food industry, *in: Green Bio-Processes* (pp. 229–244). *Springer.* https://doi.org/10.1007/978-981-13-3263-0_12.

57. Tian, W., Chen, C., Lei, X., Zhao, J., & Liang, J. (2018) CASTp 3.0: computed atlas of surface topography of proteins. *Nucleic Acids Research, 46*, W363–W367. https://doi.org/10.1093/nar/gky473.

58. Urbániková, Ľ., Vršanská, M., Mørkeberg Krogh, K. B. R., Hoff, T., & Biely, P. (2011) Structural basis for substrate recognition by *Erwinia chrysanthemi* GH30 glucuronoxylanase. *The FEBS Journal, 278,* 2105–2116. https://doi.org/10.1111/j.1742-4658.2011.08127.x.

59. Verma, A. K., & Goyal, A. (2016) A novel member of family 30 glycoside hydrolase subfamily 8 glucuronoxylan endo-β-1, 4-xylanase (*Ct*XynGH30) from *Clostridium thermocellum* orchestrates catalysis on arabinose decorated xylans. *Journal of Molecular Catalysis B: Enzymatic.* 129, 6–14. https://doi.org/10.1016/j.molcatb.2016.04.001.

60. Vuong, T. V., & Wilson, D. B. (2010) Glycoside hydrolases: Catalytic base/nucleophile diversity. *Biotechnology and Bioengineering, 107*, 195–205. https://doi.org/10.1002/bit.22838.

61. Wiederstein, M., & Sippl, M. J. (2007) ProSA-web: interactive web service for the recognition of errors in three-dimensional structures of proteins. *Nucleic Acids Research, 35*, W407–W410. https://doi.org/10.1093/nar/gkm290.

62. Yuan, S., Chan, H. C. S., & Hu, Z. (2017) Using PyMOL as a platform for computational drug design. *Wiley Interdisciplinary Reviews: Computational Molecular Science,* 7. https://doi.org/10.1002/wcms.1298

Chapter 5

Enzymatic degumming of Ramie (*Boehmeria nivea*) bast fibres and Pineapple (*Ananas comosus*) leaf fibres by xylobiohydrolase, mannanase and pectate lyase

5.1 Introduction

Natural fibres are increasingly valued for their renewable, biodegradable, and sustainable nature, making them vital resources in a wide range of industries, especially textiles (Kozłowski & Mackiewicz-Talarczyk, 2020). Among these, ramie (*Boehmeria nivea*) bast fibres and pineapple (*Ananas comosus*) leaf (PAL) fibres have attracted considerable attention due to their unique properties and broad applicability. Ramie, often referred to as the "queen of natural fibres," is renowned for its exceptional luster, high tenacity and microbial resistivity, as well as its silk-like appearance, making it a highly desirable material in clothing fabrics, industrial packaging, canvas and twines (Rehman et al., 2019). Similarly, PAL fibre is a strong and stiff fibre known for its excellent mechanical properties and potential as a sustainable alternative to synthetic fibres (Asim et al., 2015). Despite their promising characteristics, the effective processing of these fibres remains challenging due to their inherent structural complexity and the presence of non-cellulosic components (Zhu et al., 2022). Both

ramie and PAL fibres are well-suited for textile applications and enzymatic degumming due to their high cellulose content, which provides strength and durability. However, their processing presents unique challenges (Saxena et al., 2017). In India, while ramie fibres are traditionally processed, pineapple leaves are often discarded as agricultural waste after harvest, creating a disposal problem for farmers. This underutilized biomass holds significant potential for the production of high-value fibres, provided efficient and sustainable extraction technologies are implemented. Despite India being one of the leading producers of pineapple, particularly the Queen variety in Assam, the lack of advanced technologies for fibre extraction and value addition limits its utilization (Saloni et al., 2017). Other countries such as Brazil, by contrast, have developed markets for value-added products derived from pineapple leaves, highlighting the need for technological advancements in India.

The raw fibres, *viz.* ramie and PAL fibres, are primarily composed of cellulose, which constitutes 65–75% in ramie and 69.5–71.5% in PAL fibres (Jose et al., 2016; Li et al., 2016). However, they are embedded in a matrix of non-cellulosic substances such as pectin, hemicellulose, lignin and wax, collectively referred to as "gums." These components bind the fibres together, making mechanical separation difficult and reducing their suitability for industrial applications. In ramie, the gum content ranges from 20–30%, comprising 4–5% pectin, 14–16% hemicellulose and 0.8–1.5% lignin (Li et al., 2016). PAL contains 4.4–4.7% lignin, 1.0–1.2% pectin, 19.5% hemicelluloses and other impurities (Daud et al., 2014; Jose et al., 2016). These gummy substances must be removed to yield pure cellulose fibres with desirable properties, such as enhanced hydrophilicity and dyeing efficiency (Ding et al., 2023). However, conventional degumming methods, which often involve chemical treatments with

sodium hydroxide, are associated with several drawbacks, including fibre damage, high energy consumption and the generation of hazardous effluents (Lyu et al., 2021).

The challenges associated with chemical degumming leads to the search for environmentally sustainable alternatives (Shadhin et al., 2023). Enzymatic degumming has emerged as a promising biotechnological approach for processing plant fibres (Subash & Muthiah, 2021). Unlike chemical methods, enzymes are substrate-specific, targeting pectin, hemicellulose and other non-cellulosic components without degrading the cellulose matrix. This precision minimizes fibre damage and improves fibre quality, yielding softer, more desirable textures for textile applications (Subash & Muthiah, 2021). Moreover, enzymatic degumming is less energy-intensive, reduces environmental contamination and shortens processing time. Enzymatic degumming significantly reduces wastewater generation compared to chemical methods, aligning with green technology initiatives in the textile industry (Amankwah et al., 2024).

In this study, an eco-friendly enzymatic degumming approach was developed and optimized for ramie and PAL fibres using three carbohydrate-active enzymes: xylobiohydrolase, pectate lyase, and mannanase. These enzymes play a critical role in selectively breaking down gum components, producing fibres with minimal residual gum content. Mannanase and xylobiohydrolase degrade hemicelluloses in plant fibres. Mannanase breaks down mannans (Wang et al., 2017a), while xylanase targets xylans (Mendonça et al., 2023). Pectinase is crucial in enzymatic degumming as it degrades pectic substances (Haile & Ayele, 2022). These enzymes loosen cell structures, enhancing their reach, improving gum degradation efficiency. Xylobiohydrolase degrades xylan, disrupting cross-links with cellulose and pectin, while pectate lyase cleaves pectin, weakening the pectin–cellulose interface. Mannanase further breaks

down galactomannans, reducing the cohesion of matrix components. This combined enzymatic activity leads to structural weakening, increased porosity, and reduced fibre bundle adhesion, making gum removal more efficient.

Recent research efforts have explored various enzymatic formulations and microbial sources to optimize degumming efficiency of ramie and PAL fibres. The enzymatic degumming of ramie was optimized using a thermoalkaliphilic xylanase from *Bacillus halodurans* CM1 and a commercial pectinase (Suhendar et al., 2024). Their optimal conditions (50°C, 3h) resulted in a significant increase in brightness and reducing sugar yield indicating efficient impurity removal and polysaccharide breakdown (Suhendar et al., 2024). Treatment of ramie fibres by an alkaline pectate lyase, BacPelA, at 60°C and pH 10.0 for 4 h showed a significant weight loss of 20.5% indicating its effectiveness in breaking down the pectin that holds the fibres together (Zhou et al., 2023). A recombinant alkaline thermostable β-mannanase (ManB) from *Thermobifida fusca* exhibited high stability in alkaline conditions (Wang et al., 2017). When ManB was combined with *Bacillus* sp. HG-28, producing pectinase and xylanase, degumming efficiency of ramie fibres improved from 13% with ManB alone to 75.2%, demonstrating the synergistic potential of multiple enzymes (Wang et al., 2017). Bio-degumming of raw pineapple leaves using multiple degumming-related enzymes secreted by *Bacillus subtilis* XW-18 was reported (Tan et al., 2025). They showed that *B. subtilis* XW-18 produces a rich combination of pectin-degrading, hemicellulose-degrading and lignin-degrading enzymes. The results showed that *B. subtilis* XW-18 effectively degummed raw pineapple leaves, crushed leaves and manually extracted fibres, producing high-quality fibres with superior physical and mechanical properties. The synergistic action of multiple enzymes is crucial for

efficient microbial or enzymatic degumming, displaying the potential of *B. subtilis* XW-18 for degumming applications (Tan et al., 2025). The use of laccase and xylanase enzymes in low-concentration alkaline-pretreated PAL fibres have shown to effectively increase cellulose content from 57% to 74% while reducing the lignin and hemicellulose contents (Tian et al., 2023). Despite these advancements, no study has specifically evaluated the combined action of xylobiohydrolase, pectate lyase, and mannanase for degumming ramie and PAL fibres. Our study aims to address this gap by formulating and optimizing a novel enzymatic treatment tailored to these fibres. The goal was to enhance the fibre quality while ensuring sustainability, making this approach a viable alternative to chemical degumming.

Enzymatic degumming not only addresses the limitations of conventional methods, but also aligns with the principles of sustainable development (Subash & Muthiah, 2021). By reducing environmental impacts and enhancing fibre properties, this approach holds promise for advancing the utility of ramie and PAL fibres in the textile industry. This research contributes to the broader goals of sustainable fibre processing and offers a pathway for the efficient utilization of underexploited resources like pineapple leaves.

5.2 Materials and Methods

5.2.1 Substrates and reagents

Polygalacturonic acid (PGA), locust bean galactomannan, beechwood xylan, D-xylose, D-mannose, and carbon tape were obtained from Sigma-Aldrich Co. LLC., USA. Luria-Bertani medium was sourced from Himedia Pvt. Ltd., India. Sodium arsenate, ammonium molybdate, sodium hydroxide, sulfuric acid, hydrochloric acid, acetone, acetonitrile, acetic acid, and Folin's reagent were procured from Merck Limited, India.

5.2.2 Retrieval of decorticated ramie and PAL fibres

Ramie plants were harvested after 50-60 days, corresponding to the optimal stage for fibre quality and yield. Mechanically decorticated ramie fibres measuring 200-300 cm in length were obtained from the ICAR Ramie Research Station, Assam, India. The fibres showed a brown-reddish hue with minimal separation. Pineapple leaves were collected from 16-18 months old plants at the post-fruit-harvest stage, when leaves are typically discarded, from local plantations in Boko, Assam, India. The PAL fibres were extracted by scratching the pineapple leaf on a flat surface, using a knife and wooden spatula. The fibres were washed for removing the remaining gummy substances from the fibre surface. The coarser bundles were gently combed with fine pins in the wet condition to separate them into their fine fibre form. Then, it was kept in the hot air oven for drying for 48 h. After the extraction, the PAL fibres with a light-greenish colour with mostly separated fibres and a length of around 30-40 cm was produced. Both the fibres were chopped into 1.3-1.5 cm in length for further use.

5.2.3 Selection and production of enzymes for degumming of ramie and PAL fibres

Two enzymes, a pectate lyase, *Ct*PL1B (Chakraborty et al., 2015) and a mannanase, *Rf*GH5_7 (Goyal et al., 2019), were selected for degumming of the ramie and PAL fibres in combination with xylobiohydrolase, *Ac*GH30A as described in Section 2.3.4. Separate stocks of *E. coli* BL21 competent cells, each harboring plasmids encoding *Ct*PL1B, *Ac*GH30A, or *Rf*GH5_7, were independently cultivated in LB medium containing kanamycin (50 $\mu g \cdot mL^{-1}$). A 500 mL culture of *E. coli* BL21 (DE3) was incubated at 37 °C with shaking at 180 rpm and growth was monitored until the absorbance at 600 nm (A_{600}) reached 0.6, indicating the mid-exponential phase. Enzyme expression was induced by adding 1 mM isopropyl-β-D-thiogalactopyranoside (IPTG), followed by incubation at 24 °C with shaking at 180 rpm for 12 h. After induction, cells were harvested by centrifugation at 6000x***g*** for 10 min at 4 °C. The resulting pellet was resuspended in 15 mL of 50 mM Tris-HCl buffer (pH 7.5) and lysed by sonication for 30 min (10 s pulse, 10 s rest, 35% amplitude) using a Vibra Cell ultrasonic processor (Sonics, USA). The lysate was then clarified by centrifugation at 16000x***g*** for 45 min at 4 °C to remove cell debris. The different resulting supernatants, containing the crude enzymes *Ac*GH30A, *Ct*PL1B and *Rf*GH5_7 separately, was collected for further analysis. Protein concentration was determined by using the Folin-Lowry method, with bovine serum albumin (BSA) as the standard (Lowry et al., 1951). The biochemical characteristics of the enzymes *Ac*GH30A, *Rf*GH5_7 and *Ct*PL1B are listed in Table 5.1.

Table 5.1 Biochemical properties of purified *Ac*GH30A, *Ct*PL1B and *Rf*GH5_7.

	Xylobiohydrolase (*Ac*GH30A)	**Pectate lyase (*Ct*PL1B)**	**Mannanase (*Rf*GH5_7)**
GenBank Accession No.	AEV68404.1	ABN53381.1	WP_0099844671.1
Microorganism	*Acetivibrio clariflavus*	*Clostridium thermocellum*	*Ruminococcus flavefaciens*
Size/Mol. wt.	514 aa, 58 kDa	353 aa, 40 kDa	307 aa, 35 kDa
Optimum parameters	pH- 7.0, temp. 80 °C for 2 min (reaction time). Active within pH 4.0-9.0	pH-9.8, temp. 50 °C for 1 h (reaction time). Active within pH 8.0-10.0	pH- 6.0, 60 °C for 5 min (reaction time). Active within pH 6.0-9.0
Substrate	Beechwood Xylan (73.2 U/mg)	Polygalacturonic acid (18.50 U/mg)	Locust bean galactomannan (298.5 U/mg)
References	Singh et al., 2024	Chakraborty et al., 2015	Goyal et al., 2019

5.2.4 Enzyme assay

5.2.4.1 *Pectate lyase (CtPl1B)*

Pectate lyase activity of crude *Ct*PL1B was measured using 0.1% (w/v) polygalacturonic acid (PGA) in 50 mM Glycine–NaOH buffer (pH 9.8) with 0.6 mM $CaCl_2$. The 1 mL reaction, containing 20 µL enzyme, was incubated at 50 °C for 15 min and stopped by incubating on ice for 10 min, followed by centrifugation (13000x***g***, 5 min). The release of unsaturated oligogalacturonates was quantified at 235 nm (ε = 4,600 $M^{-1}cm^{-1}$) using a UV–Vis spectrophotometer (Chakraborty et al., 2015).

5.2.4.2 *Mannanase (RfGH5_7)*

The enzyme activity of crude mannanase, *Rf*GH5_7 was determined by a 100 µL reaction containing 1% (w/v) locust bean galactomannan in 50 mM Tris-HCl buffer (pH 7.5) and 10 µL enzyme, incubated at 60 °C for 5 min. Reducing sugars were

quantified using Somogyi method (Somogyi 1945), with mannose as the standard (Goyal et al., 2019).

5.2.4.3 *Xylobiohydrolase (AcGH30A)*

The enzyme activity of crude *Ac*GH30A was determined by using a reaction mixture of 100 µL containing 10 µL of crude *Ac*GH30A and 2.0% (w/v) final concentration of beechwood xylan in sodium phosphate buffer (50 mM, pH 7.0) by incubating at 80°C for 2 min. The activity of the enzyme was calculated by quantifying the amount of reducing sugars produced from the enzyme-substrate reactions using the method developed by Nelson (Nelson, 1944) and Somogyi (Somogyi, 1945), as mentioned in Section 3.2.4.

5.2.5 Degumming of ramie and PAL fibre by enzymes at small scale

5.2.5.1 *Optimization of degumming enzyme concentration*

Ramie and PAL fibres were cut into 1.3–1.5 cm pieces for the degumming experiment. A total of 10 mg of these chopped fibres were placed in a 2 mL microcentrifuge tube and treated with different crude enzyme concentrations. A reaction temperature of 50 °C and pH 7.5 was selected for the enzymatic degumming process, as all three enzymes, xylobiohydrolase (*Ac*GH30A), pectate lyase (*Ct*PL1B) and mannanase (*Rf*GH5_7) exhibited substantial activity and pH stability within these conditions (Table 5.1). Although their individual optimal conditions varied, each enzyme retained sufficient catalytic activity at 50 °C for at least 1 h and remained stable within the pH range encompassing 7.5, thereby allowing their simultaneous utilisation for enzymatic degumming. Stock solutions of crude *Ac*GH30A (8.3 $U \cdot mL^{-1}$; 20 $mg \cdot mL^{-1}$), *Ct*PL1B (12 $U \cdot mL^{-1}$; 20 $mg \cdot mL^{-1}$) and *Rf*GH5_7 (10 $U \cdot mL^{-1}$; 20 $mg \cdot mL^{-1}$) were diluted with 50 mM Tris-HCl buffer (pH 7.5) to achieve the range

of concentrations from 1 to 15 mg·mL^{-1} as mentioned in Table 5.2. The fibres were subjected to enzymatic degumming using either individual enzymes, binary mixtures of two enzymes, or ternary mixtures containing three enzymes. In all mixtures, the volume and concentration of each crude enzyme were maintained in equal proportions, ensuring an equiproportional composition within the mixtures (Table 5.2). Each crude enzyme was tested individually at six concentrations: 1, 2.5, 5, 10, 15, and 20 mg·mL^{-1}. The corresponding enzymatic activities were: for *Ac*GH30A, 0.4, 1.0, 2.1, 4.1, 6.2, and 8.3 U·mL^{-1}; for *Ct*PL1B, 0.6, 1.5, 3.0, 5.9, 8.9, and 12 U·mL^{-1}; and for *Rf*GH5_7, 0.5, 1.2, 2.5, 4.9, 7.4, and 10 U·mL^{-1}, respectively. For binary mixtures, equal volumes of two enzyme solutions at the same concentration were mixed in a 1:1 ratio, while ternary mixtures were prepared by combining equal volumes of all three enzyme solutions in a 1:1:1 ratio. This ensured that in both binary and ternary treatments, the concentration (mg·mL^{-1}) of each enzyme in the final mixture was equal to its corresponding value in the individual enzyme treatments. All reactions were carried out in a final volume of 1.5 mL. A negative control was conducted simultaneously, in which decorticated fibres were incubated in 1.5 mL of 50 mM Tris-HCl buffer (pH 7.5) without the addition of enzymes. A positive control using NaOH (5 g·L^{-1}) was also performed in parallel as a reference to compare enzymatic degumming with chemical degumming, providing a baseline for evaluation and highlighting the efficiency of enzymatic treatment (Rajulapati et al. 2020). The degumming reactions were performed at 50 °C with agitation at 100 rpm for 60 min in a shaking water bath. After the treatment, the enzymes were removed and the fibres were washed 5 - 6 times with water. The washed fibres were dried at 60 °C for 24 h.

The degumming efficiency was determined by measuring the % weight loss of ramie and PAL fibres after treatment, using the formula given below,

$$\text{Weight loss (\%)} = \left(\frac{W_i - W_f}{W_i}\right) \times 100$$

Where W_i represents the initial weight of the fibre before enzymatic treatment and W_f is the final weight of the fibre after degumming. All experiments were conducted in triplicate, and the mean values were reported in the study.

Table 5.2 Enzyme and non-enzymatic treatment setups for fibres.

Treatment type	**Enzymes/Treatment used**	**Concentrations of enzyme mixture (mg·mL⁻¹) or NaOH**
Single enzyme	*Ct*PL1B, *Ac*GH30A, *Rf*GH5_7	1, 2.5, 5, 10, 15, 20
Dual enzyme mix	(i) *Ac*GH30A + *Ct*PL1B, (ii) *Ct*PL1B + *Rf*GH5_7, (iii) *Ac*GH30A + *Rf*GH5_7	1, 2.5, 5, 10, 15, 20
Triple enzyme mix	*Ct*PL1B+*Ac*GH30A+*Rf*GH5_7	1, 2.5, 5, 10, 15, 20
Negative control	No enzyme (Buffer only)	—
Positive control	NaOH	5 g·L⁻¹

5.2.5.2 *Optimization of enzyme degumming time*

The optimization of degumming time was carried out by separately treating 10 mg of ramie and 10 mg of pineapple leaf (PAL) fibres with crude enzymes *Ct*PL1B (6.2 U·mL⁻¹; 15 mg·mL⁻¹), *Ac*GH30A (8.9 U·mL⁻¹; 15 mg·mL⁻¹), and *Rf*GH5_7 (7.4 U·mL⁻¹; 15 mg·mL⁻¹) dissolved in 50 mM Tris-HCl buffer (pH 7.5). The reactions were performed at 50°C and agitated at 100 rpm for varying durations of 15, 30, 45, 60, 120 and 180 min (Table 5.3). The fibres were treated with single enzymes, binary mixtures, or ternary combinations. In all enzyme mixtures, the volume and concentration (15 mg·mL⁻¹) of each enzyme were kept equal, maintaining an equiproportional mixture in terms of enzyme concentration and added volume. The final enzyme concentration and reaction volume were 15 mg·mL⁻¹ and 1.5 mL,

respectively (Table 5.3). Negative control was run in parallel, where decorticated fibres were incubated in 1.5 mL of 50 mM Tris-HCl buffer (pH 7.5) without the enzymes. A positive control using NaOH (5 $g \cdot L^{-1}$) was also run in parallel. The effectiveness of degumming was assessed by measuring the weight loss in fibres after each treatment.

Table 5.3 Enzyme treatment of ramie and PAL fibres at small scale and scale up setup.

Treatment type	Enzymes used	Total concentration ($mg \cdot mL^{-1}$)
Single enzyme	*Ct*PL1B (8.9 $U \cdot mL^{-1}$), *Ac*GH30A (6.2 $U \cdot mL^{-1}$), *Rf*GH5_7 (7.4 $U \cdot mL^{-1}$)	15
Dual enzyme mix	(i) *Ac*GH30A + *Ct*PL1B, (ii) *Ct*PL1B + *Rf*GH5_7, (iii) *Ac*GH30A + *Rf*GH5_7	15
Triple enzyme mix	*Ct*PL1B+*Ac*GH30A+*Rf*GH5_7	15
Negative control	No enzymes (buffer only)	—
Positive control	NaOH	5 $g \cdot L^{-1}$

5.2.6 Scale-up of degumming of ramie and PAL fibres at shake flask level

The degumming process for ramie and pineapple leaf (PAL) fibres was scaled up from 10 mg in 1.5 mL to 100 mg in 15 mL crude enzymes at the optimized concentration of 15 $mg \cdot mL^{-1}$, with the treatment conducted in a 100 mL conical flask. The fibre length was increased to 10 cm to accommodate the larger volume. In the scaled-up system, 100 mg of fibres were treated with 15 mL of enzymatic solutions prepared in 50 mM Tris-HCl buffer (pH 7.5), under optimized conditions of 50°C, 100 rpm and a treatment duration of 60 min. The single enzyme treatments included *Ac*GH30A (15 $mg \cdot mL^{-1}$, 6.19 $U \cdot mL^{-1}$), *Ct*PL1B (15 $mg \cdot mL^{-1}$, 8.9 $U \cdot mL^{-1}$) and *Rf*GH5_7 (15 $mg \cdot mL^{-1}$, 7.4 $U \cdot mL^{-1}$). The equiproportional binary enzyme mixtures was prepared by combining 7.5 mL of each enzyme solution (15 $mg \cdot mL^{-1}$) in a 1:1

volumetric ratio, maintaining equal concentration and volume contributions of the individual enzymes in the mixture. Similarly, the ternary enzyme mixture was prepared by mixing 5 mL of each enzyme solution (15 mg·mL^{-1}) in a 1:1:1 volumetric ratio, ensuring equal representation of each enzyme in terms of added volume and concentration (Table 5.4). A negative control using buffer-only (50 mM Tris-HCl, pH 7.5) was run in parallel. Another negative control using *E. coli* cell extract was included to assess whether non-specific cellular components (e.g., endogenous proteins, metabolites, or other biomolecules) contributed to degumming independently of the expressed recombinant enzymes, an *E. coli* cell extract was prepared using the same culture volume as that used for enzyme extraction from transformed *E. coli*. A positive control using NaOH (5 g·L^{-1}) was also included for comparison.

Table 5.4 Scale-up of enzyme degumming treatments of ramie and PAL fibres.

Treatment type	Enzymes used	Total concentration (mg·mL^{-1})
Single enzyme	*Ct*PL1B (8.9 U·mL^{-1}), *Ac*GH30A (6.2 U·mL^{-1}), *Rf*GH5_7 (7.4 U·mL^{-1})	15
Dual enzyme mix	(i) *Ac*GH30A + *Ct*PL1B, (ii) *Ct*PL1B + *Rf*GH5_7, (iii) *Ac*GH30A + *Rf*GH5_7	15
Triple enzyme mix	*Ct*PL1B+*Ac*GH30A+*Rf*GH5	15
Negative control	No enzymes (buffer only)	—
Negative control	*E. coli* cell extract	—
Positive control	NaOH	5 g·L^{-1}

5.2.7 Field emission scanning electron microscopy analysis of ramie and PAL fibres

The effect of enzyme treatment on the surface topography of fibres (treated and untreated samples) was analysed by field emission scanning electron microscopy,

FESEM (Sigma 300 FESEM, 300 kX). PAL and ramie fibres were treated with *Ac*GH30A, *Ct*PL1B, or *Rf*GH5_7, individually or in combinations, at 15 mg·mL^{-1} for 60 min. Enzyme-treated samples were dried at 60 °C for 12 h before analysis. The untreated decorticated PAL and ramie fibres and the fibres treated with NaOH (5 g.L^{-1}) were taken as a negative and positive control, respectively, and were also analysed by FESEM for comparison. Samples were cut to 1.3 cm, placed on carbon tape on an FESEM stub and images were collected at 5000× magnification with a 2 µm scale bar.

5.2.8 ATR-FTIR analysis of ramie and PAL fibres

The removal of pectin and hemicellulosic impurities from ramie and PAL fibres was analysed using Attenuated Total Reflection-Fourier Transform Infrared (ATR-FTIR) spectroscopy (IRAffinity IS, Shimadzu, Japan). Spectra of untreated, enzyme- and NaOH-treated fibres were compared to identify surface-exposed functional groups. Measurements were conducted in dehumidified conditions, scanning from 400 to 4000 cm^{-1} with 64 scans per sample, a spectral resolution of 4 cm^{-1}, and a 94 s acquisition time. ATR data were collected using a diamond crystal at a 45° angle, processed with IR LabSolutions software and plotted using OriginPro 2024.

5.2.9 Thermogravimetric analysis of ramie and PAL fibres

The thermal properties of untreated, enzyme- and NaOH-treated ramie and PAL fibres were characterized using a Thermogravimetric Analyzer (TGA, Model TGA Q 500, TA Instruments, USA) and compared with the untreated fibres. Thermogravimetric analysis examines material behavior by tracking mass changes across varying temperatures. A total of 12 mg of powdered samples was used for the

analysis. Testing was performed at a heating rate of 20 °C per min under a nitrogen gas flow, with the temperature range spanning from 25 °C to 1000 °C.

5.2.10 Mechanical properties of enzyme-treated ramie or PAL fibres

The physical properties of enzyme-treated ramie and PAL fibres samples were analysed with a Universal Testing Machine (UTM, Zwick Roell, Z005, Germany) at 25 °C. UTM analysis was conducted to determine the mechanical properties, including tensile strength, Young's Modulus and ultimate tensile strength of ramie and PAL fibre. The analysis was performed using pneumatic grips with the following parameters: pressure of 5 bar, a gauge length of 3 cm, and a control force load range between 5 N and 100 N. Approximately, 100 mg of fibres with 10 cm in length, grouped together in bundles, were positioned on the sample holder (pneumatic grip). Tensile testing was carried out according to the American society for testing and materials (ASTM) D638 standard method. Data acquisition and analysis were performed using Text Xport-III software, version V1.2. At least three specimens were tested for each sample and the mean values were recorded.

5.2.11 Statistical analysis of datasets

Statistical analysis was performed on experimental data sets, including controls (buffer, *E. coli* cell extract, NaOH) and enzyme treatments (*Ac*GH30A, *Ct*PL1B, *Rf*GH5_7, dual- and three-enzyme mixtures). Data were analysed using one-way ANOVA and Tukey's multiple comparison test in GraphPad Prism (Version 8.0.1), with p-values < 0.05 ($n = 3$) considered significant.

5.3 Results and Discussion

5.3.1 Production and assay of enzymes

Crude enzyme extracts were prepared from 500 mL cultures of *E. coli* BL21 (DE3) cells, each expressing one of the following recombinant enzymes: *Ac*GH30A (xylobiohydrolase), *Ct*PL1B (pectate lyase) and *Rf*GH5_7 (mannanase). After sonication and centrifugation, the supernatants were filtered through 0.45 µm PVDF membranes to remove cell debris. The resulting cell-free extracts were subsequently used in enzymatic degumming assays. Protein concentrations of the crude extracts, as determined by the Folin–Lowry method, were 21 $mg \cdot mL^{-1}$ for *Ac*GH30A, 20 $mg \cdot mL^{-1}$ for *Ct*PL1B, and 22 $mg \cdot mL^{-1}$ for *Rf*GH5_7. At 20 $mg \cdot mL^{-1}$ concentration, crude *Ac*GH30A exhibited an enzymatic activity of 8.3 $U \cdot mL^{-1}$ using beechwood xylan as substrate. *Ct*PL1B showed 12 $U \cdot mL^{-1}$ activity against polygalacturonic acid, while *Rf*GH5_7 demonstrated 10 $U \cdot mL^{-1}$ activity with locust bean galactomannan.

5.3.2 Degumming of ramie and PAL fibres by enzymes at small scale

5.3.2.1 *Optimization of enzyme concentration*

The enzymatic degumming process was optimised by evaluating a range of enzyme concentrations (1-20 $mg \cdot mL^{-1}$) for *Ac*GH30A, *Ct*PL1B, and *Rf*GH5_7 at 50 °C, 100 rpm, and 60 min. Each enzyme was tested independently to assess its individual degumming potential, as well as in various combinations to investigate synergistic interactions. The efficiency of degumming was measured by the percentage of fibre weight loss, with higher values indicating more effective removal of non-cellulosic materials such as pectin and hemicellulose (Table 5.5).

A concentration-dependent increase in weight loss was observed up to 15 $mg \cdot mL^{-1}$ for both ramie and pineapple leaf (PAL) fibres, beyond which no

significant improvement was noted, suggesting saturation of enzyme activity. Among the single-enzyme treatments, *Ct*PL1B was the most effective, resulting in 10.6 ± 0.5% weight loss in ramie and 18.4 ± 0.3% in PAL fibres, indicating its high pectinolytic activity. *Ac*GH30A and *Rf*GH5_7 produced slightly lower weight losses, suggesting their selective activity towards hemicellulose and mannan, respectively (Table 5.5).

Dual-enzyme treatments displayed synergistic effects. The combination of *Ac*GH30A with *Ct*PL1B yielded the highest degumming efficiency in ramie (11.0 ± 0.3%), while the *Ct*PL1B and *Rf*GH5_7 mixture was most effective for PAL fibres, achieving 16.5 ± 0.2% weight loss (Table 5.5 and 5.6). These results likely reflect enhanced degradation of pectin and xylan in ramie and pectin and mannan in PAL fibres, which possess higher levels of mannan and pectin (Li et al. 2024). The triple-enzyme mixture of *Ac*GH30A, *Ct*PL1B, and *Rf*GH5_7 showed intermediate efficiency, producing 10.9 ± 0.3% and 16.4 ± 0.3% weight loss for ramie and PAL fibres, respectively. The slightly reduced effectiveness compared to dual-enzyme treatments may be attributed to potential enzyme competition, interference, reduced effective enzyme concentrations, or suboptimal reaction dynamics. Chemical degumming using NaOH (5 $g \cdot L^{-1}$) resulted in 14.6 ± 0.5% weight loss for ramie and 19.6 ± 0.6% for PAL fibres, slightly higher than enzymatic treatments but with the potential risk of damaging fibre integrity due to its non-selective action.

Table 5.5 Weight loss (%) of ramie fibres at different enzyme concentrations.

Concentration (mg·mL⁻¹)	Single enzyme			Dual enzyme			Triple enzyme
	A	B	C	A + B	B + C	A + C	A + B + C
1	2.1 ± 0.2	2.5 ± 0.5	2.0 ± 0.2	2.8 ± 0.4	3.0 ± 0.3	2.7 ± 0.2	3.2 ± 0.3
2.5	4.3 ± 0.4	4.9 ± 0.3	4.1 ± 0.3	5.2 ± 0.2	5.5 ± 0.5	5.0 ± 0.5	5.7 ± 0.4
5	6.8 ± 0.3	7.5 ± 0.4	6.6 ± 0.3	7.8 ± 0.3	8.2 ± 0.3	7.5 ± 0.3	8.3 ± 0.3
10	9.1 ± 0.4	9.8 ± 0.3	9.0 ± 0.4	9.5 ± 0.4	9.7 ± 0.4	9.5 ± 0.4	9.2 ± 0.5
15	9.8 ± 0.3	10.6 ± 0.5	10 ± 0.2	11.0 ± 0.3	10.4 ± 0.4	11.5 ± 0.3	10.9 ± 0.3
20	9.5 ± 0.5	10.4 ± 0.2	10.1 ± 0.4	11.2 ± 0.3	9.9 ± 0.5	11.4 ± 0.2	10.5 ± 0.5

A = AcGH30A, B = CtPL1B, C = RfGH5_7. Data represent mean weight loss (%) ± standard deviation for ramie fibres at different enzyme concentrations. The resulting data were analyzed using one-way ANOVA followed by Tukey's multiple comparison test, revealing statistical significance ($p < 0.0001$).

Table 5.6 Weight loss (%) of PAL fibres at different enzyme concentrations.

Concentration (mg·mL⁻¹)	Single enzyme			Dual enzyme			Triple enzyme
	A	B	C	A + B	B + C	A + C	A + B + C
1	4.2 ± 0.4	4.8 ± 0.3	4.0 ± 0.5	5.3 ± 0.3	5.5 ± 0.3	5.0 ± 0.3	5.7 ± 0.4
2.5	7.3 ± 0.3	8.1 ± 0.3	7.0 ± 0.3	8.5 ± 0.3	8.9 ± 0.3	8.2 ± 0.3	8.7 ± 0.3
5	11.0 ± 0.5	12.5 ± 0.3	10.8 ± 0.4	12.3 ± 0.3	12.8 ± 0.2	12 ± 0.4	12.1 ± 0.5
10	14.5 ± 0.4	16.0 ± 0.5	14.2 ± 0.6	15.8 ± 0.4	14.9 ± 0.4	15.2 ± 0.5	15.0 ± 0.3
15	15.6 ± 0.3	18.4 ± 0.3	15.8 ± 0.5	17.8 ± 0.3	16.5 ± 0.2	16.2 ± 0.4	16.4 ± 0.3
20	15.1 ± 0.5	18.0 ± 0.2	15.3 ± 0.3	17.4 ± 0.5	16.3 ± 0.4	16.0 ± 0.2	16.1 ± 0.5

A = AcGH30A, B = CtPL1B, C = RfGH5_7. Data represent mean weight loss (%) ± standard deviation for PAL fibres at different enzyme concentrations. The resulting data were analyzed using one-way ANOVA followed by Tukey's multiple comparison test, revealing statistical significance ($p < 0.0001$).

5.3.2.2 *Optimization of enzyme degumming time*

The optimum degumming time of ramie and PAL fibres was determined by treating 10 mg of fibres in a 1.5 mL reaction volume with *Ac*GH30A (15 mg.mL^{-1}; 6.2 U.ml^{-1}), *Ct*PL1B (15 mg.mL^{-1}; 8.9 U.ml^{-1}) or *Rf*GH5_7 (15 mg.mL^{-1}; 7.4 U.ml^{-1}) in 50 mM Tris-HCl buffer (pH 7.5) at 50 °C and 100 rpm. The effectiveness of degumming was assessed by measuring the weight loss (%) of fibres at different time intervals (15-180 min) across single-enzyme treatments, dual-enzyme mixtures, and the three-enzyme combination. The weight loss (%) of both fibres increased with treatment time, reaching its maximum at 60 min, beyond which it remained stable or showed minimal

improvement (Table 5.7 and 5.8). *Ct*PL1B exhibited the highest degumming efficiency among single-enzyme treatments, achieving 9.8 ± 0.5% weight loss in ramie fibres and 18.3 ± 0.4% in PAL fibres at 60 min (Table 5.7 and 5.8). The dual-enzyme mixtures exhibited a synergistic effect, with *Ac*GH30A + *Ct*PL1B demonstrating the highest degumming efficiency for ramie fibres (10.2 ± 0.3% at 60 min), while *Ct*PL1B + *Rf*GH5_7 showed the best performance for PAL fibres (17.7 ± 0.6% at 60 min). The triple-enzyme combination (*Ac*GH30A + *Ct*PL1B + *Rf*GH5_7) also performed well, resulting in 10.5 ± 0.5% weight loss for ramie and 16.4 ± 0.3% for PAL fibres (Table 5.7 and 5.8). Beyond 60 min, no substantial improvement in weight loss was observed. The chemical degumming using NaOH (5 g·L^{-1}) for 60 min, gave 15.0 ± 0.5% and 19.2 ± 0.4% weight loss for ramie and PAL fibres, respectively, which were comparable to the enzymatic treatment efficiency.

Table 5.7 Weight loss (%) of ramie fibres at different time intervals.

Time (min)	Single enzyme			Dual enzyme			Triple enzyme	NaOH
	A	B	C	A + B	B + C	A + C	A + B + C	
15	4.2 ± 0.3	3.8 ± 0.4	4.0 ± 0.4	5.5 ± 0.4	4.9 ± 0.3	5.0 ± 0.3	5.8 ± 0.4	6.2 ± 0.4
30	6.1 ± 0.4	5.9 ± 0.3	6.3 ± 0.4	7.8 ± 0.3	7.2 ± 0.4	7.5 ± 0.5	8.0 ± 0.4	10.5 ± 0.4
45	8.2 ± 0.3	7.9 ± 0.4	8.4 ± 0.2	9.1 ± 0.4	8.8 ± 0.4	9.0 ± 0.3	9.5 ± 0.3	13.1 ± 0.6
60	9.7 ± 0.4	9.8 ± 0.5	9.5 ± 0.5	10.2 ± 0.3	10 ± 0.4	10.1 ± 0.3	10.5 ± 0.5	15.0 ± 0.5
120	9.6 ± 0.3	9.4 ± 0.4	9.7 ± 0.4	10.1 ± 0.5	9.9 ± 0.4	10.4 ± 0.4	10.4 ± 0.3	14.8 ± 0.3
180	9.5 ± 0.5	9.3 ± 0.5	9.6 ± 0.5	10.0 ± 0.3	9.8 ± 0.4	9.9 ± 0.3	10.3 ± 0.4	14.7 ± 0.4

A = AcGH30A, B = CtPL1B, C = RfGH5_7. Data represent mean weight loss (%) ± standard deviation for ramie fibres at different periods of incubation. The resulting data were analyzed using one-way ANOVA followed by Tukey's multiple comparison test, revealing statistical significance ($p < 0.0001$).

Table 5.8 Weight loss (%) of PAL fibres at different time intervals.

Time (min)	Single enzyme			Dual enzyme			Triple enzyme	NaOH
	A	B	C	A + B	B + C	A + C	A + B + C	
15	6.2 ± 0.3	7.5 ± 0.4	6.1 ± 0.3	7.8 ± 0.6	8.0 ± 0.5	7.2 ± 0.6	8.5 ± 0.4	12.0 ± 0.4
30	10.3 ± 0.4	12.2 ± 0.3	10.0 ± 0.4	12.5 ± 0.5	13.2 ± 0.3	11.8 ± 0.3	13.0 ± 0.5	16.0 ± 0.5
45	14.1 ± 0.5	17.0 ± 0.5	13.8 ± 0.5	15.2 ± 0.4	17.3 ± 0.4	14.6 ± 0.4	15.2 ± 0.4	18.5 ± 0.6
60	15.8 ± 0.5	18.3 ± 0.4	16.7 ± 0.4	15.6 ± 0.2	17.7 ± 0.6	15.6 ± 0.4	16.4 ± 0.3	19.2 ± 0.4
120	16.1 ± 0.3	18.1 ± 0.5	16.2 ± 0.5	15.8 ± 0.6	17.5 ± 0.4	15.4 ± 0.3	16.2 ± 0.4	18.8 ± 0.6
180	16.6 ± 0.4	18.0 ± 0.6	16.6 ± 0.3	15.4 ± 0.4	18.2 ± 0.6	15.7 ± 0.5	15.6 ± 0.3	19.9 ± 0.3

A = AcGH30A, B = CtPL1B, C = RfGH5_7. Data represent mean weight loss (%) ± standard deviation for PAL fibres at different periods of incubation. The resulting data were analyzed using one-way ANOVA followed by Tukey's multiple comparison test, revealing statistical significance ($p < 0.0001$).

5.3.3 Scale up of degumming of ramie and PAL fibres at shake flask level

The enzymatic degumming process for ramie and pineapple leaf (PAL) fibres was successfully scaled up from 10 mg in 1.5 mL to 100 mg in 15 mL of enzyme solution (15 mg·mL^{-1}) while maintaining the optimised conditions of 50 °C, 100 rpm, and 60 min. This scale-up aimed to evaluate the effectiveness of single, dual, and triple enzyme combinations using longer fibre strands (10 cm), thereby assessing the practical applicability of the process for industrial use.

In the case of ramie, the single-enzyme treatments revealed *Ct*PL1B (pectate lyase) as the most effective, achieving a weight loss of 11.2 ± 0.3%. *Ac*GH30A and *Rf*GH5_7 followed with weight losses of 10.3 ± 0.4% and 10.1 ± 0.7%, respectively (Table 5.9). Among the dual-enzyme treatments, *Ac*GH30A combined with *Ct*PL1B led to the highest fibre weight loss (11.0 ± 0.2%), indicating a synergistic effect between hemicellulose and pectin degradation. Interestingly, the triple-enzyme mixture of *Ac*GH30A, *Ct*PL1B, and *Rf*GH5_7 resulted in slightly lower weight loss (9.8 ± 0.3%), suggesting that overlapping enzymatic activities may not yield additional benefits in ramie degumming at this scale. A study investigating combined xylanase and pectinase

treatment of ramie fibre reported a weight loss of 9.5% under optimized bleaching conditions (Abidin et al., 2023), which aligns well with the current observed weight losses for *Ct*PL1B and combinations. Similarly, the use of a recombinant Bacillus-derived pectate lyase (BspPel) yielded a 9.2% weight loss by enzymatic treatment alone and up to 20.8% when combined with mild alkaline chemicals (Zheng et al., 2020). The present results for ramie are within the reported range and shows the efficacy of pectin and hemicellulose-degrading enzymes.

A similar trend was observed for PAL fibres. *Ct*PL1B again demonstrated the highest degumming efficiency among single-enzyme treatments, with 19.1 ± 0.5% weight loss, followed by *Ac*GH30A (16.5 ± 0.4%) and *Rf*GH5_7 (16.3 ± 0.5%) (Table 5.9). The dual-enzyme mixture of *Ct*PL1B and *Rf*GH5_7 was most effective, achieving an 18.0 ± 0.4% weight loss. The triple-enzyme combination, however, resulted in a marginally lower weight loss of 17.3 ± 0.3%.

The degumming efficiency of the enzymatic treatments was comparable to that of alkaline chemical degumming using sodium hydroxide, which produced a 15.0 ± 0.6% weight loss in ramie and 21.0 ± 0.4% in PAL fibres. Although NaOH treatment resulted in slightly higher weight loss, this may be attributed to its non-selective mode of action, which can also degrade structural cellulose, potentially compromising fibre strength. Control samples treated with *E. coli* extracts lacking enzyme-encoding plasmids, as well as buffer-only controls, exhibited minimal weight loss (≤1.5%), confirming that enzymatic activity is essential for effective and selective degumming.

A comparison with the study by Liang et al. (2015), where purified pectate lyase from *Bacillus pumilus* achieved 27.4% weight loss of ramie fibres after 4 h of treatment,

highlights the efficiency of our enzymatic system, which produced 11.3% weight loss within only 60 min (Liang et al. 2015). Although direct comparison is limited by variations in fibre source, enzyme purity and concentration, reaction conditions, and experimental scale, the results provide a meaningful context. These findings suggest that optimised enzyme formulations can deliver effective degumming in shorter reaction times, thereby lowering process time and energy demands and improving the industrial applicability of the method.

Table 5.9 Weight loss (%) of ramie and PAL fibres in scaled-up degumming treatments.

Weight loss (%)	Single enzyme			Dual enzyme			Triple enzyme	NaOH	*E. coli*	Buffer
	A	B	C	A + B	B + C	A + C	A + B + C			
Ramie	10.3±0.4	11.2±0.3	10.3±0.4	11±0.2	10±0.3	10.7±0.4	9.8±0.3	15±0.6	1.1±0.4	1.2±0.4
PAL	16.5±0.4	19.1±0.5	16.3±0.5	17±0.4	18±0.4	16.5±0.5	17.3±0.3	21±0.6	1.3±0.5	1.5±0.5

A = AcGH30A, B = CtPL1B, C = RfGH5_7. Data represent mean weight loss (%) ± standard deviation for ramie and PAL fibres at different type of treatments. The fibres were subjected to treatment under optimized conditions, specifically for 60 min at 50 °C and 100 rpm. The resulting data were analyzed using one-way ANOVA followed by Tukey's multiple comparison test, revealing statistical significance ($p < 0.0001$).

5.3.4 FESEM analysis of the ramie and PAL fibres

The FESEM micrographs of untreated ramie (Fig. 5.1A) and PAL fibres (Fig. 5.2A) revealed an uneven and rough surface, indicating the presence of pectin, non-cellulosic components and gummy wax substance. These structural impurities contribute to the rigidity and stiffness of the fibres, making them unsuitable for further processing without effective degumming. Upon enzymatic treatment, substantial morphological changes were observed. The ramie fibres treated with individual enzymes, *Ac*GH30A (Fig. 5.1B), *Ct*PL1B (Fig. 5.1C) and *Rf*GH5_7 (Fig. 5.1D) exhibited partially smooth surface, suggesting a degree of removal of non-cellulosic components. A similar trend was observed in PAL fibres treated with the same enzymes (Fig. 5.2B-D), where the effect of enzymatic degumming was evident. However, the

degree of degumming achieved with single-enzyme treatments was less pronounced than with enzyme mixtures. The fibres treated with enzyme combinations, i.e., *Ac*GH30A + *Ct*PL1B (Fig. 5.1E, 5.2E), *Ct*PL1B + *Rf*GH5_7 (Fig. 5.1F, 5.2F), *Ac*GH30A + *Rf*GH5_7 (Fig. 5.1G, 5.2G) and *Ac*GH30A + *Ct*PL1B + *Rf*GH5_7 (Fig. 5.1H, 5.2H) exhibited enhanced removal of the non-cellulosic components from ramie and PAL fibres. The enzyme treated fibres became smoother than untreated fibres, indicating enhanced pectin degradation and detachment of impurities resulting from the combined action of these enzymes. The enzyme treated fibres displayed a highly refined and clean surface, resembling the chemical degumming outcome.

Alkali-treated ramie and PAL fibres (NaOH, 5 $g.L^{-1}$; Fig. 5.1I, 5.2I) showed the cleanest and smoothest morphology as compared with enzymatically treated samples. In the case of PAL fibres, NaOH-treated fibres exhibited a more dissociated fibre structure, which is characteristic of the strong chemical action of NaOH in pectin removal. The chemical treatment effectively broke down the fibre-bound gum, resulting in extensive fibre separation. The enzymatic treatments produced a comparable degumming effect while potentially being more environmentally friendly. FESEM micrographs highlight the effectiveness of enzymatic degumming strategies, demonstrating that optimized multi-enzyme formulations can achieve a degree of fibre purification similar to conventional alkaline treatment, thereby offering a sustainable alternative for fibre processing.

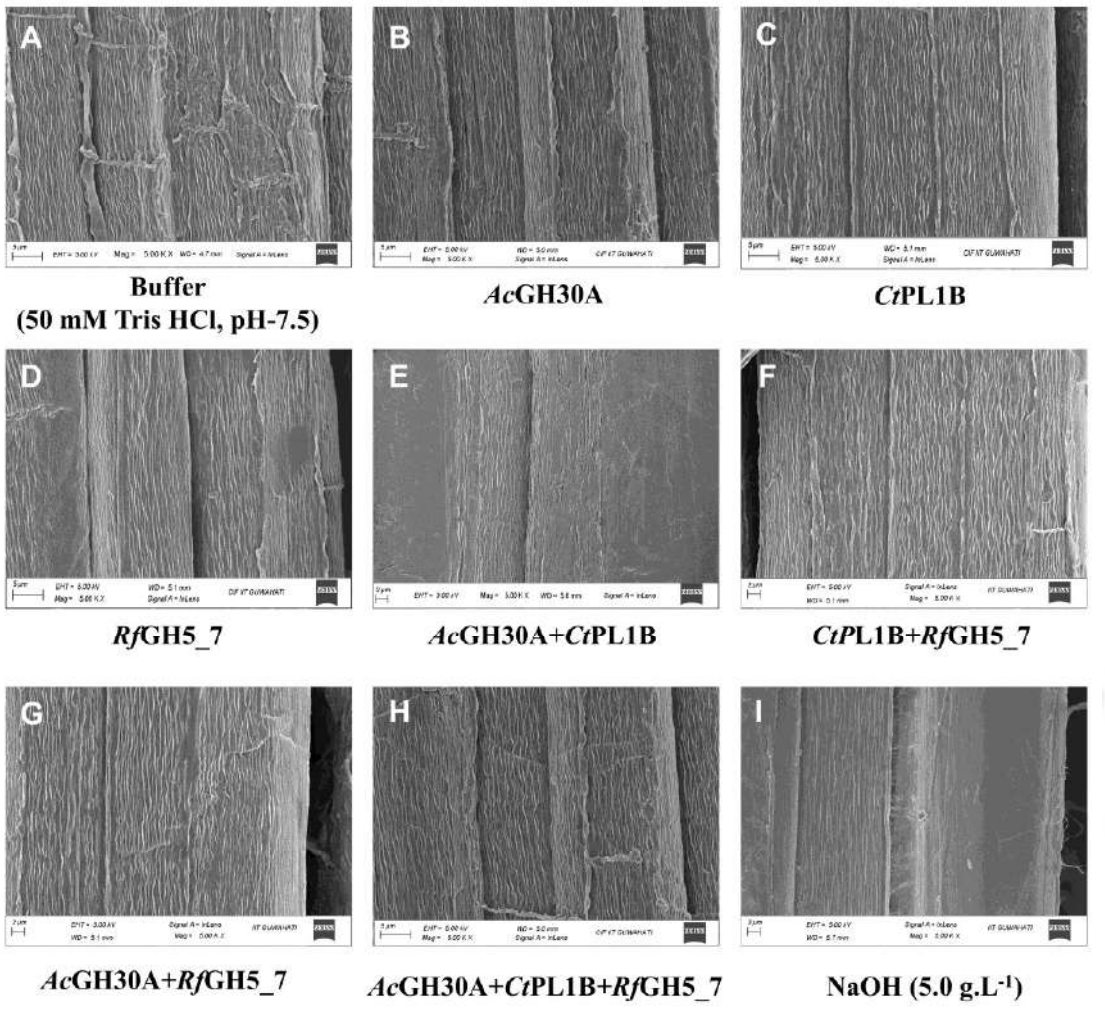

Fig. 5.1 FESEM analysis of the untreated, enzyme- and NaOH-treated ramie fibres. A uniform enzyme concentration of 15 mg·mL^{-1} was used for all treatments. (a) Untreated ramie fibre. Ramie fibres treated by (b) *Ac*GH30A, (c) *Ct*PL1B, (d) *Rf*GH5_7, (e) *Ac*GH30A+*Ct*PL1B, (f) *Ct*PL1B+*Rf*GH5_7, (g) *Ac*GH30A+*Rf*GH5_7, (h) *Ac*GH30A+*Ct*PL1B+*Rf*GH30A and (i) NaOH (5.0 g.L^{-1}). All FESEM images were collected at magnification 5000X by Sigma 300 FESEM (300 kX).

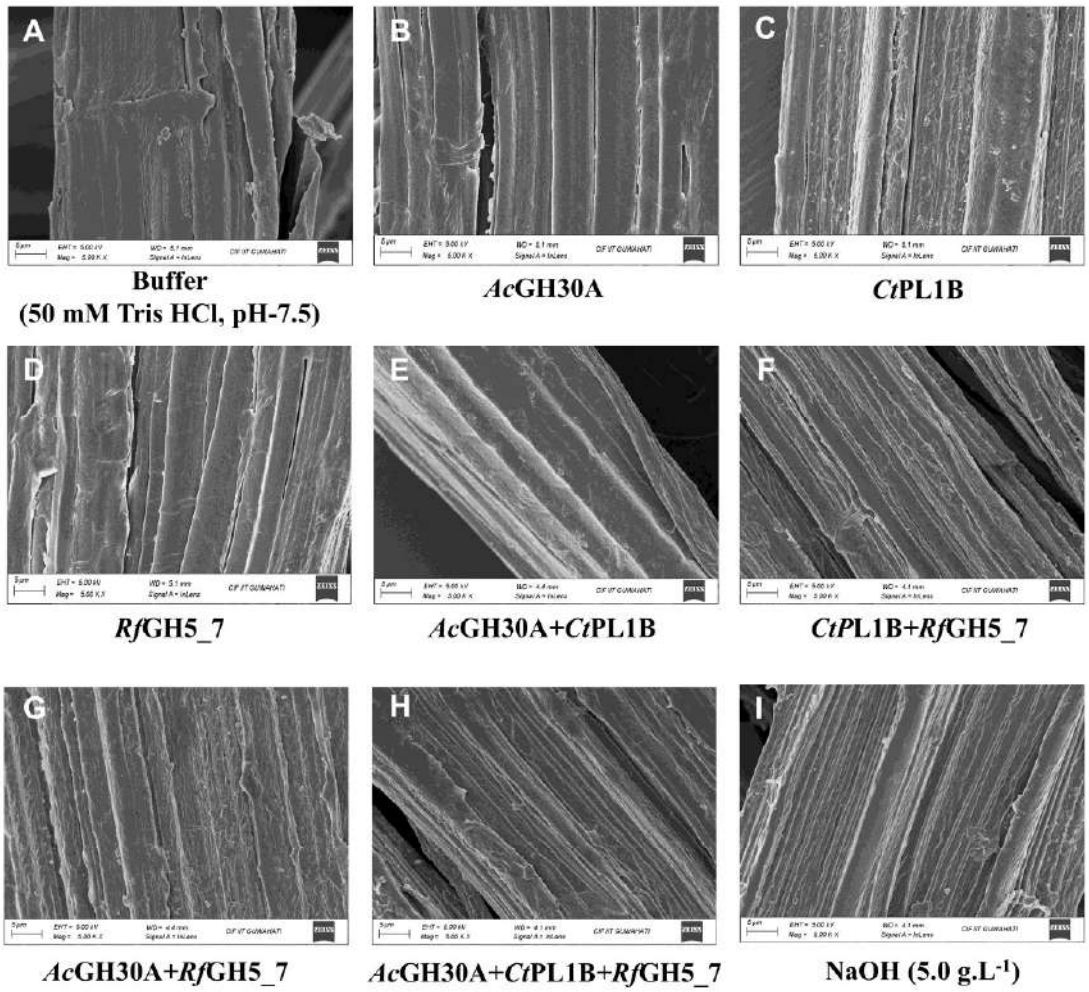

Fig. 5.2 FESEM analysis of the untreated, enzyme- and NaOH-treated PAL fibres. A uniform enzyme concentration of 15 mg·mL^{-1} was used for all treatments. (a) Untreated PAL fibre. PAL fibres treated by (b) *Ac*GH30A, (c) *Ct*PL1B, (d) *Rf*GH5_7, (e) *Ac*GH30A+*Ct*PL1B, (f) *Ct*PL1B+*Rf*GH5_7, (g) *Ac*GH30A+*Rf*GH5_7, (h) *Ac*GH30A+*Ct*PL1B+*Rf*GH30A and (i) NaOH (5.0 g.L^{-1}). All FESEM images were collected at magnification 5000X by Sigma 300 FESEM (300 kX).

5.3.5 ATR-FTIR analysis of ramie and PAL fibres

The ATR-FTIR spectra of enzyme- and NaOH-treated ramie and PAL fibres revealed distinct changes in functional groups, confirming the removal of non-cellulosic components such as pectin and hemicellulose. A significant decrease in intensity at 3300-3500 cm^{-1} (O–H stretching) was observed, most prominently in NaOH-treated fibres, indicating a significant loss of amorphous matrix components (Fig 5.3 and 5.4). Similar reductions in O–H stretching near 3300 cm^{-1} were previously reported following microbial degumming of ramie (Shu et al. 2020). The band at 2918 cm^{-1}, corresponding to C–H stretching in alkane groups, diminished after both enzymatic and chemical treatments, highlighting the degradation of pectin-bound waxy materials such as cutin and suberin (Sisti et al. 2016; Rajulapati et al. 2020). Enzyme-treated samples exhibited milder but consistent spectral shifts compared to NaOH, suggesting selective action. *Ac*GH30A treatment reduced absorption in the 1480–1100 cm^{-1} region (C–H bending), indicating the removal of methylated side chains from hemicelluloses, particularly xylan (Geminiani et al. 2022). An increase in band intensity at 1025 cm^{-1} (C-O stretching of alcohols) after treatment with *Ac*GH30A, *Ct*PL1B, or *Rf*GH5_7 suggests glycosidic bond cleavage in hemicelluloses. These effects were more pronounced in dual enzyme treatments, highlighting their synergistic action. A decrease in the 1731 cm^{-1} band (C=O stretching in carboxyl esters) following *Ct*PL1B and its combinations with other enzymes suggested enzymatic removal of methyl-esterified pectin residues (Chaves et al. 2024). This reduction, also reported by Sisti et al. (2016), was most significant in triple enzyme treatments (*Ac*GH30A+*Ct*PL1B+*Rf*GH5_7) (Sisti et al. 2016). Characteristic cellulose bands at 668 cm^{-1} (C–OH out-of-plane bending), 1108 cm^{-1} (OH plane bending), and 1375 cm^{-1}

(C–O–C) remained prominent in all treated samples, indicating preservation and increase in the relative proportion of cellulose (Qu et al. 2020). ATR-FTIR results confirmed the effective removal of pectin and hemicellulose by enzyme and NaOH treatments, exposing cellulose microfibrils. Enzymes *Ac*GH30A, *Ct*PL1B and *Rf*GH5_7, as well as their dual- and three-enzyme, provided efficient and targeted degumming, enhancing fibre quality.

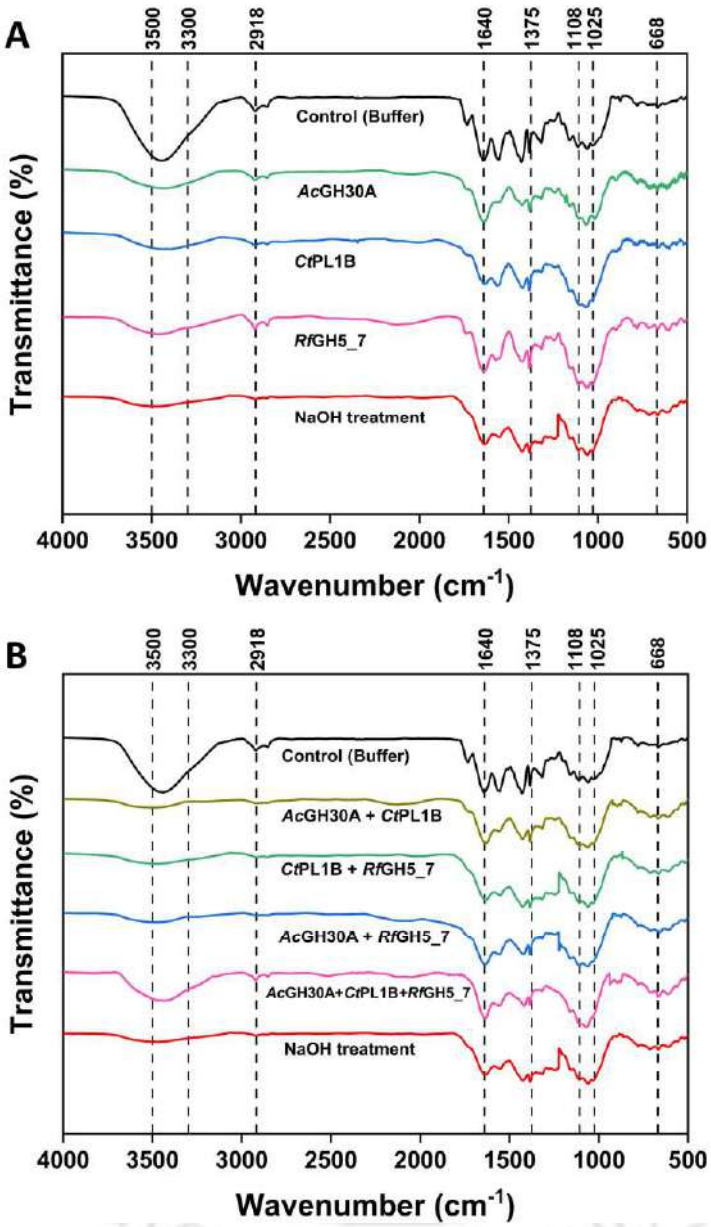

Fig. 5.3 ATR-FTIR spectra of untreated, enzyme- and NaOH-treated ramie fibres. (A) Spectral comparison of ramie fibres treated with *Ac*GH30A (xylobiohydrolase, 15 mg·mL⁻¹), *Ct*PL1B (pectate lyase, 15 mg·mL⁻¹), and *Rf*GH5_7 (mannanase, 15 mg·mL⁻¹) against untreated (Buffer; 50 mM Tris HCl, pH-7.5) and NaOH-treated ramie fibre. (B) Spectral analysis of dual-enzyme combinations (*Ac*GH30A + *Ct*PL1B, *Ct*PL1B + *Rf*GH5_7, *Ac*GH30A + *Rf*GH5_7, each at 15 mg·mL⁻¹) and the triple-enzyme combination (*Ac*GH30A + *Ct*PL1B + *Rf*GH5_7, 15 mg·mL⁻¹) compared to untreated (Buffer; 50 mM Tris HCl, pH-7.5) and NaOH-treated ramie fibre. The observed spectral changes indicate the removal of non-cellulosic components and structural modifications following enzymatic degumming.

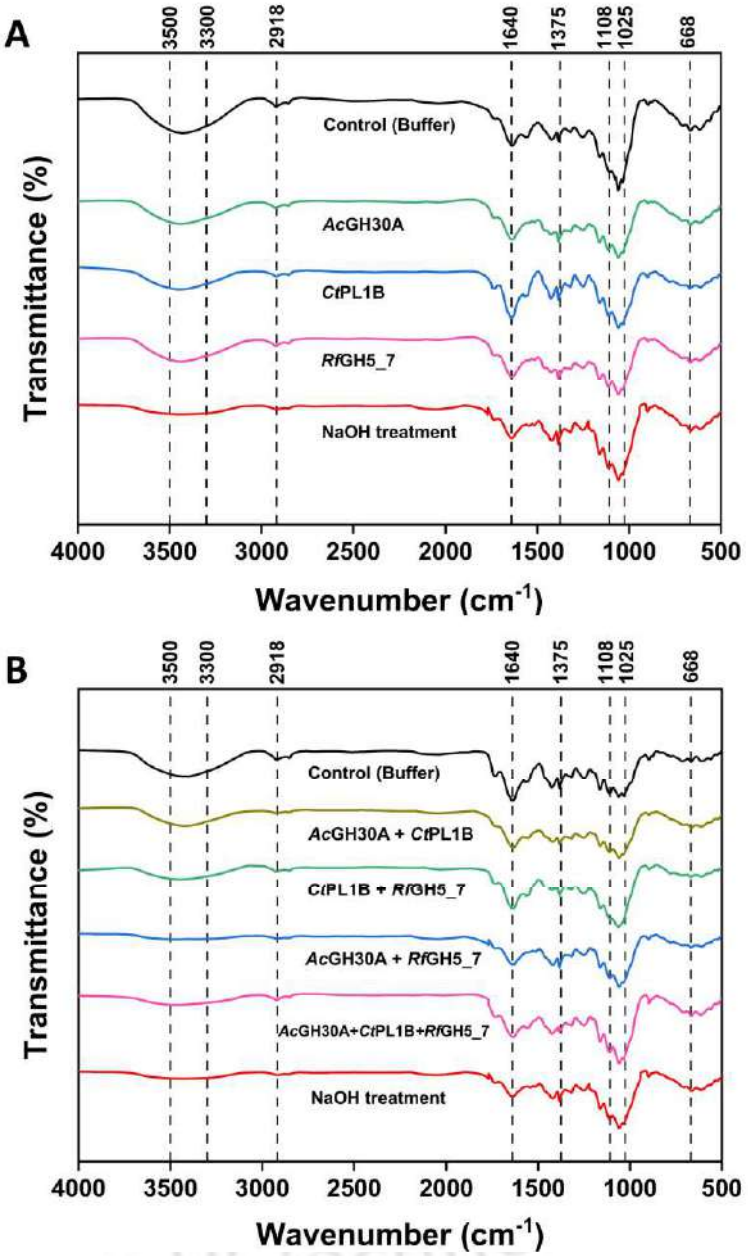

Fig. 5.4 ATR-FTIR spectra of untreated, enzyme- and NaOH-treated pineapple leaf (PAL) fibres. (A) Spectral comparison of PAL fibres treated with *Ac*GH30A (xylobiohydrolase, 15 mg·mL⁻¹), *Ct*PL1B (pectate lyase, 15 mg·mL⁻¹), and *Rf*GH5_7 (mannanase, 15 mg·mL⁻¹) against untreated (Buffer; 50 mM Tris HCl, pH-7.5) and NaOH-treated PAL fibre. (B) Spectral analysis of dual-enzyme combinations (*Ac*GH30A + *Ct*PL1B, *Ct*PL1B + *Rf*GH5_7, *Ac*GH30A + *Rf*GH5_7, each at 15 mg·mL⁻¹) and the triple-enzyme combination (*Ac*GH30A + *Ct*PL1B + *Rf*GH5_7, 15 mg·mL⁻¹) compared to untreated (Buffer; 50 mM Tris HCl, pH-7.5) and NaOH-treated PAL fibre. The observed spectral changes indicate the removal of non-cellulosic components and structural modifications following enzymatic degumming.

5.3.6 Thermogravimetric analysis of untreated and treated ramie and PAL fibres

Thermogravimetric analysis (TGA) was conducted to assess the thermal stability of enzyme- and NaOH-treated ramie and pineapple leaf (PAL) fibres. The differential thermogravimetric (DTG) curve of ramie fibres exhibited three distinct degradation events (Fig. 5.5), while PAL fibres showed two significant transitions (Fig. 5.6). The initial mass loss between 30 °C and 200 °C corresponded to moisture evaporation in ramie. This initial moisture-related peak was absent in PAL fibres, indicating lower residual water content. A shoulder peak observed between 200 °C and 300 °C in both fibres was attributed to the degradation of non-cellulosic materials (Fig. 5.5 and 5.6). The primary degradation, occurring between 300 °C and 380 °C, shows the degradation of cellulose. Peak intensity in the DTG curves represents the rate of mass loss. Lower intensity of peaks suggests reduced cellulose availability, possibly due to partial degradation or removal during processing (Mazian et al. 2019; Chaves et al. 2024).

Untreated ramie and PAL fibres showed initial degradation temperatures of 338.8 °C and 361 °C, respectively, indicating the presence of thermally unstable pectin and hemicellulose. NaOH-treated fibres demonstrated the highest thermal stability, with degradation onset at 361.3 °C in ramie and 381.7 °C in PAL (Fig. 5.5 and 5.6). Among single enzyme treatments, fibres treated with *Ct*PL1B showed the most significant thermal resistance, with ramie degrading at 356.3 °C and PAL at 374.7 °C, indicating the effectiveness of *Ct*PL1B in hydrolysing pectic substances, a major contributor to fibre impurities (Fig. 5.5 and 5.6).

Enzymatic treatment with *Ac*GH30A and *Rf*GH5_7 also enhanced thermal properties. Ramie fibres treated with *Ac*GH30A and *Rf*GH5_7 degraded at 353.1 °C and 350.3 °C, respectively. In PAL, both treatments resulted in degradation at 373 °C.

Dual enzyme treatments exhibited synergistic effects. The combination of *Ac*GH30A and *Ct*PL1B increased degradation temperature to 355.7 °C for ramie and 375.7 °C for PAL. *Ct*PL1B combined with *Rf*GH5_7 raised degradation temperatures to 354.7 °C and 374.7 °C for ramie and PAL, respectively. The *Ac*GH30A and *Rf*GH5_7 combination yielded the highest degradation temperature for PAL, reaching 377.1 °C and 353.7 °C for ramie. The three-enzyme mixture (*Ac*GH30A + *Ct*PL1B + *Rf*GH5_7) resulted in thermal degradation at 354.7 °C for ramie and 376.3 °C for PAL (Fig. 5.5 and 5.6).

All enzyme-treated fibres demonstrated thermal degradation above 350 °C, meeting the thermal stability threshold for textile applications (Lin et al. 2022). These enhancements in thermal stability were caused by the effective removal of hemicellulose and pectin, leading to an increase in fibre crystallinity. The findings are consistent with previous studies reporting that thermal stability improves upon removing non-cellulosic components (Bakshi et al. 2024). Another report mentioned that hemicellulose in ramie and related fibres decomposes between 200-300 °C, while pectin contributes to initial weight loss at even lower temperatures (Neto et al., 2021). In contrast, cellulose, due to its higher crystallinity, is more thermally stable and degrades at 300-400 °C. Therefore, the removal of pectin and hemicellulose during chemical treatment improves fibre thermal stability by delaying the onset of thermal degradation (Neto et al., 2021). Consistent findings were presented on TGA data across various cellulosic fibres which confirmed that amorphous components such as hemicellulose and pectin are responsible for the early onset of thermal degradation (Nurazzi et al., 2021). Their elimination through alkali or silane treatments raises the degradation onset temperature and improves fibre–matrix compatibility in composites.

Similarly, alkaline-treated pineapple crown fibres exhibited higher thermal stability than untreated fibres, as revealed by DTG curves (Bernardes et al., 2023). The increase in stability was attributed to the removal of amorphous fractions by NaOH, leading to higher crystallinity and, consequently, improved thermal stability.

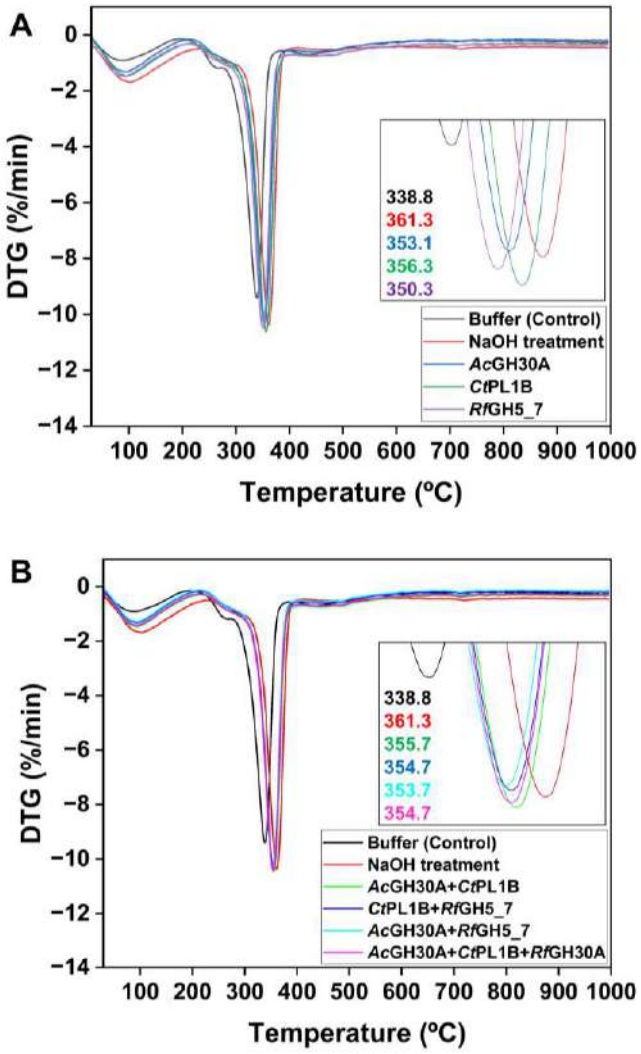

Fig. 5.5 Thermogravimetric analysis of untreated, enzyme- and NaOH-treated ramie fibres. The inset graphs show the enlarged view of the primary peaks and their values in their respective colours. (a) DTG curves showing the thermal degradation profiles of ramie fibres treated with *Ac*GH30A (xylobiohydrolase), *Ct*PL1B (pectate lyase), and *Rf*GH5_7 (mannanase) compared to untreated (Buffer; 50 mM Tris HCl, pH-7.5) and NaOH-treated ramie fibre. (b) DTG curves illustrating the thermal decomposition peaks of dual-enzyme combinations and the triple-enzyme combination against untreated (Buffer; 50 mM Tris HCl, pH-7.5) and NaOH-treated ramie fibres.

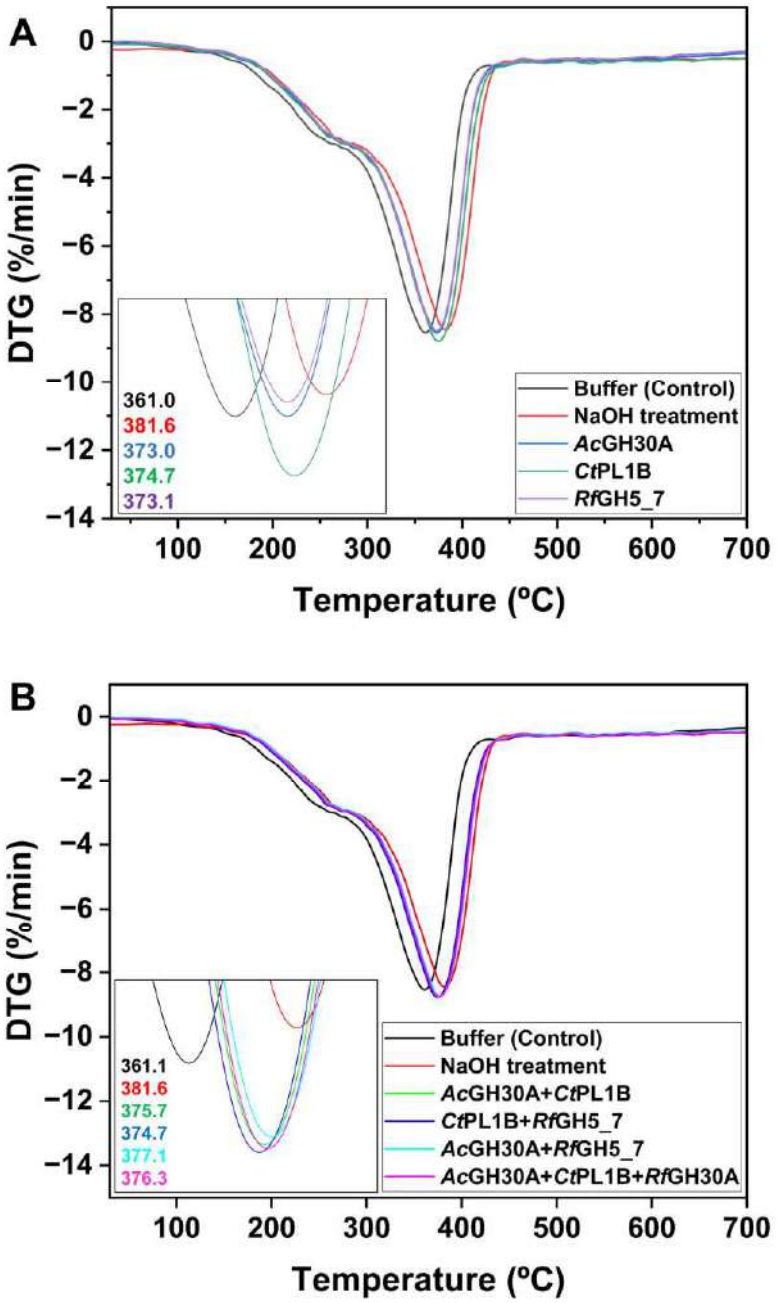

Fig. 5.6 Thermogravimetric analysis of untreated, enzyme- and NaOH-treated pineapple leaf (PAL) fibres. The inset graphs show the enlarged view of the primary peaks and their values in their respective colours. (a) DTG curves showing the thermal degradation profiles of PAL fibres treated with *Ac*GH30A (xylobiohydrolase), *Ct*PL1B (pectate lyase), and *Rf*GH5_7 (mannanase) compared to untreated (Buffer; 50 mM Tris HCl, pH-7.5) and NaOH-treated PAL fibre. (b) DTG curves illustrating the thermal decomposition peaks of dual-enzyme combinations and the triple-enzyme combination against untreated (Buffer; 50 mM Tris HCl, pH-7.5) and NaOH-treated PAL fibres.

5.3.7 Mechanical properties of treated and untreated ramie and PAL fibres

The mechanical properties of decorticated ramie and pineapple leaf (PAL) fibres, including enzyme-treated variants, were assessed at 25 °C using a universal testing machine. Results for ultimate tensile strength (UTS), Young's modulus and elongation percentage are summarised in Tables 5.10 and 5.11. Raw ramie fibres exhibited a UTS of 388 MPa and Young's modulus of 10.5 GPa, reflecting the presence of non-cellulosic materials such as pectin, hemicellulose, and waxes. Enzymatic degumming significantly enhanced mechanical characteristics. Among single enzymes, *Ct*PL1B yielded the highest UTS and Young's modulus, 414.7 MPa and 18.1 GPa, respectively, demonstrating efficient pectin removal and fibre reinforcement. *Ac*GH30A and *Rf*GH5_7 also improved UTS to 407.9 MPa and 399.5 MPa, respectively, highlighting the structural role of hemicellulose and mannan. The *Ac*GH30A + *Ct*PL1B combination further increased UTS to 418.3 MPa, displaying the synergistic action of these enzymes. Untreated PAL fibres exhibited a UTS of 270 MPa and Young's modulus of 13.85 GPa. *Ct*PL1B yielded the highest Young's modulus for PAL fibres, as was also observed for ramie, increasing from 13.85 to 19.95 GPa and indicating that even minimal pectin removal can substantially improve stiffness. The increase in Young's modulus after enzymatic treatment is attributed to the removal of non-cellulosic components, allowing greater alignment and packing of cellulose microfibrils. Treatment with *Rf*GH5_7 improved UTS to 316.8 MPa, and the combination of *Ct*PL1B + *Rf*GH5_7 raised it to 323.2 MPa. NaOH-treated PAL fibres achieved the highest UTS of 335.3 MPa, indicating the highest removal of matrix materials but at the cost of increased brittleness.

Elongation percentage generally decreased following treatment. For ramie, *Ct*PL1B led to the lowest elongation at 3.1 %, while only the *Ac*GH30A + *Ct*PL1B maintained the highest elongation at 3.9 %, suggesting that selective degradation of matrix polymers helps maintain flexibility. NaOH-treated ramie fibres showed the lowest elongation at 2.5 %, indicating excessive stiffness. In PAL fibres, NaOH treatment resulted in a slightly higher elongation of 3.4 %. *Ac*GH30A-treated samples showed moderate ductility, with elongation values of 3.2 % for ramie and 3.5 % for PAL fibres.

Enzyme combinations showed superior performance compared to individual enzymes in strengthening fibres. Although NaOH treatment achieved the highest tensile strength, it also led to the lowest ductility, indicating that the complete removal of non-cellulosic components increases the crystallinity and stiffness of the fibre. This is consistent with findings by Birniwa et al. (2023), who reported increased tensile strength and reduced water absorption in NaOH- and acrylic acid-treated flax fibres (Birniwa et al. 2023). As cellulose content increases in the fibre, both Young's modulus and tensile strength improve due to the development of a more crystalline and aligned fibre network (Cabradilla and Zeronian 1975). The mechanical properties of enzyme-treated fibres were comparable to that of chemically degummed samples, supporting enzymatic degumming as a viable, environmentally sustainable alternative. This study contributes to the advancement of biotechnology in fibre processing, presenting a scalable, sustainable alternative to conventional chemical treatments for natural fibres, specifically ramie and pineapple leaf fibre (Fig. 5.7).

Table 5.10 UTM analysis of scaled up enzyme and chemical degummed ramie fibre.

Treatment method	Tensile strength (MPa)	Std. Dev.	Young's Modulus (GPa)	Std. Dev.	% Elongation
Buffer (50 mM Tris HCl, pH-7.5)	388	20.4	10.5	0.6	3.8
*Ac*GH30A	407.9	18.2	16.3	0.5	3.2
*Ct*PL1B	414.7	22.1	18.1	0.6	3.1
*Rf*GH5_7	399.5	25.6	14.7	0.3	2.6
*Ac*GH30A + *Ct*PL1B	418.3	23.4	15.2	0.5	3.9
*Ct*PL1B + *Rf*GH5_7	411.2	19.5	17.4	0.7	3.4
*Ac*GH30A + *Rf*GH5_7	416.2	22.3	15.6	0.9	3.8
*Ac*GH30A + *Ct*PL1B + *Rf*GH5_7	402.5	24.5	16.8	0.3	2.7
NaOH (5 $g.l^{-1}$)	465.8	26.1	22.4	0.8	2.5

Table 5.11 UTM analysis of scaled up enzyme and chemical degummed PAL fibres.

Treatment method	Tensile strength (MPa)	Std. Dev.	Young's Modulus (GPa)	Std. Dev.	% Elongation
Buffer (50 mM Tris HCl, pH-7.5)	270	14.8	13.85	0.9	2.7
*Ac*GH30A	308.4	20	12.75	0.9	3.5
*Ct*PL1B	313.2	22.7	19.95	1.2	2.1
*Rf*GH5_7	316.8	16.1	14.95	1.1	3
*Ac*GH30A + *Ct*PL1B	317.5	21.1	15.3	0.7	2.3
*Ct*PL1B + *Rf*GH5_7	323.2	22.2	12.25	0.7	2.4
*Ac*GH30A + *Rf*GH5_7	310.6	17	8.05	1	3.4
*Ac*GH30A + *Ct*PL1B + *Rf*GH5_7	312.2	18.7	15.65	1	2.9
NaOH (5 $g.l^{-1}$)	335.3	18.9	13.15	1.3	3.4

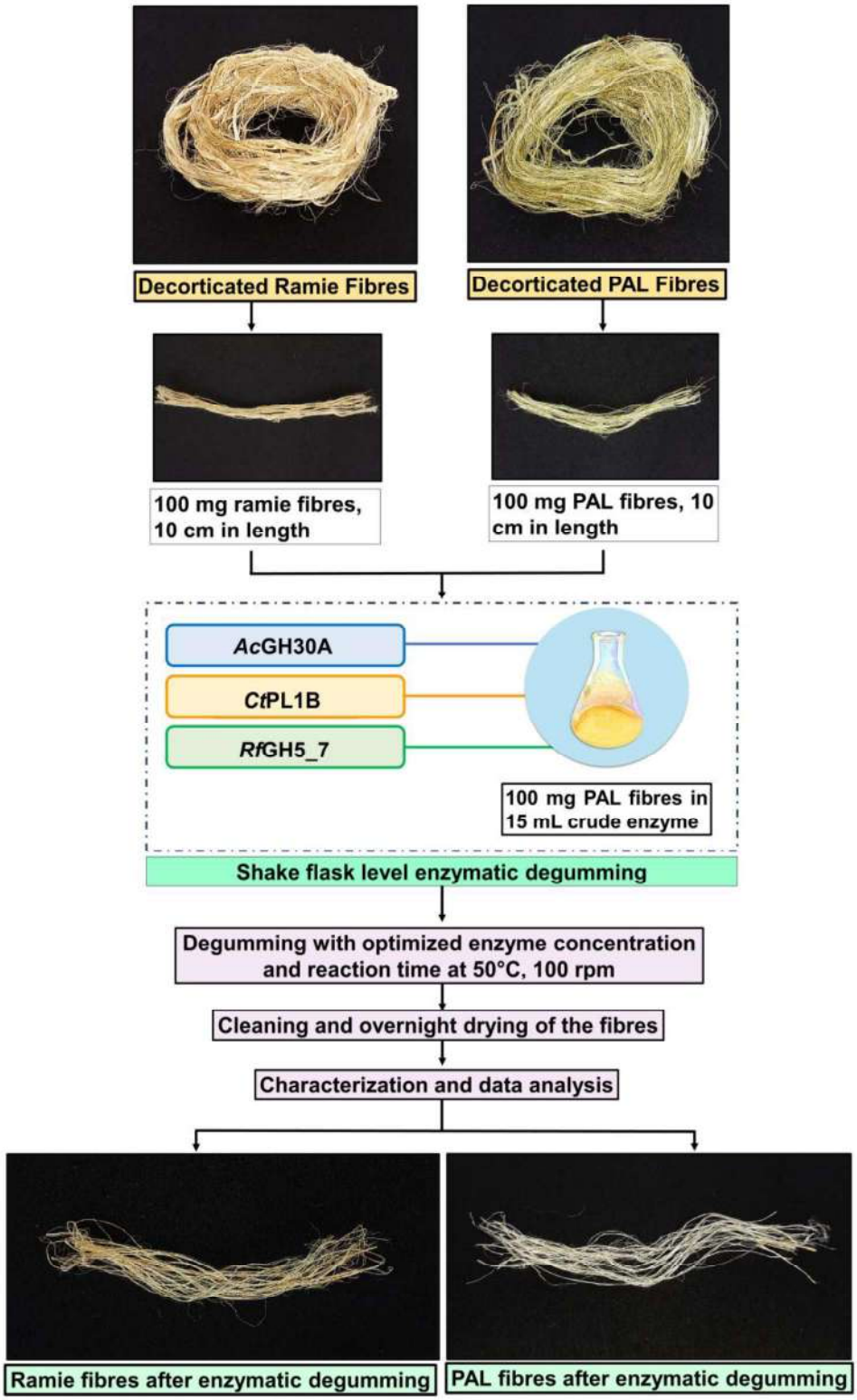

Fig 5.7 Schematic presentation of the enzymatic degumming process of ramie and pineapple leaf fibres. The final fibre image depicts the degummed ramie and pineapple leaf fibres, highlighting the removal of non-cellulosic components.

5.4 Conclusion

This study demonstrated the effectiveness of enzymatic degumming as a sustainable alternative for processing natural fibres, specifically ramie (*Boehmeria nivea*) and pineapple (*Ananas comosus*) leaf (PAL) fibres. Using three carbohydrate-active enzymes, *Ac*GH30A (xylobiohydrolase), *Ct*PL1B (pectate lyase) and *Rf*GH5_7 (mannanase), either individually or in various combinations, the degumming process achieved significant removal of non-cellulosic components, thereby improving the quality and mechanical properties of the fibres.

Optimised small and shake flask-scale treatments efficiently removed gummy substances while preserving cellulose structure. FESEM, ATR-FTIR, and thermogravimetric analyses confirmed pectin and hemicellulose removal, smoother fibre surfaces, altered functional groups, and enhanced thermal stability. The results underscore enzymatic degumming as an eco-friendly, efficient alternative to chemical methods, minimising fibre damage and pollution. Dual-enzyme mixtures- *Ac*GH30A + *Ct*PL1B for ramie and *Ct*PL1B + *Rf*GH5_7 for PAL and the ternary mix showed superior performance. Tensile strength values (418.3 MPa for ramie; 323.2 MPa for PAL) were comparable to NaOH-treated fibres (5 $g \cdot L^{-1}$), with reduced environmental impact.

Enzymatic degumming offers a sustainable alternative to conventional chemical methods by minimising fibre damage and reducing environmental impact, while producing fibres with mechanical and thermal properties comparable to those obtained through chemical treatment. These findings highlight its potential for eco-friendly processing in textile and composite industries. Future scope of this study lies in optimising enzyme ratios to match the gum composition of each fibre, developing

cost-effective enzyme production strategies, and scaling up the process for industrial application to enhance commercial viability. While this study demonstrates the feasibility of enzymatic degumming at the laboratory scale, its sustainability and industrial relevance remain preliminary, requiring larger-scale trials for full assessment and validation.

References

1. Abidin K. Y., Nurhayati N., Nandyawati D., et al (2023). Enzymatic degumming using xylanase and pectinase to improve brightness and fineness quality of ramie fiber (*Boehmeria nivea* l.) as textile raw material. *Indonesian Journal of Biotechnology & Bioscience,* 10, 76–85.
2. Amankwah, W., Chen, X., Xie, X., Liu, F., Ma, Y., & Li, Y. (2024). Bio-degumming of ramie fiber using an integrated spiral symmetry stream anaerobic bioreactor. *Textile Research Journal*, *94*(17–18), 1897–1908. https://doi.org/10.1177/00405175241238447
3. Asim, M., Abdan, K., Jawaid, M., Nasir, M., Dashtizadeh, Z., Ishak, M. R., & Hoque, M. E. (2015). A review on pineapple leaves fibre and its composites. *International Journal of Polymer Science*, *2015*(1), 950567. https://doi.org/10.1155/2015/950567
4. Bakshi, M. I., Sohail, A., Karimah, A., Ridho, M. R., Hastuti, N., Side, T. H. R., Darwis, A., Subiyanto, B., Wulandari, A. P., & Fatriasari, W. (2024). Effect of degumming of two selected Indonesian Ramie (*Boehmeria nivea)* accessions on the anatomical, chemical, mechanical, and thermal properties. *Industrial Crops and Products*, *216*, 118725. https://doi.org/10.1016/j.indcrop.2024.118725
5. Bernardes G. P., de Prá Andrade M., Poletto M. (2023). Effect of alkaline treatment on the thermal stability, degradation kinetics, and thermodynamic parameters of pineapple crown fibres. *Journal of Materials Research and Technology*, *23*, 64-76. https://doi.org/10.1016/j.jmrt.2022.12.179
6. Birniwa, A. H., Abdullahi, S. S., Ali, M., Mohammad, R. E. A., Jagaba, A. H., Amran, M., Avudaiappan, S., Maureira-Carsalade, N., & Flores, E. I. S. (2023). Recent trends in treatment and fabrication of plant-based fiber-reinforced epoxy composite: A review. *Journal of Composites Science*, 7(3), Article 3. https://doi.org/10.3390/jcs7030120
7. Cabradilla, K. E., & Zeronian, S. H. (1975). Factors influencing the tensile properties of ramie. *Journal of Applied Polymer Science*, *19*(2), 503–517. https://doi.org/10.1002/app.1975.070190214
8. Chakraborty, S., Fernandes, V. O., Dias, F. M. V., Prates, J. A. M., Ferreira, L. M. A., Fontes, C. M. G. A., Goyal, A., & Centeno, M. S. J. (2015). Role of pectinolytic enzymes identified in *Clostridium thermocellum* cellulosome. *PLOS ONE*, *10*(2), e0116787. https://doi.org/10.1371/journal.pone.0116787
9. Chaves, D. M., Araújo, J. C., Gomes, C. V., Gonçalves, S. P., Fangueiro, R., & Ferreira, D. P. (2024). Extraction, characterization and properties evaluation of pineapple leaf fibers from Azores pineapple. *Heliyon*, *10*(4). https://doi.org/10.1016/j.heliyon.2024.e26698
10. Daud, Z., Awang, H., Kassim, A. S. M., Hatta, M. Z. M., & Aripin, A. M. (2014). Comparison of pineapple leaf and cassava peel by chemical properties

and morphology characterization. *Advanced Materials Research*, *974*, 384–388. https://doi.org/10.4028/www.scientific.net/AMR.974.384

11. Ding, J., Zhou, C., & Dong, Z. (2023). Trend of ramie industry development: A review of green degumming and the utilization of processing residues. *Journal of Cleaner Production*, *384*, 135487. https://doi.org/10.1016/j.jclepro.2022.135487
12. Geminiani, L., Campione, F. P., Corti, C., Luraschi, M., Motella, S., Recchia, S., & Rampazzi, L. (2022). Differentiating between natural and modified cellulosic fibres using ATR-FTIR spectroscopy. *Heritage*, *5*(4), Article 4. https://doi.org/10.3390/heritage5040213
13. Goyal, D., Kumar, K., Centeno, M. S. J., Thakur, A., Pires, V. M. R., Bule, P., Fontes, C. M. G. A., & Goyal, A. (2019). Molecular cloning, expression and biochemical characterization of a family 5 glycoside hydrolase first endo-mannanase (*Rf*GH5_7) from *Ruminococcus flavefaciens* FD-1 v3. *Molecular Biotechnology*, *61*(11), 826–835. https://doi.org/10.1007/s12033-019-00205-2
14. Haile, S., & Ayele, A. (2022). Pectinase from microorganisms and its industrial applications. *The Scientific World Journal*, *2022*(1), 1881305. https://doi.org/10.1155/2022/1881305
15. Jose, S., Salim, R., & Ammayappan, L. (2016). An overview on production, properties, and value addition of pineapple leaf fibers (PALF). *Journal of Natural Fibers*, *13*(3), 362–373. https://doi.org/10.1080/15440478.2015.1029194
16. Kozłowski, R. M., & Mackiewicz-Talarczyk, M. (2020). 1A - Introduction to natural textile fibres. In R. M. Kozłowski & M. Mackiewicz-Talarczyk (Eds.), *Handbook of Natural Fibres (Second Edition)* (pp. 1–13). Woodhead Publishing. https://doi.org/10.1016/B978-0-12-818398-4.00001-3
17. Li, Z., Li, Z., Ding, R., & Yu, C. (2016). Composition of ramie hemicelluloses and effect of polysaccharides on fiber properties. *Textile Research Journal*, *86*(5), 451–460. https://doi.org/10.1177/0040517515592811
18. Liang, C., Gui, X., Zhou, C., Xue, Y., Ma, Y., & Tang, S.-Y. (2015). Improving the thermoactivity and thermostability of pectate lyase from *Bacillus pumilus* for ramie degumming. *Applied Microbiology and Biotechnology*, *99*(6), 2673–2682. https://doi.org/10.1007/s00253-014-6091-y
19. Lin, G., Tang, Q., Huang, H., Yu, J., Li, Z., & Ding, B. (2022). Process optimization and comprehensive utilization of recyclable deep eutectic solvent for the production of ramie cellulose fibers. *Cellulose*, *29*(7), 3689–3701. https://doi.org/10.1007/s10570-022-04501-0
20. Lyu, P., Zhang, Y., Wang, X., & Hurren, C. (2021). Degumming methods for bast fibers—A mini review. *Industrial Crops and Products*, *174*, 114158. https://doi.org/10.1016/j.indcrop.2021.114158
21. Mazian, B., Bergeret, A., Benezet, J.-C., & Malhautier, L. (2019). A comparative study of the effect of field retting time on the properties of hemp

fibres harvested at different growth stages. *Fibers*, *7*(12), Article 12. https://doi.org/10.3390/fib7120108

22. Mendonça, M., Barroca, M., & Collins, T. (2023). Endo-1,4-β-xylanase-containing glycoside hydrolase families: Characteristics, singularities and similarities. *Biotechnology Advances*, *65*, 108148. https://doi.org/10.1016/j.biotechadv.2023.108148
23. Mudi, C., & and Shaw, A. (2025). Investigations on the mechanical performance and durability of ramie fibers under various environmental conditions. *Journal of Natural Fibers*, 22(1), 2433043. https://doi.org/10.1080/15440478.2024.2433043
24. Neto, J. S., de Queiroz, H. F., Aguiar, R. A., & Banea, M. D. (2021). A review on the thermal characterisation of natural and hybrid fiber composites. *Polymers*, *13*(24), 4425. https://doi.org/10.3390/polym13244425
25. Nelson, N. (1944). A photometric adaptation of the Somogyi method for the determination of glucose. *J. Biol. Chem*, *153*(2), 375–380.
26. Nurazzi, N., Asyraf, M. R. M., Rayung, M., Norrrahim, M. N. F., Shazleen, S. S., Rani, M. S. A., ... & Abdan, K. (2021). Thermogravimetric analysis properties of cellulosic natural fiber polymer composites: A review on influence of chemical treatments. *Polymers*, *13*(16), 2710. https://doi.org/10.3390/polym13162710
27. Østby, H., & Várnai, A. (2023). Hemicellulolytic enzymes in lignocellulose processing. *Essays in biochemistry*, *67*(3), 533-550. https://doi.org/10.1042/EBC20220154
28. Qu, Y., Yin, W., Zhang, R., Zhao, S., Liu, L., & Yu, J. (2020). Isolation and characterization of cellulosic fibers from ramie using organosolv degumming process. *Cellulose*, 27(3), 1225–1237. https://doi.org/10.1007/s10570-019-02835-w
29. Rajulapati, V., Dhillon, A., kumar Gali, K., Katiyar, V., & Goyal, A. (2020). Green bioprocess of degumming of jute fibers and bioscouring of cotton fabric by recombinant pectin methylesterase and pectate lyases from *Clostridium thermocellum*. *Process Biochemistry*, *92*, 93–104. https://doi.org/10.1016/j.procbio.2020.02.024
30. Rehman, M., Gang, D., Liu, Q., Chen, Y., Wang, B., Peng, D., & Liu, L. (2019). Ramie, a multipurpose crop: Potential applications, constraints and improvement strategies. *Industrial Crops and Products*, *137*, 300–307. https://doi.org/10.1016/j.indcrop.2019.05.029
31. Saloni, S., Sindhu, Chauhan, D. K., & Tiwari, S. (2017). Pineapple production and processing in north eastern India. *Journal of Pharmacognosy and Phytochemistry*, *6*(6S), 665–672.
32. Saxena, S., Raja, A. S. M., & Arputharaj, A. (2017). Challenges in sustainable wet processing of textiles. In S. S. Muthu (Ed.), *Textiles and Clothing*

Sustainability: Sustainable Textile Chemical Processes (pp. 43–79). Springer. https://doi.org/10.1007/978-981-10-2185-5_2

33. Shadhin, M., Rahman, M., Jayaraman, R., Chen, Y., Mann, D., & Zhong, W. (2023). Natural biomass & waste biomass fibers – Structures, environmental footprints, sustainability, degumming methods, & surface modifications. *Industrial Crops and Products*, *204*, 117252. https://doi.org/10.1016/j.indcrop.2023.117252
34. Shu, T., Bai, Y., Wang, Y., Wang, H., Li, P., Xiang, M., Yu, T., Xu, H., & Yu, L. (2020). A high-efficiency and eco-friendly degumming process for ramie fibers. *Journal of Cleaner Production*, *276*, 124217. https://doi.org/10.1016/j.jclepro.2020.124217
35. Singh, Y. R., Thakur, A., Fontes, C. M., & Goyal, A. (2024). A novel thermophilic recombinant obligate xylobiohydrolase (*Ac*GH30A) from *Acetivibrio clariflavus* orchestrates the deconstruction of xylan polysaccharides. *Carbohydrate Polymers*, 340, 122295. https://doi.org/10.1016/j.carbpol.2024.122295
36. Sisti, L., Totaro, G., Vannini, M., Fabbri, P., Kalia, S., Zatta, A., & Celli, A. (2016). Evaluation of the retting process as a pre-treatment of vegetable fibers for the preparation of high-performance polymer biocomposites. *Industrial Crops and Products*, *81*, 56–65. https://doi.org/10.1016/j.indcrop.2015.11.045
37. Somogyi, M. (1945). A new reagent for the determination of sugars. *Journal of Biological Chemistry*, *160*(1), 61–68. https://doi.org/10.1016/s0021-9258(18)43097-9
38. Subash, M. chares, & Muthiah, P. (2021). Eco-friendly degumming of natural fibers for textile applications: A comprehensive review. *Cleaner Engineering and Technology*, *5*, 100304. https://doi.org/10.1016/j.clet.2021.100304
39. Suhendar, D., Dimas Azka Maulana, M., Sutrisno, A., Waltam, D. R., Yohan Abidin, K., Nandyawati, D., Nurhayati, N., Widyasti, E., Wahjono, E., Adihayyu Monconegoro, D., Haniyya, H., Sriherwanto, C., Laksamana Putra, N., & Rahmani, N. (2024). Optimization of enzymatic ramie degumming using thermoalkaliphilic xylanase from *Bacillus halodurans* CM1 and a commercial pectinase. *Biocatalysis and Biotransformation*, *42*(6), 749–759. https://doi.org/10.1080/10242422.2024.2367641
40. Tan, M., Peng, J., Peng, S., Huang, L., & Li, K. (2025). Synergistic action of multiple degumming-related enzymes secreted by *Bacillus subtilis* XW-18: Decisive factor for driving the bio-degumming process of raw pineapple leaves. *International Journal of Biological Macromolecules*, *297*, 139888. https://doi.org/10.1016/j.ijbiomac.2025.139888
41. Tian, Y., Teng, L., Yang, J., Jin, H., Guo, H., Wu, H. and Li, C., (2024). Characterization of pineapple leaf fiber following enzymatic degumming. *environment*, *24*, 26.

42. Wang, Y., Shu, T., Fan, P., Zhang, H., Turunen, O., Xiong, H., & Yu, L. (2017). Characterization of a recombinant alkaline thermostable β-mannanase and its application in eco-friendly ramie degumming. *Process Biochemistry*, *61*, 73–79. https://doi.org/10.1016/j.procbio.2017.06.008

43. Zheng, X., Zhang, Y., Liu, X., Li, C., Lin, Y., & Liang, S. (2020). High-level expression and biochemical properties of a thermo-alkaline pectate lyase from Bacillus sp. RN1 in Pichia pastoris with potential in ramie degumming. *Frontiers in Bioengineering and Biotechnology*, *8*, 850. https://doi.org/10.3389/fbioe.2020.00850

44. Zhou, C., Cao, Y., Xue, Y., Liu, W., Ju, J., & Ma, Y. (2023). Structure of an alkaline pectate lyase and rational engineering with improved thermo-alkaline stability for efficient ramie degumming. *International Journal of Molecular Sciences*, *24*(1), Article 1. https://doi.org/10.3390/ijms24010538

45. Zhu, L., Lin, J., Pei, L., Luo, Y., Li, D., & Huang, Z. (2022). Recent advances in environmentally friendly and green degumming processes of silk for textile and non-textile applications. *Polymers*, *14*(4), Article 4. https://doi.org/10.3390/polym1404065

LIST OF PUBLICATIONS

Published/In press/accepted (From Thesis)

Research Articles

1. **Yumnam Robinson Singh**, Abhijeet Thakur, Carlos M. G. A. Fontes and Arun Goyal (2024) A novel thermophilic recombinant obligate xylobiohydrolase (*Ac*GH30A) from *Acetivibrio clariflavus* orchestrates the deconstruction of xylan polysaccharides. ***Carbohydrate Polymers.*** **(JIF: 12.5).**
2. **Yumnam Robinson Singh**, Jebin Ahmed and Arun Goyal (2024) Small angle X-ray scattering and *in silico* based structure and function analysis of a novel xylobiohydrolase (*Ac*GH30A) from *Acetivibrio clariflavus.* ***Journal of Biomolecular Structure and Dynamics.*** **(JIF: 2.7).**
3. **Yumnam Robinson Singh**, Nelson Mutum, Ruhina Naz and Arun Goyal (2025). Eco-friendly enzymatic degumming of Ramie (*Boehmeria nivea*) bast fibres and Pineapple (*Ananas comosus*) leaf fibres by xylobiohydrolase, pectate lyase and mannanase. (*Under review)*

Book Chapters

1. **Yumnam Robinson Singh** and Arun Goyal (2025) Sustainable enzymatic solutions for industrial applications: Degumming of bast fibres, biodeinking, and biobleaching. in lignocellulosic biomass and enzymes: Fundamentals, emerging technologies and applications (pp. 311-331). Singapore: Springer Nature Singapore.

Other Publications

1. Bipasha Choudhury, **Yumnam Robinson Singh**, Kaustubh Chandrakant Khaire, Nazneen Ahmed, Kedar Sharma, Carlos MGA Fontes, and Arun Goyal (2025) Cellulosomal *Ac*Xyn30B_12 from *Acetivibrio clariflavus* acts synergistically with *Ac*GH30A upon the hydrolysis of complex carbohydrates. ***International Journal of Biological Macromolecules.*** **(JIF: 8.5)**.
2. Madhulika Shrivastava, **Yumnam Robinson Singh**, Arun Goyal (2024) Structure analysis of a putative exo-rhamnogalacturonan lyase, of polysaccharide lyase family 26 from *Bacteroides thetaiotaomicron* by computational methods. ***Journal of Proteins and Proteomics*****.**
3. Biswajit Jana, Shubhankar Ghorai, **Yumnam Robinson Singh**, Nira Parshi, Dipika Pan, Sumit Kumar Pramanik, Arun Goyal, Jhuma Ganguly (2023) Phenomenal performance of Polysaccharide based Microgel-nanocomposite Template for distinctive binding of Picric Acid in Aqueous medium and Cancer Cell Recognition. ***Materials Today Chemistry.*** **(JIF: 6.7).**
4. Purabi Dutta, **Yumnam Robinson Singh**, Shubhankar Ghorai, Pijus Ghorai, Arun Goyal, and Jhuma Ganguly (2025). Fabrication and assessment of crosslinked hydrogel template for the efficacy of drug delivery. (*In preparation)*

LIST OF CONFERENCES

Conferences/Symposia/Meetings

1. **Yumnam Robinson Singh** and Arun Goyal (2024) Unveiling the biochemical, structural and degumming application attributes of a thermostable xylobiohydrolase, *Ac*GH30A from *Acetivibrio clariflavus.* International Conference on Advanced Bioprocessing Technologies for Biomass Conversion- Sustainability and Bioresource Management (IBA-IFIBIOP XI, 2024) December 1-6, 2024, The Hong Kong Polytechnic University (PolyU), Hong Kong, China.
2. **Yumnam Robinson Singh,** Abhijeet Thakur, Jebin Ahmed, Carlos M. G. A. Fontes and Arun Goyal (2024) Biochemical and structure investigation of *Ac*GH30A, a thermophilic xylobiohydrolase from *Acetivibrio clariflavus.* Research and Industrial Conclave 2024, An Amalgamation of Academia, Industry & Start-ups. August 9-11, 2024, Indian Institute of Technology Guwahati, Guwahati, Assam, India.
3. **Yumnam Robinson Singh**, Abhijeet Thakur, Jebin Ahmed and Arun Goyal (2023) Biochemical and in silico characterization of a novel xylobiohydrolase (*Cc*GH30A) from thermophilic bacterium *Clostridium clariflavum*. Research and Industrial Conclave 2023, An Amalgamation of Academia, Industry & Start-ups., May 14-16, 2023, Indian Institute of Technology Guwahati, Guwahati, Assam, India.
4. **Yumnam Robinson Singh**, Jebin Ahmed and Arun Goyal (2022) *In silico* structural and functional analysis of a novel xylanase (*Cc*GH30A) from *Clostridium clariflavum.* International Carbohydrate Conference (CARBO-XXXVI) on Emerging Trends in Glycochemistry, Glycobiology & Technology, December 5-7, 2022, IIT Bombay, Maharashtra, India.
5. **Yumnam Robinson Singh**, Abhijeet Thakur, Carlos M. G. A. Fontes and Arun Goyal (2022) Purification and biochemical characterization of a thermophilic xylobiohydrolase (*Cc*GH30A) from *Clostridium clariflavum*. Research and Industrial Conclave 2022, An Amalgamation of Academia, Industry & Start-ups. January 21-23, 2022, Indian Institute of Technology Guwahati, Guwahati, Assam, India.
6. Nazneen Ahmed, Kedar Sharma, **Yumnam Robinson Singh**, Kaustubh Chandrakant Khaire, Carlos M. G. A. Fontes and Arun Goyal (2022) Purification and characterization of endo-β-xylanase (*Cc*GH30B) from *Clostridium clariflavum*. Research and Industrial Conclave, An Amalgamation of Academia, Industry & Start-ups. January 21-23, 2022, Indian Institute of Technology Guwahati, Guwahati, Assam, India.

7. **Yumnam Robinson Singh**, Abhijeet Thakur, Carlos M. G. A. Fontes and Arun Goyal (2021) Expression, purification and biochemical characterization of a recombinant putative glucuronoxylanase (*Cc*GH30A) from *Clostridium clariflavum*. International Conference on Sustainable Energy and Environmental Challenges (VI SEEC), December 27-29, 2021, Lucknow, Uttar Pradesh, India.
8. **Yumnam Robinson Singh**, Abhijeet Thakur, Carlos M. G. A. Fontes and Arun Goyal (2021) Expression, purification and biochemical characterization of a recombinant putative glucuronoxylanase (*Cc*GH30A) from *Clostridium clariflavum*. International conference on Biotechnology for Sustainable Agriculture, Environment and Health (BSAEH), April 4-0, 2021, Jaipur, Rajasthan, India.

Workshops

1. Attended workshop on "Computational Structure-Based Screening and Explicit Molecular Dynamics" cloud based hands-on workshop, organized by Schrödinger. 21-22 September, 2021
2. Attended workshop on "Artificial Intelligence for all" hands-on workshop, organized by Indian Institute of Technology Guwahati, Guwahati, Assam, India. 14th May, 2023.

Awards and Honours

1. Awarded with **Anusandhan National Research Foundation (ANRF; formerly SERB) International Travel Scheme from DST** to present his work titled, "Unveiling the biochemical, structural and degumming application attributes of a thermostable xylobiohydrolase, *Ac*GH30A from *Acetivibrio clariflavus*" at the International Conference on Advanced Bioprocessing Technologies for Biomass Conversion- Sustainability and Bioresource Management (IBA-IFIBIOP XI, 2024) held at Hong Kong, China from 1-6 December, 2024.

VITAE

The author was born on September 01, 1993 in the town of Wangjing Wangkhei, Thoubal (Manipur). He passed Secondary Examination (10th Class) conducted by Central Board of Secondary Examination, New Delhi in 2009 and Higher Secondary Examination (12th Class) conducted by Central Board of Secondary Examination, New Delhi in 2011. He completed B.Sc. (Biotechnology) from Down Town College of Allied Health Sciences, under Srimanta Sankaradeva University of Health Sciences, Guwahati, Assam in 2015. He completed M.Sc. (Molecular Biology and Biotechnology) from Tezpur University, Tezpur, Assam, India in July, 2018.

Mr. Yumnam Robinson Singh joined the PhD program in July, 2019 at Department of Biosciences and Bioengineering, Indian Institute of Technology Guwahati, Guwahati 781 039, Assam, India. He successfully completed the coursework with 8.29/10 CPI. He delivered the open (PhD Synopsis) Seminar on 3rd April 2025 and presented his thesis work before the Doctoral Committee and his performance was satisfactory. He submitted the PhD thesis in 23rd April 2025.

14 Sustainable Enzymatic Solutions for Industrial Applications: Degumming of Bast Fibres, Biodeinking, and Biobleaching

Yumnam Robinson Singh and Arun Goyal

Abbreviations

EDTA	Ethylenediaminetetraacetic acid
AOX	Adsorbable organic halides
MnP	Manganese peroxidases
LiP	Lignin peroxidases
VOCs	Volatile organic compounds

1 Introduction

Enzymatic degumming, deinking, and biobleaching are essential biotechnological processes that utilize enzymes to improve the quality and sustainability of various industrial processes. These processes are integral to plant fibre degumming, paper recycling, and pulp production. This chapter provides a detailed overview of these enzymatic methods and emphasizes their underlying mechanisms, advantages, and significance in promoting environmental sustainability. Enzymatic degumming of textile fibres has emerged as a sustainable alternative to traditional chemical methods, offering significant environmental benefits and improved fibre quality (Abidin et al., 2023). This process utilizes specific enzymes, such as xylanase and pectinase, to effectively remove non-cellulosic components from natural fibres, thereby enhancing their suitability for textile applications. Recent studies have demonstrated that enzymatic treatments can lead to superior fibre strength, whiteness, and

Y. R. Singh · A. Goyal (✉)
Department of Biosciences and Bioengineering, Indian Institute of Technology, Guwahati, Guwahati, Assam, India
e-mail: yrsingh@iitg.ac.in; arungoyl@iitg.ac.in

R. K. Kapoor, K. Rajan (eds.), *Lignocellulosic Biomass and Enzymes*,
https://doi.org/10.1007/978-981-96-3037-0_14

overall fineness compared with conventional degumming methods, which often rely on harsh chemicals (Cheng et al., 2020). A study on ramie fibres highlighted the effectiveness of a combination of xylanase from *Bacillus halodurans* and commercial pectinase, achieving notable improvements in physical properties such as weight loss and tenacity under optimized conditions (Abidin et al., 2023).The eco-friendly nature of enzymatic degumming aligns with the growing demand for sustainable practices in the textile industry, making it a promising area for further research and development (Cheng et al., 2020; Subash & Muthiah, 2021).

Deinking is a critical stage in recycling paper, which removes ink and other contaminants from the fibres. This stage is crucial for producing high-quality recycled paper that adequately fulfils customer expectations (Sežun et al., 2023). Traditionally, deinking operations have utilized chemical and mechanical processes that may harm the environment and involve high costs. Deinking has been revolutionized by introduction of enzymatic deinking, an efficient and ecologically better alternative. Enzymatic deinking includes using specific enzymes capable of breaking down ink particles, such as cellulases and xylanases, to enhance their removal from paper fibres (Saxena & Singh Chauhan, 2017). The catalytic action of enzymes not only enhances the efficiency of the deinking process but also preserves the integrity of the paper fibres, thereby ensuring the quality of the recycled products. Enzymatic deinking reduces reliance on toxic chemicals, thereby reducing environmental pollution (Kumar et al., 2023).

Biobleaching is an advanced enzymatic method that enhances the whiteness and brightness of pulp and paper products. The treatment involves enzymes, such as lignolytic enzymes and cellulases, which degrade lignin and other chromophores within the wood pulp, reducing chlorine-based bleaching chemicals (Bajpai, 2018). The addition of enzymes during biobleaching positively affects the environmental sustainability of the bleaching process while simultaneously improving the quality of the product. Usually, the biobleaching process involves the addition of enzymes to the pulp, followed by a washing step that removes the depolymerized lignin together with other impurities (Wei et al., 2021). The results from this process have shown brightness equal to, or even surpassing, that obtained by conventional chemical bleaching while significantly reducing the production of toxic byproducts (Chaurasia & Bhardwaj, 2019). Biobleaching makes paper production more environment friendly by reducing the use of chemicals and lowering energy consumption.

2 Need for Fibre Degumming

The need for fibre degumming arises from enhancing the quality and usability of natural fibres in various applications, particularly in the textile industry. Degumming is a critical process that removes non-cellulosic components, such as pectin, hemicellulose, and lignin, which can negatively affect the mechanical properties and dyeing characteristics of the fibre (Cheng et al., 2020; Subash & Muthiah, 2021). For instance, in bast fibres, such as ramie and kenaf, inadequate degumming can

lead to coarse, brittle fibres unsuitable for high-quality textile applications (Subash & Muthiah, 2021). Recent studies have demonstrated that enzymatic degumming not only improves the softness and lustre of fibres, but also preserves their tensile strength, making them more desirable for fabric production (Abidin et al., 2023; Bakshi et al., 2024; Kaur et al., 2020). Traditional chemical degumming methods often involve harsh chemicals that can be harmful to the environment, underscoring the importance of developing eco-friendly degumming techniques (Lyu et al., 2021). Enzymatic approaches, such as those utilizing specific bacterial strains, have shown promising results in effectively removing gum while minimizing the environmental impact, aligning with the growing demand for sustainable practices in the textile industry. This shift towards more sustainable degumming methods essential for enhancing the overall performance and marketability of natural fibres, ensuring their competitiveness against synthetic alternatives in a rapidly evolving and changing market.

3 Bast Fibres

Bast fibres, also known as phloem fibres, are derived from the phloem tissue of certain dicotyledonous plants, including economically significant crops such as flax, hemp, jute, and ramie (Sadrmanesh & Chen, 2019). These fibres are characterized by their softness, flexibility, and strength, making them highly suitable for various applications, particularly in textiles and composite materials. The extraction of bast fibres typically involves retting, which can be performed using microbial action, chemical treatments, or enzymatic methods. This process facilitates the separation of fibres from the woody core (xylem) and other surrounding tissues (Kozłowski & Mackiewicz-Talarczyk, 2020). Enzymatic retting, in particular, utilizes pectinolytic enzymes to degrade pectin, which binds the fibres together, resulting in a cleaner and more efficient extraction process. It has been shown that bast fibres possess favorable mechanical properties, including high tensile strength and low density, making them ideal for reinforcing composite materials (George et al., 2016). Moreover, as a renewable and biodegradable resource, bast fibres are increasingly recognized for their potential to replace synthetic fibres in various industries, such as apparel and fashion, automotive, and aerospace industries, contributing to more sustainable practices and reducing the detrimental environmental impact associated with conventional materials. The growing interest in bast fibres has been reflected in numerous studies exploring their properties, extraction methods, and applications, highlighting their role in promoting eco-friendly alternatives in textiles and beyond.

3.1 Structure and Composition of Bast Fibres

Bast fibres, derived from the phloem of dicotyledonous plants, exhibit a complex structure and composition that contributes to their unique properties and

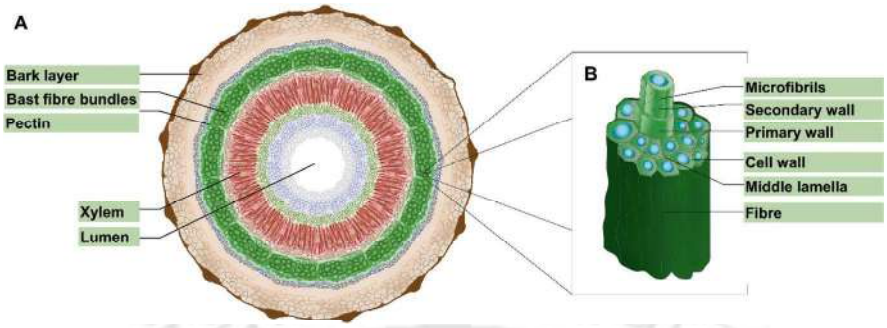

Fig. 14.1 (**a**) Schematic representation of the cross section of a bast stem, (**b**) Bast fibre bundle

applications. These fibres primarily consist of cellulose, hemicellulose, lignin, pectin, and waxes, with cellulose being the most abundant component, typically comprising 60–80% of the dry weight of the fibre (Kozłowski et al., 2020; Sadrmanesh & Chen, 2019). The structural organization of bast fibres includes the primary wall of a rigid network of cellulose microfibrils embedded within a matrix of hemicellulose and pectin, which provides flexibility and strength (Fig. 14.1). The fibres are characterized by a hollow lumen that aids nutrient transport within the plant. Simultaneously, the overall morphology includes elongated bundles of fibrils that exhibit a high length-to-diameter ratio, enhancing their mechanical properties (Zimniewska et al., 2011). Recent studies have highlighted the variability in the composition and properties of bast fibres, which can be affected by factors such as plant species, cultivation conditions, and extraction methods, underscoring the importance of optimizing these parameters for specific industrial applications (Santos et al., 2024).

4 Degumming Methods for Plant-Based Textile Fibres

4.1 Physical Extraction of Plant Fibres

The physical extraction of plant fibres involves mechanical processes designed to separate fibres from the plant matrix while preserving their structural integrity. One common method is decortication, in which plant stems or leaves are subjected to mechanical forces that break down the non-fibrous components, allowing the fibres to be extracted. This process typically involves using machines equipped with blunt knives or rollers that crush and beat the plant material, effectively separating the fibres from the surrounding tissues (Lyu et al., 2021). After decortication, the extracted fibres often contain residual mucilage and other impurities, necessitating a washing step to remove these contaminants. Decortication is typically followed by fibre cleaning and opening using machines. Recent advancements in extraction technology have improved the efficiency of this process, allowing for higher fibre yields and better quality. For example, studies have shown that optimizing

parameters such as moisture content and processing speed can significantly enhance the quality of extracted fibres, making them more suitable for applications in textiles and composites (Cheng et al., 2020; Lyu et al., 2021). Additionally, physical extraction methods are generally more environmentally friendly than chemical methods, as they do not involve harsh chemicals, thereby reducing the ecological footprint of fibre production. Physical extraction techniques can be easily scaled for industrial applications, allowing for efficient production of large quantities of fibres.

The physical extraction of plant fibres, which is advantageous for its simplicity and environmental friendliness, also presents several drawbacks. Mechanical processes can result in a high degree of fibre breakage, particularly for more delicate fibres, leading to shorter lengths, which may be less desirable for specific applications. Physical extraction often requires significant energy input, which contributes to operational costs and environmental impact. The equipment used can also be complex and expensive, which poses challenges for small-scale producers. Although physical extraction methods are beneficial in many respects, the trade-offs between fibre quality, processing efficiency, and environmental impact must be carefully considered in the context of specific applications and production scales.

4.2 Chemical Degumming of Plant Fibres

Chemical degumming of plant fibres primarily involves the use of alkaline solutions, such as sodium hydroxide (NaOH), to effectively remove hemicellulose, lignin, and pectin from bast fibres (Lyu et al., 2021). The mechanism of chemical degumming begins with the alkaline treatment, which disrupts the hydrogen bonds and ester linkages that hold the cellulosic fibres and non-cellulosic components together within the fibre structure. As the alkali penetrates the fibre, it hydrolyses hemicellulose and pectin, leading to their solubilization and subsequent removal. This process cleans the fibres and alters their surface morphology, enhancing their wettability and dye uptake in subsequent textile applications. Studies have shown that different components are removed at varying rates; for instance, lignin removal tends to be slower and more heterogeneous than that of hemicellulose, which can be more readily solubilized under alkaline conditions (Zhang et al., 2021). The effectiveness of chemical degumming can be influenced by factors such as temperature, concentration of the alkali solution, and treatment duration, which need to be optimized to minimize fibre degradation while maximizing gum removal.

Chemical degumming presents several challenges, including the potential degradation of fibre strength due to harsh treatment conditions, resulting in coarse and brittle fibres that are less desirable for high-quality textiles. Studies have highlighted that while chemical methods can produce clean fibres, they often lead to environmental concerns due to the toxic waste generated during the process (Cheng et al., 2020). For instance, the discharge of alkaline effluents can pose significant risks to water sources and ecosystems, if not properly managed. Moreover, the process typically requires high temperatures and long reaction times, further contributing to energy consumption and environmental impacts (Lyu et al., 2021). As a result, there

is growing interest in exploring alternative methods, such as enzymatic and biochemical degumming, which can achieve similar or superior results with reduced environmental footprints, thus promoting more sustainable practices in the textile industry (Subash & Muthiah, 2021). Recent research has indicated that integrating microbial or enzymatic treatments with chemical processes can mitigate some of these drawbacks, improve fibre quality, and reduce environmental harm.

4.3 Semi-Physical Degumming Methods of Plant Fibres

Semi-physical extraction methods for plant fibres involve a combination of mechanical and chemical treatments to separate the fibres from the plant matrix. These methods aim to strike a balance between the efficiency of mechanical extraction and the effectiveness of chemical processes, while minimizing the drawbacks of each approach (Lyu et al., 2021; Sutka et al., 2013). One semi-physical method is steam explosion, in which plant biomass is subjected to high-pressure steam followed by sudden decompression, causing the fibres to separate due to the rapid expansion of water vapor within the plant structure (Jacquet et al., 2011). Studies have shown that steam explosion can effectively extract cellulose fibres from various sources, including ramie and hemp, with minimal chemical usage and reduced energy consumption compared with traditional mechanical methods (Song et al., 2019; Sutka et al., 2013). Another semi-physical approach is alkali treatment, in which plant materials are mechanically crushed or chopped, followed by immersion in a dilute alkali solution, typically sodium or potassium hydroxide. The alkali helps to swell the plant cells and break down the lignin–hemicellulose matrix, facilitating the separation of fibres (Subash & Muthiah, 2021). This method has been successfully applied to extract fibres from jute, kenaf, and hemp, producing high-quality fibres suitable for reinforcing polymer composites. The combination of mechanical and chemical treatments in semi-physical extraction methods allows for more efficient fibre separation while maintaining the desirable properties of the extracted fibres, making them a promising alternative to conventional extraction techniques.

4.4 Enzymatic Degumming of Plant Fibres

Enzymatic degumming is an eco-friendly and efficient method for eliminating non-cellulosic substances, including pectin, hemicellulose, and lignin from plant fibres, particularly bast fibres such as ramie, hemp, and flax (Subash & Muthiah, 2021). This process utilizes specific enzymes, such as pectinases, xylanases, and laccases, to selectively break down the gum that binds the fibres together, facilitating their separation without compromising the structural integrity of the fibres (Abidin et al., 2023). Enzymatic and chemical degumming methods share the common goal of achieving cleaner fibres by removing non-cellulosic substances. Both degumming processes share some similarities, but their approaches differ significantly, with enzymatic degumming relying on biological catalysts, and chemical

degumming using harsh chemicals. Initially, plant fibres like hemp, ramie, and flax are prepared with decortication, followed by cleaning and washing to remove dirt and loose particles (Fig. 14.2). The fibres are then treated with enzymes or chemicals, depending on the approach. After degumming, the fibres were washed with water to remove the degraded components and residual chemicals or enzymes (Fig. 14.2). Then, the fibres are dried and sent forward for different applications. Recent advancements in enzyme technology have led to the development of customized enzyme cocktails and optimized process parameters, further enhancing the efficiency and applicability of enzymatic degumming in textile and composite industries (Kaur et al., 2020).

4.4.1 Mechanism of Enzymatic Degumming of Plant Fibres

Enzymatic degradation of plant fibres, such as ramie and hemp, involves the degradation of pectin and hemicellulose components using pectinolytic and hemicellulolytic enzymes (Table 14.1). Pectinolytic enzymes, particularly pectate lyases, play a key role in the removal of pectin from the fibre surface. Xylanases also contribute to the degumming process by breaking down xylan from hemicellulose portion. Enzymes act on the gum components, making the fibres more accessible for further processing. A list of the different enzymes utilized in enzymatic degumming is presented in Table 14.1. Combining partial chemical treatment with enzymatic degumming using microbial formulations has been shown to produce durable, soft, and lustrous fibres, while utilizing fewer chemicals (Guo et al., 2013; Yadav et al., 2022).

4.4.2 Advantages of Enzymatic Degumming of Plant Fibres

Enzymatic degumming of plant fibres offers several advantages over traditional chemical methods, making it an increasingly preferred choice in the textile industry. One of the primary benefits of enzymatic degumming is its eco-friendliness. It significantly reduces the use of harsh chemicals, which can harm the environment and human health. For instance, studies have shown that enzymatic treatments can effectively remove non-cellulosic components from plant fibres without employing the high temperatures and pressures associated with chemical methods, thereby

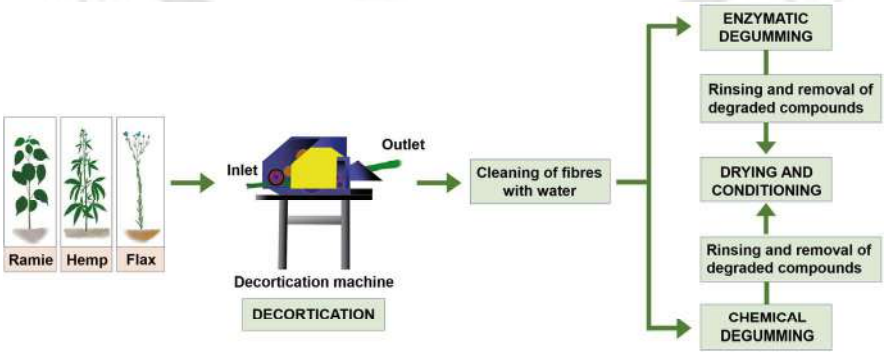

Fig. 14.2 The general process followed during enzymatic and chemical degumming

Table 14.1 Different enzymes used in enzymatic degumming, biodeinking, and biobleaching

Enzyme	Activity	Application	Role in process	References
Pectinases	Hydrolyse pectin	Degumming	Break down pectin in plant fibres, reducing gum content in fibres.	Abidin et al. (2023), Li et al. (2013)
Xylanases	Hydrolyse xylan (hemicellulose)	Degumming, biodeinking, biobleaching	Break down hemicellulose, facilitating the removal of lignin in biobleaching and improving biodeinking efficiency.	Abidin et al. (2023), Kaur et al. (2020), Subash and Muthiah (2021)
Proteases	Cleaves peptide bonds in proteins	Degumming	Remove proteinaceous impurities in degumming improving fibre quality.	Guo et al. (2013)
Cellulases	Hydrolyse cellulose to glucose	Biodeinking,	Enhance fibre cleaning by removing residual ink in biodeinking	Akbarpour et al. (2018), Indumathi et al. (2022)
Amylases	Break down starch into sugars	Biodeinking	Remove starch-based coatings or fillers during biodeinking, aiding in ink removal from printed paper.	Dixit et al. (2023), Pasin et al. (2024)
Lipases	Hydrolyse triglycerides into glycerol and free fatty acids	Biodeinking	Eliminate fatty sticky substances (pitch) in pulp for biodeinking.	Dixit et al. (2022), Sundaramahalingam et al. (2024)
Laccases	Oxidize phenolic compounds	Biodeinking, biobleaching	Degrade lignin by oxidizing phenolic structures, reducing lignin content during biobleaching.	Arias et al. (2003), Balda et al. (2024), Fillat et al. (2010, 2012)

(continued)

Table 14.1 (continued)

Enzyme	Activity	Application	Role in process	References
Manganese peroxidases (MnP)	Oxidize Mn^{2+} to Mn^{3+}, which oxidizes lignin	Biobleaching	Degrade non-phenolic lignin, reducing lignin content in biobleaching.	Saleem et al. (2018), Sasaki et al. (2001)
Lignin peroxidases (LiP)	Oxidize lignin using hydrogen peroxide (H_2O_2)	Biobleaching	Degrade both phenolic and non-phenolic lignin compounds, facilitating lignin removal in biobleaching.	Iimori et al. (1998), Orozco Colonia et al. (2019)

minimizing energy consumption and pollution (Lyu et al., 2021). Moreover, enzymatic degumming enhances the mechanical properties of the fibres, resulting in softer, more lustrous, and more robust materials that are better suited for textile applications. It has been reported that fibres treated with enzymes exhibit improved tensile strength and a higher aspect ratio; in other words, the fibre becomes longer relative to its width, which is crucial for the durability and performance of textiles (Subash & Muthiah, 2021). Moreover, the enzymatic processes allow for greater control over the degumming process, leading to more uniform fibre quality as compared with the often inconsistent results of chemical treatments. Therefore, the adoption of enzymatic degumming aligns with the industry's shift towards sustainable practices, providing a viable alternative that meets both environmental and quality standards.

4.4.3 Limitations and Future Perspectives of Enzymatic Degumming

Enzymatic degumming of plant fibres presents several limitations compared to traditional chemical methods, along with promising future perspectives. One significant limitation is the high cost associated with enzyme production and application, which hinders the widespread adoption of this method in commercial settings. Studies have indicated that enzymatic processes can effectively remove pectin and other non-cellulosic components. However, they often require longer processing times and specific conditions such as optimal temperature and pH to achieve the desired results. The efficiency of enzymatic degumming can vary depending on the type of fibre and the complexity of the gum composition, which may necessitate the development of customized enzyme cocktails for different plant materials. Despite these challenges, the future of enzymatic degumming appears promising, particularly as advancements in biotechnology continue to enhance enzyme efficacy and reduce cost. Research efforts are increasingly focusing on optimizing enzyme formulations and exploring the use of microbes to improve the efficiency of the degumming process. The growing demand for sustainable and eco-friendly processing methods aligns with the principles of enzymatic degumming, positioning it as a

potential alternative to chemical methods in the textile industry. As innovations in enzyme technology progress, there is potential for enzymatic degumming to become more competitive, offering high-quality fibres with minimal environmental impact.

4.5 Microbial Degumming of Plant Fibres

Microbial degumming of plant fibres, particularly bast fibres such as kenaf and ramie, has emerged as an eco-friendly alternative to traditional chemical methods. This process involves the use of specific bacteria and fungi that secrete enzymes capable of degrading pectin, hemicellulose, and lignin, which bind the fibres together. Recent studies have identified microbes responsible for efficient degumming, including *Bacillus* spp., *Acinetobacter, Chryseobacterium, Dysgonomonas, and Lactococcus* (Cheng et al., 2020; Ray Chaudhuri et al., 2020; Yang et al., 2019). These bacteria produce a range of enzymes, including pectinases, xylanases, and ligninases, which work synergistically to break down the gum and separate the fibres without compromising their structural integrity. The microbial degumming process typically involves inoculating plant material with a consortium of these beneficial microbes and allowing them to ferment under controlled conditions (Duan et al., 2021). This method not only reduces the need for harsh chemicals but also preserves the desirable properties of the fibres, such as tensile strength and flexibility, making them suitable for various applications, including textiles and composites (Cheng et al., 2020). As the demand for sustainable and eco-friendly fibre processing continues to grow, microbial degumming offers a promising solution that aligns with the principles of green chemistry and economy.

5 Biodeinking

Enzymatic deinking is an innovative and eco-friendly approach for recycling paper that utilizes specific enzymes to effectively remove ink from paper fibres. This method has recently gained attention for its ability to achieve high-quality deinked pulp while minimizing environmental impact. Recent studies have demonstrated that combining different enzymes can enhance deinking efficiency, achieving brightness levels that surpass those of traditional chemical methods, thus making enzymatic deinking a promising alternative in the pulp and paper industry (Saxena & Singh Chauhan, 2017).

5.1 Wastepaper as a Sustainable Resource for Paper Manufacturing

Wastepaper is an exceptional raw material in the paper industry because it offers significant environmental benefits and resource conservation. Recycling wastepaper reduces the demand for virgin wood pulp, preserves forests, and minimizes

ecological disruptions. India generates approximately 12 million tons of wastepaper annually, with a recovery rate of approximately 57% (Mondal et al., 2022). The potential for wastepaper recycling in India is immense; increasing the recovery rate could lead to considerable environmental benefits, including significant savings in raw materials, energy, and water. For instance, recycling one ton of wastepaper can save 70% raw materials, 60% coal, and 43% energy compared to producing paper from virgin pulp (Jain & Kumar, 2019). Enhancing wastepaper recycling could not only reduce the environmental impact, but also create job opportunities and contribute to the economy, potentially transforming waste into a valuable resource.

A crucial step in this recycling process is deinking, which removes ink and contaminants from the paper fibres, allowing for the production of high-quality recycled pulp. Recent studies have highlighted the effectiveness of enzymatic deinking methods that utilize specific enzymes, such as cellulases and xylanases, to facilitate ink removal. The optimization of enzymatic processes has been shown to improve the efficiency of ink removal from various types of printed paper, making enzymatic deinking a promising alternative for maximizing the potential of wastepaper as a sustainable raw material (Wang et al., 2018).

5.2 Biodeinking and its Advantages

Biodeinking is an innovative and environmentally friendly approach to the deinking process in paper recycling that utilizes enzymes to remove inks and contaminants from wastepaper. This method addresses several limitations associated with conventional deinking techniques, which often rely on harsh chemicals that can damage paper fibres and generate harmful effluents (V. Kumar et al., 2023). Enzymes such as cellulases, xylanases, and lipases play a crucial role in biodeinking by breaking down the bonds between ink particles and cellulose fibres, facilitating their removal without compromising the integrity of the fibres (Saxena & Singh Chauhan, 2017). Reports have shown that biodeinking can achieve comparable or even superior results in terms of the brightness and cleanliness of recycled paper compared to traditional methods, while significantly reducing chemical usage and environmental impact (Kumar & Dutt, 2021). In addition, biodeinking processes can be optimized for various types of paper waste, making them versatile and adaptable to different recycling scenarios. Implementing biodeinking enhances the quality of recycled paper and contributes to a more sustainable circular economy by minimizing waste and promoting resource conservation (Kumar et al., 2023; Sežun et al., 2023). As the demand for sustainable practices in the paper industry continues to grow, biodeinking stands out as a promising solution that aligns with ecological goals and regulatory requirements, paving the way for a more sustainable future for paper recycling.

5.3 Mechanism of Biodeinking

Biodeinking is an innovative process that utilizes enzymes to remove ink from wastepaper, significantly enhancing the recycling of paper products while minimizing the environmental impact. The mechanism of biodeinking primarily involves the action of specific enzymes that target the bonds between ink particles and cellulose fibres. Key enzymes used in this process include cellulases, xylanases, and laccases (Saxena & Singh Chauhan, 2017). The key enzymes used for the biodeinking process are listed in Table 14.1. Cellulases break down cellulose, which helps to expose ink particles and facilitates their detachment from the fibre surface. Xylanases target hemicellulose, loosen the fibre matrix, and further aid in ink release. In contrast, laccases are particularly effective in degrading lignin. They can oxidize phenolic compounds in inks, promoting the removal of ink particles that are otherwise tightly bound to the fibres (V. Kumar et al., 2023). Recent studies have demonstrated that a combination of these enzymes can yield superior results. For example, sequential treatment with xylanase, followed by laccase, enhanced deinking efficiency compared to single-enzyme treatments. This synergistic action improves the ink removal and reduces the need for harsh chemicals traditionally used in deinking processes, thereby promoting a more sustainable recycling framework (V. Kumar et al., 2023).

5.4 Conventional Deinking

Conventional deinking methods have been the cornerstone of paper recycling, focusing primarily on chemical and physical techniques for removing ink from paper waste. Chemical deinking typically involves the use of surfactants, alkalis, and other agents to facilitate the detachment of ink particles from the cellulose fibres. This process often requires significant amounts of water and generates a considerable volume of wastewater, which can be environmentally harmful if not properly treated. It has been reported that combining chemical treatment with physical methods, such as flotation and washing, increases the ink removal efficiency (Kumar & Dutt, 2021). For example, the flotation process utilizes air bubbles to lift ink particles to the surface, which can be skimmed off, thereby significantly improving the brightness and quality of the recycled pulp. However, this conventional approach is being increasingly scrutinized because of its reliance on toxic chemicals and the associated environmental impact. Innovations in enzymatic deinking have emerged as complementary strategies, demonstrating that enzymatic treatments can achieve comparable or superior pulp brightness and strength while reducing the need for harsh chemicals (Sežun et al., 2023). Integrating enzymatic methods with traditional physical processes can optimize the deinking efficiency, leading to more sustainable recycling methods that minimize chemical usage and wastewater generation, thus addressing some of the key limitations of conventional deinking methods (Kumar & Dutt, 2021; Sežun et al., 2023).

5.4.1 Chemical Deinking

5.4.1.1 Alkaline Deinking

This method is highly effective in removing a wide range of inks and contaminants by utilizing widely available chemicals, such as sodium hydroxide (Kumar & Dutt, 2021). Alkaline conditions enhance ink detachment from fibres, thereby improving the brightness of the recycled pulp. However, alkaline deinking can weaken paper fibres if not carefully controlled, and it requires high pH levels, which can pose environmental risks owing to chemical waste generation (Sežun et al., 2023).

5.4.1.2 Acid Deinking

Acid deinking is also effective in removing inks and has a less detrimental impact on paper quality than alkaline methods. The process involves the use of acids, such as hydrochloric acid (HCl) or sulfuric acid (H_2SO_4), to lower the pH of the pulp slurry. It is suitable for certain printed materials, such as glossy papers. The technique tends to be more expensive because of the cost of the strong acids used, and poses hazards related to the handling and disposal of these chemicals, which can also lead to environmental concerns (Kumar & Dutt, 2021).

5.4.1.3 Chelation Deinking

This method effectively removes heavy metals from inks and is potentially less damaging to paper fibres than other chemical methods. The mechanism involves the addition of chelating agents, such as ethylenediaminetetraacetic acid (EDTA), to the pulp slurry. This can improve the overall quality of the recycled pulp. Chelation deinking has limited effectiveness in removing different inks and can negatively impact the paper quality. Additionally, the availability of chelating agents and required equipment can be constraints (Bajpai, 2012; Sežun et al., 2023).

5.4.2 Physical Deinking

5.4.2.1 Froth Flotation

The froth flotation method is widely used because it effectively separates ink from fibres. It works by injecting air into the slurry of paper pulp, creating bubbles that carry ink particles to the surface for removal, thus enhancing the brightness of the recycled paper. The effectiveness of this method can vary based on factors such as ink type and pulp consistency, and may not be as effective for all types of inks, particularly those that are more hydrophilic (Virk et al., 2013).

5.4.2.2 Washing

This technique involves washing the pulp with water to remove contaminants and effectively reducing the ink levels when combined with other methods. The washing process can be labour intensive and may require multiple stages to achieve satisfactory results, making it less efficient (Virk et al., 2013).

5.5 Limitations and Future Recommendations for Biodeinking

Biodeinking, while promising as an eco-friendly alternative to traditional deinking methods, has several limitations that must be addressed for broader industrial applications. One significant challenge is the variability in the composition of the waste-paper, which can affect the efficiency of enzymatic action. Different types of inks, such as those used in laser printing versus offset printing, require specific enzymatic treatments, and the presence of additives and fillers in paper can hinder enzyme accessibility to ink particles (Singh et al., 2019b). The effectiveness of biodeinking can be influenced by operational conditions, such as temperature, pH, and enzyme concentration, necessitating precise optimization for each recycling scenario. Recent reports indicate that although biodeinking can achieve satisfactory results, it often does not match the efficiency of conventional chemical methods in terms of ink removal and pulp brightness, particularly for certain ink types (Mondal et al., 2022). Future recommendations include the development of enzyme cocktails that combine multiple enzyme types to more effectively target a broader range of ink compositions. Moreover, integrating biodeinking with physical methods such as flotation or ultrasonic treatment can enhance the overall deinking efficiency. Research should also focus on optimizing process parameters and scaling up from laboratory to industrial applications, ensuring that the biodeinking process is economically viable while maintaining high-quality recycled paper products. Lastly, further exploration of the use of genetically engineered enzymes or novel microbial sources may yield more effective and robust solutions for biodeinking, paving the way for a more sustainable paper recycling industry.

6 Biobleaching

Biobleaching is an eco-friendly approach for bleaching pulp in the paper industry, utilizing enzymes instead of harsh chemicals. This method employs enzymes such as xylanases and laccases to selectively remove lignin from pulp, enhancing its brightness and whiteness without compromising the fibre strength (Table.14.1). Recent studies have shown the potential of biobleaching to achieve brightness levels comparable to or better than those of conventional chemical bleaching, while significantly reducing the environmental impact associated with chemical usage (Chaurasia & Bhardwaj, 2019). Enzymes such as xylanases can break down hemicellulose, loosen the fibre matrix, and facilitate lignin removal, whereas laccases can oxidize phenolic compounds in lignin. Integrating biobleaching with physical methods, such as ultrasonic treatment, has further improved the efficiency of the process (Wei et al., 2021).

6.1 Biobleaching and its Advantages

Biobleaching is an innovative and environmentally friendly method employed in the pulp and paper industry to enhance the brightness of paper products, while minimizing the use of harmful chemicals. One of the primary advantages of biobleaching is its ability to significantly reduce the consumption of chlorine-based bleaching agents, thereby lowering the generation of toxic byproducts and pollutants such as adsorbable organic halides (AOX), which are harmful to aquatic ecosystems. Studies have shown that biobleaching can achieve brightness levels comparable or even superior to those of conventional chemical methods while preserving the integrity and strength of paper fibres (Chaurasia & Bhardwaj, 2019). In combination with mediator molecules, laccases have proven effective in oxidizing phenolic compounds in lignin, further improving bleaching efficiency. Biobleaching operates under milder conditions, typically at neutral pH and moderate temperature, contributing to energy savings and reduced operational costs (Bajpai, 2018). The implementation of biobleaching aligns with the growing demand for sustainable practices in the paper industry, making it a viable alternative as environmental regulations become increasingly stringent. Biobleaching is a promising solution for producing high-quality, environmentally friendly paper products, contributing to a more sustainable approach in the pulp and paper sector.

6.2 Application of Enzymes in Biobleaching

Enzymes have gained significant attention in the pulp and paper industry for their role in biobleaching, which is an eco-friendly alternative to traditional chemical bleaching methods. Recent studies have reported the effectiveness of various enzymes, including xylanases, laccases, and manganese peroxidases, in enhancing the bleaching process while reducing the environmental impact (Table 14.1). Xylanases play a crucial role in depolymerizing hemicellulose, which improves the accessibility of cellulose fibres and enhances the efficiency of subsequent bleaching chemicals. This enzymatic treatment reduces the number of kappa pulps and improves their brightness and physical strength (Kumar, 2021). The Kappa number is an important parameter in the paper and pulp industries. The Kappa number measures the residual lignin in the pulp after chemical pulping (Susanti, 2024). Lignin binds the cellulose fibres together, and removing lignin is crucial for producing high-quality paper. Laccases, when used with mediator molecules, have shown promising results in degrading lignin and improving pulp whiteness (Tiwari et al., 2023). A combination of laccase and xylanase resulted in a 46.32% reduction in kappa number and a 13.21% increase in brightness for mixed wood pulp, indicating synergistic effects of these enzymes (Angural et al., 2020). Moreover, the use of manganese peroxidases has been reported to further enhance the delignification process, contributing to a higher pulp quality and lower chemical consumption (Singh et al., 2019a). Integrating these enzymes into biobleaching processes improves the

quality of recycled paper and aligns with the industrial shift towards more sustainable and environmentally friendly practices.

6.3 Conventional Bleaching Processes

Conventional bleaching processes in the pulp and paper industry are essential for enhancing the brightness and quality of paper products; however, they have various drawbacks. Here is a detailed list of primary bleaching methods and their limitations.

6.3.1 Chlorine Bleaching

This method uses chlorine gas to oxidize and dissolve lignin in the pulp, thereby effectively removing the colour. Chlorine bleaching generates toxic organochlorine compounds that can lead to significant environmental pollution and health hazards. This process also results in the formation of dioxins, which are persistent environmental pollutants (Axegård, 2019).

6.3.2 Hydrogen Peroxide Bleaching

This method uses hydrogen peroxide as a bleaching agent to effectively remove residual lignin and improve the pulp brightness. Hydrogen peroxide is unstable and requires careful handling and storage. The presence of metal ions can also influence its effectiveness by catalysing its decomposition and reducing its bleaching efficiency (Isaza Ferro et al., 2021).

6.3.3 Ozone Bleaching

Ozone is a powerful oxidizing agent used to bleach pulp, effectively breaking down lignin and other colour-causing substances. Ozone bleaching requires specialized equipment for generation and application, which can increase the capital and operational costs. Additionally, ozone is a hazardous gas that requires strict safety measures during its handling (Tripathi et al., 2020).

6.3.4 Sodium Hypochlorite Bleaching

Sodium hypochlorite, commonly known as bleach, oxidizes lignin and improves the pulp whiteness. This method can lead to fibre degradation if not carefully controlled, resulting in a loss of pulp strength. It also generates chlorine-containing byproducts, which can harm the environment (Rajabi & Zabizadeh, 2018).

6.3.5 Peracetic Acid Bleaching

Peracetic acid combines acetic acid and hydrogen peroxide to bleach pulp and remove lignin. Although effective, peracetic acid can be corrosive and requires careful handling. Their use may also generate volatile organic compounds (VOCs), which can contribute to air pollution (Sharma et al., 2020).

6.4 Limitations and Future Perspectives of Biobleaching

Biobleaching, while offering a more sustainable alternative to traditional bleaching methods in the pulp and paper industry, has several limitations that must be addressed before its broader adoption. One primary challenge is the variability in the composition of raw materials, such as the type of wood used and the nature of inks in recycled paper, which can affect the efficiency of enzymatic action (Kumar, 2021). Different types of lignin and hemicellulose present in various wood species may require specific enzymes, which complicates the development of universal enzyme formulations. The effectiveness of biobleaching can be influenced by operational conditions, such as temperature, pH, and enzyme concentration, necessitating precise optimization for each application (Angural et al., 2023; Wei et al., 2021). Furthermore, although biobleaching can significantly reduce harmful chemicals, the cost of enzyme production and the need for specialized equipment can be barriers to implementation, particularly for smaller mills. Future perspectives for biobleaching include the development of enzyme cocktails that can combine multiple enzymes to target a broader range of substrates more effectively. Researchers should also optimize the process parameters and scale from laboratory to industrial applications to ensure economic viability. Integrating biobleaching with other sustainable practices, such as using renewable energy sources and improving process efficiency, will further support its adoption in the industry. By addressing these limitations and exploring innovative solutions, biobleaching can contribute significantly to a more environmentally friendly pulp and paper industry.

7 Conclusion

Enzymatic degumming, biodeinking, and biobleaching represent innovative and eco-friendly approaches in the textile, pulp, and paper industries that promote sustainable practices while enhancing product quality. Enzymatic degumming utilizes specific enzymes such as pectinases, xylanases, and cellulases to effectively remove non-cellulosic components from plant fibres such as ramie and hemp. This method can significantly improve fibre properties, including weight loss, whiteness index, and tensile strength, while reducing reliance on harsh chemicals. Combining enzymatic and chemical degumming is the most efficient, with successive treatments leading to superior gum removal and fibre quality results. In contrast, biodeinking focuses on removing ink from wastepaper using enzymes such as cellulases, xylanases, and pectinases. These enzymes facilitate the detachment of ink particles from the fibre surface, thereby improving the brightness and cleanliness of the recycled paper. Biodeinking can replace traditional chemical deinking methods with comparable effectiveness, while being more eco-friendly. Biobleaching employs enzymes such as xylanases, laccases, and manganese peroxidases to degrade lignin and hemicellulose, which are responsible for the brown colour and impurities in the pulp. Biobleaching contributes to a more sustainable bleaching process while maintaining high-quality standards by minimizing the use of chlorine-based chemicals.

The use of enzyme cocktails, combining various enzymes, has been explored to enhance the biobleaching process, leading to better overall pulp quality and brightness. Collectively, these enzymatic processes exemplify a sustainable approach in the textile, pulp, and paper industries, facilitating the production of high-quality products, while addressing environmental concerns and promoting eco-friendly practices.

References

Abidin, K. Y., Nurhayati, N., Nandyawati, D., & Sabbathini, G. C. (2023). Enzymatic degumming using xylanase and pectinase to improve brightness and fineness quality of ramie fiber (Boehmeria nivea L.) as textile raw material. *JurnalBioteknologi Dan Biosains Indonesia, 10*(1), 76–85. Retrieved from https://ejournal.brin.go.id/JBBI/article/view/1744

Akbarpour, I., Ghasemian, A., Resalati, H., & Saraeian, A. (2018). Biodeinking of mixed ONP and OMG waste papers with cellulase. *Cellulose, 25*(2), 1265–1280. https://doi.org/10.1007/s10570-017-1641-y

Angural, S., Rana, M., Sharma, A., Warmoota, R., Puri, N., & Gupta, N. (2020). Combinatorial biobleaching of Mixedwood pulp with lignolytic and hemicellulolytic enzymes for paper making. *Indian Journal of Microbiology, 60*(3), 383–387. https://doi.org/10.1007/s12088-020-00867-6

Angural, S., Jassal, S., Warmoota, R., Rana, M., Puri, N., & Gupta, N. (2023). An integrated approach for pulp biobleaching: Application of cocktail of enzymes. *Environmental Science and Pollution Research, 30*(19), 57155–57163. https://doi.org/10.1007/s11356-023-25941-6

Arias, M. E., Arenas, M., Rodríguez, J., Soliveri, J., Ball, A. S., & Hernández, M. (2003). Kraft pulp biobleaching and mediated oxidation of a nonphenolic substrate by laccase from streptomyces cyaneus CECT 3335. *Applied and Environmental Microbiology, 69*(4), 1953–1958. https://doi.org/10.1128/AEM.69.4.1953-1958.2003

Axegård, P. (2019). The effect of the transition from elemental chlorine bleaching to chlorine dioxide bleaching in the pulp industry on the formation of PCDD/Fs. *Chemosphere, 236*, 124386. https://doi.org/10.1016/j.chemosphere.2019.124386

Bajpai, P. (2012). Biodeinking. In P. Bajpai (Ed.), Biotechnology for pulp and paper processing (pp. 139–158). Springer US. https://doi.org/10.1007/978-1-4614-1409-4_9.

Bajpai, P. (2018). Biobleaching. In P. Bajpai (Ed.), *Biotechnology for pulp and paper processing* (pp. 159–213). Springer. https://doi.org/10.1007/978-981-10-7853-8_10

Bakshi, M. I., Sohail, A., Karimah, A., Ridho, M. R., Hastuti, N., Side, T. H. R., Darwis, A., Subiyanto, B., Wulandari, A. P., & Fatriasari, W. (2024). Effect of degumming of two selected Indonesian Ramie (*Boehmeria nivea)* accessions on the anatomical, chemical, mechanical, and thermal properties. *Industrial Crops and Products, 216*, 118725. https://doi.org/10.1016/j.indcrop.2024.118725

Balda, S., Sharma, A., Gupta, N., Capalash, N., & Sharma, P. (2024). Deinking of old newsprint (ONP) pulp with an engineered laccase: A greener approach for paper recycling. *Biomass Conversion and Biorefinery, 14*(3), 3965–3974. https://doi.org/10.1007/s13399-022-02509-x

Chaurasia, S. K., & Bhardwaj, N. K. (2019). Biobleaching—An ecofriendly and environmental benign pulp bleaching technique: A review. *Journal of Carbohydrate Chemistry, 38*(2), 87–108. https://doi.org/10.1080/07328303.2019.1581888

Cheng, L., Duan, S., Feng, X., Zheng, K., Yang, Q., Xu, H., Luo, W., & Peng, Y. (2020). Ramie-degumming methodologies: A short review. *Journal of Engineered Fibers and Fabrics, 15*, 1558925020940105. https://doi.org/10.1177/1558925020940105

Dixit, M., Gupta, G. K., Pathak, P., Bhardwaj, N. K., & Shukla, P. (2022). An efficient endoglucanase and lipase enzyme consortium (ELEC) for deinking of old newspaper and ultrastructural analysis of deinked pulp. *Biomass Conversion and Biorefinery*. https://doi.org/10.1007/s13399-022-03310-6

Dixit, M., Chhabra, D., & Shukla, P. (2023). Optimization of endoglucanase-lipase-amylase enzyme consortium from *Thermomyceslanuginosus* VAPS25 using multi-objective genetic algorithm and their bio-deinking applications. *Bioresource Technology, 370*, 128467. https://doi.org/10.1016/j.biortech.2022.128467

Duan, S., Xu, B., Cheng, L., Feng, X., Yang, Q., Zheng, K., Gao, M., Liu, Z., Liu, C., & Peng, Y. (2021). Bacterial strain for bast fiber crops degumming and its bio-degumming technique. *Bioprocess and Biosystems Engineering, 44*(12), 2503–2512. https://doi.org/10.1007/s00449-021-02622-7

Fillat, A., Colom, J. F., & Vidal, T. (2010). A new approach to the biobleaching of flax pulp with laccase using natural mediators. *Bioresource Technology, 101*(11), 4104–4110. https://doi.org/10.1016/j.biortech.2010.01.057

Fillat, U., Prieto, A., Camarero, S., Martínez, Á. T., & Martínez, M. J. (2012). Biodeinking of flexographic inks by fungal laccases using synthetic and natural mediators. *Biochemical Engineering Journal, 67*, 97–103. https://doi.org/10.1016/j.bej.2012.05.010

George, M., Chae, M., & Bressler, D. C. (2016). Composite materials with bast fibres: Structural, technical, and environmental properties. *Progress in Materials Science, 83*, 1–23. https://doi.org/10.1016/j.pmatsci.2016.04.002

Guo, F., Zou, M., Li, X., Zhao, J., & Qu, Y. (2013). An effective degumming enzyme from bacillus sp. Y1 and synergistic action of hydrogen peroxide and protease on enzymatic degumming of ramie fibers. *BioMed Research International, 2013*(1), 212315. https://doi.org/10.1155/2013/212315

Iimori, T., Miyawaki, S., Machida, M., & Murakami, K. (1998). Biobleaching of unbleached and oxygen-bleached hardwood kraft pulp by culture filtrate containing manganese peroxidase and lignin peroxidase fromPhanerochaetechrysosporium. *Journal of Wood Science, 44*(6), 451–456. https://doi.org/10.1007/BF00833409

Indumathi, T., Jayaraj, R., Kumar, P. S., Sonali, J. M. I., Krishnaswamy, V. G., Ghfar, A. A., & Govindaraju, S. (2022). Biological approach in deinking of waste paper using bacterial cellulase as an effective enzyme catalyst. *Chemosphere, 287*, 132088. https://doi.org/10.1016/j.chemosphere.2021.132088

Isaza Ferro, E., Ruuttunen, K., Perrin, J., & Vuorinen, T. (2021). Sustainable bleaching of *Eucalyptus sp.* kraft pulp with hypochlorous acid, ozone and hydrogen peroxide. *Industrial Crops and Products, 172*, 114004. https://doi.org/10.1016/j.indcrop.2021.114004

Jacquet, N., Quiévy, N., Vanderghem, C., Janas, S., Blecker, C., Wathelet, B., Devaux, J., & Paquot, M. (2011). Influence of steam explosion on the thermal stability of cellulose fibres. *Polymer Degradation and Stability, 96*(9), 1582–1588. https://doi.org/10.1016/j.polymdegradstab.2011.05.021

Jain, R. K., & Kumar, V. (2019). Status, prospects & perspectives of Indian paper industry. *Paper and Biomaterials, 4*(1), 57–64. https://doi.org/10.26599/PBM.2019.9260008

Kaur, A., Varghese, L. M., Battan, B., Patra, A. K., Mandhan, R. P., & Mahajan, R. (2020). Bio-degumming of banana fibers using eco-friendly crude xylano-pectinolytic enzymes. *Preparative Biochemistry & Biotechnology, 50*(5), 521–528. https://doi.org/10.1080/10826068.2019.1710713

Kozłowski, R. M., & Mackiewicz-Talarczyk, M. (2020). 1A—Introduction to natural textile fibres. In R. M. Kozłowski & M. Mackiewicz-Talarczyk (Eds.), *Handbook of natural fibres* (2nd ed., pp. 1–13). Woodhead Publishing. https://doi.org/10.1016/B978-0-12-818398-4.00001-3

Kozłowski, R. M., Mackiewicz-Talarczyk, M., Wielgusz, K., Praczyk, M., & Allam, A. M. (2020). 5A—Bast fibres: Flax. In R. M. Kozłowski & M. Mackiewicz-Talarczyk (Eds.), *Handbook of natural fibres* (2nd ed., pp. 93–162). Woodhead Publishing. https://doi.org/10.1016/B978-0-12-818398-4.00006-2

Kumar, A. (2021). Biobleaching: An eco-friendly approach to reduce chemical consumption and pollutants generation. *Physical Sciences Reviews, 6*(4). https://doi.org/10.1515/psr-2019-0044

Kumar, A., & Dutt, D. (2021). A comparative study of conventional chemical deinking and environment-friendly bio-deinking of mixed office wastepaper. *Scientific African, 12*, e00793. https://doi.org/10.1016/j.sciaf.2021.e00793

Kumar, V., Pathak, P., Harsh, N. S. K., & Bhardwaj, N. K. (2023). Biodeinking: An eco-friendly alternative for chemicals based recycled fiber processing. *Physical Sciences Reviews, 8*(9), 1941–1965. https://doi.org/10.1515/psr-2019-0045

Li, M., Wang, H. X., Sun, X., & Lu, F. P. (2013). Research on alkaline pectinase for hemp degumming. *Advanced Materials Research, 821–822*, 355–359. https://doi.org/10.4028/www.scientific.net/AMR.821-822.355

Lyu, P., Zhang, Y., Wang, X., & Hurren, C. (2021). Degumming methods for bast fibers—A mini review. *Industrial Crops and Products, 174*, 114158. https://doi.org/10.1016/j.indcrop.2021.114158

Mondal, S., Biswal, D., Pal, K., Rakshit, S., Kumar Halder, S., Mandavgane, S. A., Bera, D., Hossain, M., & Chandra Mondal, K. (2022). Biodeinking of waste papers using combinatorial fungal enzymes and subsequent production of butanol from effluent. *Bioresource Technology, 353*, 127078. https://doi.org/10.1016/j.biortech.2022.127078

Orozco Colonia, B. S., LorenciWoiciechowski, A., Malanski, R., Junior Letti, L. A., & Soccol, C. R. (2019). Pulp improvement of oil palm empty fruit bunches associated to solid-state biopulping and biobleaching with xylanase and lignin peroxidase cocktail produced by *Aspergillus sp.* LPB-5. *Bioresource Technology, 285*, 121361. https://doi.org/10.1016/j.biortech.2019.121361

Pasin, T. M., Betini, J. H. A., de Lucas, R. C., et al. (2024). Biochemical characterization of an acid-thermostable glucoamylase from Aspergillus japonicus with potential application in the paper bio-deinking. *Biotechnology Progress, 40*(1), e3384. https://doi.org/10.1002/btpr.3384

Rajabi, F., & Zabizadeh, S. M. (2018). Evaluating the properties of bleached Chemi-mechanical pulp (CMP) with one and two-stage of sodium hypochlorite and hydrogen peroxide. *Iranian Journal of Wood and Paper Science Research, 33*(2), 205–217. https://doi.org/10.22092/ijwpr.2018.120401.1458

Ray Chaudhuri, S., Gogoi, M., Biswas, T., Chatterjee, S., Chanda, C., Jamatia, R., Modak, A., Sett, S. K., & Mukherjee, I. (2020). Optimization of bio-chemical degumming of Ramie fiber for improved strength & luster. *Biotechnology Reports, 28*, e00532. https://doi.org/10.1016/j.btre.2020.e00532

Sadrmanesh, V., & Chen, Y. (2019). Bast fibres: Structure, processing, properties, and applications. *International Materials Reviews, 64*(7), 381–406. https://doi.org/10.1080/09506608.2018.1501171

Saleem, R., Khurshid, M., & Ahmed, S. (2018). Laccases, manganese peroxidases and xylanases used for the bio-bleaching of paper pulp: An environmental friendly approach. *Protein and Peptide Letters, 25*(2), 180–186. https://doi.org/10.2174/0929866525666180122100133

Santos, C. M., Santos, T. F., Aquino, M. S., MavinkereRangappa, S., Siengchin, S., & Suyambulingam, I. (2024). Era of bast fibers-based polymer composites for replacement of man-made fibers. *Heliyon, 10*(8), e29761. https://doi.org/10.1016/j.heliyon.2024.e29761

Sasaki, T., Kajino, T., Li, B., Sugiyama, H., & Takahashi, H. (2001). New pulp biobleaching system involving manganese peroxidase immobilized in a silica support with controlled pore sizes. *Applied and Environmental Microbiology, 67*(5), 2208–2212. https://doi.org/10.1128/AEM.67.5.2208-2212.2001

Saxena, A., & Singh Chauhan, P. (2017). Role of various enzymes for deinking paper: A review. *Critical Reviews in Biotechnology, 37*(5), 598–612. https://doi.org/10.1080/07388551.2016.1207594

Sežun, M., Karlovits, I., & Kavčič, U. (2023). Chemical and enzymatic deinking efficiency of agricultural and industrial waste fiber-based paper packaging. *Journal of the Science of Food and Agriculture, 103*(3), 1069–1076. https://doi.org/10.1002/jsfa.11815

Sharma, N., Bhardwaj, N. K., & Singh, R. B. P. (2020). Environmental issues of pulp bleaching and prospects of peracetic acid pulp bleaching: A review. *Journal of Cleaner Production, 256*, 120338. https://doi.org/10.1016/j.jclepro.2020.120338

Singh, G., Kaur, S., Khatri, M., & Arya, S. K. (2019a). Biobleaching for pulp and paper industry in India: Emerging enzyme technology. *Biocatalysis and Agricultural Biotechnology, 17*, 558–565. https://doi.org/10.1016/j.bcab.2019.01.019

Singh, A., Kaur, A., Yadav, R. D., & Mahajan, R. (2019b). An efficient eco-friendly approach for recycling of newspaper waste. *3 Biotech, 9*(2), 51. https://doi.org/10.1007/s13205-019-1590-2

Song, Y., Jiang, W., Nie, K., Zhang, Y., Ben, H., Han, G., & Ragauskas, A. J. (2019). An alkali-free method to manufacture ramie fiber. *Textile Research Journal, 89*(17), 3653–3659. https://doi.org/10.1177/0040517518811946

Subash, M. C., & Muthiah, P. (2021). Eco-friendly degumming of natural fibers for textile applications: A comprehensive review. *Cleaner Engineering and Technology, 5*, 100304. https://doi.org/10.1016/j.clet.2021.100304

Sundaramahalingam, M. A., Vijayachandran, P., Rajeshbanu, J., & Sivashanmugam, P. (2024). Production of lipase from Priestiaendophytica SSP strain and its potential application in deinking of printed paper. *Biomass Conversion and Biorefinery, 14*(13), 13861–13875. https://doi.org/10.1007/s13399-022-03556-0

Susanti, S. (2024). Influence of kappa number on enhancing pulp brightness through stage D0 with ClO2 bleaching process: Environmental implications and considerations. *ENVIRO: Journal of Tropical Environmental Research, 25*(2), Article 2. https://doi.org/10.20961/enviro.v25i2.85211

Sutka, A., Kukle, S., Gravitis, J., & Berzins, A. (2013). Chemical and physical modification of hemp fibres by steam explosion technology. *IOP Conference Series: Materials Science and Engineering, 49*(1), 012053. https://doi.org/10.1088/1757-899X/49/1/012053

Tiwari, A., Chen, C.-W., Haldar, D., Patel, A. K., Dong, C.-D., & Singhania, R. R. (2023). Laccase in biorefinery of lignocellulosic biomass. *Applied Sciences, 13*(8), 4673. https://doi.org/10.3390/app13084673

Tripathi, S. K., Bhardwaj, N. K., & Roy Ghatak, H. (2020). Developments in ozone-based bleaching of pulps. *Ozone: Science & Engineering, 42*(2), 194–210. https://doi.org/10.1080/01919512.2019.1647407

Virk, A. P., Puri, M., Gupta, V., Capalash, N., & Sharma, P. (2013). Combined enzymatic and physical deinking methodology for efficient eco-friendly recycling of old newsprint. *PLoS One, 8*(8), e72346. https://doi.org/10.1371/journal.pone.0072346

Wang, F., Zhang, X., Zhang, G., Chen, J., Sang, M., Long, Z., & Wang, B. (2018). Studies on the environmentally friendly deinking process employing biological enzymes and composite surfactant. *Cellulose, 25*(5), 3079–3089. https://doi.org/10.1007/s10570-018-1778-3

Wei, S., Liu, K., Ji, X., Wang, T., & Wang, R. (2021). Application of enzyme technology in biopulping and biobleaching. *Cellulose, 28*(16), 10099–10116. https://doi.org/10.1007/s10570-021-04182-1

Yadav, A., Simha, P., Sathe, P., Gantayet, L. M., & Pandit, A. (2022). Coupling chemical degumming with enzymatic degumming of ultrasound pre-treated ramie fiber using *Bacillus subtilis* ABDR01. *Environmental Technology & Innovation, 28*, 102666. https://doi.org/10.1016/j.eti.2022.102666

Yang, Q., Duan, S., Cheng, L., Feng, X., Zheng, K., Xie, C., Liu, Z., & Pen, Y. (2019). Engineering of a bacillus subtilis strain deficient in cellulase: Application in degumming of ramie. *Fibers and Polymers, 20*(1), 57–62. https://doi.org/10.1007/s12221-019-8444-8

Zhang, X., Guo, J., Ma, Y., Lyu, L., Ji, Y., Guo, Y., & Hao, X. (2021). Green degumming technology of hemp and a comparison between chemical and biological degumming. *ACS Omega, 6*(50), 35067–35075. https://doi.org/10.1021/acsomega.1c05831

Zimniewska, M., Wladyka-Przybylak, M., & Mankowski, J. (2011). Cellulosic bast fibers, their structure and properties suitable for composite applications. In S. Kalia, B. S. Kaith, & I. Kaur (Eds.), *Cellulose Fibers: Bio- and Nano-polymer composites: Green chemistry and technology* (pp. 97–119). Springer. https://doi.org/10.1007/978-3-642-17370-7_4

Carbohydrate Polymers 340 (2024) 122295

Contents lists available at ScienceDirect

Carbohydrate Polymers

journal homepage: www.elsevier.com/locate/carbpol

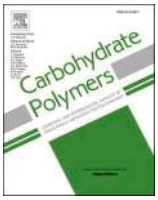

A novel thermophilic recombinant obligate xylobiohydrolase (*Ac*GH30A) from *Acetivibrio clariflavus* orchestrates the deconstruction of xylan polysaccharides

Yumnam Robinson Singh [a], Abhijeet Thakur [a], Carlos M.G.A. Fontes [b,c], Arun Goyal [a,*]

[a] *Carbohydrate Enzyme Biotechnology Laboratory, Department of Biosciences and Bioengineering, Indian Institute of Technology, Guwahati, Guwahati, Assam 781039, India*

[b] *NZYTech – Genes & Enzymes, Estrada do Paço do Lumiar, Campus do Lumiar, Edifício E - R/C, 1649-038 Lisbon, Portugal*

[c] *CIISA – Faculdade de Medicina Veterinária, Universidade de Lisboa, Avenida da Universidade Técnica, 1300-477 Lisbon, Portugal*

ARTICLE INFO

Keywords:
Xylan
Xylobiohydrolase
Xylobiose
Beechwood xylan
Acetivibrio clariflavus

ABSTRACT

GH30 xylobiohydrolases, an expanding enzyme category, need deeper insights for optimal use. The primary aim of this study was to characterize a new xylobiohydrolase, *Ac*GH30A of GH30 family from *Acetivibrio clariflavus*. The gene encoding *Ac*GH30A was cloned using pET28a(+) vector and expressed in *E. coli* BL21(DE3) cells. *Ac*GH30A was purified by immobilized metal-ion affinity chromatography. SDS-PAGE analysis of *Ac*GH30A showed molecular mass of ~58 kDa. *Ac*GH30A showed optimum temperature 80 °C and optimum pH 7.0. *Ac*GH30A was stable (maintaining >80 % of control activity) in pH range, 4–7 and temperature range, 30 °C -70 °C when incubated for 90 min. *Ac*GH30A displayed melting temperature, 72 °C and half-life, 21 days at 4 °C. The enzyme activity of *Ac*GH30A was enhanced by 10 mM Ca^{2+} and Mg^{2+} ions by 25 % and 21 %, respectively, whereas 10 mM Co^{2+}, Zn^{2+}, Fe^{2+}, and Cu^{2+} ions significantly reduced it. *Ac*GH30A showed activity against various xylan polysaccharides displaying highest V_{max}, 139 U.mg^{-1} and K_M, 0.71 mg.ml^{-1} against 4-*O*-methyl glucuronoxylan under optimum conditions. TLC, HPLC and LC-MS analyses of *Ac*GH30A hydrolyzed products from xylan substrates revealed the release of sole product, xylobiose, confirming it as an obligate xylobiohydrolase. *Ac*GH30A being a highly thermostable enzyme can be potentially utlilized in various biotechnological applications.

1. Introduction

Xylans, the primary component of hemicellulose present in lignocellulosic biomass, are the second most prevalent polysaccharides present in plants, succeeded by cellulose (Fonseca-Maldonado et al., 2014; He et al., 2014). They are heteropolysaccharides that principally consist of xylose and arabinose. The backbone of xylan is a linear polymer composed of xylopyranosyl residues linked by β-1,4-glycosidic bonds, having an equatorial configuration. The polysaccharide structure contains a variety of substituted groups, including arabinose, ferulic acid, glucuronic acid, acetyl and *p*-coumaric acid, that are integrated within the backbone (Moreira & Filho, 2016). Conformational analysis by X-ray diffraction showed that the xylan in plant cells is present as a 2-fold and 3-fold helical structures (Moreira & Filho, 2016; Simmons et al., 2016). The complete depolymerization of xylan is a complex process that requires the enzymes capable of breaking the backbone glycosidic linkages as well as enzymes that can remove substituted groups (Juturu & Wu, 2012).

Xylanases (EC 3.2.1.8) are a class of glycoside hydrolases that can hydrolyze the linear polysaccharide β-1,4-xylan into simpler products, such as xylooligosaccharides, xylobiose and xylose (Juturu & Wu, 2012; Sepulchro et al., 2020). Xylanases have been harnessed for a wide range of applications, such as enhancing the quality of bread (Guo et al., 2018), clarifying must and juices (Juturu & Wu, 2012), degumming bast fibres (Wang et al., 2019), pre-bleaching kraft pulps (Kaur et al., 2016; Kumar et al., 2016), and treating hemicellulosic waste (El Enshasy et al., 2016; Jamaldheen et al., 2019). The versatility of xylanolytic enzymes makes them valuable tools for improving processes and products in different industries.

Endo-β-1,4-xylanases belonging to glycoside hydrolase family 30 exhibits significant catalytic diversity. The family GH30 contains *endo-*

* Corresponding author.
E-mail address: arungoyl@iitg.ac.in (A. Goyal).

https://doi.org/10.1016/j.carbpol.2024.122295
Received 1 March 2024; Received in revised form 15 May 2024; Accepted 18 May 2024
Available online 23 May 2024

Abbreviations

GH - glycoside hydrolase
Ac - *Acetivibrio clariflavus*
TLC - thin-layer chromatography
IMAC - immobilized metal ion affinity chromatography
SDS-PAGE -sodium dodecyl sulphate-polyacrylamide gel electrophoresis
HPLC - high-performance liquid chromatography
LC-MS - liquid chromatography-mass spectrometry
ESI - electrospray ionization
ACN - acetonitrile

β-1,4-xylanases which hydrolyse xylans containing 4-*O*-methyl-D-glucuronic acid or D-glucuronic acid side chain residues and are called glucuronoxylanase (Puchart et al., 2021). A specific glucuronoxylanase, *St*Xyn30A from *Streptomyces turgidiscabies* C56, has a conserved arginine residue at the subsite −2, which is essential for recognizing glucuronic acid side chains (Maehara et al., 2018). These enzymes are primarily found in bacterial GH30_8 subfamily. The family GH30 also contains non-D-glucuronic acid specific xylanases, such as *Tl*Xyn30A from *Talaromyces leycettanus* (Šuchová, Puchart, & Biely, 2021), which are not specific to glucuronoxylan and can also hydrolyze arabinoxylan and rhodymenan. Numerous xylanases from the GH30 family displaying different modes of action have been studied, among which only a limited number showing xylobiohydrolase activity have been reported. Xylobiohydrolases from GH30 family reported till now majorly come from fungal sources, and they show two different modes of action. *Tt*Xyn30A (Katsimpouras et al., 2019) and *Tc*Xyn30B (Nakamichi et al., 2019) from *Thermothelomyces thermophila* and *Talaromyces cellulolyticus*, respectively, displayed both *exo*- and *endo*-acting catalytic behaviour. Both enzymes released 4-*O*-methyl-D-glucuronic acid embedded xylooligosaccharides and xylobiose from glucuronoxylan substrates. *Aa*Xyn30A from the fungus *Acremonium alcalophilum* was reported as an almost strict xylobiohydrolase (Šuchová et al., 2020). It showed maximum activity on rhodymenan, releasing isomeric xylotrioses. *Aa*Xyn30A cleaves xylobiose from the non-reducing end of the xylan. *Sl*Xyn30A from the yeast *Sugiyamaella lignohabitans* is a GH30 xylanase that releases acidic xylooligosaccharides from glucuronoxylan and shows auxiliary xylobiohydrolase activity (Šuchová et al., 2022). The initial enzymes identified for the exclusive release of xylobiose from birchwood and oat spelt xylan were xylanase V from *Aeromonas caviae* ME-1 (Kubata et al., 1994) and xylobiohydrolase from *Aspergilus sydowii* MG49 (Ghosh & Nanda, 1994). A detailed investigation into their mode of action has not been conducted yet and their GH families remains unknown. Subsequently, xylobiohydrolases from both GH11 and GH30 families were examined and characterized. Other two xylobiohydrolases, compost 21_GH11 (Evangelista et al., 2019) and MetXyn11 (Mello et al., 2017) from GH11 family (that contains mostly *endo*-acting xylanases) were reported liberating only xylobiose as the only reaction product from xylan.

Acetivibrio clariflavus is a bacterium characterized by its thermophilic nature, anaerobic metabolism, gram-positive cell structure and ability to form spores (Artzi et al., 2014). This bacterium was initially isolated from anaerobic sludge obtained from a thermophilic methanogenic bioreactor (Shiratori et al., 2006, 2009). The analysis of the *Acetivibrio clariflavus* genome revealed that the bacterium utilizes an elaborate system of cellulosomal complexes containing multiple enzymes to break down lignocellulosic biomass into simpler products (Dassa et al., 2012). *Acetivibrio clariflavus* is the only thermophilic bacterium that has been reported to produce a complex cellulosomal system after the discovery of a cellulosomal system in *Clostridium thermocellum* (Artzi et al., 2014; Lamed & Bayer, 1988). It produces both cell-free and cell-bound cellulosome complexes. Bioinformatics study revealed the presence of 79 dockerin containing proteins in *Acetivibrio clariflavus*, indicating the abundant presence of cellulosome structures (Artzi et al., 2014). Several glycoside hydrolases from the *Acetivibrio clariflavus* have been characterized, but many more remain unexplored. The gene (GenBank accession number AEV68404.1) encoding a putative xylanolytic enzyme, *Ac*GH30A from the cellulosomal complex of *Acetivibrio clariflavus,* belongs to the GH30 family.

In this study, the gene encoding the xylobiohydrolase (*Ac*GH30A) was cloned, expressed, purified and characterized. During the study of the enzyme, *Ac*GH30A, Šuchová, Puchart, and Biely (2021) and Crooks et al. (2021) also reported their work on the same enzyme. Despite some overlaps in the findings, our report presents more detailed and valuable data on the characteristics of *Ac*GH30A. It is hypothesized that the in-depth biochemical characterization of *Ac*GH30A will enhance the understanding regarding its capabilities as a thermophilic xylobiohydrolase of bacterial origin. The new results from the current study, shed light on the greater potential of the enzyme with regard to its commercial usage, such as its thermophilic enzyme properties, stability and capability to produce xylobiose from wide variety of xylan polymers. The biochemical characteristics of *Ac*GH30A discovered in this study may be beneficial for the enzymatic digestion of xylan based biomasses to produce xylobiose, renowned for its superior prebiotic properties (Manisseri & Gudipati, 2012).

2. Materials and methods

2.1. Bacterial strains, vectors and chemicals

The genomic DNA of *Acetivibrio clariflavus* was procured from the collection of microorganisms and cell culture, DSMZ (Deutsche Sammlung von Mikroorganismen und Zellkulturen), Braunchweig, Germany. *Escherichia coli* strains, TOP10 cells and BL21 (DE3) cells were used for cloning and expression of the recombinant enzyme, respectively. The PCR-amplified products were cloned and expressed using the pET28a(+) expression vector. pET28a(+) plasmid, *E. coli*. TOP10 and BL21 (DE3) cells were acquired from Novagen (Madison, WI, USA). Taq DNA Polymerase was purchased from New England Biolabs (Ipswich, MA, USA). Restriction enzymes *Nhe*I and *Xho*I, and T4 DNA ligase were purchased from Promega Corp. (Fitchburg, WI, USA). Multiple xylan polysaccharides, each composed of a primary chain formed by a linear sequence of xylose units linked through β-1,4-glycosidic bonds, were obtained from different sources. Natural xylan polysaccharides *viz.* Beechwood xylan, larchwood xylan, rye arabinoxylan and wheat arabinoxylan (low viscosity), birchwood acetylated xylan and standards *viz.* D-xylose, xylobiose, xylotriose, xylotetraose and xylopentaose were procured from Megazyme Ltd. (Wicklow, Ireland). Xylan, M.W. 20,000–30,000 and xylan corn cob were purchased from Carbosynth Ltd. (Compton, UK). The polysaccharides, 4-O-Methyl glucuronoxylan, oat spelt xylan and carboxy methyl cellulose sodium salt were purchased from Sigma-Aldrich Co. LLC. (St. Louis, MO, USA). Various in-house xylan substrates namely, banana stem xylan, water hyacinth xylan, sugarcane tops xylan (Khaire et al., 2021), alkali pretreated sugarcane tops xylan (Khaire et al., 2022), neem saw dust xylan (Sharma, Khaire, et al., 2020) and acacia sawdust xylan (Sharma, Morla, et al., 2020) were also used for the study. The silica-coated plates for thin-layer chromatography (TLC Silica gel 60 F_{254}, 20 cm × 20 cm) were acquired from Merck Ltd. (Darmstadt, Germany).

2.2. Molecular architecture of AcGH30A

The sequence data of gene encoding *Ac*GH30A with GenBank accession AEV68404.1 was retrieved from the NCBI (http://www.ncbi.nlm.nih) database. The conserved domains present in the gene was found by using the NCBI conserved domain database (CDD) (http://www.ncbi.nlm.nih.gov/cdd/). The signal peptide sequence contained by the gene was determined by the SignalP 5.0 server (https://se

Table 1
PCR reaction composition for amplification of gene encoding *Ac*GH30A.

Contents	Volume (μL)	Final concentration
DNA template (106 ng/μL)	0.5	0.9 ng/μL
Forward primer (15 μM)	1.5	0.37 μM
Reverse primer (15 μM)	1.5	0.37 μM
100 mM dNTP mix	0.2	0.33 mM
Taq DNA Polymerase (5 U/μL)	0.5	0.04 U/μL
10× reaction buffer	6	1×
Sigma water, pH 8.0	49.8	–
Total	60	–

rvices.healthtech.dtu.dk/services/SignalP-5.0/). The sequence configuration of the *Ac*GH30A gene was examined and drawn using DOG 2.0 software to visualize the length of different domains present in the gene.

2.3. Amplification of gene encoding AcGH30A and cloning

The amplification of gene (GenBank accession AEV68404.1) encoding *Ac*GH30A, spanning a length of 1518 base pairs, was performed *via* polymerase chain reaction (PCR) using Taq DNA polymerase and specific oligonucleotide primers. The genomic DNA of *Acetivibrio clariflavus* was used as the template for the amplification. For directional cloning, *Nhe*I/*Xho*I restriction sites were utilized to incorporate the PCR product into the expression vector pET28a(+). The oligonucleotide primers utilized in this process were:

Forward primer 5′-GGTGGTGCTAGCGCATCAACTGTTACCGTTGATTGGGAC-3′.

Reverse primer 5′-ACCACCCTCGAGTTATTGTTCTACCGGGAATTTTTGAATC-3′.

The total volume of the PCR mix containing the template, polymerase enzyme, primers, dNTPs and buffer was 60 μL (Table 1).

After the initial denaturation of the template DNA at 95 °C for 5 min, the PCR was conducted for 30 cycles under the following parameters, (i) Denaturation at 95 °C for 30 s, (ii) Annealing at 72 °C for 60 s, (iii) Extension at 72 °C for 60 s. The last extension step was executed for 10 min at 72 °C by using a thermal cycler (Bio-Rad T100, Hercules, CA, USA). The PCR products were analyzed by 0.8 % (*w/v*) agarose gel electrophoresis, to check their size and purity. After confirming the PCR-amplicon of interest on the gel, it was separated from the agarose gel with the help of a gel extraction kit (Sigma-Aldrich Co. LLC., St. Louis, MO, USA). The PCR product and the pET28a(+) vector was digested by restriction enzymes *Nhe*I and *Xho*I, and then ligated by T4 DNA ligase (Promega Corp., Fitchburg, WI, USA). The recombinant plasmid containing the gene encoding *Ac*GH30A was used for transformation of competent *E. coli* TOP10 cells by heat-shock treatment (Froger & Hall, 2007). The transformed cells were grown on Luria-Bertani medium plate containing kanamycin (50 μg.mL^{-1}) at 37 °C for 12 h. The positive clones were confirmed by isolating the plasmid, followed by restriction digestion and the sequence was confirmed by outsourcing the DNA sequencing.

2.4. Expression and purification of AcGH30A

The plasmid containing the gene of *Ac*GH30A protein was isolated from *E. coli* TOP10 cells and transformed into the competent *E. coli* BL-21 (DE3) cells by heat-shock treatment method. The transformed *E. coli* BL21 cells were cultured in Luria-Bertani (LB) broth incubated at 37 °C and 180 rpm using an orbital shaker incubator, till the cells reached the mid-exponential growth phase, detected by absorbance at 550 nm. The over-expression of the protein was induced by adding 1 mM IPTG final concentration to the LB broth and cells were further growth at 24 °C with 180 rpm for 12 h. The grown cells were centrifuged at 8000 *g* for 15 min at 4 °C to separate the cells. The cells were resuspended in sodium phosphate buffer (50 mM, pH 7.5) containing 300 mM NaCl and 50 mM imidazole and subjected to ultrasonication to lyse the *E. coli* BL-21 cells to recover the protein. Ultrasonication was set at 33 % amplitude with 2 s of pulses ON and 8 s OFF. The sonicated cell lysate was centrifuged at 16000 *g* for 50 min at 4 °C to obtain the cell extract. The cell extract was filtered through a 0.45 μm PVDF membrane using a syringe filter. *Ac*GH30A in filtrate was purified by using a 5 mL Ni^{2+} ion-chelating column (His GraviTrap, GE Healthcare, Chicago, IL, USA). The same buffer used for resuspension of cells was used as wash buffer. The bound protein was eluted by elution buffer, 50 mM sodium-phosphate buffer (pH 7.5) containing 300 mM NaCl and 300 mM imidazole. The salt and imidazole from the eluted protein were eliminated by dialysis, using sodium phosphate buffer (50 mM, pH 7.0). The protein, *Ac*GH30A was further purified by size exclusion chromatography (SEC) at 25 °C, using HiLoad Superdex 75 pg column (GE Healthcare, GE Healthcare, Chicago, IL, USA) installed with fast protein liquid chromatography (FPLC) system (AKTA Prime, GE Healthcare, Chicago, IL, USA). The sodium phosphate buffer (50 mM, pH 7.0) was utilized as the mobile phase. The molecular mass and purity of the purified *Ac*GH30A enzyme were evaluated by using a 12 % (*w/v*) SDS-PAGE (Laemmli, 1970). The enzyme activity of *Ac*GH30A after each purification step was assessed by following the procedure described in Section 2.5. The concentration of the purified *Ac*GH30A was determined by Lowry method (Lowry, Rosebrough, Farr, & Randall, 1951) using BSA as standard and also by using NanoDrop spectrophotometer (2000c, Thermo Fisher Scientific, Waltham, MA, USA). The molar extinction coefficient (ε) of *Ac*GH30A, 122,730 M^{-1} cm^{-1} was used which was determined by submitting the amino acid sequence to the ExPASy server (http://web.expasy.org/protparam/).

2.5. Assay of enzyme activity

The assays for biochemical characterization of *Ac*GH30A were performed using a working solution of *Ac*GH30A (50 μg.mL^{-1}) prepared by diluting the *Ac*GH30A stock (500 μg.mL^{-1}) obtained after SEC. The assays were conducted with a reaction mixture of 100 μL containing 10 μL of *Ac*GH30A (50 μg.mL^{-1}) and 2.0 % (w/v) final concentration of beechwood xylan in sodium phosphate buffer (50 mM, pH 7.0) by incubating at 80 °C for 2 min. A negative control, containing only 2.0 %, (w/v) beechwood xylan in 100 μL of sodium phosphate buffer (50 mM, pH 7.0) without the enzyme, was run in parallel for each reaction. The activity of *Ac*GH30A against various xylan substrates were examined. The enzyme activity of crude *Ac*GH30A enzyme and after IMAC and SEC purification steps was determined by using 2.0 % (w/v) beechwood xylan following the same conditions as mentioned above. The activity of the enzyme was calculated by quantifying the amount of reducing sugars produced from the enzyme-substrate reactions using the method developed by Nelson (Nelson, 1944) and Somogyi (Somogyi, 1945) with plotting a standard curve for D-xylose. 25 parts of the copper reagent A (NS-A) were added with 1 part of copper reagent B (NS-B) to make Nelson-Somogyi-D (NS-D) solution (Nelson, 1944). After the completion of the enzyme-substrate reaction, 100 μL of the enzyme-substrate mixture was mixed with 100 μL of NS-D reagent, followed by incubation in a boiling water bath for 20 min for deactivating the enzyme and the reaction between the NS-D and reducing sugars. The mixture was cooled and added with 100 μL of arsenomolybdate colour reagent (NS-C) reagent. The volume of the mixture was adjusted to 1 mL by further adding 700 μL sodium phosphate (50 mM, pH 7.0) buffer. The absorbance of the final mixture was recorded at 500 nm using a spectrophotometer (Multiskan SkyHigh, Thermo Fisher Scientific, Waltham, MA, USA). One unit (U) of enzyme (1 μmol.min^{-1}) was defined as the enzyme quantity needed to generate 1 μmole of xylose per minute. The enzyme activity (U.mL^{-1} or μmol.min^{-1}.mL^{-1}) is defined as the amount of enzyme per mL needed to generate 1 μmole of xylose per min. Whereas, the specific enzyme activity (U.mg^{-1} or μmol.min^{-1}.mg^{-1}) is defined as the enzyme quantity per milligram required to produce 1 μmole of xylose, per minute under the optimum conditions of reaction.

2.6. Determination of optimum pH and pH stability

The optimum pH of *Ac*GH30A was investigated by conducting enzyme-substrate reaction with beechwood xylan at different pH conditions at constant temperature, 80 °C. Different buffer systems for various pH range used were sodium acetate buffer (pH 3.5–5.5), sodium phosphate buffer (pH 6.0–8.0) and glycine-NaOH buffer (pH 8.5–10.5) at 50 mM concentration. To examine the stability of *Ac*GH30A at different pH environment, 10 μL (5 mg.mL^{-1}) of stock solution of the recombinant enzyme, *Ac*GH30A was added to 990 μL of different buffers with in a pH range of 4.0 to 8.0 and the enzyme solutions of 1 mL (50 μg.mL^{-1}) were incubated for 90 min at 25 °C. From this, an aliquot of 10 μL enzyme was taken for 100 μL reaction mixture and assayed under optimum conditions of 80 °C for 2 min as described in Section 2.5.

2.7. Determination of optimum temperature and thermal stability

The optimum temperature required for the activity of *Ac*GH30A was evaluated by conducting the identical enzyme-substrate reactions at different temperatures, spanning from 20 to 95 °C. The reaction mixture, 100 μL containing 10 μL of *Ac*GH30A (50 μg.mL^{-1}) and 2.0 % (*w/v*) beechwood xylan in sodium phosphate buffer (50 mM, pH 7.0) were incubated at varying temperatures for 2 min. The reactions were terminated after 2 min of incubation and the reducing sugar analysis was performed by using the methods of Nelson (Nelson, 1944) and Somogyi (Somogyi, 1945). The thermostability of *Ac*GH30A was investigated by incubating the stock solution of the enzyme at different temperatures for 90 min, prior to the enzyme-substrate reactions conducted at optimum temperature and pH. 10 μL of *Ac*GH30A (50 μg.mL^{-1}) from the incubated stocks was added with 90 μL of 2.0 % (w/v) beechwood xylan at 80 °C for 2 min in a sodium phosphate buffer system (50 mM, pH 7.0). The thermal properties of *Ac*GH30A were also assessed by Circular Dichroism (CD) spectroscopy, using the purified enzyme at 1 mg.mL^{-1} concentration, dissolved in sodium phosphate buffer (50 mM, pH 7.0). Variations in the spectrum as a function of temperature was measured using a spectropolarimeter (JASCO J-815, Jasco Corp., Heckmondwike, UK). The enzyme sample and the corresponding buffer without enzyme were analyzed at the rate of 50 nm.min^{-1} and bandwidth of 1 nm. Far-UV (190–240 nm) CD spectrum was recorded at the intervals of 5 °C, with increase in the temperature from 25 °C to 110 °C. CD ellipticity was plotted against wavelength and temperature to analyze the thermal properties of *Ac*GH30A. The melting temperature (T_m) of *Ac*GH30A was calculated by plotting the change in CD spectra captured at 222 nm (FAR-UV) and examining the pattern of thermal denaturation. The transition curve at 222 nm was normalized using the formula: %denaturation = (θ_{25} - θ_{Temp}) / (θ_{25} – θ_{110}). The T_m value was calculated through non-linear fitting using the Boltzmann method (Ruíz et al., 2022). The half-life ($t_{1/2}$) of *Ac*GH30A at different temperatures was determined by incubating the enzyme at 4 °C, 30 °C, 60 °C and 70 °C and an aliquot of enzyme was taken at different time intervals *viz.*, 0 to 24 h. All the assays were performed at optimum temperature of 80 °C and optimum pH of 7.0 using beechwood xylan as substrate. The half-life was calculated by plotting relative residual activity against the incubation period. The half-life of *Ac*GH30A was calculated based on the assumption that enzyme degradation followed first-order kinetics, where the half-life ($t_{1/2}$) = ln2/k, with 'k' representing the rate constant (Han & Lim, 2004; Sárossy et al., 2013).

2.8. Substrate specificity analysis of AcGH30A

The enzyme activity of *Ac*GH30A against various commercial, natural and pretreated substrates was investigated under optimized assay conditions. Each assay mixture of 100 μL containing 10 μL of *Ac*GH30A (50 μg.mL^{-1}) and 2.0 %, (*w/v*) of respective substrates in sodium phosphate buffer (50 mM, pH 7.0) was incubated at 80 °C for 2 min. The reducing sugar analysis and the enzyme activity calculation was performed as mentioned in Section 2.5.

2.9. Determination of kinetic parameters

The kinetic properties of *Ac*GH30A were examined by conducting enzyme assays, with varying concentrations (from 0.005 %, w/v to upto 3 %, w/v) of substrates, at optimum temperature and pH conditions. The substrates employed for the enzyme kinetics investigation included 4-*O*-methyl glucuronoxylan (Sigma-Aldrich Co. LLC., St. Louis, MO, USA), xylan M.W. 20,000–30,000 (Carbosynth Ltd., Compton, UK), beechwood xylan (Megazyme Ltd., Wicklow, Ireland) and larchwood xylan (Megazyme Ltd., Wicklow, Ireland). In each assay, 90 μL of the respective substrate was mixed and added with 10 μL of *Ac*GH30A (50 μg.mL^{-1}). Identical reaction mixtures without the enzymes were used as negative controls. The estimation of reducing sugars and the subsequent calculation of enzyme activity after the enzyme reaction were conducted as outlined in Section 2.5. The values for K_M, V_{max}, and the turnover number (k_{cat}) were determined using the Michaelis-Menten equation, assuming steady-state conditions. All enzyme reactions were executed in triplicate. The calculated data are presented as mean values with their corresponding standard deviations (mean ± SD). The GraphPad Prism software was used to calculate the kinetic parameters (Swift, 1997).

2.10. Influence of metal ions and chemical agents on enzyme activity

The capability of the different metal ions to change the catalytic activity of *Ac*GH30A was investigated. For this study, enzyme-substrate reactions were supplemented separately with different metal salts, including $CaCl_2$, $MgCl_2$, $CuCl_2$, $CoCl_2$, $FeCl_3$, $MgSO_4$, $MnSO_4$, $ZnSO_4$, $NiSO_4$, $CuSO_4$, NaCl and KCl. The effect of the chelating agents like EDTA and EGTA on the activity of *Ac*GH30A were also examined. The enzyme was pretreated with each additive at two different concentrations, *i.e.*, 1 mM and 10 mM, by diluting it with the respective additive solution. Twenty microliter of enzyme, *Ac*GH30A (500 μg.mL^{-1}) with respective additive in 200 μL total volume was incubated at 25 °C for 20 min. Afterwards, the pretreated enzyme samples were subjected to standard enzyme assay against 2 % (*w/v*) beechwood xylan, as previously described in Section 2.5. The activity was expressed as a percentage of the activity level in the absence of each additive (control sample).

2.11. Study of hydrolytic mechanism by AcGH30A by TLC

The hydrolysis products generated by *Ac*GH30A from various xylan substrates were examined using thin-layer chromatography (TLC). To prepare the samples for TLC analysis, 20 μL of *Ac*GH30A solution (50 μg.mL^{-1}) was incubated with 180 μL of xylan substrates (1.0 %, w/v). The xylan substrates used were beechwood xylan, larchwood xylan, 4-*O*-methyl glucuronoxylan, rye arabinoxylan, wheat arabinoxylan and oat spelt xylan. These substrates were dissolved with sodium phosphate buffer (50 mM, pH 7.0) and incubated at 70 °C for 60 min. The time-dependent TLC analysis of *Ac*GH30A hydrolysed beechwood xylan was performed to investigate the pattern of product formation over time. For this analysis, 10 μL of *Ac*GH30A solution (50 μg.mL^{-1}) and 90 μL of 1.0 % (*w/v*) beechwood xylan in sodium phosphate buffer (50 mM, pH 7.0), was incubated at 40 °C for different time durations *viz.* 1, 2, 5, 10, 15, 30, and 60 min and 2, 4, 6, 12, and 24 h. A negative control consisting of an equal volume of the reaction mixture without the enzyme was included in the study. To inactivate the enzyme, present in reaction mixtures, an equal volume of absolute ethanol was added. The reaction mixture was centrifuged at 14,000 *g* for 10 min at 25 °C to separate the undigested substrate. The resulting clear supernatant (~200 μL), containing enzyme reaction product, was carefully moved to a fresh 1.5 mL microcentrifuge tube. The hydrolysed products present in the supernatant were concentrated to 10–20 μL in a hot air oven at 70 °C for 12 h. D-xylose, xylobiose, xylotriose, xylotetraose and xylopentaose (each 1.0

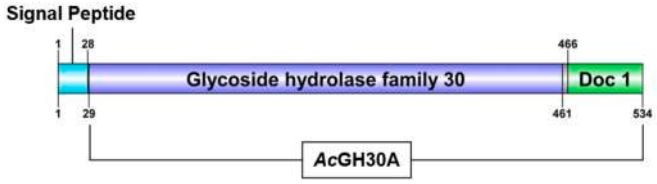

Fig. 1. Molecular organization of the *Ac*GH30A. The amino acid sequence on *Ac*GH30A was consists of 3 major domain sequences, (i) Signal peptide (1–28 aa) at the N-terminal, (ii) GH30 catalytic module (29–461 aa) and (iii) Linker sequence (432–465 aa) followed by (iv) Dockerin 1 at C-terminal (466–534 aa).

mg.mL^{-1}) were utilized as the standards. The concentrated hydrolyzed samples (0.6 μL each) and 1.0 μL (1 mg.mL^{-1}) of each standard were loaded over the TLC plate (Silica gel-coated aluminium plate, Merck, Darmstadt, Germany). TLC plate was inserted into a developing chamber containing a solvent system composed of chloroform, glacial acetic acid and water mixed with a ratio of 6:7:1 (Valls et al., 2010). After drying the TLC plate in a hot air oven, the spots developed on the plate were visualized by using a staining solution consisting of 0.5 % (*w/v*) α-naphthol and sulfuric acid/methanol in a 5:95 ratio (*v*/v).

2.12. HPLC analysis of AcGH30A hydrolyzed products

The hydrolytic mechanism of *Ac*GH30A against beechwood xylan was investigated by analyzing the hydrolyzed products using high-performance liquid chromatography (HPLC). The enzyme, *Ac*GH30A, 120 μL (100 μg.mL^{-1}) with 1.0 % (w/v) beechwood xylan dissolved in sodium phosphate buffer (50 mM, pH 7.0) in total volume of 1.2 mL reaction mixture was incubated at 70 °C for 60 min. The reaction was stopped by inactivating the enzyme by adding an equal volume of absolute ethanol and further procedure was followed as outlined in Section 2.11 for preparing the hydrolyzed product sample. The supernatant was dried in a hot air oven at 75 °C for 24 h and then dissolved in 500 μL distilled water. The sample was filtered through a 0.45 μm membrane using a syringe filter to remove impurities. Xylobiose (1 mg.mL^{-1}) was utilized as the standard. The column for oligosaccharide separation (Rezex RSO-Oligosaccharide column, 200 × 10 mm, Phenomenex, Inc., Torrance, CA, USA) with a guard column (Rezex RSO-Oligosaccharide guard, 60 × 10 mm, Phenomenex, Inc., Torrance, CA, USA) attached with HPLC (Shimadzu Corporation, Kyoto, Japan) was used. Milli-Q water was utilized as the mobile phase with a flow rate of 0.3 mL.min^{-1}. The samples were run in the isocratic mode with injection volume of 20 μL. The column temperature was set at 80 °C. The eluted samples were analyzed by using a refractive index detector.

2.13. Liquid chromatography-mass spectrometry of AcGH30A hydrolyzed product

The enzyme, *Ac*GH30A reaction product released from beechwood xylan was prepared according to the protocol described in Section 2.12. 500 μL of the reaction mixture was used to prepare the analyte samples, consisting of 50 μL of *Ac*GH30A (100 μg.mL^{-1}) and 1.0 % (w/v) beechwood xylan dissolved in sodium phosphate buffer (50 mM, pH 7.0). The mixture was incubated at 70 °C for 60 min. The reaction was terminated by inactivating the enzyme by adding an equal volume of absolute ethanol to the reaction mixture. Subsequently, the product was dried at 75 °C for 12 h. The dried sample was reconstituted in 500 μL of acetonitrile/Milli-Q water (1:1) and analyzed. This sample containing *Ac*GH30A hydrolysed products were analyzed by Liquid chromatography-mass spectrometry (LC-MS) instrument (Agilent 6410 Triple Quad MS-MS, Agilent Technologies, Inc., Santa Clara, CA, USA). A carbohydrate column (4.6 × 150 mm, ZORBAX, Agilent Technologies, Inc., Santa Clara, CA, USA) encased with 5 μm size particles for chromatography was used. The mobile phase comprised acetonitrile/Milli-Q water (70:30). The flow rate of the mobile phase through the column was 600 μL.min^{-1}. Electrospray ionization was operated in positive ion mode. The scan range was set at 25–1200 *m/z*.

3. Results and discussion

3.1. Molecular organization of AcGH30A

The full-length gene (GenBank accession AEV68404.1) encoding the enzyme, *Ac*GH30A is a 534 amino acid protein whose molecular framework revealed the presence of a signal peptide of 28 amino acids (1–28 aa) at N-terminal followed by a GH30 family catalytic domain of 433 amino acid residues (29–461 aa) and a dockerin type I of 68 amino acids (466–534 aa) at the C-terminal, connected by a linker sequence of 5 amino acids (432–465 aa) to GH30 catalytic domain (Fig. 1).

The presence of dockerin I domain indicates the potential participation of *Ac*GH30A in cellulosome assembly and protein-protein interactions. The DNA sequence encoding GH30 family catalytic domain (433 aa) and the dockerin 1 (68 aa) including the linker sequence of 5 amino acid between the two domains was cloned with the expression vector, pET-28a(+). The N-terminal of the cloned protein, *Ac*GH30A included an additional sequence of 8 amino acids (MGHHHHHH) derived from the pET-28a(+) vector, containing the His6-tag. The signal peptide sequence was excluded from the cloning sequence. Consequently, the resulting protein encoded by the cloned DNA sequence comprised a total of 514 amino acid residues.

3.2. Cloning, over-expression and purification of recombinant AcGH30A

*Ac*GH30A expressed as a soluble protein. The recombinant enzyme was purified by immobilized metal-ion affinity chromatography (IMAC) using 1 mL Ni^{2+} ion-chelating affinity columns, followed by the size exclusion chromatography using HiLoad Superdex 75 pg column. The purified enzyme obtained after IMAC showed an extra band on SDS-PAGE analysis (Fig. 2, lane 7). However, the purified *Ac*GH30A after size exclusion chromatography (SEC), exhibited a single homogeneous protein band on SDS-PAGE analysis (Fig. 2, lane 8), indicating a molecular mass of approximately, 58 kDa. This molecular mass closely matched the calculated value of 57.78 kDa, determined by protparam program using the amino acid sequence of protein. The purification of crude *Ac*GH30A enzyme in cell extract with specific activity, 6.2 U.mg^{-1} by IMAC gave 87.5 U.mg^{-1} resulting in 14-fold purification (Table 2). Which on further purification by SEC gave 109.6 U.mg^{-1} giving over 16-fold purification as compared with crude enzyme (Table 2). The amount of purified *Ac*GH30A protein after SEC obtained from 0.5 L culture grown in Luria-Bertani medium was 7 mg. The total yield of enzyme activity of *Ac*GH30A after SEC purification was 72 %.

3.3. Determination of optimum pH and pH stability

The enzyme, *Ac*GH30A exhibited above 85 % of activity over a wide range of pH, between 5 and 8 with a maximum enzymatic activity at pH 7.0 (Fig. 3A). The pH stability analysis of *Ac*GH30A after 90 min incubation at 25 °C showed that, the activity remained above 80 % between pH 4.0 and 7.0 (Fig. 3B). At pH 8, the enzyme maintained 67 % of activity, suggesting the excellent flexibility with pH, which can be beneficial for various commercial applications. *Aa*Xyn30A, a fungal xylobiohydrolase purified from *Acremonium alcalophilum* showed similar optimum pH in the alkaline range, 7.5–10 (Šuchová et al., 2020). Other fungal xylanases, *Tt*Xyn30A (Nakamichi et al., 2020), *Sl*Xyn30A (Šuchová et al., 2022) and *Tc*Xyn30B (Katsimpouras et al., 2019) with auxiliary xylobiohydrolase activity showed optimum pH in acidic range with pH 4.0, 3.5 and 5.0, respectively.

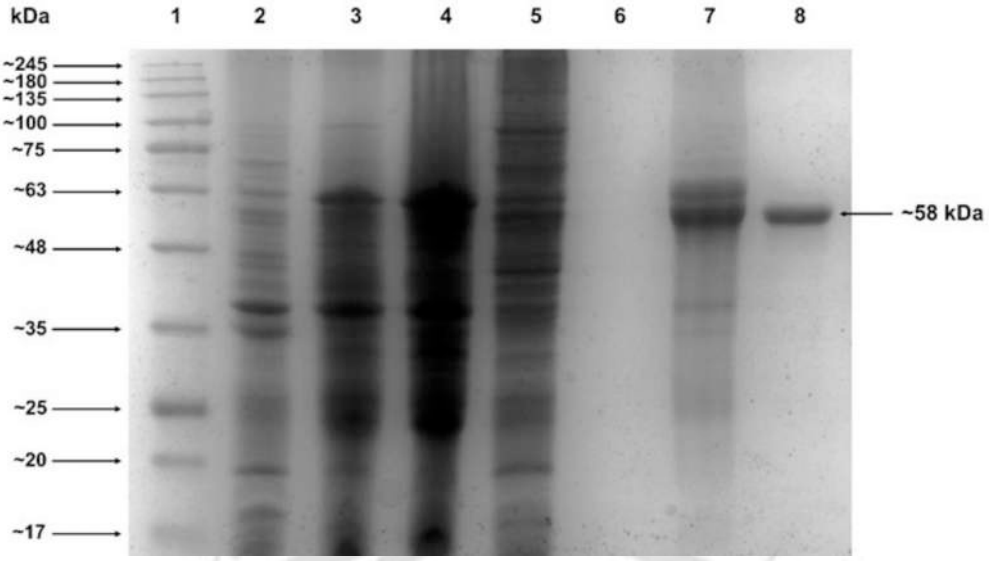

Fig. 2. SDS-PAGE (12 %, *w/v* gel) showing expression and purification of *Ac*GH30A after metal ion affinity chromatography and size exclusion chromatography. Lane 1: Protein molecular-mass marker, Lane 2: Un-induced *E. coli* BL-21 DE3 cells pellet, Lane 3: Induced cells pellet of *E. coli* BL-21 DE3, Lane 4: Induced cells pellet of *E. coli* BL-21 DE3 cells after sonication, Lane 5: Cell extract (Supernatant obtained after centrifugation of the sonicated induced cells pellet of *E. coli* BL-21 DE3), Lane 6: Last wash from column, Lane 7: Purified protein *Ac*GH30A after metal ion affinity chromatography and Lane 8: Purified protein *Ac*GH30A (~58 kDa) after size exclusion chromatography.

Table 2
Purification of *Ac*GH30A enzyme.

Fractionation step	Volume (mL)	*Ac*GH30A			Protein concentration ($mg.mL^{-1}$)	SA** ($U.mg^{-1}$)	Fold purification
		EA* ($U.ml^{-1}$)	Total Units	Overall % yield			
Cell lysate	10	106	1060	100	17	6.24	1
IMAC	10	96.3	962.5	90.8	1.1	87.5	14
SEC	14	54.8	723.5	72.4	0.5	109.6	16.7

Enzyme activity was determined against 2.0 %, (w/v) beechwood xylan in sodium phosphate buffer (50 mM, pH 7.0), at 80 °C for 2 min.
* Enzyme activity.
** Specific enzyme activity.

3.4. Determination of optimum temperature and thermal stability of *Ac*GH30A

Assays of *Ac*GH30A at different temperatures revealed its maximum activity at 80 °C. *Ac*GH30A retained over 94 % of its residual activity up to 85 °C, thereafter it drastically decreased and showed ~30 % activity at 100 °C (Fig. 3C). This makes it an exceptionally superior bacterial thermophilic xylobiohydrolase characterized so far within GH30 family. To the best of our knowledge, this is the first bacterial xylobiohydrolase from GH30 family showing optimum temperature as high as 80 °C. The investigation of thermostability of *Ac*GH30A showed that it retained 77 % of its residual activity at 70 °C for 90 min (Fig. 3D). Crooks et al. (2021) reported the thermal properties of the catalytic module, *Ac*Xbh30A-CD of the full-length *Ac*Xbh30A xylobiohydrolase (named *Ac*GH30A in present study) displaying a similar pattern with optimum temperature of 73 °C at pH 6.0. The optimum temperature and thermostability of *Ac*GH30A were much higher when compared with other GH30 family enzymes with xylobiohydrolase activity. A xylobiohydrolase, *Aa*Xyn30A from *Acremonium alcalophilum* exhibited optimum temperature within a range of 40 to 50 °C, giving maximum activity (Šuchová et al., 2020). *Aa*Xyn30A displayed limited stability at 50 °C, retaining only 6 % of its activity after 1 h incubation, whereas it maintained 68 % of its activity at 40 °C. *Tt*Xyn30A, a xylanase with auxiliary xylobiohydrolase activity isolated from *Thermothelomyces thermophila* showed highest enzyme activity at 50 °C, but it experienced a rapid decline in activity at temperature above 55 °C (Katsimpouras et al., 2019). Similarly, *Tc*Xyn30B (Nakamichi et al., 2019) from *Talaromyces cellulolyticus* and *Sl*Xyn30A (Šuchová et al., 2022) from *Sugiyamaella lignohabitans,* showed a decline in their activity after 50 °C. The distinctive thermostability of *Ac*GH30A can be advantageous and favourable as compared with the other commercial xylobiohydrolases for a variety of biotechnological applications. Combining *Ac*GH30A with thermophilic xylanases can provide several benefits such as *Ac*GH30A can be used in processes to reduce the risk of contamination, as it can operate at high temperatures without denaturation as also reported earlier for thermophilic enzymes (Collins et al., 2005). Furthermore, combining *Ac*GH30A with other enzymes, such as β-glucanase, can enhance the efficiency of enzymatic hydrolysis of complex plant cell wall polysaccharides for manufacturing biofuels and value-added bio-products (Ajeje et al., 2021).

Thermal stability analysis of *Ac*GH30A, by measuring the changes observed in the CD spectrum with increasing temperature revealed that the secondary structure elements remained intact up to 70 °C (Fig. 4A). However, secondary structure was partially unfolded at 75 °C and completely denatured at 85 °C. The melting temperature, T_m of *Ac*GH30A where the folded and unfolded state of protein is in 50:50 ratio, calculated by the CD data obtained at 222 nm was found to be ~72 °C (Fig. 4B).

The half-life, $t_{1/2}$ of *Ac*GH30A were 1.75 h and 21 days at temperatures 70 °C and 4 °C, respectively. The $t_{1/2}$ of enzyme at 30 °C and 60 °C were 6.5 and 2 days, respectively (Fig. 5).

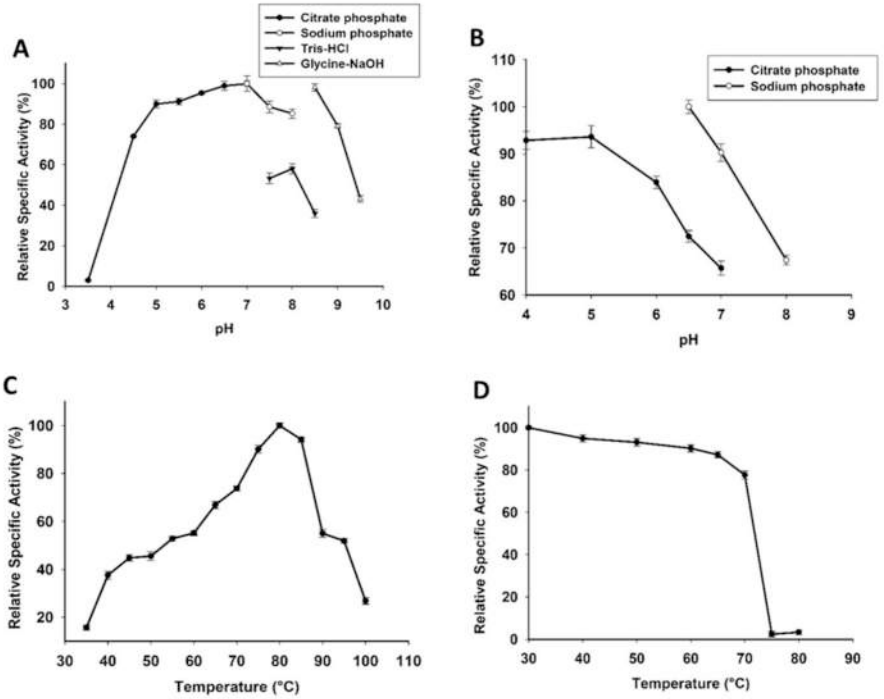

Fig. 3. Effect of pH and temperature on enzyme activity of *Ac*GH30A. (A) The optimum pH profile in different buffer systems, (B) The pH stability profile at different pH, (C) The optimum temperature profile and (D) Thermo-stability profile of *Ac*GH30A.

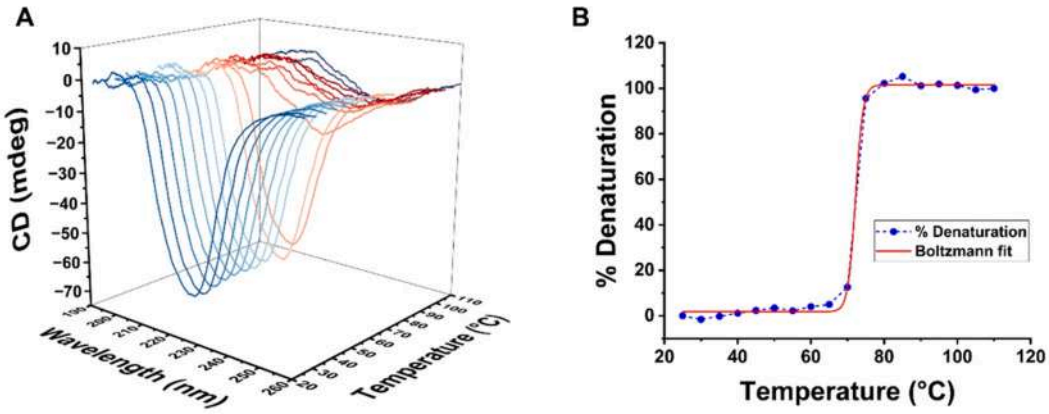

Fig. 4. Circular dichroism spectra of *Ac*GH30A (1.0 mg.ml^{-1}) in 50 mM sodium phosphate pH 7.0 (A) Circular dichroism spectra as a function of wavelength and temperature (B) Plot of % denaturation *vs* temperature for calculating melting temperature, T_m.

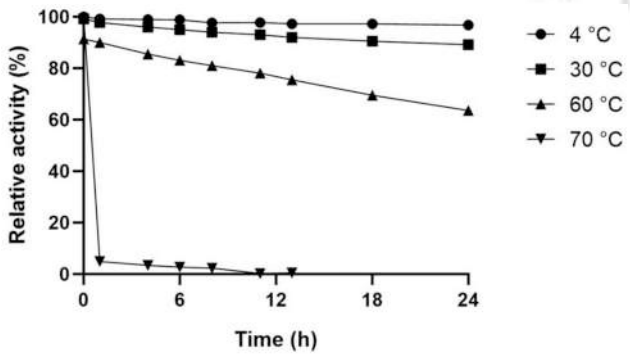

Fig. 5. Time course of inactivation of *Ac*GH30A at different temperatures 4, 30, 60 and 70 °C. Plot of residual enzyme activity *vs* time.

3.5. Substrate specificity analysis of *AcGH30A*

The enzyme activity of *Ac*GH30A against various natural substrates was investigated under optimum assay conditions. *Ac*GH30A displayed efficient hydrolysis of the xylan main-chain-based polysaccharides and showed a preference for glucuronoxylans as compared with arabinoxylans (Table 3). *Ac*GH30A demonstrated maximum specific activity of 136.2 U.mg^{-1} against 4-O-Methyl glucuronoxylan followed by xylan M. W. 20,000–30,000 (130.4 U.mg^{-1}), beechwood xylan (126.2 U.mg^{-1}), Larchwood xylan (122.1 U.mg^{-1}) and other xylan substrates. It also showed a moderate activity of 52.3 U.mg^{-1} towards oat spelt xylan. *Ac*GH30A showed limited specific activity against low viscosity (9.3 U. mg^{-1}) and insoluble (9.1 U.mg^{-1}) wheat arabinoxylan, followed by rye arabinoxylan (3.2 U.mg^{-1}) (Table 3). *Ac*GH30A gave much higher xylobiohydrolase activity against beechwood xylan containing 13 % glucuronic acid side chains as compared with the arabinoxylans where

Table 3
Substrate specificity of *Ac*GH30A.

Substrate (2 %, *w/v*)	Specific activity (U.mg^{-1})
4-O-Methyl glucuronoxylan (Sigma)	136.2 ± 0.6
Xylan, M.W. 20,000–30,000 (Carbosynth)	130.4 ± 1.1
Beechwood xylan (Megazyme)	126.2 ± 2.5
Larchwood xylan (Megazyme)	122.1 ± 3.2
Acacia sawdust xylan[a]	88.2 ± 1.4
Neem saw dust xylan[a]	77.3 ± 0.7
Sugarcane tops xylan[a]	63.3 ± 1.0
Banana stem xylan[a]	51.5 ± 2.2
Oat spelt xylan (Sigma)	52.3 ± 0.5
Alkali pretreated Sugarcane tops xylan[a]	26.0 ± 1.0
Wheat arabinoxylan, Low viscosity (Megazyme)	9.3 ± 0.3
Wheat arabinoxylan, insoluble (Megazyme)	9.1 ± 0.9
Water hyacinth xylan[a]	4.8 ± 0.9
Rye arabinoxylan (Megazyme)	3.2 ± 0.4
Birchwood Acetylated (Megazyme)	–
Xylan Corn Cob (Carbosynth)	–
Carboxy methyl cellulose (Sigma)	–

– *No activity detected.*
[a] In-house xylan substrates.

percentage of arabinose side chain is much higher (37–39 %) (Liab et al., 2000; Weng et al., 2023). *Ac*GH30A was not able to fully convert them to xylobiose due to the presence of side chain moieties. This suggest that the activity of *Ac*GH30A may potentially be improved by pre-treating xylan substrates with enzymes like β-glucuronidase and arabinofuranosidase, which can cleave the side chain components, glucuronic acid and arabinose residues, respectively. Consequently, this process would enhance the accessibility of the xylan backbone for *Ac*GH30A action.

In case of the *in-house* xylan substrates, *Ac*GH30A showed higher activity of 77.3 U.mg^{-1} with neem saw dust xylan (Sharma, Khaire, et al., 2020) and 88.2 U.mg^{-1} with acacia sawdust xylan (Sharma, Morla, et al., 2020) and lower activity, 63.3 U.mg^{-1} with xylan isolated from sugarcane tops and 26 U.mg^{-1} with alkali pretreated sugarcane top (Khaire et al., 2021). Neem saw dust xylan and acacia sawdust xylan were reported to contain ~10.5 % (*w*/w) and 15 % (w/w) of glucuronic acid units, respectively. Neem saw dust xylan having lower glucuronic acid than acacia xylan showed lower activity which could be due the differences in their solubility and the exact branching structure. Sugarcane tops xylan showed the presence of 16 % (w/w) D-glucuronic acid and 10 % (w/w) of L-arabinose residues (Khaire et al., 2021). Alkali pretreated sugarcane tops xylan contained 15 % (w/w) D-glucuronic acid and 11 % (w/w) L-arabinose residues (Khaire et al., 2022). 4-O-Methyl glucuronoxylan has a primary chain made up of β-(1 → 4)-

Table 4
Kinetic properties of *Ac*GH30A.

Substrate	V_{max} (U. mg^{-1})	K_M (mg. ml^{-1})	k_{cat} (s^{-1})	k_{cat}/K_M (ml.mg^{-1} s^{-1})
4-O-Methyl glucuronoxylan (Sigma, USA)	139 ± 6	0.71 ± 0.04	134.2 ± 3	189.1 ± 3.8
Xylan, M. W. 20,000–30,000 (Carbosynth, UK)	132 ± 3	0.49 ± 0.03	126.9 ± 2.2	259.1 ± 4.1
Beechwood xylan (Megazyme, Ireland)	129 ± 5	0.45 ± 0.05	124 ± 3	275.5 ± 3.7
Larchwood xylan (Megazyme, Ireland)	128 ± 6	0.41 ± 0.04	123.3 ± 4.2	301.1 ± 2.2

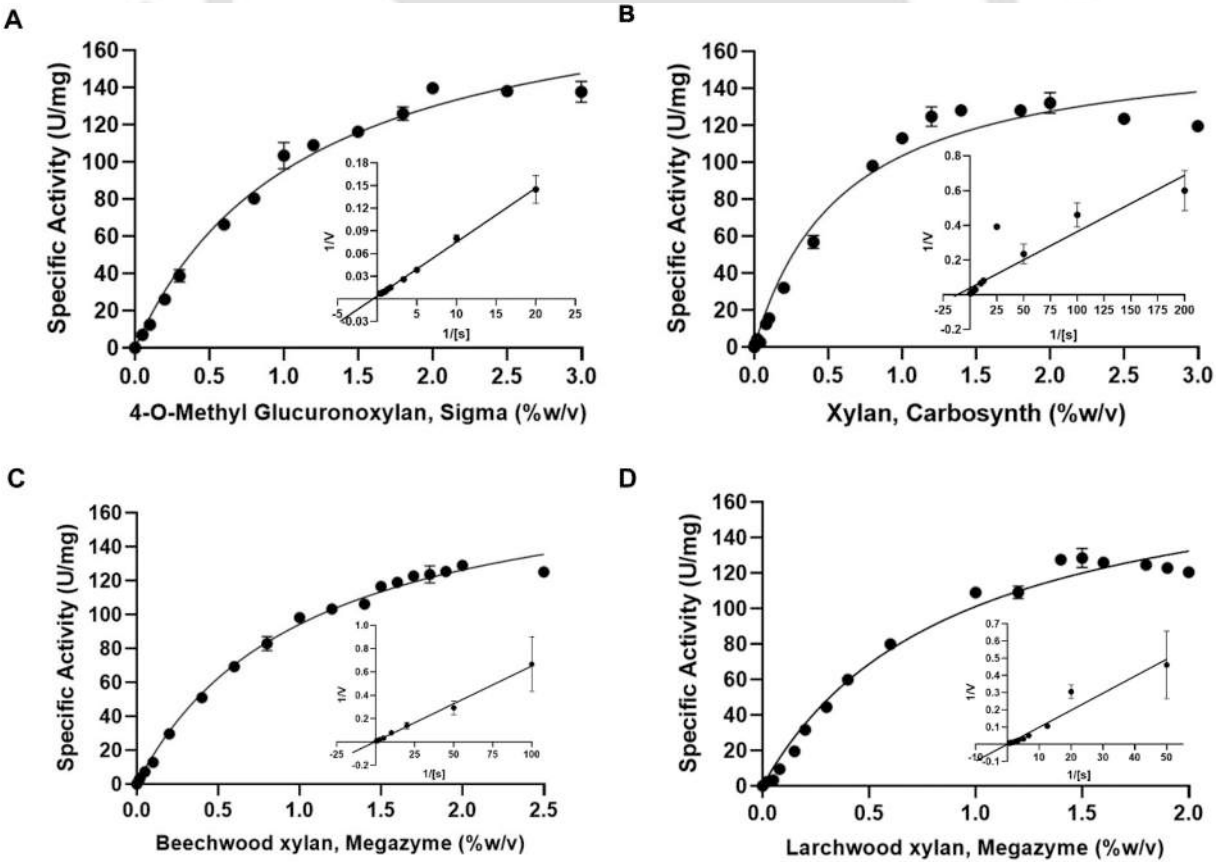

Fig. 6. Michaelis-Menten kinetics of *Ac*GH30A against (A) 4-O-Methyl glucuronoxylan (Sigma-Aldrich, USA) (B) Xylan, M.W. 20,000–30,000 (Carbosynth Ltd., UK) (C) Beechwood xylan (Megazyme Ltd., Ireland) (D) Larchwood xylan (Megazyme Ltd., Ireland). The enzyme assays were conducted at pH of 7.0 and 80 °C. The reaction mixtures contained of 10 μL of *Ac*GH30A (50 μg.mL^{-1}) and different concentrations of substrates dissolved in 90 μL of sodium-phosphate buffer (pH 7.0). The enzyme assays were conducted in triplicate. The inset graphs are Lineweaver-Burk plots of *Ac*GH30A with respective substrate.

Table 5
Effect of metal-ions and chelating agents on the activity of *Ac*GH30A.

Metal-ion/reagent additive	Relative enzyme activity of *Ac*GH30A (%)	
	1 mM	10 mM
Control	100	100
Ca^{2+}	108.9 ± 1.5	125.1 ± 1.3
Mg^{2+}	116.7 ± 1.4	123.0 ± 1.7
Mn^{2+}	99.7 ± 1.4	103.0 ± 1.5
K^{+}	99.7 ± 2.3	92.3 ± 1.9
Ni^{2+}	104.8 ± 2.8	99.5 ± 2.4
Na^{+}	97.6 ± 3.2	96.0 ± 2.9
Co^{2+}	84.7 ± 1.6	79.0 ± 1.2
Fe^{2+}	91.5 ± 2.7	80.2 ± 2.2
Cu^{2+}	69.7 ± 1.6	66.9 ± 1.6
Zn^{2+}	73.1 ± 1.1	58.9 ± 1.3
EDTA	100.9 ± 2.5	99.2 ± 2.1
EGTA	99.5 ± 3.4	98.1 ± 3.3

Fig. 7. Thin-layer chromatography (TLC) analysis of *Ac*GH30A action against various xylan substrates. The reaction mixture (100 μL) contained 10 μL *Ac*GH30A (50 μg.mL^{-1}) and 1 % (*w/v*) substrate dissolved in 50 mM sodium phosphate buffer (pH 7.0), incubated at 80 °C for 2 min. Lane 1. Beechwood xylan, Lane 2. Larchwood xylan, Lane 3. 4-O-Methyl glucuronoxylan, Lane 4. Rye arabinoxylan, Lane 5. Wheat arabinoxylan and Lane 6. Oat spelt xylan with standards (Lane S) xylose, xylobiose, xylotriose, xylotetraose and xylopentaose.

linked D-xylopyranosyl units that contains varying number of 4-*O*-methyl α-D-glucuronic acid at 2 position as side-chain substitutions, which are linked by α-(1 → 2) glycosidic bond to the main chain (Barbat et al., 2008). The chemical composition and structure of natural xylan substrates such as beechwood, birchwood and larchwood xylan can vary slightly depending on the source and extraction method (Teleman et al., 2002). The general structure of these xylans is a linear polymer of xylose residues linked by (1 → 4) glycosidic bonds, with several xylose units substituted with groups like acetyl, glucuronic acid and 4-*O*-methyl glucuronic acid. Beechwood xylan is reported to have a monosaccharide composition of Xylose: Glucuronic Acid: Other sugars = 80.8: 11.4: 7.8 (Nieto-Domínguez et al., 2019). Overall, the structure of xylan substrates is characterized by a backbone of β-(1,4)-linked xylose residues, which are substituted with various side chains, making them important components of hemicellulosic plant cell wall polysaccharides. Arabinoxylans are also composed of a backbone chain made up of β-(1 → 4)-linked xylose residues with L-arabinofuranosyl residues as side chain substitutions linked with the main chain at positions 2 or 3 (He et al., 2021).

Xylanases of GH30 family are usually glucuronoxylanases, which require the presence of glucuronic acid substitutions for substrate recognition and their activity, but the capability of *Ac*GH30A to cleave arabinoxylans, a polysaccharide devoid of glucuronic acid, to produce xylobiose suggest that it does not require the presence of glucuronic acid moieties for its action. Similar broad substrate specificity of enzyme activity was also observed with other xylobiohydrolase from the GH30 family such as *Aa*Xyn30A, which generated xylobiose as the main product from beechwood glucuronoxylan, rhodymenan and wheat arabinoxylan (Šuchová et al., 2020). Other GH30 family xylanases with auxiliary xylobiohydrolase activity from fungal origin, *Tt*Xyn30A (Katsimpouras et al., 2019) and *Sl*Xyn30A (Šuchová et al., 2022) also showed activity, preferably against glucuronoxylan followed by arabinoxylan. This result suggests that the activity of *Ac*GH30A resembles more to the fungal GH30 xylanases which show broad substrate specificity, rather than with bacterial GH30 xylanases which show activity only against glucuronoxylans. *Ac*GH30A also showed enzyme activity on various in-house xylan substrates, listed in Table 3.

*Ac*GH30A showed no activity against the cellulosic substrates, a beneficial property needed for the extraction of cellulose fibres in the textile and paper processing industries by selectively degrading the xylan components of the plant biomass. These findings suggested that xylobiohydrolase, *Ac*GH30A can also contribute to the degumming of plant fibres used in textile in combination with other enzymes such as endoxylanases and pectinolytic enzymes (Bhalla et al., 2015; Chiliveri et al., 2016).

3.6. 3.6 Kinetic parameters of *Ac*GH30A

The kinetic parameters of *Ac*GH30A were determined by using 4-*O*-methyl glucuronoxylan (Fig. 6A), xylan M.W. 20,000–30,000 (Fig. 6B) beechwood xylan (Fig. 6C) and larchwood xylan (Fig. 6D) as substrate at 80 °C in 50 mM sodium phosphate buffer, pH 7.0. All the kinetic parameters obtained for the 4 substrates are mentioned in Table 4. Out of 4 substrates, 4-*O*-methyl glucuronoxylan gave maximum V_{max}, 139 (U.mg^{-1}) followed by xylan M.W. 20,000–30,000 (132 U.mg^{-1}), beechwood xylan (129 U.mg^{-1}), larchwood xylan (128 U.mg^{-1}) shown in Fig. 6 and Table 4. The reaction of *Ac*GH30A with 4-O-Methyl glucuronoxylan gave the turn over number (k_{cat}) 134.2 s^{-1} and catalytic efficiency (k_{cat}/K_M) 189.1 mL.mg^{-1}.s^{-1} (Table 4). However, Šuchová, Puchart, and Biely (2021) reported a significantly lower k_{cat} value of 17.7 s^{-1} for *Hc*Xyn30A (named in present study as *Ac*GH30A) for beechwood 4-*O*-methylglucuronoxylan (GX) at 37 °C in 50 mM sodium phosphate buffer pH 6.0. The k_{cat} value of *Ac*GH30A against GX found was much higher in our studies, which could be due to the analysis of kinetic parameters at optimum temperature, 80 °C and optimum pH 7.0. A fungal xylobiohydrolase, *Aa*Xyn30A showed the V_{max}, 9.03 U.mg^{-1} and k_{cat} of 7.85 s^{-1} for 4-*O*-methylglucuronoxylan (Šuchová et al., 2020), which were also much lower than the reported values in the present study.

Most of xylobiohydrolases such as *Sl*Xyn30A (Šuchová et al., 2022), *Tt*Xyn30A (Katsimpouras et al., 2019) and *Tc*Xyn30B (Nakamichi et al., 2019) reported till date are strongly bifunctional in nature having core endoxylanase activity. A GH30 glucuronoxylanase, *Sl*Xyn30A from *S. lignohabitans* with auxiliary xylobiohydrolase activity, showed V_{max}, 24.2 U.mg^{-1} k_{cat} of 20.2 s^{-1} and k_{cat}/K_M of 1.2 mL.mg^{-1}.s^{-1} with glucuronoxylan (GX). Another bifunctional, glucuronoxylanase, *Tt*Xyn30A from *T. thermophila* displayed V_{max}, 24.3 U.mg^{-1}, k_{cat} of 7.21 s^{-1} and a catalytic efficiency k_{cat}/K_M of 4.24 mL.mg^{-1}.s^{-1} against beechwood glucuronoxylan, whereas, *Tc*Xyn30B from *Talaromyces cellulolyticus* gave V_{max}, 7.1 U.mg^{-1}, k_{cat} of 20.9 s^{-1} and k_{cat}/K_M of 1.1 mL.mg^{-1}.s^{-1}. Evidently, *Ac*GH30A showed the higher V_{max}, turnover number and catalytic efficiency against the natural xylan substrates as compared with the other xylobiohydrolases reported till date. A higher V_{max} of *Ac*GH30A will allow a faster conversion of substrate into product, which is crucial in various biotechnological processes. Enhanced turnover number and catalytic efficiency suggest that a smaller amount of enzyme is required to achieve the same level of substrate conversion compared to other reported enzymes.

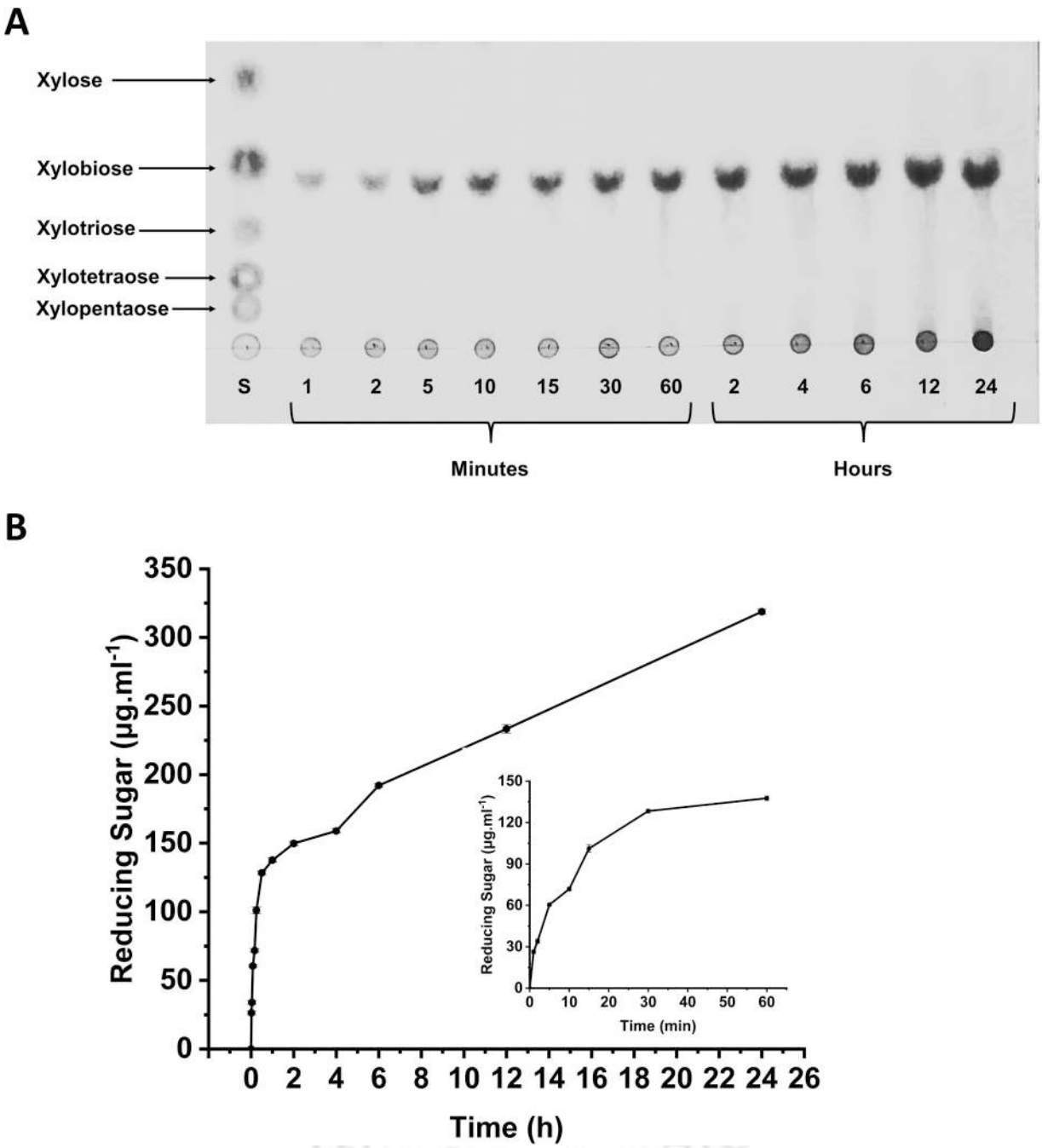

Fig. 8. Thin-layer chromatography (TLC) analysis of time-dependent hydrolysis of beechwood xylan (1 %, w/v) by *Ac*GH30A incubated at 40 °C, pH 7.0 for 1 min to 24 h. (A) TLC chromatogram. Standards (S) used were xylose, xylobiose, xylotriose, xylotetraose and xylopentaose. (B) Quantitative graph of reducing sugar produced with time by *Ac*GH30A at different time periods.

3.7. Effects of metal ions and chemical agents on AcGH30A activity

The enzyme activity of *Ac*GH30A was investigated in the presence of different metal ions and chemical agents at concentrations of 1 and 10 mM and outcomes were presented in Table 5. Ca^{2+} and Mg^{2+} ions enhanced the enzyme activity of *Ac*GH30A at both the concentrations of 1 and 10 mM. The enzyme activity of *Ac*GH30A at 10 mM concentration of Ca^{2+} and Mg^{2+} increased by 25 % and 23 %, respectively, whereas, Co^{2+}, Zn^{2+}, Fe^{2+} and Cu^{2+} ions, drastically reduced the enzyme activity. The decrease in enzymatic activity in the presence of heavy metal ions might be due to their interference with the amino acid residues at the active site. The chelating agents, EDTA, which can chelate a broad range of metal ions and EGTA, which has high affinity for calcium ions, effectively reduce the activity of xylanases that contain metal ions at their catalytic sites (Prakash et al., 2012). However, in the case of *Ac*GH30A, they showed no significant effect on the activity of the enzyme. It indicated that *Ac*GH30A does not necessarily require metal ions for its enzymatic activity.

3.8. Analysis of hydrolytic mechanism of AcGH30A by TLC

The TLC chromatogram of enzyme hydrolyzed products released from different xylan substrates *viz.*, beechwood xylan, larchwood xylan, 4-*O*-methyl glucuronoxylan, rye arabinoxylan, wheat arabinoxylan and oat spelt xylan, by *Ac*GH30A displayed the presence of same and only one product, xylobiose (Fig. 7). The low intensity spots of xylobiose

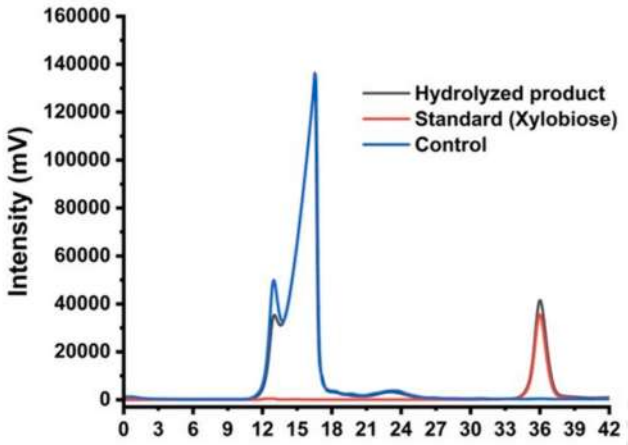

Fig. 9. HPLC analysis of *Ac*GH30A hydrolyzed products from beechwood xylan. Chromatogram showing the enzyme hydrolyzed product (in Black), control containing beechwood xylan without enzyme (in Blue) and standard xylobiose (in Red). The enzyme-substrate reaction was carried out using 100 μg.mL^{-1} of enzyme, *Ac*GH30A with 1 % (w/v) beechwood xylan in 50 mM sodium phosphate buffer, pH 7.0 at 70 °C for 60 min.

produced from arabinoxylans and oat spelt xylan showed the low activity of *Ac*GH30A against these substrates.

The TLC chromatogram of time-dependent hydrolysis of beechwood xylan by *Ac*GH30A at 40 °C also showed the release of the sole product, xylobiose (Fig. 8A). The time-dependent TLC analysis did not show the presence of any other hydrolyzed products as the incubation time progressed except the quantitative increase of the xylobiose amount (Fig. 8B). *Ac*GH30A produced 26 μg.ml^{-1} of reducing sugar from beechwood xylan at 1 min reaching up to 319 μg.ml^{-1} at 24 h incubation (Fig. 8B).

3.9. Explication of the hydrolytic mechanism of AcGH30A by HPLC analysis

The hydrolyzed products of beechwood xylan by *Ac*GH30A analyzed by HPLC showed a distinct peak at retention time, 35.8 min corresponding to xylobiose (Fig. 9). The HPLC profile of enzyme-hydrolyzed product was compared with those of control containing only substrate and the standard xylobiose (Fig. 9). The common peaks with retention times ~16.5 and ~ 13 min was observed in both the enzyme hydrolysate and the control corresponding to undigested polysaccharide which were not detectable by TLC (Fig. 9). The HPLC results revealed the release of the only product, xylobiose from beechwood xylan by *Ac*GH30A. These results confirmed that *Ac*GH30A is an obligate xylobiohydrolase enzyme.

3.10. Analysis of hydrolysed products of AcGH30A by LC-MS

The analysis of *Ac*GH30A hydrolyzed products of beechwood xylan by LCMS showed a single charge species at *m/z* 325.2 9 $[M + ACN + H]^+$ depicting the xylobiose (Fig. 10A), which corresponded to mass spectrum of standard xylobiose showing a single peak at m/z 305.0 $[M + Na]^+$ (Fig. 10B). The LC-MS analysis confirmed that xylobiose is the only product released by *Ac*GH30A from beechwood xylan. However, fungal xylobiohydrolases such as *Aa*Xyn30A (Šuchová et al., 2020), *Tt*Xyn30A (Nakamichi et al., 2020) and *Tc*Xyn30B (Nakamichi et al., 2019) from hydrolysis of beechwood 4-*O*-methyl glucuronoxylan released other xylo-oligosaccharides along with the xylobiose.

4. Conclusion

A bacterial gene encoding xylobiohydrolase, *Ac*GH30A, derived from *Acetivibrio clariflavus*, was cloned, expressed as a soluble protein and purified. The enzyme displayed maximum activity against 4-*O*-methyl glucuronoxylan followed by xylan, beechwood xylan, larchwood xylan and other xylan substrates. *Ac*GH30A demonstrated thermophilic nature with an optimum temperature of 80 °C, setting it apart as the first bacterial xylobiohydrolase from GH30 family with such an elevated

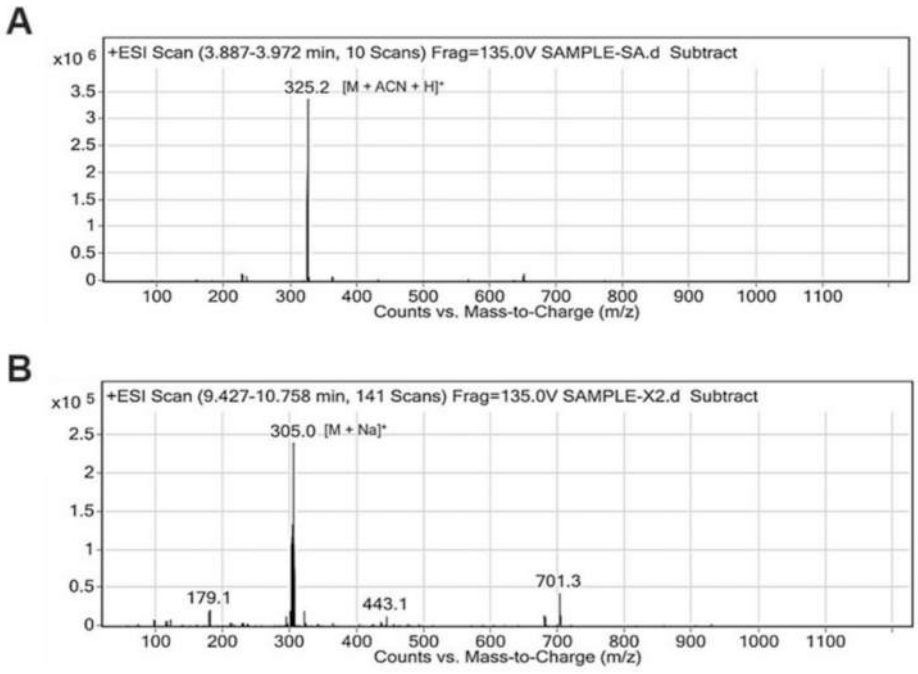

Fig. 10. (A) Positive ESI ion MS analysis of *Ac*GH30A hydrolyzed product from beechwood xylan and (B) Positive ESI ion MS analysis of xylobiose (Standard). The reaction was carried out using 100 μg.mL^{-1} of enzyme, *Ac*GH30A with 1 % (w/v) beechwood xylan in 50 mM sodium phosphate buffer, pH 7.0 at 70 °C for 60 min.

optimum temperature. *Ac*GH30A displayed remarkable stability in a wide range of temperature and pH. These findings position *Ac*GH30A as a promising candidate for applications demanding high temperatures and flexibility with pH. Thermal stability analysis by circular dichroism (CD) spectroscopy, indicated that *Ac*GH30A retained its secondary structure elements up to 70 °C, with complete loss of structure at 85 °C. *Ac*GH30A with broad stability profiles can be applied in various industries, including biofuel production, food processing, textile manufacturing, and bioremediation, offering versatility and value across different sectors. The Ca^{2+} and Mg^{2+} ions significantly enhanced the activity of *Ac*GH30A (>20 %) which can be beneficial for improving its activity and efficiency in various biotechnological applications. The analysis of *Ac*GH30A hydrolyzed products of beechwood xylan by TLC, HPLC and LC-MS revealed the release of only one product, xylobiose, confirming its obligate xylobiohydrolase activity. *Ac*GH30A is a novel bacterial enzyme displaying obligate xylobiohydrolase activity by orchestrating exclusive and sequential release of xylobiose from xylan polysaccharides. Therefore, *Ac*GH30A can be used for commercial production of xylobiose and other value-added products from xylan polysaccharides or lignocellulosic biomasses.

CRediT authorship contribution statement

Yumnam Robinson Singh: Writing – review & editing, Writing – original draft, Visualization, Validation, Software, Methodology, Investigation, Data curation. **Abhijeet Thakur:** Methodology. **Carlos M.G.A. Fontes:** Writing – review & editing, Methodology, Conceptualization. **Arun Goyal:** Writing – review & editing, Supervision, Resources, Project administration, Conceptualization.

Declaration of competing interest

CMGAF is a financial beneficiary of the company that sells the enzyme that is described in this paper.

Data availability

Data will be made available on request.

Acknowledgement

The authors are thankful to Department of Biosciences and Bioengineering, Indian Institute of Technology Guwahati, Assam, India for providing essential research facilities. The authors are thankful to Guwahati Biotech Park, Guwahati funded by Department of Biotechnology, India, project No: BT/BP/19011/1/2008 dt. 24.02.2009, for providing the LC-MS facility.

References

Ajeje, S. B., Hu, Y., Song, G., Peter, S. B., Afful, R. G., Sun, F., … Sun, H. (2021). Thermostable cellulases / xylanases from thermophilic and hyperthermophilic microorganisms: Current perspective. *Frontiers in Bioengineering and Biotechnology, 9*, Article 794304. https://doi.org/10.3389/fbioe.2021.794304

Artzi, L., Dassa, B., Borovok, I., Shamshoum, M., Lamed, R., & Bayer, E. A. (2014). Cellulosomics of the cellulolytic thermophile Clostridium clariflavum. *Biotechnology for Biofuels, 7*(1), 100. https://doi.org/10.1186/1754-6834-7-100

Barbat, A., Gloaguen, V., Moine, C., Sainte-Catherine, O., Kraemer, M., Rogniaux, H., … Krausz, P. (2008). Structural characterization and cytotoxic properties of a 4-o-methylglucuronoxylan from castanea sativa. 2. Evidence of a structure−activity relationship. *Journal of Natural Products, 71*(8), 1404–1409. https://doi.org/10.1021/np800207g

Bhalla, A., Bischoff, K. M., & Sani, R. K. (2015). Highly thermostable xylanase production from a thermophilic Geobacillus sp. strain WSUCF1 utilizing lignocellulosic biomass. *Frontiers in Bioengineering and Biotechnology, 3*. https://doi.org/10.3389/fbioe.2015.00084

Chiliveri, S. R., Koti, S., & Linga, V. R. (2016). Retting and degumming of natural fibers by pectinolytic enzymes produced from bacillus tequilensis SV11-UV37 using solid state fermentation. *SpringerPlus, 5*, 559. https://doi.org/10.1186/s40064-016-2173-x

Collins, T., Gerday, C., & Feller, G. (2005). Xylanases, xylanase families and extremophilic xylanases. *FEMS Microbiology Reviews, 29*(1), 3–23. https://doi.org/10.1016/j.femsre.2004.06.005

Crooks, C., Bechle, N. J., & St John, F. J. (2021). A new subfamily of glycoside hydrolase family 30 with strict xylobiohydrolase function. *Frontiers in Molecular Biosciences, 8*. https://doi.org/10.3389/fmolb.2021.714238

Dassa, B., Borovok, I., Lamed, R., Henrissat, B., Coutinho, P., Hemme, C. L., … Bayer, E. A. (2012). Genome-wide analysis of Acetivibrio cellulolyticus provides a blueprint of an elaborate cellulosome system. *BMC Genomics, 13*(1), 210. https://doi.org/10.1186/1471-2164-13-210

El Enshasy, H. A., Kandiyil, S. K., Malek, R., & Othman, N. Z. (2016). Microbial xylanases: Sources, types, and their applications. In V. K. Gupta (Ed.), *Vol. 3. Microbial enzymes in bioconversions of biomass* (pp. 151–213). Springer International Publishing. https://doi.org/10.1007/978-3-319-43679-1_7.

Evangelista, D. E., de Oliveira Arnoldi Pellegrini, V., Santo, M. E., McQueen-Mason, S., Bruce, N. C., & Polikarpov, I. (2019). Biochemical characterization and low-resolution SAXS shape of a novel GH11 exo-1,4-β-xylanase identified in a microbial consortium. *Applied Microbiology and Biotechnology, 103*(19), 8035–8049. https://doi.org/10.1007/s00253-019-10033-8

Fonseca-Maldonado, R., Ribeiro, L. F., Furtado, G. P., Arruda, L. M., Meleiro, L. P., Alponti, J. S., … dos P. M. Furriel, R. (2014). Synergistic action of co-expressed xylanase/laccase mixtures against milled sugar cane bagasse. *Process Biochemistry, 49*(7), 1152–1161. https://doi.org/10.1016/j.procbio.2014.03.027

Froger, A., & Hall, J. E. (2007). Transformation of plasmid DNA into E. coli using the heat shock method. *Journal of Visualized Experiments: JoVE, 6*, 253. https://doi.org/10.3791/253

Ghosh, M., & Nanda, G. (1994). Purification and some properties of a xylanase from aspergillus sydowii MG49. *Applied and Environmental Microbiology, 60*(12), 4620–4623. https://doi.org/10.1128/aem.60.12.4620-4623.1994

Guo, Y., Gao, Z., Xu, J., Chang, S., Wu, B., & He, B. (2018). A family 30 glucurono-xylanase from bacillus subtilis LC9: Expression, characterization and its application in Chinese bread making. *International Journal of Biological Macromolecules, 117*, 377–384. https://doi.org/10.1016/j.ijbiomac.2018.05.143

Han, J.-A., & Lim, S.-T. (2004). Structural changes of corn starches by heating and stirring in DMSO measured by SEC-MALLS-RI system. *Carbohydrate Polymers, 55*(3), 265–272. https://doi.org/10.1016/j.carbpol.2003.09.007

He, H.-J., Qiao, J., Liu, Y., Guo, Q., Ou, X., & Wang, X. (2021). Isolation, structural, functional, and bioactive properties of cereal arabinoxylan—a critical review. *Journal of Agricultural and Food Chemistry, 69*(51), 15437–15457. https://doi.org/10.1021/acs.jafc.1c04506

He, J., Su, L., Sun, X., Fu, J., Chen, J., & Wu, J. (2014). A novel xylanase from Streptomyces sp. FA1: Purification, characterization, identification and heterologous expression. *Biotechnology and Bioprocess Engineering, 19*(1), 8–17. https://doi.org/10.1007/s12257-013-0490-2

Jamaldheen, S. B., Thakur, A., Moholkar, V. S., & Goyal, A. (2019). Enzymatic hydrolysis of hemicellulose from pretreated finger millet (Eleusine coracana) straw by recombinant endo-1,4-β-xylanase and exo-1,4-β-xylosidase. *International Journal of Biological Macromolecules, 135*, 1098–1106. https://doi.org/10.1016/j.ijbiomac.2019.06.010

Juturu, V., & Wu, J. C. (2012). Microbial xylanases: Engineering, production and industrial applications. *Biotechnology Advances, 30*(6), 1219–1227. https://doi.org/10.1016/j.biotechadv.2011.11.006

Katsimpouras, C., Dedes, G., Thomaidis, N. S., & Topakas, E. (2019). A novel fungal GH30 xylanase with xylobiohydrolase auxiliary activity. *Biotechnology for Biofuels, 12*(1), 1–14. https://doi.org/10.1186/s13068-019-1455-2

Kaur, P., Bhardwaj, N. K., & Sharma, J. (2016). Pretreatment with xylanase and its significance in hemicellulose removal from mixed hardwood Kraft pulp as a process step for viscose. *Carbohydrate Polymers, 145*, 95–102. https://doi.org/10.1016/j.carbpol.2016.03.023

Khaire, K. C., Moholkar, V. S., & Goyal, A. (2022). A biorefinery approach for sequential extraction of commercial grade xylan and alkali lignin from alkali pretreated sugarcane tops hydrolysate. *Industrial Crops and Products, 187*, Article 115545. https://doi.org/10.1016/j.indcrop.2022.115545

Khaire, K. C., Sharma, K., Thakur, A., Moholkar, V. S., & Goyal, A. (2021). Extraction and characterization of xylan from sugarcane tops as a potential commercial substrate. *Journal of Bioscience and Bioengineering, 131*(6), 647–654. https://doi.org/10.1016/j.jbiosc.2021.01.009

Kubata, B. K., Suzuki, T., Horitsu, H., Kawai, K., & Takamizawa, K. (1994). Purification and characterization of Aeromonas caviae ME-1 xylanase V, which produces exclusively xylobiose from xylan. *Applied and Environmental Microbiology, 60*(2), 531–535. https://doi.org/10.1128/aem.60.2.531-535.1994

Kumar, V., Marín-Navarro, J., & Shukla, P. (2016). Thermostable microbial xylanases for pulp and paper industries: Trends, applications and further perspectives. *World Journal of Microbiology and Biotechnology, 32*(2), 34. https://doi.org/10.1007/s11274-015-2005-0

Laemmli, U. K. (1970). Cleavage of structural proteins during the assembly of the head of bacteriophage T4. *Nature, 227*(5259), 680–685. https://doi.org/10.1038/227680a0

Lamed, R., & Bayer, E. A. (1988). The Cellulosome of Clostridium thermocellum. In A. I. Laskin (Ed.), *Vol. 33. Advances in applied microbiology* (pp. 1–46). Academic Press. https://doi.org/10.1016/S0065-2164(08)70203-X.

Liab, K., Azadi, P., Collins, R., Tolan, J., Kim, J. S., & Eriksson, K. L. (2000). Relationships between activities of xylanases and xylan structures. *Enzyme and Microbial Technology, 27*(1), 89–94. https://doi.org/10.1016/S0141-0229(00)00190-3

Lowry, O. H., Rosebrough, N. J., Farr, A. L., & Randall, R. J. (1951). Protein measurement with the Folin phenol reagent. *Journal of Biological Chemistry, 193*(1), 265–275. https://doi.org/10.1016/S0021-9258(19)52451-6

Maehara, T., Yagi, H., Sato, T., Ohnishi-Kameyama, M., Fujimoto, Z., Kamino, K., Kitamura, Y., St John, F., Yaoi, K., & Kaneko, S. (2018). GH30 glucuronoxylan-specific xylanase from Streptomyces turgidiscabies C56. *Applied and Environmental Microbiology, 84*(4), 17–e01850. https://doi.org/10.1128/AEM.01850-17

Manisseri, C., & Gudipati, M. (2012). Prebiotic activity of purified xylobiose obtained from ragi (Eleusine coracana, Indaf-15) bran. *Indian Journal of Microbiology, 52*(2), 251–257. https://doi.org/10.1007/s12088-011-0176-4

Mello, B. L., Alessi, A. M., Riaño-Pachón, D. M., deAzevedo, E. R., Guimarães, F. E. G., Espirito Santo, M. C., … Polikarpov, I. (2017). Targeted metatranscriptomics of compost-derived consortia reveals a GH11 exerting an unusual exo-1,4-β-xylanase activity. *Biotechnology for Biofuels, 10*(1), 254. https://doi.org/10.1186/s13068-017-0944-4

Moreira, L. R. S., & Filho, E. X. F. (2016). Insights into the mechanism of enzymatic hydrolysis of xylan. *Applied Microbiology and Biotechnology, 100*(12), 5205–5214. https://doi.org/10.1007/s00253-016-7555-z

Nakamichi, Y., Fouquet, T., Ito, S., Watanabe, M., Matsushika, A., & Inoue, H. (2019). Structural and functional characterization of a bifunctional GH30-7 xylanase B from the filamentous fungus Talaromyces cellulolyticus. *Journal of Biological Chemistry, 294*(11), 4065–4078. https://doi.org/10.1074/jbc.RA118.007207

Nakamichi, Y., Watanabe, M., Matsushika, A., & Inoue, H. (2020). Substrate recognition by a bifunctional GH30-7 xylanase B from Talaromyces cellulolyticus. *FEBS Open Bio, 10*(6), 1180–1189. https://doi.org/10.1002/2211-5463.12873

Nelson, N. (1944). A photometric adaptation of the Somogyi method for the determination of glucose. *Journal of Biological Chemistry, 153*(2), 375–380. https://doi.org/10.1016/S0021-9258(18)71980-7

Nieto-Domínguez, M., Martínez-Fernández, J. A., de Toro, B. F., Méndez-Líter, J. A., Cañada, F. J., Prieto, A., … Martínez, M. J. (2019). Exploiting xylan as sugar donor for the synthesis of an antiproliferative xyloside using an enzyme cascade. *Microbial Cell Factories, 18*(1), 174. https://doi.org/10.1186/s12934-019-1223-9

Prakash, B., Vidyasagar, M., Jayalakshmi, S. K., & Sreeramulu, K. (2012). Purification and some properties of low-molecular-weight extreme halophilic xylanase from Chromohalobacter sp. TPSV 101. *Journal of Molecular Catalysis B: Enzymatic, 74*(3), 192–198. https://doi.org/10.1016/j.molcatb.2011.10.004

Puchart, V., Šuchová, K., & Biely, P. (2021). Xylanases of glycoside hydrolase family 30–an overview. *Biotechnology Advances.* , Article 107704. https://doi.org/10.1016/j.biotechadv.2021.107704

Ruíz, I., Gómez, J. A., & García, L. (2022). Use of circular dichroism in the characterization of the fusion protein SARS-CoV-2 S protein (RBD)-hFc. *Pure and Applied Chemistry, 94*(7), 829–838. https://doi.org/10.1515/pac-2021-1014

Sárossy, Z., Tenkanen, M., Pitkänen, L., Bjerre, A.-B., & Plackett, D. (2013). Extraction and chemical characterization of rye arabinoxylan and the effect of β-glucan on the mechanical and barrier properties of cast arabinoxylan films. *Food Hydrocolloids, 30*(1), 206–216. https://doi.org/10.1016/j.foodhyd.2012.05.022

Sepulchro, A. G. V., Pellegrini, V. O. A., Briganti, L., de Araujo, E. A., de Araujo, S. S., & Polikarpov, I. (2020). Transformation of xylan into value-added biocommodities using Thermobacillus composti GH10 xylanase. *Carbohydrate Polymers, 247*, Article 116714. https://doi.org/10.1016/j.carbpol.2020.116714

Sharma, K., Khaire, K. C., Thakur, A., Moholkar, V. S., & Goyal, A. (2020). Acacia xylan as a substitute for commercially available xylan and its application in the production of xylooligosaccharides. *ACS Omega, 5*(23), 13729–13738. https://doi.org/10.1021/acsomega.0c00896

Sharma, K., Morla, S., Khaire, K. C., Thakur, A., Moholkar, V. S., Kumar, S., & Goyal, A. (2020). Extraction, characterization of xylan from Azadirachta indica (neem) sawdust and production of antiproliferative xylooligosaccharides. *International Journal of Biological Macromolecules, 163*, 1897–1907. https://doi.org/10.1016/j.ijbiomac.2020.09.086

Shiratori, H., Ikeno, H., Ayame, S., Kataoka, N., Miya, A., Hosono, K., … Ueda, K. (2006). Isolation and characterization of a new Clostridium sp. that performs effective cellulosic waste digestion in a thermophilic methanogenic bioreactor. *Applied and Environmental Microbiology, 72*(5), 3702–3709. https://doi.org/10.1128/AEM.72.5.3702-3709.2006

Shiratori, H., Sasaya, K., Ohiwa, H., Ikeno, H., Ayame, S., Kataoka, N., … Ueda, K. (2009). Clostridium clariflavum sp. Nov. and Clostridium caenicola sp. Nov., moderately thermophilic, cellulose−/cellobiose-digesting bacteria isolated from methanogenic sludge. *International Journal of Systematic and Evolutionary Microbiology, 59*(7), 1764–1770. https://doi.org/10.1099/ijs.0.003483-0

Simmons, T. J., Mortimer, J. C., Bernardinelli, O. D., Pöppler, A.-C., Brown, S. P., deAzevedo, E. R., … Dupree, P. (2016). Folding of xylan onto cellulose fibrils in plant cell walls revealed by solid-state NMR. *Nature Communications, 7*(1). https://doi.org/10.1038/ncomms13902. Article 1.

Somogyi, M. (1945). A new reagent for the determination of sugars. *Journal of Biological Chemistry, 160*(1), 61–68. https://doi.org/10.1016/s0021-9258(18)43097-9

Šuchová, K., Chyba, A., Hegyi, Z., Rebroš, M., & Puchart, V. (2022). Yeast GH30 xylanase from Sugiyamaella lignohabitans is a glucuronoxylanase with auxiliary xylobiohydrolase activity. *Molecules, 27*(3). https://doi.org/10.3390/molecules27030751. Article 3.

Šuchová, K., Puchart, V., & Biely, P. (2021). A novel bacterial GH30 xylobiohydrolase from Hungateiclostridium clariflavum. *Applied Microbiology and Biotechnology, 105*(1), 185–195. https://doi.org/10.1007/s00253-020-11023-x

Šuchová, K., Puchart, V., Spodsberg, N., Mørkeberg Krogh, K. B. R., & Biely, P. (2020). A novel GH30 xylobiohydrolase from Acremonium alcalophilum releasing xylobiose from the non-reducing end. *Enzyme and Microbial Technology, 134*, Article 109484. https://doi.org/10.1016/j.enzmictec.2019.109484

Swift, M. L. (1997). GraphPad prism, data analysis, and scientific graphing. *Journal of Chemical Information and Computer Sciences, 37*(2), 411–412. https://doi.org/10.1021/ci960402j

Teleman, A., Tenkanen, M., Jacobs, A., & Dahlman, O. (2002). Characterization of O-acetyl-(4-O-methylglucurono) xylan isolated from birch and beech. *Carbohydrate Research, 337*(4), 373–377. https://doi.org/10.1016/S0008-6215(01)00327-5

Valls, C., Vidal, T., Gallardo, O., Diaz, P., Javier Pastor, F. I., & Blanca Roncero, M. (2010). Obtaining low-HexA-content cellulose from eucalypt fibres: Which glycosyl hydrolase family is more efficient? *Carbohydrate Polymers, 80*(1), 154–160. https://doi.org/10.1016/j.carbpol.2009.11.006

Wang, R., Liu, Z., Cheng, L., Duan, S., Feng, X., Zheng, K., Cheng, Y., & Zeng, J. (2019). A novel endo-β-1,4-xylanase GH30 from Dickeya dadantii DCE-01: Clone, expression, characterization, and ramie biological degumming function. *Textile Research Journal, 89*(4), 463–472. https://doi.org/10.1177/0040517517748511

Weng, V., Cardeira, M., Bento-Silva, A., Serra, A. T., Brazinha, C., & Bronze, M. R. (2023). Arabinoxylan from corn fiber obtained through alkaline extraction and membrane purification: Relating bioactivities with the phenolic compounds. *Molecules, 28*(15). https://doi.org/10.3390/molecules28155621. Article 15.

Journal of Biomolecular Structure and Dynamics

ISSN: (Print) (Online) Journal homepage: www.tandfonline.com/journals/tbsd20

Small angle X-ray scattering and *in silico* based structure and function analysis of a novel xylobiohydrolase (*Ac*GH30A) from *Acetivibrio clariflavus*

Yumnam Robinson Singh, Jebin Ahmed & Arun Goyal

To cite this article: Yumnam Robinson Singh, Jebin Ahmed & Arun Goyal (25 Nov 2024): Small angle X-ray scattering and *in silico* based structure and function analysis of a novel xylobiohydrolase (*Ac*GH30A) from *Acetivibrio clariflavus* , Journal of Biomolecular Structure and Dynamics, DOI: 10.1080/07391102.2024.2431192

To link to this article: https://doi.org/10.1080/07391102.2024.2431192

Published online: 25 Nov 2024.

JOURNAL OF BIOMOLECULAR STRUCTURE AND DYNAMICS
https://doi.org/10.1080/07391102.2024.2431192

Taylor & Francis
Taylor & Francis Group

Small angle X-ray scattering and *in silico* based structure and function analysis of a novel xylobiohydrolase (*Ac*GH30A) from *Acetivibrio clariflavus*

Yumnam Robinson Singh, Jebin Ahmed and Arun Goyal

Carbohydrate Enzyme Biotechnology Laboratory, Department of Biosciences and Bioengineering, Indian Institute of Technology Guwahati, Guwahati, Assam, India

ABSTRACT

Xylobiohydrolase plays a crucial role in the hydrolysis of xylan, a complex polysaccharide present in the cell walls of plants. This study focuses on the solution structure and substrate binding analysis of a novel xylobiohydrolase, *Ac*GH30A, from *Acetivibrio clariflavus*. Secondary structure analysis of *Ac*GH30A in an aqueous environment using Circular Dichroism and *in silico* modeling revealed an α/β/α sandwich structure with a central β-barrel comprising eight β-strands. Superposition of the homology-modelled structure of *Ac*GH30A with its closest homolog showed that the active-site contains Glu175 and Glu268 as the catalytic residues. Molecular docking confirmed xylobiose as the preferred ligand, showcasing polar interactions with the catalytic amino acids, indicating its xylobiohydrolase activity. *Ac*GH30A displayed a high binding affinity with xylobiose with an association constant (K_a) of 7.83×10^5 M^{-1}, as determined by isothermal titration calorimetry. Molecular dynamics (MD) simulations of *Ac*GH30A and *Ac*GH30A-xylobiose complex in solution showed reduced RMSD, R_g and SASA values, confirming the stability and compactness of the complex. MD simulations further highlighted the crucial role of Glu175 in hydrogen bonding with the ligand, which acts as an acid or base. Small-angle X-ray scattering (SAXS) analysis of *Ac*GH30A showed its molecular shape as an earbud with a globular structure existing in a monodispersed state, which was corroborated by dynamic light scattering (DLS). The hydrodynamic radius (R_h) of *Ac*GH30A, determined by DLS, was 3.7 nm. This study significantly contributed valuable insights into the structure and functional aspects of *Ac*GH30A.

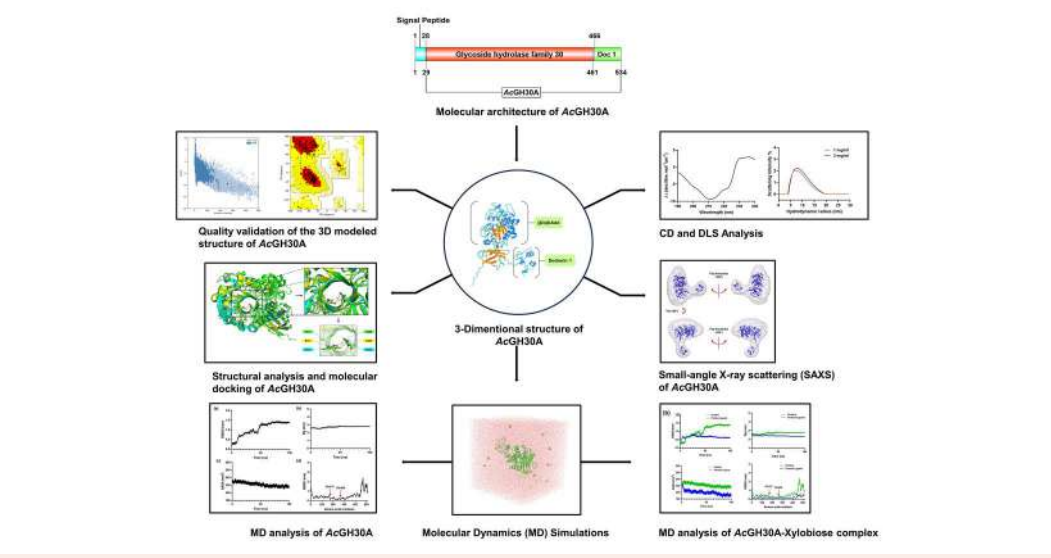

Abbreviations: GH: Glycoside hydrolases; *Ac*: *Acetivibrio clariflavus*; CD: Circular Dichroism; SAXS: Small angle X-ray scattering; DLS: Dynamic light scattering; MD: Molecular dynamics; MSA: Multiple sequence alignment.

ARTICLE HISTORY
Received 23 December 2023
Accepted 23 April 2024

KEYWORDS
Xylobiohydrolase; Xylobiose; *Acetivibrio clariflavus*; MD simulation; SAXS

1. Introduction

Xylans are the second most abundant polymer present in the plant kingdom. They are the primary component of the hemicellulose present in plants (Fonseca-Maldonado et al., 2014; He et al., 2014). Structurally, they are heteropolysaccharides in which the backbone is composed of xylose

CONTACT Arun Goyal arungoyl@iitg.ac.in Carbohydrate Enzyme Biotechnology Laboratory, Department of Biosciences and Bioengineering, Indian Institute of Technology Guwahati, Guwahati, Assam, India.

monomers linked by β-1,4-glycosidic linkages (Curry et al., 2023). The main chain is decorated with a diverse group of side-chain moieties, *viz*., glucuronic acid, arabinose, *p*-coumaric acid and ferulic acid (Thakur et al., 2019). Xylans are structurally very diverse and their structures differ based on the species, the specific part and the age of the plant. Xylans hold great potential to be used for various industrial purposes as a renewable source of energy and chemicals. To harness the energy and chemicals from xylan, they are required to be broken down into simpler forms, *viz*. oligosaccharides and monosaccharides. The degradation process of xylans is complex and its degradation can be achieved by physical processes like pyrolysis or enzymatic hydrolysis using xylanases. The enzymatic breakdown of xylan requires a combined and systematic action of several xylanolytic and auxiliary enzymes. These auxiliary enzymes are acetyl xylan esterase, α-arabinofuranosidase, feruloyl esterase, xylan methylesterase and β-glucuronidase (Moreira & Filho, 2016). The enzymatic degradation process is preferable owing to its environment-friendly nature (Juturu & Wu, 2012).

Glycoside hydrolases (GH) constitute a large category of enzymes responsible for catalyzing the hydrolytic cleavage of glycosidic linkages present in complex carbohydrates (Henrissat & Davies, 1997; Vuong & Wilson, 2010). Xylanases are a class of enzymes comprising β-(1→4)-endo xylanase, β-(1→4)-xylobiohydrolase and β-(1→4)-xylosidase which are involved in complete breakdown of xylan into xylose monomers (Collins et al., 2005). Xylanases specifically target xylan, recognizing the β-1,4-glycosidic bonds between the xylose units in the xylan polymer. β-(1→4)-Endo xylanase hydrolyses xylan into xylooligosaccharides (XOS), which are short chains of xylose units linked by β-1,4-glycosidic bonds (El Enshasy et al., 2016). β-(1→4)-Xylobiohydrolase acts on xylan polysaccharides or XOS and releases xylobiose units (Kadowaki et al., 2021; Katsimpouras et al., 2019). β-(1→4)-Xylosidase utilizes xylan, XOS or xylobiose as substrates cleaving the xylose units from the non-reducing end (Rohman et al., 2019). β-Xylanase and β-xylosidase from various glycoside hydrolase families have been reported, while xylobiohydrolase has been reported from only the GH30 family (Puchart et al., 2021; Šuchová et al., 2021). The catalytic mechanism of xylobiohydrolase involves the nucleophilic attack of a catalytic residue (usually a glutamate or aspartate) on the glycosidic bond, leading to its cleavage (Puchart et al., 2021; Šuchová et al., 2021). The GH30 family contains xylanases primarily targeting glucuronoxylan. The family GH30 exclusively included xylobiohydrolases, which are exo-acting enzymes, releasing xylobiose units from the non-reducing ends of xylan chains or XOS (Puchart et al., 2021).

The documented enzymes exhibiting xylobiohydrolase activity till date have been only from fungal origin. Two glucuronoxylanases from GH30 family, *Tc*Xyn30B (Nakamichi et al., 2020) and *Tt*Xyn30A (Nikolaivits et al., 2021) from *Talaromyces cellulolyticus* and *Thermothelomyces thermophila*, respectively have been found to release xylobiose from the non-reducing end of xylan substrates, along with their endoxylanase activity. However, both displayed different levels of endoxylanase activities. In the case of *Tc*Xyn30B, the xylobiohydrolase activity was more significant than its endoglucuronoxylanase activity, whereas *Tt*Xyn30A exhibits both modes of action at approximately equal levels. Recently, another similar glucuronoxylanase, *Sl*Xyn30A, from yeast *Sugiyamaella lignohabitans* displaying xylobiohydrolase activity was reported (Šuchová et al., 2022). The most stringent xylobiohydrolase, *Aa*Xyn30A, was reported from a cellulolytic fungus *Acremonium alcalophilum* (Šuchová et al., 2020). Numerous glycoside hydrolases from clan A of the GH30 family following the retaining-type of reaction mechanism share a common structural feature. They contain TIM barrel as a standard structural feature with a pair of aspartic or glutamic acid residues in the catalytic cleft primarily formed by β-α loops, participating in the catalysis (Henrissat et al., 1995; Puchart et al., 2021).

Acetivibrio clariflavus is a thermophilic, anaerobic, gram-positive, spore-forming bacterium. The whole genome of *C. clariflavum* has been sequenced and several enzymes produced by it have been characterized. Exploring new and novel enzymes from this microorganism may help current methodologies by improving the efficacy of lignocellulosic materials breakdown. Out of various candidate organisms for thermophilic consolidated bioprocessing (Chen et al., 2018; Gao et al., 2020), *Acetivibrio clariflavus* has attained little attention as compared with the model cellulolytic thermophile *Clostridium thermocellum*, which has been extensively studied in the last decade (St John et al., 2014). A gene encoding a family GH30 enzyme from *Acetivibrio clariflavus* was identified and designated as *Ac*GH30A. *Ac*GH30A is a xylobiohydrolase of family 30 of glycoside hydrolases belonging to the cellulosomal complex from *Acetivibrio clariflavus*. The gene encoding *Ac*GH30A containing a GH30 family catalytic module and a dockerin 1 was cloned, expressed, purified and biochemically characterized earlier (Singh et al., 2024).

In the current study, the structure and functional characteristics of xylobiohydrolase, *Ac*GH30A, were explored by *in silico* and small-angle x-ray scattering (SAXS) approaches. The molecular structure of *Ac*GH30A using its amino acid sequence by homology modeling was generated and validated. Molecular dynamics (MD) simulation of the *Ac*GH30A model was conducted to evaluate the stability and structural characteristics. Molecular docking studies with ligands were performed to assess the catalytic mechanism and the amino acid residues involved in ligand binding. The docked complex of *Ac*GH30A with the ligand was analyzed by MD simulation to detect the structural changes after the ligand binding. The solution structure characteristics of *Ac*GH30A were investigated by small angle X-ray scattering (SAXS) and dynamic light scattering (DLS). During the present study of the enzyme *Ac*GH30A, John et al. (St John et al., 2022) reported the crystal structure of the catalytic module (named as *Ac*Xbh30A) of the full-length xylobiohydrolase, *Ac*GH30A. While there are certain similarities in the results, our report provides more valuable information regarding the solution structure characteristics of the full-length xylobiohydrolase, *Ac*GH30A, containing additional Dockerin 1 domain at C-terminal. The structure analyses of *Ac*GH30A by

computational methods also provided a detailed understanding of ligand binding and perfect matching of modeled structure with its solution structure by SAXS.

2. Methodology

2.1. Analysis of the amino acid sequence of AcGH30A

The amino acid sequence of a xylobiohydrolase belonging to family 30 glycoside hydrolase here named *Ac*GH30A (514 aa) from bacterium *Acetivibrio clariflavus* ATCC 19732 (Uniprot id: G8LU16), was obtained from NCBI database (https://www.ncbi.nlm.nih.gov/protein/AEV68404.1). The locus tag and GenBank accession number are Clocl_1795 and AEV68404.1. The physicochemical parameters of *Ac*GH30A, such as theoretical molecular weight and isoelectric point, were calculated by the protparam server (https://web.expasy.org/protparam/) (Gasteiger et al., 2005). The identification of the sequences responsible for the constituent domains of *Ac*GH30A was accomplished by entering the sequence in the conserved domain database (http://www.ncbi.nlm.nih.gov/cdd/) provided by National Center for Biotechnology Information and also using the Interproscan (http://www.ebi.ac.uk/interpro/) server (Jones et al., 2014). The *Ac*GH30A amino acid sequence was checked for the signal peptide sequences by using the PSignal (http://www.cbs.dtu.dk/services/SignalP-3.0) server. The domains present in *Ac*GH30A sequence were outlined and illustrated using DOG 2.0 software (Ren et al., 2009). To compare and obtain the similarity index with the homologous proteins, the PSI-BLAST program was performed using the amino acid sequence of *Ac*GH30A against the PDB database. Multiple sequence alignment (MSA) of *Ac*GH30A was performed with homologous protein sequences with reported structures, obtained after PSI-BLAST, to examine its conserved sequences, semi-conserved and catalytic amino acid residues. The amino acid sequences of *Ac*GH30A homologs were obtained from the Uniprot database (http://www.uniprot.org) and incorporated into MSA analysis. The alignment was performed using the Clustal Omega tool (http://www.ebi.ac.uk/Tools/msa/clustalo/) (Madeira et al., 2022) offered by EMBL-EBI services. The results of the alignment of the sequences were visualized by ESPript 3.0 (http://espript.ibcp.fr/ESPript/ESPript/) (Robert & Gouet, 2014).

2.2. Artificial intelligence-based homology modelling of AcGH30A

The *in silico* 3-dimensional model of *Ac*GH30A was constructed by using the amino acid sequence (with His-tag at N-terminal) in Alphafold2 Google Colab platform (https://colab.research.google.com/github/sokrypton/ColabFold/blob/main/AlphaFold2.ipyn), also known as ColabFold (Mirdita et al., 2022). AlphaFold2 is an artificial intelligence-based deep learning algorithm developed by DeepMind technologies (Jumper et al., 2021). ColabFold utilizes MMseqs2 (Many-against-Many sequence searching) homology search along with AlphaFold2 for fast structure prediction. ColabFold is comprised of three major parts. First is the MMseqs2-based homology search server to prepare MSAs and acquire the suitable template sequences. The second part is a Python library linked with the MMseqs2 server to prepare data for structural inference and visualization. The third part is the Jupyter Notebooks for accessing and using the Python library. The topology of secondary structural elements of the *Ac*GH30A model was obtained by using the PDBSum server (http://www.ebi.ac.uk/thornton-srv/databases/pdbsum/Generate.html) (Laskowski et al., 2018). The CASTp 3.0 server (http://sts.bioe.uic.edu/castp/calculation.html) was utilized to determine the potential ligand-binding sites of *Ac*GH30A and the accessibility of these sites to solvent molecules, including the area with a default probe radius of 1.4 Å (Tian et al., 2018).

2.3. Computational quality evaluation and validation of the modelled structure of AcGH30A

The 3D structure model generated from Alphafold2 was relaxed and energy minimized by submitting it to Yasara energy minimization server (http://www.yasara.org/minimizationserver.htm). Energy minimization by Yasara server optimizes the atomic positions and relieves steric clashes within the model (Land & Humble, 2018). The quality of the energy-minimized 3D model generated from Alphafold2 was analyzed and verified by submitting the structure to SAVES v6.0 (https://saves.mbi.ucla.edu/) validation server for calculating multiple structural parameters such as ERRAT and Verify3D score (Lüthy et al., 1992). The structural accuracy of the 3D structure model of *Ac*GH30A was evaluated by generating a Ramachandran plot using the Procheck server (MacArthur et al., 1994). The statistical Z-score of the 3D modeled structure, a statistical metric that evaluates the correspondence between the energy of a provided structure and that of experimental structures (PDB and NMR), was computed and graphically represented through ProSA server (https://prosa.services.came.sbg.ac.at/prosa.php) to detect the erroneous structural elements (Wiederstein & Sippl, 2007).

2.4. Determination of secondary structure elements of AcGH30A

The quantitative prediction of the secondary structural components of *Ac*GH30A was conducted by using various web-based services, namely Psipred (http://bioinf.cs.ucl.ac.uk/psipred/) (McGuffin et al., 2000), SOPMA (https://npsa-prabi.ibcp.fr/NPSA/npsa_sopma.html) (Geourjon & Deléage, 1995) and 2Struc (http://2struc.cryst.bbk.ac.uk/twostruc) (Klose et al., 2010). The relative amount of distinct secondary structure elements in *Ac*GH30A was examined by using circular dichroism (CD). Purified *Ac*GH30A at a concentration of 0.5 mg/ml in a 50 mM sodium phosphate buffer at pH 7.0 was utilized for CD analysis. The CD spectrum of *Ac*GH30A within the far-UV region (190-240 nm) was recorded using a spectropolarimeter (JASCO J-815, Jasco Corporation). CD data were obtained with the sample temperature set at 25 °C, with a scanning rate of 50 nm/min and a spectral range of 1 nm. Molar residual weight (g/mol), millidegrees, and

protein concentration (g/L) were used to calculate the molar residual ellipticity (MRE,10^3.deg.cm^{2}dmol^{-1}). To depict as a function of wavelength, the molar residual ellipticity (MRE,10^3.deg.cm^{2}dmol^{-1}) was transformed into the molar extinction coefficient ($\Delta\varepsilon$, decilitre mol^{-1}cm^{-1}). The range of $\Delta\varepsilon$ values spanning from 190 nm to 240 nm was submitted to K2D3 server (http://cbdm-01.zdv.uni-mainz.de/~andrade/k2d3/) for the quantification of α-helix and β-sheets proportions (Louis-Jeune et al., 2012). The resulting mean residue ellipticity was plotted as a function of wavelength. The resulting data on secondary structure elements from both the circular dichroism (CD) analysis and web-based servers were compared.

2.5. Molecular dynamics simulation of AcGH30A modelled structure

MD simulation of the modelled structure of *Ac*GH30A was executed by using GROMACS v5.1.4 software (Berendsen et al., 1995) with Gromos53a6 force field. The simulation was performed on the High-Performance Computing facility (Param-Ishan) situated at the Indian Institute of Technology Guwahati, India. The pdb2gmx command line was used to generate a GROMACS topology file. A single point charge (SPC) simulation box with 46,968 solvent molecules and 15 Cl^- counter ions was prepared for the simulation. The Cl^- ions were added to neutralize the charge present over the 3D model of *Ac*GH30A generated by Alphafold. The energy of the protein simulation system was minimized using gmx_mpi grompp to remove steric clashes. The system was equilibrated by executing position-restrained (NVT) and pressure-restrained (NPT) runs to relax the system gradually. Each equilibration step was conducted for 500 ps with iteration time of 2 fs (Hess et al., 2008). The final protein-solvent system was employed for the final molecular dynamics (MD) simulation, spanning 100 ns with an iteration period of 2 fs. The Root Mean Square Deviation (RMSD) and Root Mean Square Fluctuation (RMSF) of amino acid residues were analyzed as functions of time to assess variations in the protein backbone during the simulation. The radius of gyration (R_g) and solvent accessible surface area (SASA) was computed to obtain insights of the overall shape and surface characteristics of *Ac*GH30A.

2.6. Protein–ligand interaction study of AcGH30A by molecular docking and isothermal titration calorimetry

Molecular docking simulation of *Ac*GH30A was performed with appropriate ligands to determine the catalytically participating amino acid residues by evaluating the interactions with the ligands. Autodock 4.2.1 (Morris et al., 2009), a software package provided with MGLTools 1.5.6 (http://mgltools.scripps.edu/) was utilized for the study. The ligands used were glucuronic acid, xylobiose, xylotriose, xylotetraose and 2^2-(4-O-Methyl-α-D-Glucuronyl)-xylobiose. The ligands were obtained in 3D SDF format from the PubChem database (https://pubchem.ncbi.nlm.nih.gov) and converted into PDB format by using OpenBabel 2.3.2a software (O'Boyle et al., 2011). The docking procedure performed was as previously reported (Ahmed et al., 2022). The dimensions of the grid box surrounding the active-site were set to 34, 36 and 48 Å for the x, y, and z axes, respectively. The spacing between the sites was 0.375 Å. The coordinates for the center grid box were established at 7.028 (x), 14.306 (y), and −8.472 Å (z). Fifty iterations of the Lamarckian Genetic Algorithm were performed to acquire 50 distinct conformations for each ligand. The Gibbs free energy (ΔG), also referred to as binding free energy, corresponding to different ligands-*Ac*GH30A molecular docking, was obtained and analyzed. ΔG represents the change in Gibbs free energy associated with the binding of a ligand molecule to a receptor or protein target (Morris et al., 2009). A more negative ΔG value indicates a stronger binding affinity between the ligand and the receptor, suggesting a more stable complex formation. The ligand-protein conformation with the lowest ΔG (binding free energy) was selected to generate the protein and ligand complex for subsequent investigations. The 2D schematic diagram of the docked complexes between the protein and ligand was visualized using Ligplot + software (Laskowski & Swindells, 2011) to analyze the polar and non-polar interactions.

The binding affinity of *Ac*GH30A with the best ligand, xylobiose, was experimentally assessed using isothermal titration calorimetry (MicroCal ITC, Malvern Panalytical Pvt. Ltd., UK). The concentration of protein and ligand was 1 mg/mL (0.0173 mM) and 0.025 mg/mL (0.09 mM), respectively. The titrations were executed at 30 °C. The enzyme *Ac*GH30A and the ligand were dissolved in sodium phosphate buffer (50 mM, pH 7.0). During titration, *Ac*GH30A solution in the reaction cell was continuously stirred at 300 rev/min. The titration was carried out with 25 successive injections of 1.5 µl ligand at 150 s intervals. The results were analyzed by non-linear regression using a single-site binding model using the system-integrated software Microcal ORIGIN, version 5.0. The association (K_a) and dissociation (K_d) constants were calculated from the fitted data.

2.7. MD Simulation of AcGH30A-ligand complex

MD simulation was performed to study the interactions between *Ac*GH30A and the ligand using GROMACS v5.14 software with GROMOS96 43A1 force field to calculate the protein forces. The docked complex of *Ac*GH30A with the xylobiose was chosen for the simulation due to their least binding energy of −4.3 kcal/mol. The ligand topology for the xylobiose was prepared by using PRODRG server (Schüttelkopf & van Aalten, 2004). An SPC cubic simulation box was created with 31,044 solvent (water) molecules and the protein-ligand complex. The charge neutralization of the docked complex of *Ac*GH30A-xylobiose was achieved by further adding 15 Cl^- counter ions. The energy of the protein-ligand simulation system was minimized using gmx_mpi grompp to remove steric clashes. The system was equilibrated by executing position-restrained (NVT) and pressure-restrained (NPT), followed by the execution of final molecular

dynamics (MD) simulation for 100 ns, as mentioned in section 2.5. After the simulation, the interactions between the ligand and the catalytic residues at the active-site in the docked complexes were visualized using PyMOL V2.3.3 software (Yuan et al., 2017). Root Mean Square Deviation (RMSD) and Root Mean Square Fluctuation (RMSF) of amino acid residues were analyzed as a time-dependent function to assess variations in the protein backbone during the simulation. The RMSD and RMSF values were computed using the commands gmx_mpi rmsd and gmx_mpi rmsf, respectively. The radius of gyration (R_g) and solvent accessible surface area (SASA) were computed by using gmx_mpi sasa and gmx_mpi gyrate commands, respectively. The simulation outcomes of the complex were compared with the results derived from simulation studies of ligand-free *Ac*GH30A. The 2D depiction illustrating the interaction between the protein and ligand was generated using Ligplot + software (Laskowski & Swindells, 2011).

2.8. Small angle X-ray scattering analysis of AcGH30A

The DNA sequence encoding *Ac*GH30A consisting of a GH30 family catalytic module (433 aa) and a dockerin 1 (68 aa), including the linker sequence of 5 amino acids between the modules, was cloned, expressed and purified (Singh et al., 2024). The low-resolution scattering data for *Ac*GH30A at a concentration of 3 mg/ml were obtained utilizing a small-angle X-ray scattering system (SAXSpace, Anton Paar) to investigate the molecular shape and conformational behaviour of *Ac*GH30A in solution. Before the collection of SAXS data, the *Ac*GH30A samples and the corresponding buffer were centrifuged at 22,000 × g for 45 min at 4 °C. The incident X-rays were generated using a line collimation system and were directed through the sample, contained within a thermostated 1 mm diameter quartz capillary. The source of X-rays in the SAXSpace machine was a Primux 3000 sealed tube (Anton Paar, Austria) with copper (Cu) as the anode, emitting the incident radiation of fixed wavelength of 1.5 Å. The scattering of x-rays at small angles (0.1° to 10°) from protein at a temperature of 10 °C was recorded from two separate exposures, each lasting 30 min. The scattering pattern of the matched buffer (50 mM sodium phosphate, pH 7.0) was also recorded and subtracted from the *Ac*GH30A sample and the absolute scattering pattern of only the protein was obtained.

To generate the SAXS profile originating from the protein molecules in the solution, SAXS Quant software was employed to subtract the buffer contribution, resulting in the scattering intensity (I) as a function of the momentum-transfer vector (q) (where $q = 4\pi\sin\theta/\lambda$, with q = scattering vector, λ = wavelength, and 2θ = scattering angle) (Roblin et al., 2013). The processing of data, normalization to an absolute scale, and averaging procedures were carried out using the ATSAS package. The initial data processing was conducted using PRIMUS software. The radius of gyration (R_g) was determined by the Guinier equation and the indirect Fourier transform method with the GNOM package. The distance distribution function, p(r), was also computed using GNOM, and the maximum diameter, D_{max}, was derived. The persistence length (L) of *Ac*GH30A was determined through the formula $[\sqrt{12}\{(R_g^2) - (R_c^2)\}]$ (Balasubramaniam et al., 2020). The molecular weight of *Ac*GH30A was determined from the scattering pattern using the Qp package. The *ab initio* method was utilized to produce the low-resolution shapes of *Ac*GH30A from the scattering curve generated by DAMMIF. The reconstruction of dummy structural models for *Ac*GH30A was executed through the implementation of 20 independent iterations of DAMMIF. The verification of these 20 models was subsequently conducted using DAMAVER to establish the resultant *ab initio* configuration. The reconstruction of the scattering shape of *Ac*GH30A was achieved through the application of GASBOR, an *ab initio* modeling-based, chain-like ensemble modeling program. The modelled structures of the *Ac*GH30A were visualized by using UCSF Chimera (Pettersen et al., 2004).

2.9. Size distribution analysis of AcGH30A by dynamic light scattering (DLS)

The DLS analysis of *Ac*GH30A was conducted using the Litesizer 500 Particle Analyzer (Anton Paar in Graz, Austria) to determine the hydrodynamic diameter (D_h) of *Ac*GH30A at concentrations of 1 and 3 mg/mL. The DLS of *Ac*GH30A was also performed in the presence of xylobiose (X2) procured from Tokyo Chemical Industry Co., Ltd., Japan, to observe its effect on the D_h of *Ac*GH30A. Two separate mixtures were prepared by dissolving *Ac*GH30A with different final concentrations of X2, 0.0173 and 0.0346 mM. *Ac*GH30A without xylobiose was used as a control. The final concentration of *Ac*GH30A mixed with xylobiose was kept at 0.0173 mM (1 mg/mL). Protein solutions (1.5 mL) were centrifuged at 13,000 g for 15 min. The resulting supernatant was filtered through a 0.45 µm PVDF filter membrane using a syringe filter before analysis. Measurements were acquired through a 40 mW diode laser with a wavelength of 658 nm, positioned at a backscatter angle of 175°. The experiments were conducted under a constant temperature of 25 °C, regulated by a Peltier-based temperature controller. Particle size analysis was conducted using the Kalliope software.

3. Results and discussion

3.1. Sequence analysis of AcGH30A

The amino acid sequence of xylobiohydrolase, *Ac*GH30A, consists of different modules. Sequence analysis of full-length *Ac*GH30A by the SignalP 3.0 server revealed that it contains a signal peptide of 28 amino acid residues at the N-terminus, suggesting that *Ac*GH30A is an extracellular enzyme and a part of the secretory pathway. The catalytic module of *Ac*GH30A, belonging to the glycoside hydrolase family 30, comprises 454 amino acids, followed by dockerin 1, spanning 58 amino acids at the C-terminal of the sequence. The two modules are linked by a linker sequence of 5 amino acids (Figure 1). The presence of dockerin 1 module indicates the

participation of *Ac*GH30A in the cellulosomal complex of *Acetivibrio clariflavus*.

The BLASTP similarity search revealed identical homologues of *Ca*Xyn30A (PDB ID: 5CXP) from *Clostridium acetobutylicum,* followed by *Cp*Xyn30A (PDB ID: 4FMV) from *Ruminiclostridium papyrosolvens*, *Tt*Xyn30A mutant E188A (PDB ID: 7O0E_A), and *Tt*Xyn30A double mutant EE (PDB ID: 7O0E_AAA) from *Thermothelomyces thermophilus*, XynA (PDB ID: 1NOF) from *Dickeya chrysanthemi*, and Xyn30B (PDB ID: 6IUJ) from *Talaromyces cellulolyticus* (Table 1). *Ca*Xyn30A and *Cp*Xyn30A are two exceptional enzymes among all the reported GH30 enzymes that have been reported to show non-specific endoxylanase activity. Their non-specific mode of action is the result of differences in the configuration of their catalytic clefts. In *Ca*Xyn30A, arginine is replaced by a glycine residue, whereas in *Cp*Xyn30A, it is replaced by tryptophan, making it capable of disintegrating both arabinoxylan and glucuronoxylan (St John et al., 2014, 2018). The high homology of *Ac*GH30A with non-specific xylanases, which does not require the presence of glucuronic acid substitutions for their action, suggests a lack of requirement for the availability of the glucuronic acid moiety for its catalytic activity. The presence of the conserved arginine residue was found to be important for another GH30 glucuronoxylan-specific xylanase A (*St*Xyn30A) isolated from *Streptomyces turgidiscabies* (Maehara et al., 2018). Molecular modelling of *St*Xyn30A suggested Arg296 as a conserved residue. To better understand the mechanism involved in the recognition of glucuronic acid moieties, Arg296 mutants of *St*Xyn30A were prepared and analyzed. The enzymatic activity of the Arg296 mutant against glucuronoxylan was significantly reduced compared to that of the wild-type enzyme (Maehara et al., 2018). The amino acid sequence of *Ac*GH30A also showed high similarity with fungal xylanases. The closest fungal homologues were *Tt*Xyn30A (PDB ID: 7O0E) from *Thermothelomyces thermophila* (Nikolaivits et al., 2021) and Xyn30B (PDB ID: 6IUJ) (Nakamichi et al., 2020) from *Talaromyces cellulolyticus* (Table 1). Both fungal xylanases show bifunctional endo- and exo-xylanase activities.

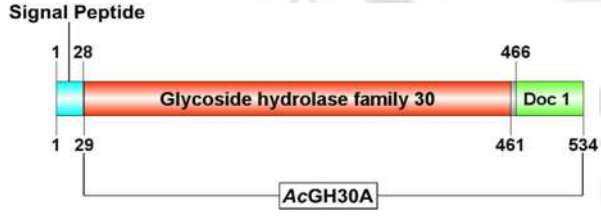

Figure 1. Molecular architecture of full-length *Ac*GH30A amino acid sequence showing the GH family 30 catalytic module (red), flanked by signal peptide (cyan) at the N-terminal and Dockerin 1 module (green) at the C-terminal. Cloned and expressed *Ac*GH30A construct contained catalytic and dockerin 1 module.

The alignment of amino acid sequence of *Ac*GH30A with multiple GH30 xylanases identified Glu175 and Glu268 as the conserved catalytic residues. Glu175 functions as an acid/base, whereas Glu268 serves as a nucleophile (Figure 2). The relative surface accessibility of the amino acid residues was analyzed using ESPript 3.0. The accessibility of the residues is displayed by a bar below the MSA, where blue is accessible, cyan is intermediate and white is buried inside the core (Figure 2). The MSA analysis also revealed the presence of a conserved bacterial arginine residue, Arg349, located on the β13 strand in *Ac*GH30A. A study of the crystal structure of *Ec*Xyn30A (PDB ID: 1NOF), a GH30 glucuronoxylanase from *Erwinia chrysanthemi*, showed that the methyl glucuronic acid interacts with the positively charged guanidium group of Arg293 (Urbániková et al., 2011). The residue, Arg349 of *Ac*GH30A, aligned with Arg293 of *Ec*Xyn30A in MSA analysis. This arginine residue is highly conserved in bacterial GH30 glucuronoxylanases.

3.2. Homology modeling of AcGH30A

Five homology models of *Ac*GH30A were acquired from ColabFold and were ranked between 1-5. The rank 1 model was used in subsequent studies. The selected model was visualized in a 3D cartoon and surface view using the USCF Chimera (Figure 3 (a, b)). The per-residue estimate of the confidence of the model was examined using a predicted local distance difference test (pLDDT) plot (Figure 3c). The pLDDT score for the majority of amino acids was above 90, indicating the high confidence and quality of the predicted model. The number of templates utilized for generating the models was assessed by the sequence coverage plot (Figure 3d), which revealed that the prediction of the homology-modelled structures was executed using more than 4000 templates for the majority of the amino acid sequence.

The topology diagram of *Ac*GH30A modelled structure illustrated the number of secondary structural elements (Figure 4a). As per the plot, there were 21 β-strands in total. The central β-barrel within the (β/α)8-fold contained eight parallel β-strands. The catalytic residues Glu175 and Glu298 of *Ac*GH30A, identified through MSA with other homologues, are situated in the catalytic cleft at the entrance of the β-barrel, allowing accessibility to the substrate (Figure 4b). Similar crystal structures were observed for *Tt*Xyn30A (PDB ID: 7O0E) and *Ca*Xyn30A (PDB ID: 5CXP) within the GH30 family

Table 1. Homologous sequences obtained from BLASTP.

Protein name	Organism	Max score	Query cover (%)	E value	% identity	Accession length	Accession ID
*Ca*Xyn30A	*Clostridium acetobutylicum* ATCC 824	198	83	4.00E-58	32.71	390	5CXP_A
*Cp*Xyn30A	*Ruminiclostridium papyrosolvens* DSM 2782	194	83	3.00E-56	32.88	396	4FMV_A
*Tt*Xyn30A *mutant E188A*	*Thermothelomyces thermophilus* ATCC 42464	191	78	2.00E-54	32.27	452	7O0E_A
*Tt*Xyn30A *double mutant EE*	*Thermothelomyces thermophilus* ATCC 42464	189	78	1.00E-53	32.04	482	7NCX_AAA
XynA	*Dickeya chrysanthemi*	168	82	7.00E-47	31.55	383	1NOF_A
Xyn30B	*Talaromyces cellulolyticus* CF-2612	168	83	8.00E-46	29.87	474	6IUJ_A

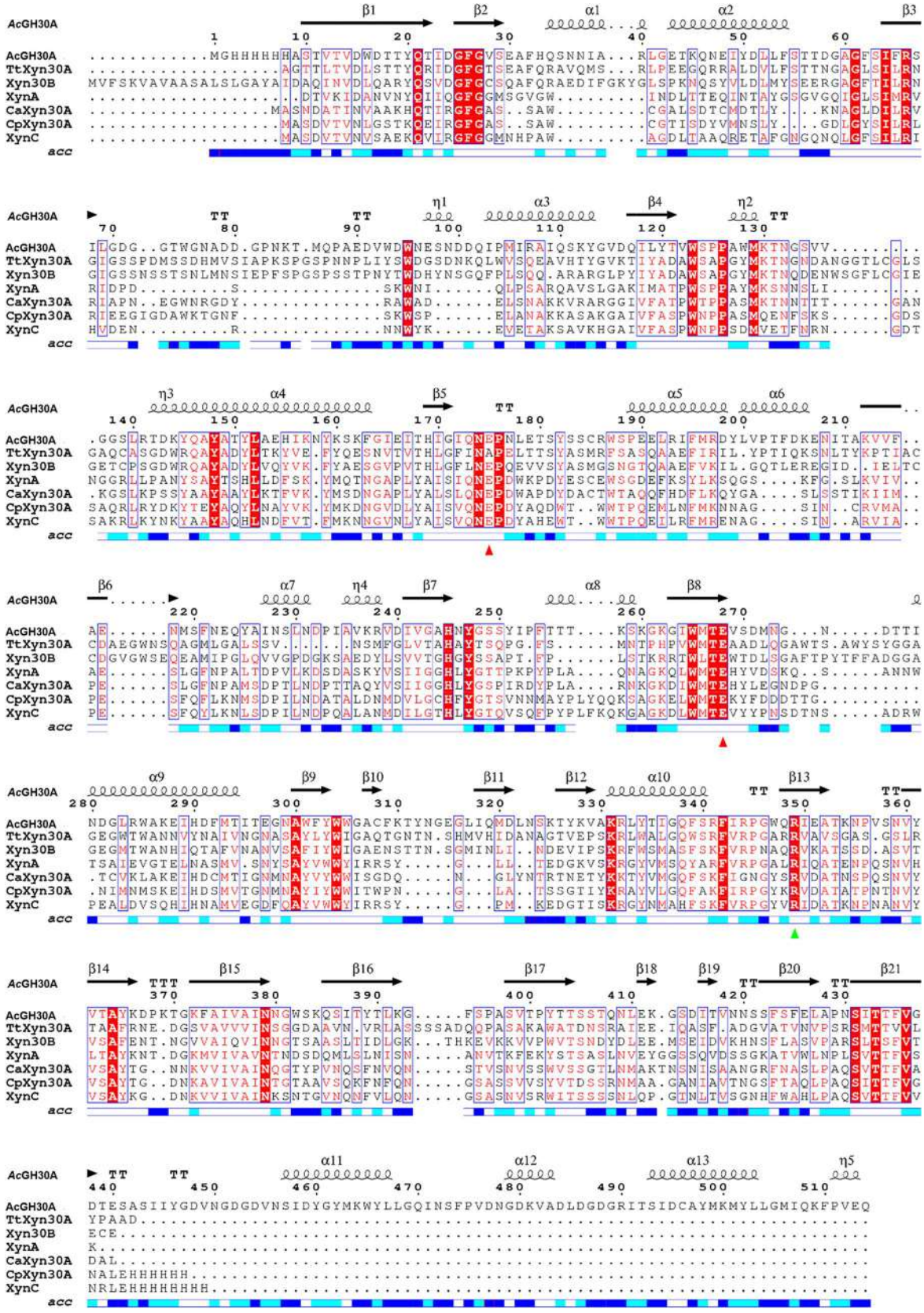

Figure 2. Multiple sequence alignment analysis. Catalytic residues are marked with red triangles and the conserved bacterial arginine residue is marked with green triangles. Accessibility of *Ac*GH30A is rendered by a bar below: blue is accessible, cyan is intermediate and white is buried.

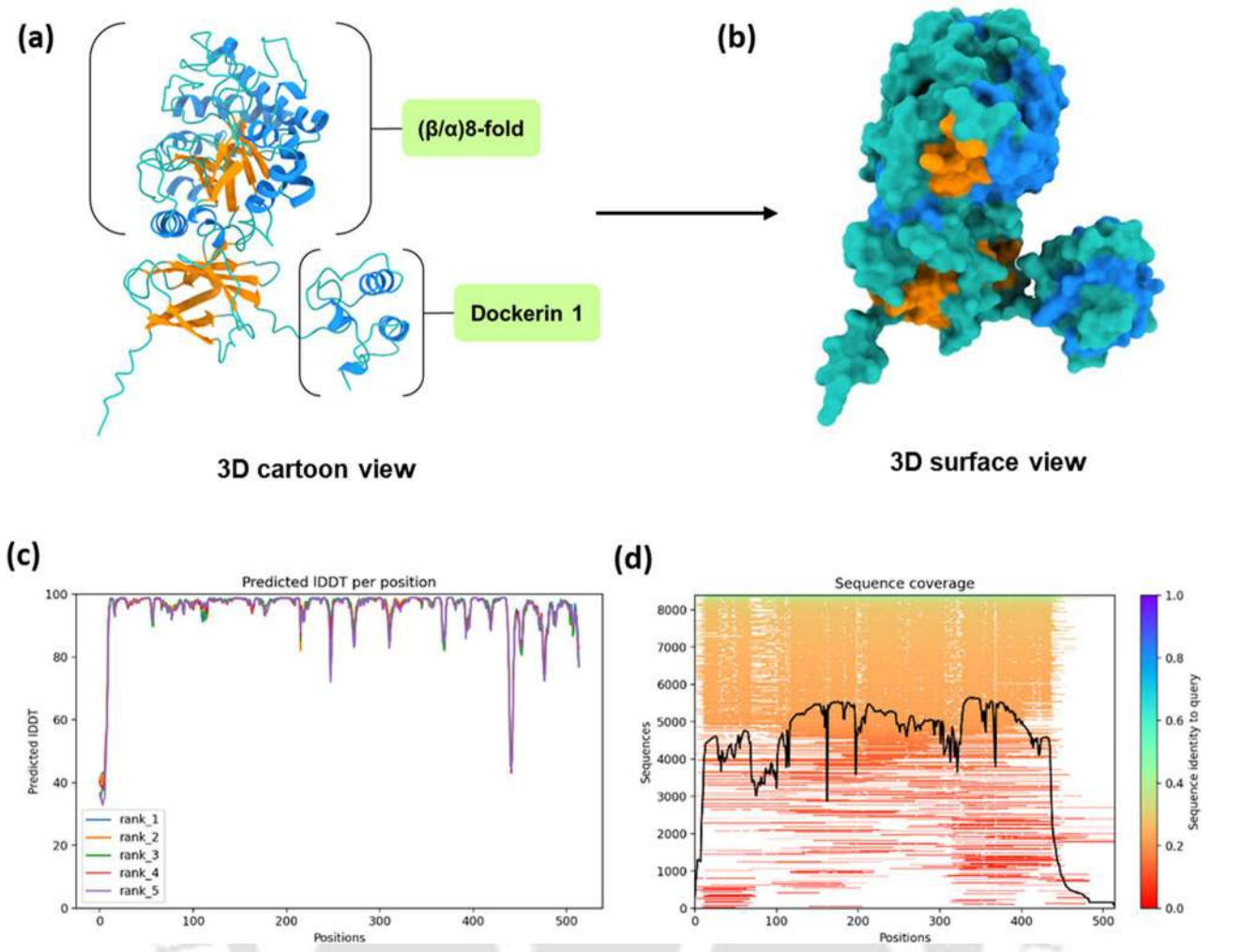

Figure 3. (a) 3-D cartoon and surface view of homology modelled structure of *Ac*GH30A (Blue- Helices, Pine green- Coils and Orange- β strands), (b) 3D surface view of the homology model, (c) pLDDT plot, and (d) Sequence coverage plot.

(Kadowaki et al., 2021; St John et al., 2018). The formation of the catalytic duo is facilitated by loops L6 (red) and β8 (blue), as shown in Figure 4c. L6 contains the nucleophile Glu175, whereas Glu268 is located at β8. Both Glu175 and Glu268 were found in conserved regions. In the modeled structure of *Ac*GH30A, it was observed that L6 and β8 played a role in bringing these two amino acids near the active-site, thereby promoting the creation of the catalytic duo. Figure 4b displays the superposition of the modeled structure of *Ac*GH30A with the crystal structures of *Ca*Xyn30A (PDB ID: 5CXP) and *Cp*Xyn30A (PDB ID: 4FMV). The lengths of *Ac*GH30A, *Ca*Xyn30A and *Cp*Xyn30A used for superposition were 514, 390 and 396 amino acid residues, respectively. The superposition of *Ac*GH30A with *Ca*Xyn30A yielded an RMSD score of 1.179 Å over 387 residues, while the superposition of *Ac*GH30A with *Cp*Xyn30A resulted in an RMSD value of 1.149 Å over 386 residues, indicating excellent alignment. This superposition highlights a consistent alignment of the catalytic residues in the homologues, specifically corresponding to Glu175 and Glu268. The configuration of the catalytic duo in the active-site of *Ac*GH30A and the two other homologues, *Ca*Xyn30A and *Cp*Xyn30A, are shown in Figure 4b. In the modeled structure of *Ac*GH30A, the distances between the catalytic residues were assessed using PyMOL v2.3.3. The minimum distance between Glu175 and Glu268 was 4 Å. Active-site analysis, conducted using the CASTp server, elucidated the features of the ligand-binding site of *Ac*GH30A (Figure 4d). The CASTp-calculated solvent-accessible surface area and volume of the catalytic site and ligand-binding pocket were 112.582 Å^2 and 53.260 Å^3, respectively.

3.3. Quality assessment and validation of the modeled structure of AcGH30A

Ramachandran plot from the Procheck server was used to examine the dihedral angles (Ψ and Φ) of the amino acid residues constituting the backbone of the *Ac*GH30A modeled structure (Figure 5a). The plot revealed that the favoured region has 87.6% residues, the allowed region has 12.4% residues, and there is no amino acid residue present in the disallowed zone. Overall model quality *Ac*GH30A, assessed *via* the ProSA server, showed an error-free model within the X-ray zone, obtaining a Z-score of −9.5 (Figure 5b). The local model quality, examined using ProSA, indicated the accuracy of every component in the modeled structure, with no amino acid residue exhibiting a positive value in the local energy plot (Figure 5c). The quality assessment of *Ac*GH30A *via* the UCLA Saves server showed a successful VERIFY 3D

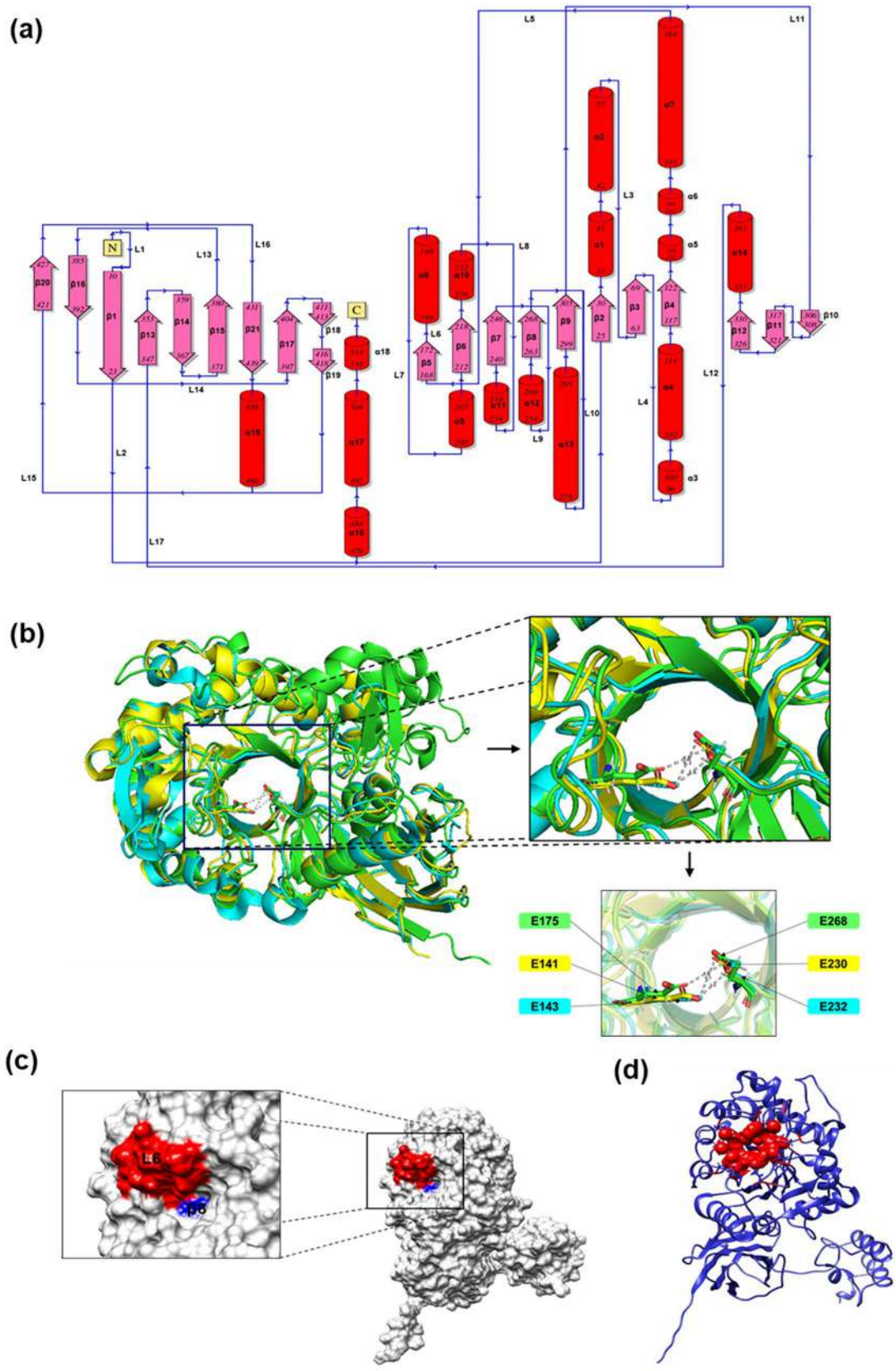

Figure 4. (a) Topology diagram of *Ac*GH30A with N- and C- terminal and secondary structure elements (α-helices, β-sheets and turns), (b) Superposition of *Ac*GH30A modeled structure (Green) with closest homologues *Ca*Xyn30A (Yellow) and *Cp*Xyn30A (Cyan) and catalytic residues in a black square, (c) Surface view of *Ac*GH30A shows loop 6 (L6) in red and β-strand 8 (β8) in blue forming the catalytic duo (in red) (d) Catalytic cleft (red) predicted by CastP server.

test, achieving an average 3D-1D score of ≥0.2 (Figure 5d). The overall quality score of the *Ac*GH30A modelled structure was determined to be 93.6% by the ERRAT server, confirming the high quality of the *Ac*GH30A modelled structure. The model's refinement, as well as the findings of its quality assessment, were satisfactory for further research.

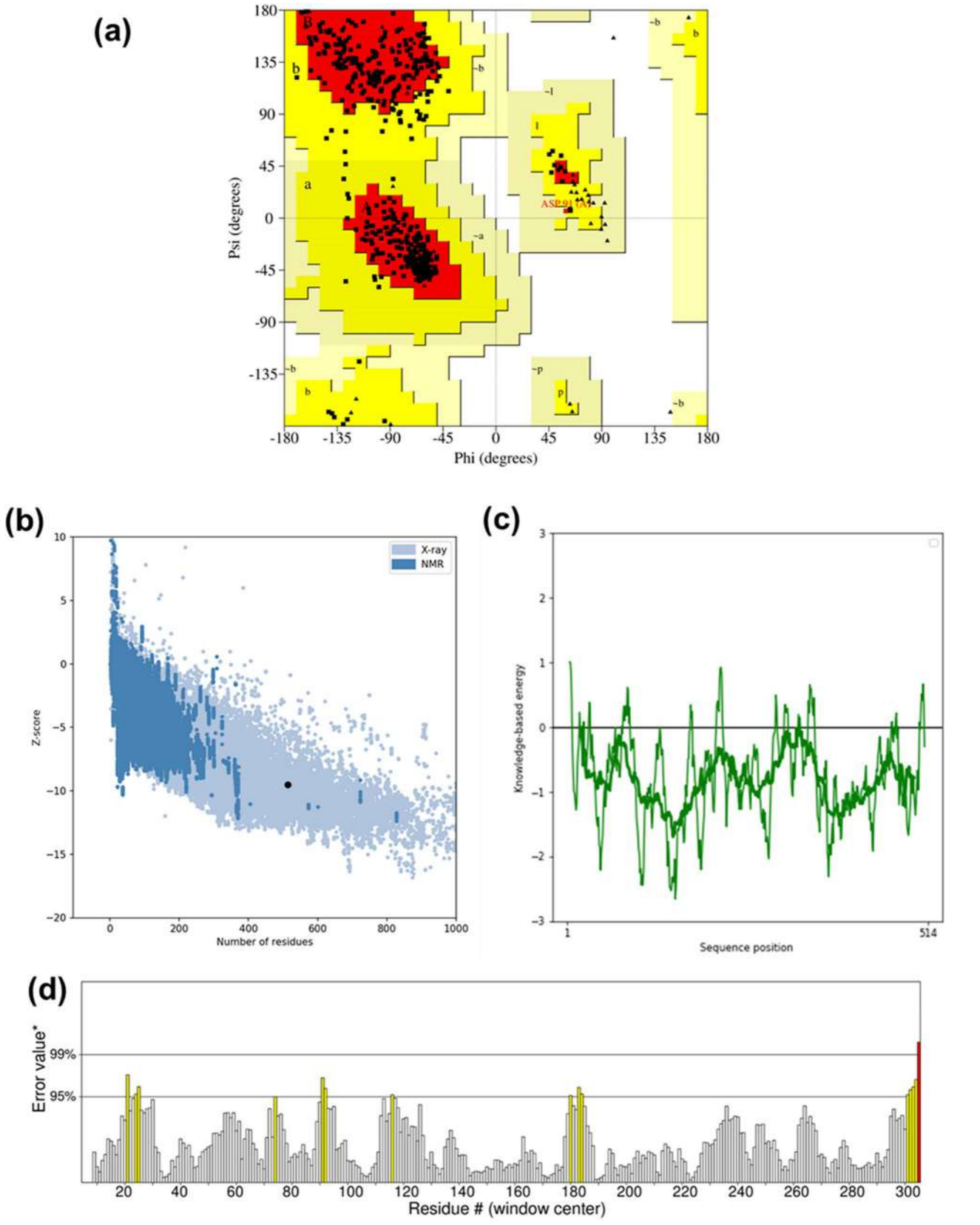

Figure 5. (a) Validation and quality assessment of *Ac*GH30A modeled structure. (b) Ramachandran plot generated by Procheck showing favoured, allowed and model quality, (c) ProSA plot of residue scores, and (d) VERIFY 3D showing the 3D-1D averaged score of the amino acid residues.

3.4. Secondary structure analysis of AcGH30A

PsiPred 4.0, a web-based system, was used to determine the secondary structure elements of *Ac*GH30A from its amino acid sequence. According to the Psipred data, *Ac*GH30A has 23.7% α-helices, 22.9% β-strands and 46.7% random coils. SOPMA and 2Struc servers were also used for determining the composition of secondary structures present in the

*Ac*GH30A. SOPMA predicted the relative proportions of α-helices, β-sheets, and random coils to be 23.93%, 23.93% and 45.91%, respectively, and with 2Struc server, it was 28.2%, 22.8% and 49.0%, respectively (Table 2). The results from the web servers suggested that the majority of *Ac*GH30A residues fold into random coils with a similar composition of α-helices and β-strands. The *in-silico* 3D model of *Ac*GH30A generated by Alphafold2 also showed similar proportions of secondary structures with 23.46% α-helices, 22.17% β-sheets and 54.4% random coils. The CD analysis results for secondary structure prediction, obtained through the K2D3 server, indicated the presence of 21.94% α-helices, 20.98% β-sheets, and 57.08% random coils (Figure 6 and Table 2). These CD findings aligned with the predictions made by web servers for analyzing secondary structure.

Table 2. Secondary structure analysis of *Ac*GH30A.

SERVER/TOOL	α-Helix (%)	β-Strands (%)	Random Coils (%)
Psipred	23.7	22.9	53.4
2struct	28.2	22.8	49.0
SOPMA	23.93	23.93	52.14
Alphafold2	23.46	22.17	54.4
CD	20.98	21.94	57.08

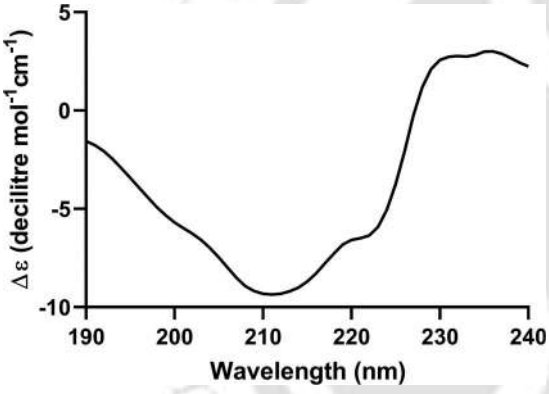

Figure 6. Far UV-CD spectrum of *Ac*GH30A analyzed by K2D3 server.

3.5. MD Simulation of AcGH30A modelled structure

The dynamic behaviour and interactions of atoms and molecules over time, globularity and stability of the *Ac*GH30A modelled structure were investigated by molecular dynamics (MD) simulation for 100 ns. By using values of the root mean square deviation (RMSD), the structural deviation from the original structure was calculated. The RMSD vs time graph (Figure 7a) revealed high fluctuation between 0.01 and 1.31 nm up to 53 ns, then the structure stabilized after 54 ns up to 100 ns, with RMSD between 1.18 and 1.45 nm. The average RMSD of the whole simulation period was found to be 1.04 nm. The radius of gyration (R_g) fluctuated between 2.5 and 2.8 nm, between 1 ns and 49 ns (Figure 7b). From 50 ns onwards, R_g values varied between 2.76 nm to 2.78 nm, showing minimal fluctuations. The R_g became stable after 49 ns till the end of 100 ns, demonstrating the structure's global compactness (Figure 7b). The average R_g was found to be 2.7 nm. The solvent accessible surface area (SASA) of *Ac*GH30A gradually declined from an initial 221.01 nm^2 to 218.21 nm^2 at 100 ns, indicating very little change, giving an average SASA value of 221.98 nm^2 (Figure 7c). The variation in SASA values was minimal, suggesting that there is no hindrance to the catalytic residues due to deformities, and therefore, they remain accessible to the substrate.

Following molecular dynamics (MD) simulation, the Root Mean Square Fluctuations (RMSF) of Cα atoms within amino acid residues were computed to evaluate the displacement of atoms across various regions in the simulated structure. The N- and C-terminals of *Ac*GH30A were identified as highly flexible residues, while residues participating in secondary structures exhibited lower flexibility in contrast to residues

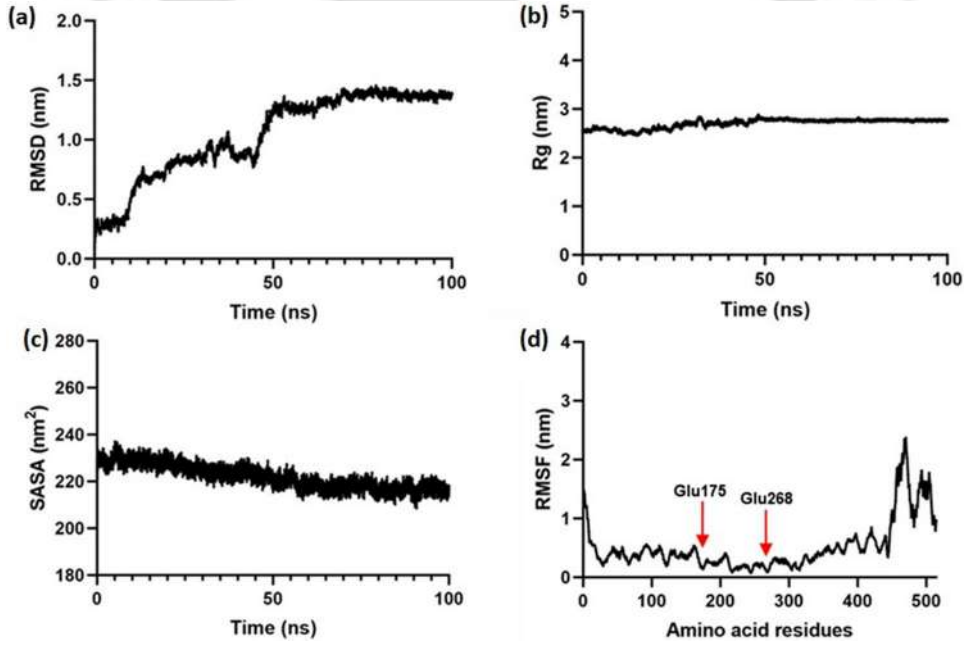

Figure 7. MD simulation analysis of *Ac*GH30A modelled structure after 100 ns simulation. (a) RMSD plot, (b) Radius of gyration (R_g) plot, (c) SASA plot, (d) RMSF plot.

Table 3. Amino acid residues of *Ac*GH30A involved in ligand binding.

Ligand	Binding energy (kcal/mol)	Polar interaction	Hydrophobic interaction
Xylobiose	−4.3	Asn174, Glu175, Glu268	Phe32, Leu178, Tyr182, Met219, Tyr247, Met272, Trp304
Glucuronic acid	−3.06	Thr255, Lys258, Thr296, Glu297	Phe254, Pro253
Xylotriose	−2.36	Glu223, Thr255	Asn222, Ile252, Pro253, Ile295,
Xylotetraose	−1.66	Thr19, Lys258,	Tyr20, Pro253, Thr255, Ser259, Glu297, Thr296,
2^2-(4-O-Methyl-α-D-Glucuronyl)-xylobiose	−0.98	Asn174, Glu175, Tyr182, Glu315	Phe32, Trp123, Leu178, Glu268, Ser270, Trp305, Lys310, Tyr312, Asn313

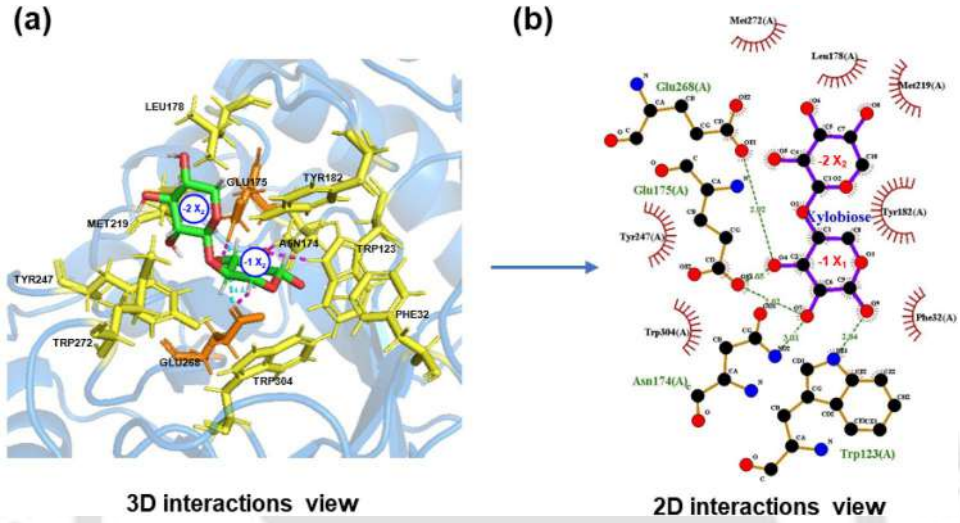

Figure 8. Docking analysis of *Ac*GH30A with the xylobiose showing (a) 3D schematic presentation and (b) 2D schematic presentation of the orientation of active-site residues with xylobiose.

located within the loop region. The catalytic residues Glu175 in L6 and Glu268 in β8 (indicated by the red arrow), exhibited lower flexibility and greater stability compared to the remaining residues in L6 and β8 (Figure 7d). The MD simulation study demonstrated that the modeled structure of *Ac*GH30A is both compact and stable, making it suitable for additional structural investigations.

3.6. Protein–ligand interaction study of AcGH30A by molecular docking and isothermal titration calorimetry

The molecular docking analysis of *Ac*GH30A with different ligands revealed its maximum binding affinity with xylobiose (binding free energy, −4.3 kcal/mol) followed by glucuronic acid (-3.06 kcal/mol), xylotriose (−2.36 kcal/mol) and 2^2-(4-O-Methyl-α-D-Glucuronyl)-xylobiose (-0.98 kcal/mol) as shown in Table 3. The highest binding affinity of *Ac*GH30A for xylobiose indicates the presence of xylobiohydrolase activity. The Ligplot software was utilized to analyze the 2-dimensional interactions between ligands and amino acid residues within the catalytic cleft. In the docked complex, xylobiose was positioned in the catalytic cleft with two subsites, −1 and −2. Figure 8a,b displays the docked complex of *Ac*GH30A with xylobiose, with the amino acid residues involved in the subsites −1 and −2. *Ac*GH30A formed hydrogen bonds with xylobiose, involving Trp123, Glu175, Asn174, and Glu268 (Table 3). Similar amino acids were found to be forming hydrogen bonds with xylobiose in the crystal structure of the catalytic module of *Ac*GH30A (dubbed as *Ac*Xbh30A) (St John et al., 2022). The corresponding amino acid residues in the crystal structure were Trp116, Glu168, Asn167 and Glu261. The catalytic nucleophile Glu268 and the acid/base catalyst Glu175 of *Ac*GH30A were positioned at 2.9 and 2.6 Å, respectively, from −1 xylose (Figure 8b). Moreover, Trp123 and Asn174 were located 2.8 Å and 3 Å away from −1 xylose. The residues, Leu178, Tyr182, Phe32, Met219, Met272, Tyr247 and Trp304 of *Ac*GH30A participated in establishing hydrophobic interactions with xylobiose (Table 3). The −2 subsite was primarily composed of Leu178, Tyr182 and Met219. The conserved bacterial amino acid residue, Arg349 present in the β13 sheet of *Ac*GH30A was distantly located from the catalytic cleft and was not involved in any interaction during molecular docking, suggesting its non-participation in catalysis. This indicated that *Ac*GH30A may not recognize or require the presence of glucuronic acid moiety as happens in glucuronoxylanse, *Ec*Xyn30A for binding and catalysis of the xylan substrate (Urbániková et al., 2011).

The cleavage of glycosidic bonds by glycoside hydrolases follows two different types of mechanisms, *viz.* retaining- and inverting-type (Brüx et al., 2006; Davies & Henrissat, 1995; Okuyama et al., 2009). In the case of retaining-type

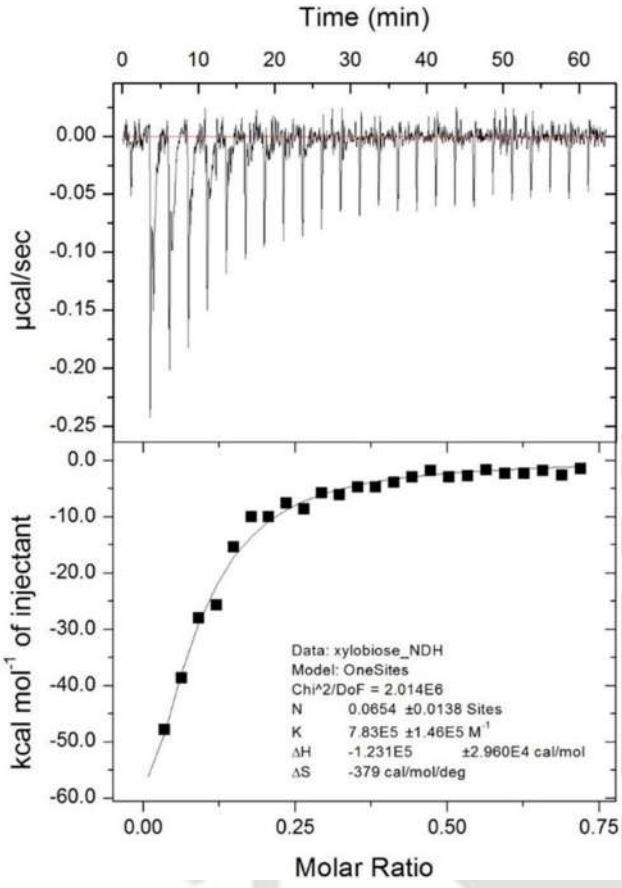

Figure 9. Isothermal titration calorimetry of *Ac*GH30A binding to xylobiose. The concentrations of *Ac*GH30A and xylobiose (ligand) used were 1 mg/mL (0.0173 mM) and 0.025 mg/mL (0.09 mM), respectively. The titrations were performed at 30 °C, involving 25 consecutive injections of 1.5 µl ligand at 150 s intervals.

enzymes, the nucleophilic catalytic residue is in closer proximity to the anomeric carbon of the sugar when compared with the inverting-type enzymes. The average distance between the catalytic duo in the retaining-type enzyme is 5.5 Å, while in the inverting-type it is 10 Å (Davies & Henrissat, 1995; Okuyama et al., 2009). The molecular docking study of the docked complex, *Ac*GH30A-xylobiose, revealed that xylobiose is placed between the catalytic duo, Glu175 and Glu268. The analysis further showed that the distance between these two catalytic residues in *Ac*GH30A was 4 Å, suggesting that it follows the retaining-type mechanism (Figure 8(a, b)).

Isothermal titration calorimetry of *Ac*GH30A was carried out using xylobiose as a ligand since *Ac*GH30A displayed the highest binding affinity with xylobiose during molecular docking. A strong binding between *Ac*GH30A and xylobiose was observed with an association constant (K_a) of 7.83×10^5 M^{-1}, which gave the value of dissociation constant (K_d) of 1.28×10^{-6} M (Figure 9).

3.7. MD Simulation of AcGH30A-ligand complex

The RMSD, R_g, SASA and RMSF of the complex *Ac*GH30A-xylobiose were calculated and analyzed. The comparisons between the molecular dynamic outcomes of the *Ac*GH30A-xylobiose complex and *Ac*GH30A were carried out to assess different parameters, investigating the stability and compactness of the docked complex after undergoing MD simulation. The docked complex displayed an average RMSD value of 0.65 nm after 40 ns, with oscillation within ±0.03 nm until 100 ns. Remarkably, this was 0.39 nm lower than the RMSD

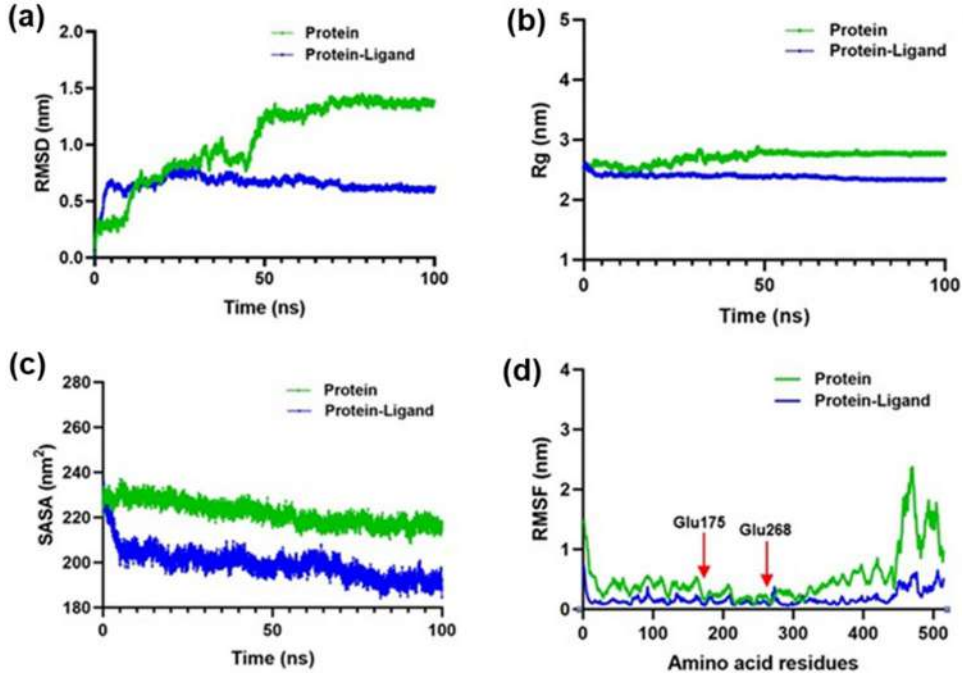

Figure 10. Comparative molecular dynamic simulation analysis of ligand (xylobiose) bound *Ac*GH30A and free *Ac*GH30A showing (a) RMSD plot, (b) Radius of gyration (R_g) plot, (c) SASA plot, (d) RMSF plot.

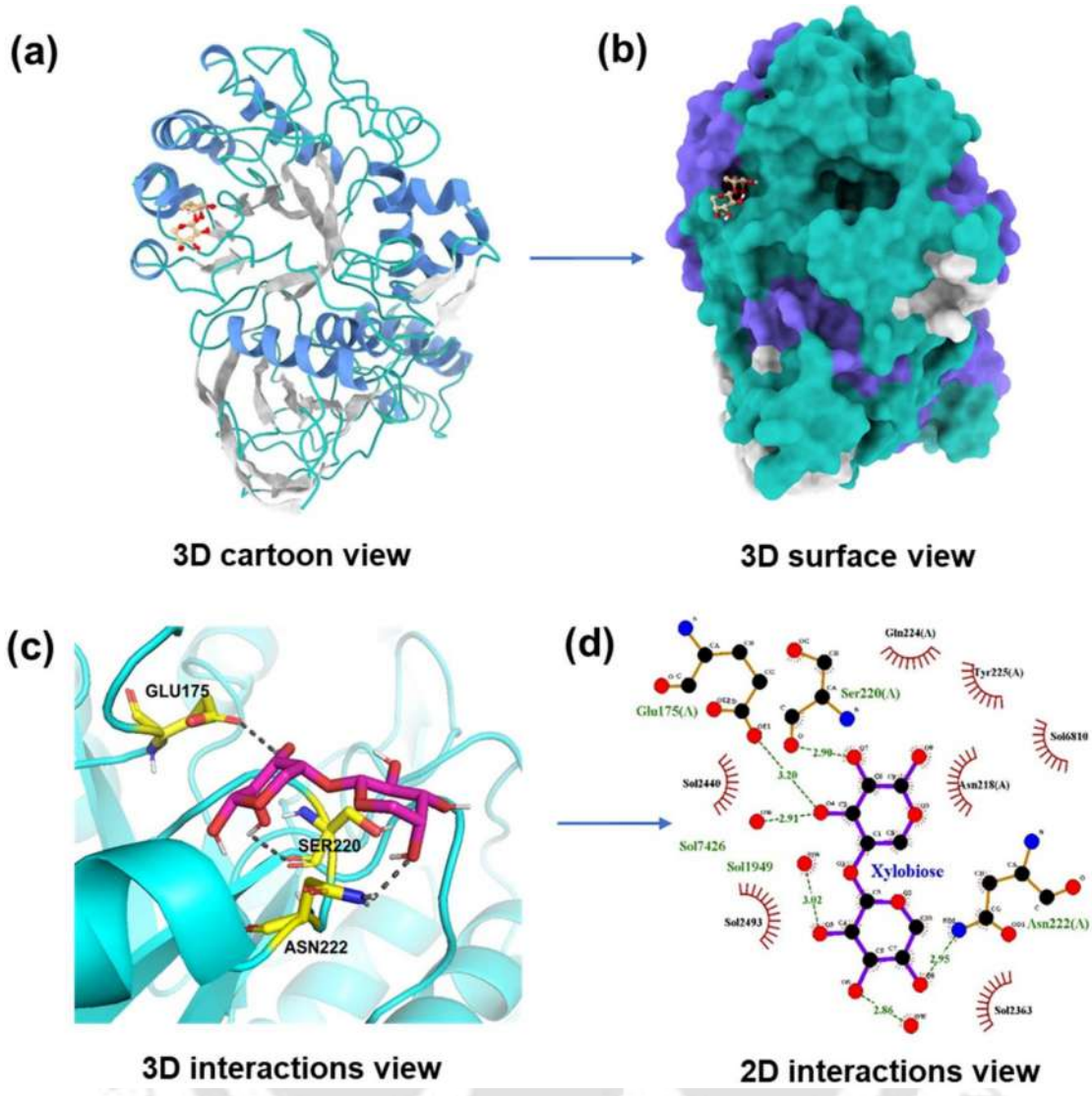

Figure 11. (a) 3D cartoon view of simulated complex structure of *Ac*GH30A with xylobiose, (b) 3D surface view of simulated complex structure of *Ac*GH30A with xylobiose (Blue- Helices, Pine green- Coils and Light grey- β strands), (c) 2D schematic representation of orientation of active-site residues of *Ac*GH30A with Xylobiose after 100 ns of simulation, and (d) 2D schematic representation of interactions between xylobiose and the protein residues.

observed for *Ac*GH30A without the ligand (Figure 10a). The RMSD value in the simulated docked complex reduced dramatically. This resulted from conformational changes induced by the binding of the ligand xylobiose in the active-site of *Ac*GH30A, in contrast to the structure of *Ac*GH30A alone. The consistent RMSD values confirmed the structural equilibrium and stability of the docked complex. Over the 100 ns simulation, the radius of gyration (R_g) for the docked complex maintained a range of 2.31 nm to 2.61 nm, with an average R_g of 2.38 nm (Figure 10b). The R_g of the docked complex was 0.32 nm less than that of *Ac*GH30A alone, suggesting that ligand binding enhanced the overall compactness and rigidity of the complex. The SASA exhibited a gradual decrease throughout the simulation, following a similar pattern to that of *Ac*GH30A over the entire trajectory up to 100 ns (Figure 10c). The average SASA during the whole simulation was found to be 199.41 nm^2, which was lower than the calculated SASA of only *Ac*GH30A by 4.27 nm^2. This suggested that the binding of the ligand to the catalytic cleft of *Ac*GH30A in the docked complex led to a reduction in solvent accessibility. The RMSF plot from the MD simulation of the complex exhibited a similar trend to that of *Ac*GH30A, with the N- and C-terminal residues displaying high flexibility (Figure 10d).

In MD simulation, the *Ac*GH30A-xylobiose docked complex showed lower-level of flexibility as compared to the *Ac*GH30A model. The reduction in flexibility at the N- and C-terminals of the complex indicated an increase in the stability and compactness in the *Ac*GH30A-xylobiose complex as compared with *Ac*GH30A. The RMSF values of the catalytic residues, Glu175 and Glu268, were found to be stable (Figure 10d). These residues exhibited negligible mobility, suggesting their geometric accuracy and capability to adopt productive catalytical conformations. In the final 3D model of the enzyme-ligand complex generated after the completion of the simulation, xylobiose was bound to the catalytic cleft present at the opening of the TIM-motif (Figure 11a, b). After 100 ns, the amino acid

residues, Glu175, Ser220 and Asn222 established hydrogen bonds with the ligand, whereas Gln224, Tyr225, and Asn218 developed hydrophobic contacts with xylobiose in the catalytic cleft (Figure 11c,d). The MD simulation study further showed that Arg349 present in β13 sheet of *Ac*GH30A is far from the catalytic cleft and therefore not involved in any interaction with xylobiose, corroborating its non-participation in catalysis. In the final 3D model of the enzyme-ligand complex generated after the completion of the simulation, the ligand was found to be bound with Glu175 and in close proximity to Glu268. It is evident from the ligand-bound model generated after molecular dynamics simulation for 100 ns that the ligand was stable and bound to the catalytic cleft with high binding affinity.

Table 4. SAXS data collection and derived parameters of *Ac*GH30A at 3.0 mg/ml.

Data-collection parameters	*Ac*GH30A
Instrument	SAXSpace Anton-Paar
Wavelength (Å)	1.54
Q range (nm^{-1})	0.135-5.95
Exposure time (min)	30 × 2
Temperature (°C)	10
Protein Concentration (mg/ml)	3
Structural parameters	
Q range (nm^{-1}) used for R_g analysis	1.6-3.5
I(0) au from Guinier	72349.9 ± 6667.96
R_g nm from Guinier	3.59 ± 0.44
I(0) from P(r)	66530
R_g nm from P(r)	3.6
D_{max} (nm)	10.88
Porod volume estimate (nm^3)	91.9
Persistent length (nm)	11.87
Resolution (nm)	5.0
Molecular mass determination	
Theoretical molecular mass (kDa)	57.79
Molecular mass from Qp (kDa)	58.27
Modelling parameters	
χ^2	0.3123
NSD	0.866 ± 0.087
Software employed	
Data processing	primus
P(r) function calculation	GNOM
Ab initio modeling	DAMMIF
Validation and averaging	DAMAVER
Structure superposition	SUPCOMB
3D graphical representation	UCSF Chimera

3.8. Small angle X-ray scattering analyses of AcGH30A

The recombinant *Ac*GH30A consists of a GH30A family catalytic module (433 aa) and the dockerin 1 (68 aa), including the linker sequence of 5 amino acids between the modules, was cloned, expressed and purified (Singh et al., 2024). The SDS-PAGE analysis showed an estimated molecular mass of 58 kDa (Singh et al., 2024). The experimentally estimated molecular mass of *Ac*GH30A was similar to the theoretical molecular mass of 57.78 kDa calculated by ExPASy ProtParam server along with the theoretical isoelectric pH of 5.22.

The structural conformation of *Ac*GH30A in solution was assessed through SAXS studies. The SAXS data for *Ac*GH30A at a concentration of 3 mg/ml were processed, analyzed and the findings are presented in Table 4. The monodisperse nature of the *Ac*GH30A was confirmed through the visual inspection and initial processing of the *Ac*GH30A scattering profiles (Figure 12a). The examination of the P(R) function obtained through Fourier transformation of the *Ac*GH30A scattering profiles revealed a symmetric profile characteristic of globular macromolecules (Figure 12b), indicating the presence of *Ac*GH30A in its monomeric state. The maximum diameter (D_{max}) and R_g of *Ac*GH30A, calculated from the P(R) plot, were 10.88 and 3.6 nm, respectively. The D_{max} is 3.02 times greater than the R_g, which confirms that the *Ac*GH30A

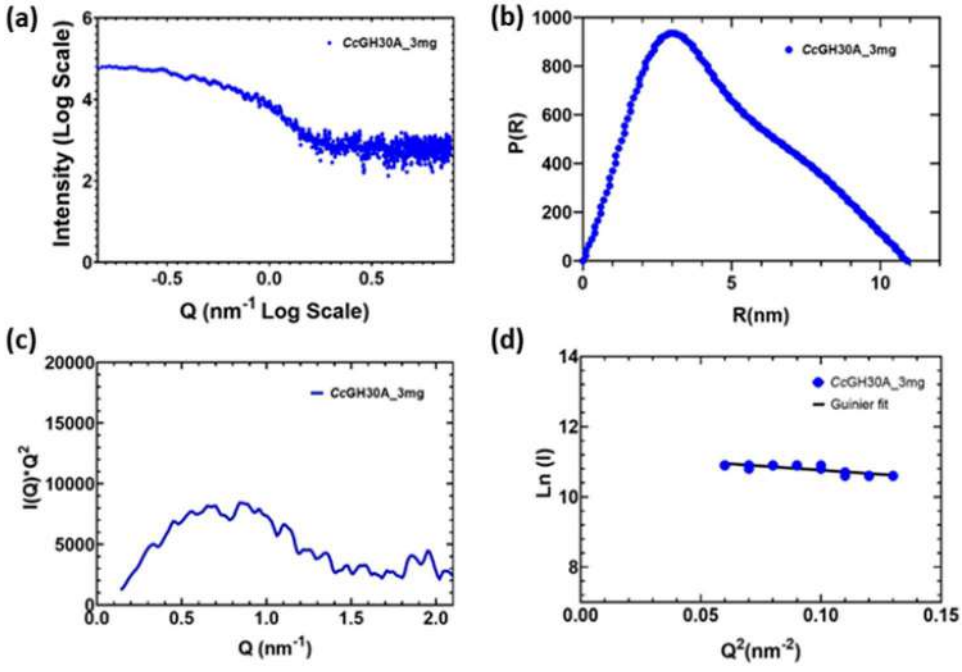

Figure 12. SAXS analysis of *Ac*GH30A. (a) Intensity profile obtained through SAXS, (b) P(R) curve of *Ac*GH30A as a function of R, (c) Kratky plot of SAXS data, and (d) Guinier plot of the SAXS intensities at 3 mg/ml.

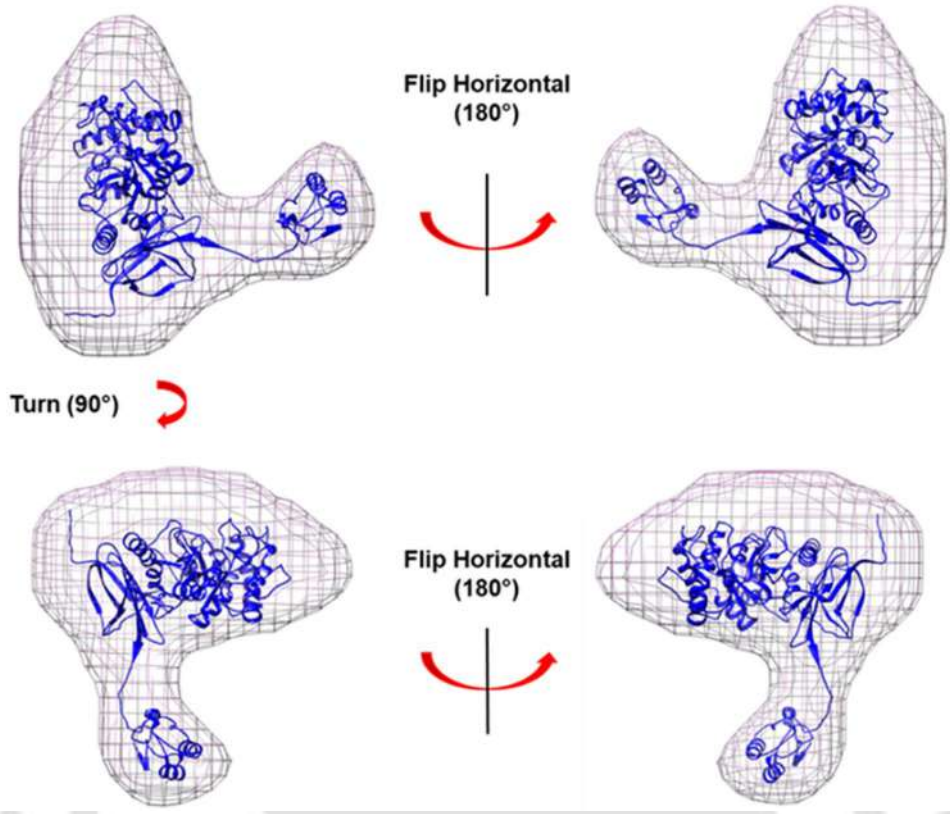

Figure 13. SAXS envelope of *Ac*GH30A at 3 mg/ml protein concentration from different angles. Molecular map of *ab initio* *Ac*GH30A fitted with the structural model of *Ac*GH30A using UCSF Chimera.

is extended and not completely globular. The assessment of the global compactness and flexibility of *Ac*GH30A in solution was conducted through Kratky plot analysis (Figure 12(c)). The Kratky plot analysis of *Ac*GH30A revealed bell-shaped peaks in the low q-region, corroborating a compact and folded structure consistent with previous reports (Ernst et al., 2020). Guinier analysis showed that the R_g of *Ac*GH30A for globular and rod shape was 3.59 ± 0.44 nm and 1.07 ± 0.01 nm, respectively. The persistence length (L) of the *Ac*GH30A molecule was found to be 11.87 nm. The linear behaviour of the fit line in the low q-region of the Guinier plot indicated the absence of aggregation and the monodispersity of *Ac*GH30A (Figure 12d).

The molecular mass of *Ac*GH30A, determined from the SAXS scattering profile using the Qp package, was found to be 58.27 kDa. This value aligns closely with both the theoretically and experimentally determined molecular mass of 57.79 kDa, further indicating the presence of a monomeric state of *Ac*GH30A in the solution. A total of 20 reconstructed models were averaged to develop the most representative *ab initio* model using DAMAVER (Ficko-Blean et al., 2009). The *ab initio* model generated by the DAMAVER program revealed a structure consisting of two globular structures, one significantly larger than the other. The molecular shape of the *ab initio* model showed an earbud-shaped envelope. When the *ab initio* model was overlayed with the 3D model of *Ac*GH30A, it evidently showed that the large globular structure belongs to the catalytic module of the enzyme and the smaller one corresponds to the dockerin 1 module (Figure 13). Both the *ab initio* and 3D models of *Ac*GH30A showed high similarity in terms of globularity and shape.

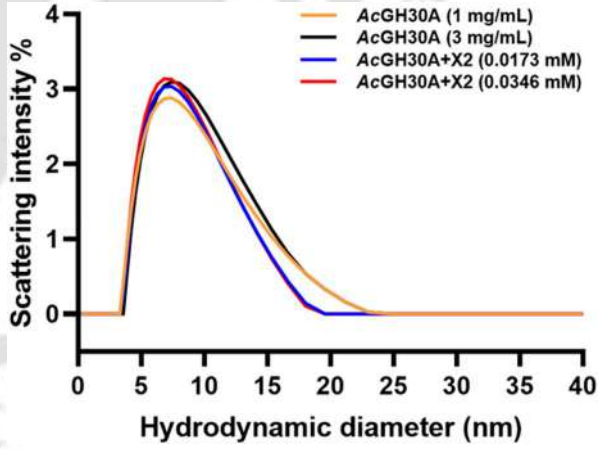

Figure 14. Particle diameter analysis of *Ac*GH30A at different concentrations of 1.0 mg/mL (orange) and 3.0 mg/mL (black) and in the presence of two different concentrations of xylobiose (X2), 0.0173 mM (blue) and 0.0346 mM (red) by DLS. The final concentration of *Ac*GH30A mixed with X2 was 1 mg/mL.

3.9. Dynamic light scattering (DLS) analysis of AcGH30A

DLS examination of particle diameter in relation to scattering intensity (%) for *Ac*GH30A at protein concentrations of 1 and

3 mg/mL and in the presence of xylobiose exhibited singular peaks, signifying the exceptional monodispersity of the protein (Figure 14). The hydrodynamic diameter (D_h) at both 1 and 3 mg/mL concentrations was 7.4 nm, with a hydrodynamic radius (R_h) of 3.7 nm, consistent with the SAXS data. The hydrodynamic radius of the protein is close to the value of R_g, which was determined to be 3.6 nm by SAXS analysis. The addition of xylobiose did not show any change in the D_h of *Ac*GH30A, resulting in a constant R_h of 3.7 nm. However, a slight increase in the scattering intensity of *Ac*GH30A was observed in the presence of xylobiose as compared with *Ac*GH30A only. Moreover, the scattering intensity further increased as the concentration of xylobiose was increased in the mixture.

4. Conclusion

A high-quality homology model of *Ac*GH30A, generated from Alphafold2, demonstrated structural accuracy, supported by Ramachandran plot analysis and secondary structure assessments. Ramachandran plot depicted that the favoured and allowed regions contained 100% amino acids and no residue in the disallowed region. The 3-dimensional model of *Ac*GH30A showed an overall quality score of 93.6% in the ERRAT server analysis. The secondary structure element analysis of *Ac*GH30A by CD revealed 21.94% α-helices, 20.98% β-sheets and 57.08% random coils aligning closely with the results of prediction from Psipred, SOPMA and 2Struc servers. The molecular docking analysis revealed a significant binding affinity of *Ac*GH30A with xylobiose with a binding free energy of −4.3 kcal/mol, validating the xylobiohydrolase activity of *Ac*GH30A. The molecular docking study suggested a retaining type mechanism supported by the positioning of xylobiose between the catalytic residues Glu175 and Glu268. The −1 subsite was predominantly composed of Trp123, Glu175, Asn174, and Glu268 residues forming hydrogen bonds with xylobiose. Isothermal titration calorimetry determined the high binding affinity of *Ac*GH30A with xylobiose with an association constant (K_a) of 7.83×10^5 M^{-1}. Molecular dynamics simulations revealed consistent conformational alterations in *Ac*GH30A following the binding of the ligand, evidenced by reduced RMSD, R_g, and SASA values of the docked complex with xylobiose as compared with the free *Ac*GH30A. The average RMSD, R_g and SASA values of *Ac*GH30A in the docked complex declined by 0.39, 0.32 and 22.57 nm^2, respectively. Small-angle X-ray scattering (SAXS) studies confirmed the monodispersity and compact globular structure of *Ac*GH30A in aqueous environment. The DLS analysis of *Ac*GH30A also showed the monodisperse state with a hydrodynamic radius (R_h) of 3.7 nm. This comprehensive study highlights the mode of action of *Ac*GH30A as a xylobiohydrolase, shedding light on its unique structural and functional features. This study will enrich our understanding of industrial xylanases, particularly in terms of their structure and functions which will facilitate the rational enzyme engineering for improving their properties.

Acknowledgements

The authors are thankful to Central Instrumentation Facility and Department of Biosciences and Bioengineering at Indian Institute of Technology Guwahati, Assam, India, for Param-Ishan supercomputing facility and Dynamic Light Scattering Analysis facility, respectively. Special thanks are extended to Dr. Ravishankar Ramachandran, Principal Scientist, and his team members at CSIR-Central Drug Research Institute (CDRI), Lucknow, India for providing the SAXS facility.

Disclosure statement

No potential conflict of interest was reported by the authors.

Funding

The author(s) reported there is no funding associated with the work featured in this article.

ORCID

Yumnam Robinson Singh http://orcid.org/0009-0000-5445-6845
Jebin Ahmed http://orcid.org/0000-0003-0280-7476
Arun Goyal http://orcid.org/0000-0003-3403-9547

References

Ahmed, J., Kumar, K., Sharma, K., Fontes, C. M. G. A., & Goyal, A. (2022). Computational and SAXS-based structure insights of pectin acetyl esterase (CtPae12B) of family 12 carbohydrate esterase from *Clostridium thermocellum* ATCC 27405. *Journal of Biomolecular Structure & Dynamics*, *40*(18), 8437–8454. https://doi.org/10.1080/07391102.2021.1911858

Balasubramaniam, K., Sharma, K., & Goyal, A. (2020). Structure and dynamics analysis of a new member heparinase II/III of family 12 polysaccharide lyase from *Pseudopedobacter saltans* by computational modeling and small-angle X-ray scattering. *Journal of Biomolecular Structure & Dynamics*, *38*(7), 2007–2020. https://doi.org/10.1080/07391102.2019.1622453

Berendsen, H. J. C., van der Spoel, D., & van Drunen, R. (1995). GROMACS: A message-passing parallel molecular dynamics implementation. *Computer Physics Communications*, *91*(1–3), 43–56. https://doi.org/10.1016/0010-4655(95)00042-E

Brüx, C., Ben-David, A., Shallom-Shezifi, D., Leon, M., Niefind, K., Shoham, G., Shoham, Y., & Schomburg, D. (2006). The structure of an inverting GH43 β-Xylosidase from *Geobacillus stearothermophilus* with its substrate reveals the role of the three catalytic residues. *Journal of Molecular Biology*, *359*(1), 97–109. https://doi.org/10.1016/j.jmb.2006.03.005

Chen, L., Du, J.-L., Zhan, Y.-J., Li, J.-A., Zuo, R.-R., & Tian, S. (2018). Consolidated bioprocessing for cellulosic ethanol conversion by cellulase–xylanase cell-surfaced yeast consortium. *Preparative Biochemistry & Biotechnology*, *48*(7), 653–661. https://doi.org/10.1080/10826068.2018.1487846

Collins, T., Gerday, C., & Feller, G. (2005). Xylanases, xylanase families and extremophilic xylanases. *FEMS Microbiology Reviews*, *29*(1), 3–23. https://doi.org/10.1016/j.femsre.2004.06.005

Curry, T. M., Peña, M. J., & Urbanowicz, B. R. (2023). An update on xylan structure, biosynthesis, and potential commercial applications. *Cell Surface (Amsterdam, Netherlands)*, *9*, 100101. https://doi.org/10.1016/j.tcsw.2023.100101

Davies, G., & Henrissat, B. (1995). Structures and mechanisms of glycosyl hydrolases. *Structure (London, England: 1993)*, *3*(9), 853–859. https://doi.org/10.1016/S0969-2126(01)00220-9

El Enshasy, H. A., Kandiyil, S. K., Malek, R., & Othman, N. Z. (2016). Microbial xylanases: Sources, types, and their applications. In V. K. Gupta (Ed.), *Microbial Enzymes in Bioconversions of Biomass* (Vol. 3, pp.

151–213). Springer International Publishing. https://doi.org/10.1007/978-3-319-43679-1_7

Ernst, H. A., Mosbech, C., Langkilde, A. E., Westh, P., Meyer, A. S., Agger, J. W., & Larsen, S. (2020). The structural basis of fungal glucuronoyl esterase activity on natural substrates. *Nature Communications*, *11*(1), 1026. https://doi.org/10.1038/s41467-020-14833-9

Ficko-Blean, E., Gregg, K. J., Adams, J. J., Hehemann, J.-H., Czjzek, M., Smith, S. P., & Boraston, A. B. (2009). Portrait of an enzyme, a complete structural analysis of a multimodular β-N-acetylglucosaminidase from *Clostridium perfringens*. *The Journal of Biological Chemistry*, *284*(15), 9876–9884. https://doi.org/10.1074/jbc.M808954200

Fonseca-Maldonado, R., Ribeiro, L. F., Furtado, G. P., Arruda, L. M., Meleiro, L. P., Alponti, J. S., Botelho-Machado, C., Vieira, D. S., Bonneil, E., Furriel, R. D P. M., Thibault, P., & Ward, R. J. (2014). Synergistic action of co-expressed xylanase/laccase mixtures against milled sugar cane bagasse. *Process Biochemistry*, *49*(7), 1152–1161. https://doi.org/10.1016/j.procbio.2014.03.027

Gao, C., Guo, L., Ding, Q., Hu, G., Ye, C., Liu, J., Chen, X., & Liu, L. (2020). Dynamic consolidated bioprocessing for direct production of xylonate and shikimate from xylan by *Escherichia coli*. *Metabolic Engineering*, *60*, 128–137. https://doi.org/10.1016/j.ymben.2020.04.001

Gasteiger, E., Hoogland, C., Gattiker, A., Duvaud, S., Wilkins, M. R., Appel, R. D., & Bairoch, A. (2005). Protein identification and analysis tools on the ExPASy server. In J. M. Walker (Ed.), *The Proteomics Protocols Handbook* (pp. 571–607). Humana Press. https://doi.org/10.1385/1-59259-890-0:571

Geourjon, C., & Deléage, G. (1995). SOPMA: Significant improvements in protein secondary structure prediction by consensus prediction from multiple alignments. *Computer Applications in the Biosciences: CABIOS*, *11*(6), 681–684. https://doi.org/10.1093/bioinformatics/11.6.681

He, J., Su, L., Sun, X., Fu, J., Chen, J., & Wu, J. (2014). A novel xylanase from *Streptomyces* sp. FA1: Purification, characterization, identification, and heterologous expression. *Biotechnology and Bioprocess Engineering*, *19*(1), 8–17. https://doi.org/10.1007/s12257-013-0490-2

Henrissat, B., Callebaut, I., Fabrega, S., Lehn, P., Mornon, J. P., & Davies, G. (1995). Conserved catalytic machinery and the prediction of a common fold for several families of glycosyl hydrolases. *Proceedings of the National Academy of Sciences of the United States of America*, *92*(15), 7090–7094. https://doi.org/10.1073/pnas.92.15.7090

Henrissat, B., & Davies, G. (1997). Structural and sequence-based classification of glycoside hydrolases. *Current Opinion in Structural Biology*, *7*(5), 637–644. https://doi.org/10.1016/S0959-440X(97)80072-3

Hess, B., Kutzner, C., van der Spoel, D., & Lindahl, E. (2008). GROMACS 4: Algorithms for highly efficient, load-balanced, and scalable molecular simulation. *Journal of Chemical Theory and Computation*, *4*(3), 435–447. https://doi.org/10.1021/ct700301q

Jones, P., Binns, D., Chang, H.-Y., Fraser, M., Li, W., McAnulla, C., McWilliam, H., Maslen, J., Mitchell, A., Nuka, G., Pesseat, S., Quinn, A. F., Sangrador-Vegas, A., Scheremetjew, M., Yong, S.-Y., Lopez, R., & Hunter, S. (2014). InterProScan 5: Genome-scale protein function classification. *Bioinformatics (Oxford, England)*, *30*(9), 1236–1240. https://doi.org/10.1093/bioinformatics/btu031

Jumper, J., Evans, R., Pritzel, A., Green, T., Figurnov, M., Ronneberger, O., Tunyasuvunakool, K., Bates, R., Žídek, A., Potapenko, A., Bridgland, A., Meyer, C., Kohl, S. A. A., Ballard, A. J., Cowie, A., Romera-Paredes, B., Nikolov, S., Jain, R., Adler, J., … Hassabis, D. (2021). Highly accurate protein structure prediction with AlphaFold. *Nature*, *596*(7873), 583–589. https://doi.org/10.1038/s41586-021-03819-2

Juturu, V., & Wu, J. C. (2012). Microbial xylanases: Engineering, production and industrial applications. *Biotechnology Advances*, *30*(6), 1219–1227. https://doi.org/10.1016/j.biotechadv.2011.11.006

Kadowaki, M. A. S., Briganti, L., Evangelista, D. E., Echevarría-Poza, A., Tryfona, T., Pellegrini, V. O. A., Nakayama, D. G., Dupree, P., & Polikarpov, I. (2021). Unlocking the structural features for the xylobiohydrolase activity of an unusual GH11 member identified in a compost-derived consortium. *Biotechnology and Bioengineering*, *118*(10), 4052–4064. https://doi.org/10.1002/bit.27880

Katsimpouras, C., Dedes, G., Thomaidis, N. S., & Topakas, E. (2019). A new fungal GH30 xylanase with xylobiohydrolase auxiliary activity. *Biotechnology for Biofuels*, *12*(1), 120. https://doi.org/10.1186/s13068-019-1455-2

Klose, D. P., Wallace, B. A., & Janes, R. W. (2010). 2Struc: The secondary structure server. *Bioinformatics (Oxford, England)*, *26*(20), 2624–2625. https://doi.org/10.1093/bioinformatics/btq480

Land, H., & Humble, M. S. (2018). YASARA: A tool to obtain structural guidance in biocatalytic investigations. *Methods in Molecular Biology (Clifton, N.J.)*, *1685*, 43–67. https://doi.org/10.1007/978-1-4939-7366-8_4

Laskowski, R. A., Jabłońska, J., Pravda, L., Vařeková, R. S., & Thornton, J. M. (2018). PDBsum: Structural summaries of PDB entries. *Protein Science: A Publication of the Protein Society*, *27*(1), 129–134. https://doi.org/10.1002/pro.3289

Laskowski, R. A., & Swindells, M. B. (2011). LigPlot+: Multiple ligand–protein interaction diagrams for drug discovery. *Journal of Chemical Information and Modeling*, *51*(10), 2778–2786. https://doi.org/10.1021/ci200227u

Louis-Jeune, C., Andrade-Navarro, M. A., & Perez-Iratxeta, C. (2012). Prediction of protein secondary structure from circular dichroism using theoretically derived spectra. *Proteins*, *80*(2), 374–381. https://doi.org/10.1002/prot.23188

Lüthy, R., Bowie, J. U., & Eisenberg, D. (1992). Assessment of protein models with three-dimensional profiles. *Nature*, *356*(6364), 83–85. https://doi.org/10.1038/356083a0

MacArthur, M. W., Laskowski, R. A., & Thornton, J. M. (1994). Knowledge-based validation of protein structure coordinates derived by X-ray crystallography and NMR spectroscopy. *Current Opinion in Structural Biology*, *4*(5), 731–737. https://doi.org/10.1016/S0959-440X(94)90172-4

Madeira, F., Pearce, M., Tivey, A. R. N., Basutkar, P., Lee, J., Edbali, O., Madhusoodanan, N., Kolesnikov, A., & Lopez, R. (2022). Search and sequence analysis tools services from EMBL-EBI in 2022. *Nucleic Acids Research*, *50*(W1), W276–W279. https://doi.org/10.1093/nar/gkac240

Maehara, T., Yagi, H., Sato, T., Ohnishi-Kameyama, M., Fujimoto, Z., Kamino, K., Kitamura, Y., St John, F., Yaoi, K., & Kaneko, S. (2018). GH30 Glucuronoxylan-specific xylanase from *Streptomyces turgidiscabies* C56. *Applied and Environmental Microbiology*, *84*(4), e01850-17. https://doi.org/10.1128/AEM.01850-17

McGuffin, L. J., Bryson, K., & Jones, D. T. (2000). The PSIPRED protein structure prediction server. *Bioinformatics (Oxford, England)*, *16*(4), 404–405. https://doi.org/10.1093/bioinformatics/16.4.404

Mirdita, M., Schütze, K., Moriwaki, Y., Heo, L., Ovchinnikov, S., & Steinegger, M. (2022). ColabFold: Making protein folding accessible to all. *Nature Methods*, *19*(6), 679–682. https://doi.org/10.1038/s41592-022-01488-1

Moreira, L. R. S., & Filho, E. X. F. (2016). Insights into the mechanism of enzymatic hydrolysis of xylan. *Applied Microbiology and Biotechnology*, *100*(12), 5205–5214. https://doi.org/10.1007/s00253-016-7555-z

Morris, G. M., Huey, R., Lindstrom, W., Sanner, M. F., Belew, R. K., Goodsell, D. S., & Olson, A. J. (2009). AutoDock4 and AutoDockTools4: Automated docking with selective receptor flexibility. *Journal of Computational Chemistry*, *30*(16), 2785–2791. https://doi.org/10.1002/jcc.21256

Nakamichi, Y., Watanabe, M., Matsushika, A., & Inoue, H. (2020). Substrate recognition by a bifunctional GH30-7 xylanase B from *Talaromyces cellulolyticus*. *FEBS Open Bio*, *10*(6), 1180–1189. https://doi.org/10.1002/2211-5463.12873

Nikolaivits, E., Pentari, C., Kosinas, C., Feiler, C. G., Spiliopoulou, M., Weiss, M. S., Dimarogona, M., & Topakas, E. (2021). Unique features of the bifunctional GH30 from *Thermothelomyces thermophila* revealed by structural and mutational studies. *Carbohydrate Polymers*, *273*, 118553. https://doi.org/10.1016/j.carbpol.2021.118553

O'Boyle, N. M., Banck, M., James, C. A., Morley, C., Vandermeersch, T., & Hutchison, G. R. (2011). Open Babel: An open chemical toolbox. *Journal of Cheminformatics*, *3*(1), 33. https://doi.org/10.1186/1758-2946-3-33

Okuyama, M., Kitamura, M., Hondoh, H., Kang, M.-S., Mori, H., Kimura, A., Tanaka, I., & Yao, M. (2009). Catalytic mechanism of retaining α-galactosidase belonging to glycoside hydrolase family 97. *Journal of Molecular Biology*, *392*(5), 1232–1241. https://doi.org/10.1016/j.jmb.2009.07.068

Pettersen, E. F., Goddard, T. D., Huang, C. C., Couch, G. S., Greenblatt, D. M., Meng, E. C., & Ferrin, T. E. (2004). UCSF Chimera—A visualization system for exploratory research and analysis. *Journal of Computational Chemistry*, *25*(13), 1605–1612. https://doi.org/10.1002/jcc.20084

Puchart, V., Šuchová, K., & Biely, P. (2021). Xylanases of glycoside hydrolase family 30—An overview. *Biotechnology Advances*, *47*, 107704. https://doi.org/10.1016/j.biotechadv.2021.107704

Ren, J., Wen, L., Gao, X., Jin, C., Xue, Y., & Yao, X. (2009). DOG 1.0: Illustrator of protein domain structures. *Cell Research*, *19*(2), 271–273. https://doi.org/10.1038/cr.2009.6

Robert, X., & Gouet, P. (2014). Deciphering key features in protein structures with the new ENDscript server. *Nucleic Acids Research*, *42*, W320–324. https://doi.org/10.1093/nar/gku316

Roblin, P., Potocki-Véronèse, G., Guieysse, D., Guerin, F., Axelos, M. A. V., Perez, J., & Buleon, A. (2013). SAXS conformational tracking of amylose synthesized by amylosucrases. *Biomacromolecules*, *14*(1), 232–239. https://doi.org/10.1021/bm301651y

Rohman, A., Dijkstra, B. W., & Puspaningsih, N. N. T. (2019). β-Xylosidases: Structural diversity, catalytic mechanism, and inhibition by monosaccharides. *International Journal of Molecular Sciences*, *20*(22), 5524. https://doi.org/10.3390/ijms20225524

Schüttelkopf, A. W., & van Aalten, D. M. F. (2004). PRODRG: A tool for high-throughput crystallography of protein–ligand complexes. *Acta Crystallographica. Section D, Biological Crystallography*, *60*(Pt 8), 1355–1363. https://doi.org/10.1107/S0907444904011679

Singh, Y. R., Thakur, A., Fontes, C. M. G. A., & Goyal, A. (2024). A novel thermophilic recombinant obligate xylobiohydrolase (AcGH30A) from Acetivibrio clariflavus orchestrates the deconstruction of xylan polysaccharides. *Carbohydrate Polymers*, *340*, 122295. https://doi.org/10.1016/j.carbpol.2024.122295

St John, F. J., Crooks, C., Kim, Y., Tan, K., & Joachimiak, A. (2022). The first crystal structure of a xylobiose-bound xylobiohydrolase with high functional specificity from the bacterial glycoside hydrolase family 30, subfamily 10. *FEBS Letters*, *596*(18), 2449–2464. https://doi.org/10.1002/1873-3468.14454

St John, F. J., Dietrich, D., Crooks, C., Balogun, P., de Serrano, V., Pozharski, E., Smith, J. K., Bales, E., & Hurlbert, J. (2018). A plasmid borne, functionally novel glycoside hydrolase family 30 subfamily 8 endoxylanase from solventogenic *Clostridium*. *The Biochemical Journal*, *475*(9), 1533–1551. https://doi.org/10.1042/BCJ20180050

St John, F. J., Dietrich, D., Crooks, C., Pozharski, E., González, J. M., Bales, E., Smith, K., & Hurlbert, J. C. (2014). A novel member of glycoside hydrolase family 30 subfamily 8 with altered substrate specificity. *Acta Crystallographica. Section D, Biological Crystallography*, *70*(Pt 11), 2950–2958. https://doi.org/10.1107/S1399004714019531

Šuchová, K., Chyba, A., Hegyi, Z., Rebroš, M., & Puchart, V. (2022). Yeast GH30 xylanase from *Sugiyamaella lignohabitans* is a glucuronoxylanase with auxiliary xylobiohydrolase activity. *Molecules (Basel, Switzerland)*, *27*(3), 751. https://doi.org/10.3390/molecules27030751

Šuchová, K., Puchart, V., Spodsberg, N., Mørkeberg Krogh, K. B. R., & Biely, P. (2020). A novel GH30 xylobiohydrolase from *Acremonium alcalophilum* releasing xylobiose from the non-reducing end. *Enzyme and Microbial Technology*, *134*, 109484. https://doi.org/10.1016/j.enzmictec.2019.109484

Šuchová, K., Puchart, V., Spodsberg, N., Mørkeberg Krogh, K. B. R., & Biely, P. (2021). Catalytic diversity of GH30 xylanases. *Molecules (Basel, Switzerland)*, *26*(15), 4528. https://doi.org/10.3390/molecules26154528

Thakur, A., Sharma, K., & Goyal, A. (2019). α-L-arabinofuranosidase: A potential enzyme for the food industry. In *Green bio-processes* (pp. 229–244). Springer. https://doi.org/10.1007/978-981-13-3263-0_12

Tian, W., Chen, C., Lei, X., Zhao, J., & Liang, J. (2018). CASTp 3.0: Computed atlas of surface topography of proteins. *Nucleic Acids Research*, *46*(W1), W363–W367. https://doi.org/10.1093/nar/gky473

Urbániková, Ľ., Vršanská, M., Mørkeberg Krogh, K. B. R., Hoff, T., & Biely, P. (2011). Structural basis for substrate recognition by *Erwinia chrysanthemi* GH30 glucuronoxylanase. *The FEBS Journal*, *278*(12), 2105–2116. https://doi.org/10.1111/j.1742-4658.2011.08127.x

Vuong, T. V., & Wilson, D. B. (2010). Glycoside hydrolases: Catalytic base/nucleophile diversity. *Biotechnology and Bioengineering*, *107*(2), 195–205. https://doi.org/10.1002/bit.22838

Wiederstein, M., & Sippl, M. J. (2007). ProSA-web: Interactive web service for the recognition of errors in three-dimensional structures of proteins. *Nucleic Acids Research*, *35*, W407–W410. https://doi.org/10.1093/nar/gkm290

Yuan, S., Chan, H. C. S., & Hu, Z. (2017). Using PyMOL as a platform for computational drug design. *WIREs Computational Molecular Science*, *7*(2), 1298. https://doi.org/10.1002/wcms.1298